DISSERTATION

IMPACTS OF UNCONVENTIONAL OIL AND GAS DEVELOPMENT

ON ATMOSPHERIC AEROSOL PARTICLES

Submitted by

Ashley R. Evanoski-Cole

Department of Atmospheric Science

In partial fulfillment of the requirements

For the Degree of Doctor of Philosophy

Colorado State University

Fort Collins, Colorado

Summer 2017

Doctoral Committee:

   Advisor: Jeffrey L. Collett, Jr.

   Sonia M. Kreidenweis
   Jeffrey R. Pierce
   Jay Ham

ABSTRACT

IMPACTS OF UNCONVENTIONAL OIL AND GAS DEVELOPMENT

ON ATMOSPHERIC AEROSOL PARTICLES

Rising demands for global energy production and shifts in the economics of fossil fuel production have recently driven rapid increases in unconventional oil and gas drilling operations in the United States. Limited field measurements of atmospheric aerosol particles have been conducted to understand the impacts of unconventional oil and gas extraction on air quality. These impacts can include emissions of greenhouse gases, the release of volatile organic compounds that can be hazardous and precursors to tropospheric ozone formation, and increases in atmospheric aerosol particles. Aerosol particles can also contribute to climate change, degrade visibility and negatively impact human health and the environment. Aerosol formation can result from a variety of activities associated with oil and gas drilling operations, including emission of particles and/or particle precursors such as nitrogen oxides from on-site power generation, evaporation or leaking of fracking fluids or the produced fuel, flaring, the generation of road dust, and increases in traffic and other anthropogenic emissions associated with growing populations near drilling locations. The work presented here details how activities associated with unconventional oil and gas extraction impact aerosol particle characteristics, sources, and formation in remote regions.

An air quality field study was conducted in the Bakken formation region during a period of rapid growth in oil production by unconventional techniques over two winters in 2013 and 2014. The location and time of year were chosen because long term IMPROVE network

monitoring records show an increasing trend in particulate nitrate concentrations and haze in the Bakken region during the winter, strongly contrasting with sharp decreases observed across most of the U.S. The comprehensive suite of instrumentation deployed for the Bakken Air Quality Study (BAQS) included measurements of aerosol concentrations, composition, and scattering, gaseous precursors important for aerosol formation, volatile organic compounds, and meteorology.

Regional measurements of inorganic aerosol composition were collected, with average concentrations of total inorganic $PM_{2.5}$ between $4.78 – 6.77$ µg m^{-3} and $1.99 – 2.52$ µg m^{-3} for all sampling sites during the 2013 and 2014 study periods, respectively. The maximum inorganic $PM_{2.5}$ concentration observed was 21.3 µg m^{-3} for a 48 hour filter sample collected at Fort Union National Historical Site, a site located within a dense area of oil wells. Organic aerosol measurements obtained during the second study at the north unit of Theodore Roosevelt National Park (THRO-N) featured an average concentration of 1.1 ± 0.7 µg m^{-3}. While oil production increased from 2013 to 2014, the lower $PM_{2.5}$ in 2014 can be explained by the meteorological differences. During the first study, increased snow cover, atmospheric stability, solar illumination, and differences in the dominant wind direction contributed to higher $PM_{2.5}$.

The enhanced concentrations of inorganic $PM_{2.5}$ measured in the Bakken region were tied to regional oil and gas development. Elevated concentrations of $PM_{2.5}$ were observed during periods of air mass stagnation and recirculation and were associated with VOC emissions aged less than a day, both indicating a predominant influence from local emissions. High $PM_{2.5}$ concentrations occurred when low i-/n-pentane VOC ratios were observed, indicating strong contributions from oil and gas operations.

The hourly measurements of gas and aerosol species in an extremely cold environment also provided a unique data set to investigate how well thermodynamic aerosol models represent the partitioning of ammonium nitrate. In general, during the coldest temperatures, the models overpredicted the formation of particulate nitrate. The formation of additional $PM_{2.5}$ in this region is more sensitive to availability of N(-III) species during the coldest periods but increasingly sensitive to available N(V) when temperatures are relatively warmer and ammonia availability increases. These measurements and modeling results show that continued growth of oil and gas drilling operations in remote areas such as the Bakken region could lead to increased $PM_{2.5}$ and impact haze formation in nearby federally protected lands.

ACKNOWLEDGEMENTS

First and foremost, I would like to acknowledge my advisor, Jeff Collett, for being an exceptional mentor and teacher. His balance of both supporting me and giving me the freedom to pursue independent research has shaped me to be the scientist I am today. His wealth of knowledge, patience and humor has been invaluable in helping me succeed and thoroughly enjoy my time at CSU. The insight and dedication offered by my committee members was also essential to the successful completion of this work. Thank you, Sonia Kreidenweis, Jeff Pierce and Jay Ham.

I also have tremendous appreciation for past and present members of the Collett research group. Katie Benedict, Andrea Clements, Arsineh Hecobian, Yi Li, Misha Schurman, Amy Sullivan, and Yong Zhou have all helped with operating instrumentation, analyzing samples, collecting measurements during field campaigns, and occasionally exchanging field work and lab horror stories. I would also like to thank Ali Boris, Yixing Shao, Derek Weber and the many other students and researchers in the atmospheric science department for insightful conversations and just for being great people to work with. Whenever I had a question I could always find someone with an answer or an idea to get started towards finding the answer. I will miss working with and being around this group of exceptional people.

The field work conducted for this research would not have been possible if not for the dedicated group of scientists who both planned and participated in the field project as well as helped with data analysis. In addition to many members of the Collett group, Bret Schichtel, William Malm, Kristi Gebhart, Derek Day, Anthony Prenni, Jenny Hand, and Barkley Sive, affiliated with the National Park Service and the Cooperative Institute for Research in the

TABLE OF CONTENTS

LIST OF TABLES

LIST OF FIGURES

1.0 INTRODUCTION

1.1 Unconventional Oil and Natural Gas Drilling Background

With the continual expansion of globalization and growth of the global economy, demand for greater energy production around the world is increasing. Although renewable energy sources are projected to increase in the future, fossil fuel use accounts for 78% of total energy use in the year 2040 (U.S. Energy Information Administration, 2016a). Global use of natural gas is projected to increase more sharply than the use of liquid fuels and exceed that of coal (Figure 1.1). A large contribution to this is the projected continued use of natural gas from unconventional drilling, which includes the extraction of oil and gas (O&G) from shale, tight sands and coalbed methane.
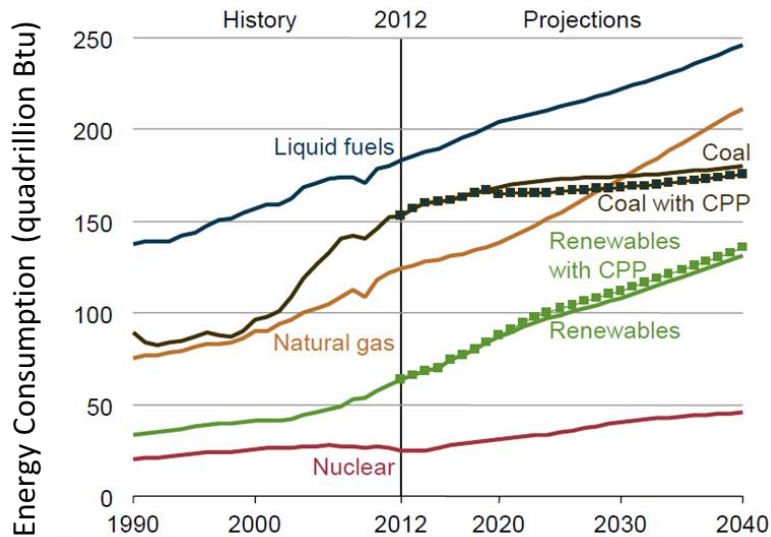
Figure 1.1: Projections of energy consumption by energy source including nuclear (red), renewables (green), natural gas (orange), coal (black), and liquid fuels (blue) through the year 2040. Square markers represent the projections which include the United States Clean Power Plant regulations (adapted from U.S. Energy Information Administration, 2016).

Unconventional O&G deposits are being explored and drilled world-wide. Estimates of recoverable shale gas predict that 7,299 trillion cubic feet exist globally (Cooper et al., 2016) and 482 trillion cubic feet exists in the United States (US Goverment Accountability Office, 2012). Figure 1.2 shows shale gas, tight gas and coalbed methane deposits around the world (PacWest Consulting Partners, 2012). The U.S. has large deposits of all three types of unconventional O&G formations and currently produces more O&G from unconventional techniques than any other country (Cooper et al., 2016).
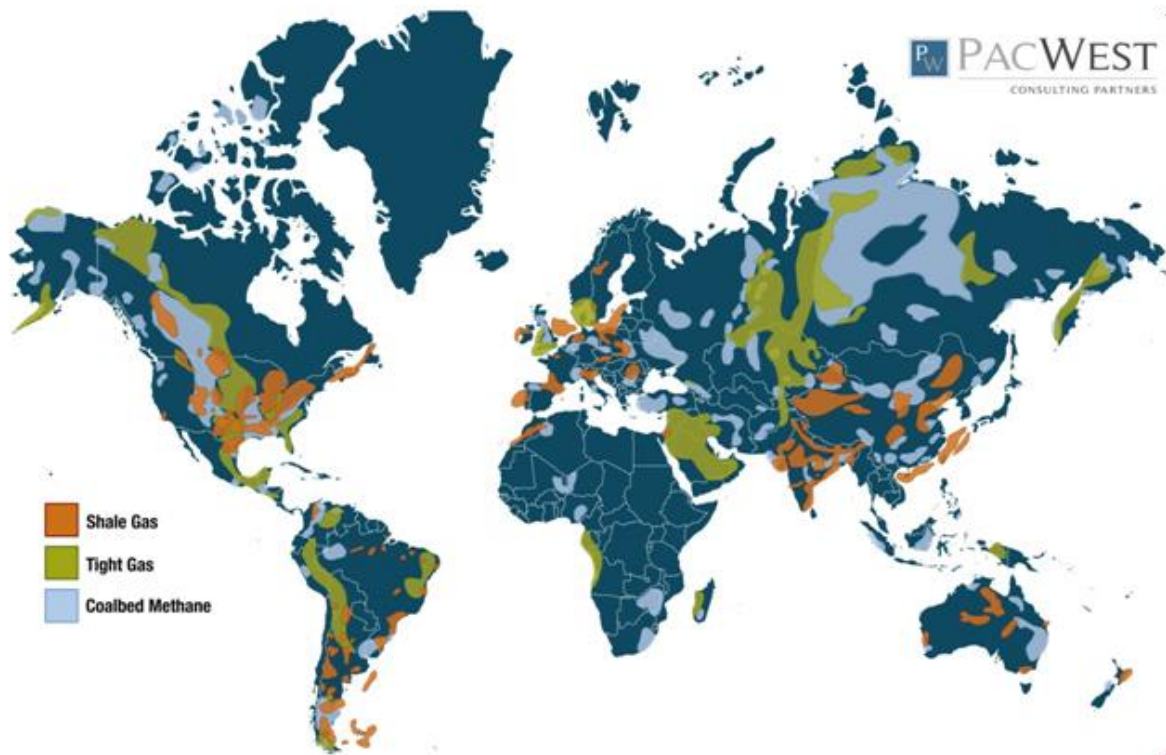
Figure 1.2: Global map of shale gas (orange), tight gas (green) and coalbed methane (light blue; PacWest Consulting Partners, 2012).

Within the U.S., the O&G industry supplies about 60% of the energy needs (US Goverment Accountability Office, 2012). In recent years, extraction from shale gas and tight oil plays has increased dramatically and is projected to continue to increase and by 2040, shale plays will make up two thirds of total production of natural gas (Figure 1.3). Extraction from tight gas,

and other conventional onshore and offshore extraction techniques are projected to decrease or remain constant. However, these projections are highly uncertain because the production rates of O&G plays that have not yet produced are estimated. Uncertainty in the future economy also contributes to this uncertainty because the prices of oil and natural gas strongly influence production.
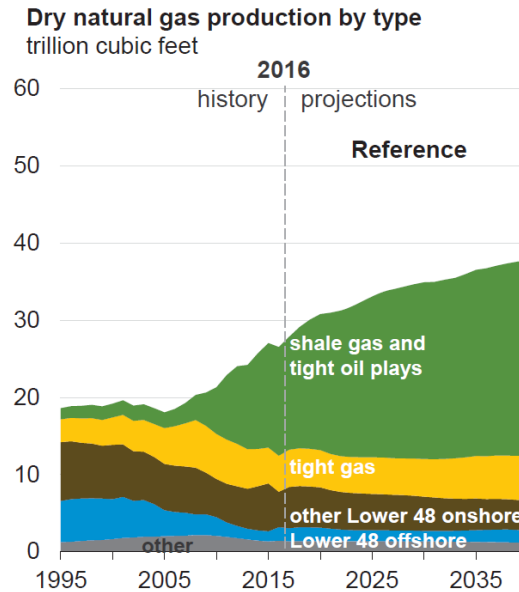
Figure 1.3: Projections of dry natural gas production in the U.S. colored by type of extraction (U.S. Energy Information Administration, 2017).

The unconventional drilling techniques of horizontal drilling and hydraulic fracturing, or "fracking," have existed since the 1930s and 1940s, respectively, but until recently conventional techniques have been more economically feasible (Blake, 2016). In tight gas, shale and coalbed methane, the O&G is trapped in small pockets within impermeable material such as coal, shale, limestone, sandstone or other hard rock. O&G deposits generally exist in layers in the subsurface, as represented in Figure 1.4, so conventional vertical drilling does not effectively reach the O&G deposits. Horizontal drilling is used to maximize the area of the deposit reached by the drilled borehole. After drilling, hydraulic fracturing is used to break up the formation, freeing the trapped O&G. In the fracturing process, hydraulic fracturing fluid, or frac fluid, is

injected into the borehole at very high pressure so that cracks and fissures are created within the

rock formation. Frac fluid contains water, salt, proppants and a mixture of chemicals to give the

fluid ideal chemical properties for effective extraction of the O&G. This blend of chemicals is

often proprietary, but includes a mixture of acids, corrosion inhibitors, friction reducers, clay

control, crosslinkers, scale inhibitors, breakers, iron control compounds, biocides, and gellants

(Frac Focus Chemical Disclosure Registry, 2017). Proppants are small particles such as silica

sand that are used to keep the induced fractures open.
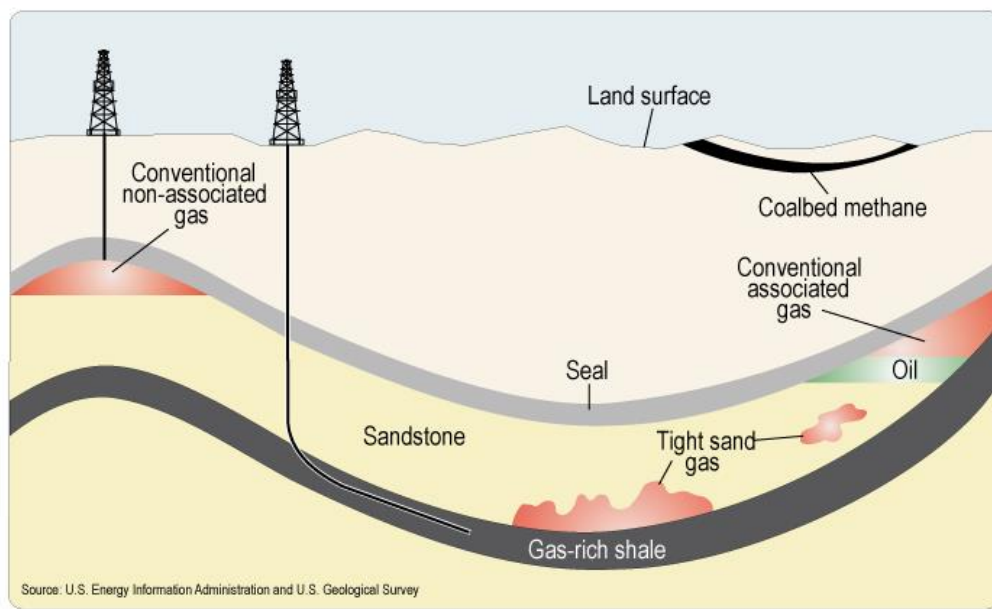
Figure 1.4: Cross sectional view of the geology of natural resources underground, including a depiction of horizontal drilling in a gas-rich shale deposit (U.S. Energy Information Administration, 2011).

Numerous potential environmental concerns are associated with unconventional O&G

drilling practices. The transportation, storage and use of frac fluids can negatively affect both

water and air quality. Evaporation and percolation pits are used to get rid of wastewater after the

fluids are used in the drilling operations (U.S. Environmental Protection Agency, 2016). This

method can allow volatile compounds present in the wastewater to evaporate (Estrada and

Bhamidimarri, 2016). If frac fluid is spilled, it can seep into the ground and potentially

contaminate soil, ground water, runoff, and surface waters. Spills can occur during

transportation in trucks, from storage containers, during well injection, and from flowback and

produced waters with the most common cause being equipment failure (Rester and Warner,

2016). Frac fluid exposed to the air can also be a source of hazardous air pollutants. The rate of

spills is not a negligible source of environmental contamination, with an estimated 2-16% of all

wells reporting at least one spill per year from the states of Colorado, New Mexico, North

Dakota, and Pennsylvania and 6,622 total spills reported from 2005-2015 in New Mexico, North

Dakota, and Pennsylvania and from 2005-2013 in Colorado (Maloney et al., 2017; Patterson et

al., 2017).

1.3 Air Quality Impacts from Oil and Natural Gas Drilling

Emissions inventories from the Denver-Julesburg, Bakken, Marcellus and several other

U.S. natural gas basins (Bar-Ilan et al., 2008; Grant et al., 2014a; Roy et al., 2014) have been

developed for unconventional drilling techniques by providing estimates for emissions of

methane and other volatile organic compounds (VOCs), nitrogen oxides (NO_x), ozone, other

hazardous air pollutants, and particulate matter (PM) which are emitted from different processes

associated with O&G development. These studies estimate a total amount of a certain compound

emitted by summing the measurements of the compound generated from different components of

the O&G extraction process, including drilling rigs, frac pumps, compressor engines, and

compressor stations. Emissions from transportation and storage, which include condensate

tanks, water tanks, and trucks, can also be included in the inventories.

In addition to emissions inventory studies, air quality studies near O&G basins have

provided information on ambient concentrations of specific compounds generated from these

processes. Many previous studies in regions of O&G development have focused on understanding methane and VOC emissions from O&G drilling operations (e.g. Field et al., 2015; Helmig et al., 2014; Moore et al., 2014; Swarthout et al., 2015; Yuan et al., 2015). In addition to ground based measurements, remote sensing techniques have been used to estimate regional concentrations of methane and VOCs (Schneising et al., 2014). Quantifying methane emissions, an extremely potent greenhouse gas, is important for understanding impacts on climate change. Methane emissions can be sporadic and often associated with leaks or failing equipment, so reducing emissions generally involves regularly scheduled equipment checks and leak tests (Lyon, 2016). Hydrogen sulfide (H_2S) is a toxic compound present in some O&G basins that can be emitted from O&G extraction processes and has negative impacts on human health (Li et al., 2014a).

Emissions of VOCs can have direct negative impacts on human health. Compounds such as benzene, toluene, ethylbenzene, m+p-xylenes and o-xylenes (BTEX) are carcinogenic and can reach high concentrations near O&G operations (Brown et al., 2015). VOCs can also form secondary pollutants such as ozone and secondary organic aerosol (SOA). High concentrations of ozone and other pollutants were also observed during years with snow cover in the Uinta basin (Edwards et al., 2014) and the Upper Green River basin (Field et al., 2015). Additionally, modeling studies have shown that VOC emissions from O&G operations near urban areas have the potential to enhance ozone formation (Rodriguez et al., 2009). Observations near the Uinta basin have shown the formation of particulate organic nitrate from the reaction between VOCs and NO_x (Lee et al., 2014).

Black carbon (BC) and NO_x emissions can originate from combustion processes in diesel engines or flaring. During the drilling process, diesel engines are used at the drilling sites to

power equipment, generating BC and NO_x emissions (Khalek et al., 2015; U.S. Environmental Protection Agency, 2012). The use of trucks to transport frac fluid, equipment and supplies, and the increased traffic can elevate BC and NO_x concentrations near the O&G operations (Korfmacher et al., 2015). The process of flaring, burning extracted natural gas that is not economical to keep or is a waste product, is performed to convert methane to carbon dioxide (CO_2), which is a less potent greenhouse gas. Flaring has also been determined to be a significant source of BC, NO_x, sulfur dioxide (SO_2), CO_2, carbon monoxide (CO) and unburned hydrocarbons (Fawole et al., 2016; Giwa et al., 2014; Stohl et al., 2013). Elevated BC concentrations, between 0.02-0.05 $\mu g\ m^{-3}$, were measured in an aircraft study in the Bakken region over an area of dense flaring (Schwarz et al., 2015). In a modeling study performed using measurements from the Marcellus shale basin, 6-18% of NO_x emissions are projected to come from O&G activities in 2020 (Roy et al., 2014).

Previous air quality studies investigating aerosol and gaseous PM precursor concentrations from locations near O&G development are limited. Considering only field campaigns conducted in the winter, when inorganic ammonium nitrate formation is favored, three locations were chosen which are shown in Table 1.1. One study took place in the Uinta basin in Utah over five consecutive winters between 2010 and 2014. This basin contains both O&G wells. Another study was conducted in Boulder, Wyoming in the Upper Green River Basin from five years between 2007 and 2011. The last study considered took place in the Colorado Front Range during the Nitrogen, Aerosol Composition, and Halogens on a Tall Tower (NACHTT) field campaign in 2011. Measurements from the Uinta Basin and Upper Green River Basin are rural and should have minimal influence from local or regional anthropogenic pollution, although the Green River Basin is sometimes downwind of the Snake River Valley, an

area of active agricultural production. The Colorado Front Range measurement location is an

urban/suburban local with impacts from anthropogenic sources including oil and natural gas

development in the Niobrara Basin (Brown et al., 2013b), mobile sources, electric power

generation, and agriculture. Each basin is highlighted in the map of U.S. shale plays (Figure

1.5).

Table 1.1: Ammonia (NH_3), nitric acid (HNO_3) and $PM_{2.5}$ measurements made during the winter in areas near intensive oil and natural gas drilling operations.

	NH_3	HNO_3	$PM_{2.5}$
Study Period	**1. Uinta Basin, UT[*1,2,3]**		
2010	-	-	7.2-8.8 (n=2)
2011	-	-	7.8-11.8 (n=3)
2012	-	0.54 ± 0.41 ppb[3]	2.7-7.9 (n=6)
2013	0.12 ppb[3]	4.5 ± 3.2 ppb[3]	4.9-19.9 (n=6)
2014	-	-	2.0-9.5 (n=6)
	2. Upper Green River Basin, WY[4]		
2006-2011	0.07 ppb (0.04 µg m^{-3})	0.08 ppb (0.19 µg m^{-3})	1.21 µg m^{-3}
	3. Front Range, CO[5]		
2011	5.79 ppb	0.202 ppb	-

* Range of daily mean $PM_{2.5}$ concentrations (µg m^{-3}) from sampling sites within the basin (n)[1] and NH_3 and HNO_3 from the Horsepool site[2,3]
1.(Stoeckenius, 2015)
2.(Lyman et al., 2013)
3.(Roberts et al., 2014)
4.(Li et al., 2014b)
5.(Young et al., 2013), median values
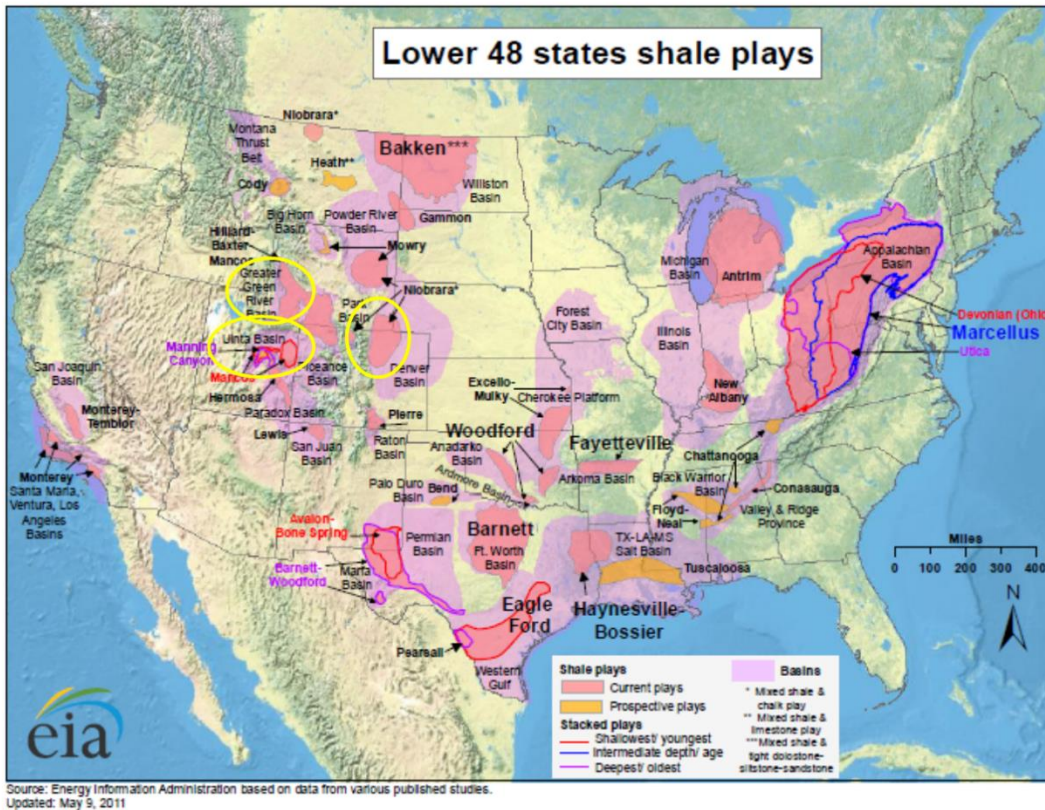
Figure 1.5: Map showing the U.S. current shale plays in salmon and the basins in purple (https://www.eia.gov/maps/maps.htm).

The concentration ranges observed for each species, HNO_3 (0.08 – 4.5 ppb), NH_3 (0.07 – 5.79 ppb), and $PM_{2.5}$ (1.21 – 19.9 µg m^{-3}), show that total $PM_{2.5}$ and precursor gases vary annually and by location. The large temporal variability observed in the Uinta Basin has been linked to differences in meteorology year to year. For example, 2012 was a relatively snow free year but 2011 and 2013 had snow cover for the majority of the study period. The snow cover led to an increase in solar radiation and formation of strong temperature inversions that acted to trap pollutants within the basin. $PM_{2.5}$ concentrations were higher in 2011 and 2013 compared to 2012 across all measurement sites.

Measurements in the Upper Green River basin in Wyoming were also elevated due to enhanced solar radiation in the presence of snow cover leading to enhanced photochemistry.

9

Elevated concentrations of HNO_3 observed during the winter measurement periods were associated with increased local NO_x emissions from the O&G development and were enhanced due to the formation of a temperature inversion and the same active winter photochemistry over the snow-covered surface that produces elevated ozone concentrations (Li et al., 2014b). The study in the Front Range used VOC tracers to determine that O&G development impacted the measurement site, but did not correlate HNO_3 concentrations to O&G activities. During the measurement period, no snowfall occurred so no enhancements in solar radiation were experienced (Brown et al., 2013b). This site is also in a unique location near large agricultural operations, so the higher NH_3 observed there compared to the Uinta and Upper Green River basins is due to local emissions from cattle feedlots and other agricultural sources (Day et al., 2012).

1.4. Aerosol Formation in Regions of Oil and Gas Development

1.4.1 Inorganic Aerosol Formation

In the atmosphere, emissions of SO_2 can oxidize to form sulfuric acid (H_2SO_4) which readily condenses into the particle phase. In the presence of NH_3, ammonium sulfate (AS) aerosol will form preferentially. If excess N(-III) exists, ammonium nitrate (AN) can form (Seinfeld and Pandis, 2006). Excess N(-III) can be calculated using Equation 1.1, by subtracting twice the measured particulate SO_4^{2-} from total N(-III), with all concentrations in molar units. When excess N(-III) is present, formation of AN is highly dependent on temperature and relative humidity and is favored in cold and humid conditions (Stelson and Seinfeld, 1982). Equation 1.1 represents a lower bound on excess N(-III) concentrations based on work by Silvern et al. (2016) and Weber et al. (2016) who suggest that in some regions, excess N(-III) can exist despite incomplete neutralization of SO_4^{2-}.

$$[N(-III)]_{excess} = [NH_4^+] + [NH_3] - 2 * [SO_4^{2-}]$$ Equation 1.1

The formation of AN and AS can be investigated using thermodynamic models such as E-AIM (Clegg et al., 1998b) or ISORROPIA (Nenes, 1998). In the models, meteorological conditions and thermodynamic properties are used to predict gas, aqueous and solid concentrations of common atmospheric constituents. First, the equilibrium between vapor and aqueous phase species in the atmosphere is considered, which is represented by step (a) in Figure 1.6. The concentration of species A in the aqueous phase [A(aq)] can be equated to the partial pressure of the species in the gas phase (p_A) multiplied by the Henry's Law coefficient (H_A) as shown in Equation 1.2. This relationship is temperature dependent, with H_A generally decreasing as temperatures increase, indicating gases are more soluble at lower temperatures (Seinfeld and Pandis, 2006). An example from E-AIM to calculate the Henry's Law coefficient for HNO_3, borrowed from Clegg et al., 1998, uses the dependencies on temperature (T) and the equilibrium constant ($K_H(HNO_3)$) as derived from experimental results (Equation 1.3).
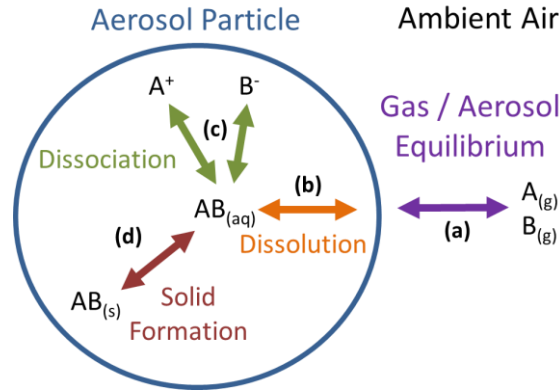
Figure 1.6: A visual representation of the gas – aerosol chemical system showing the partitioning between gas, aqueous and solid phases, modified from the model system represented in E-AIM (Clegg et al., 2016).

$$[A(aq)] = H_A p_A$$ Equation 1.2

$$ln[K_H(HNO_3)] = 359.0 - \frac{3020}{T} - 71.0\ln(T) + 0.131 \times T - 0.421 \times 10^{-4}T^2$$ Equation 1.3

The model calculates an experimental H_A, to determine the equilibrium concentrations of the gas and aqueous species, using known values of activity coefficients, enthalpies and heat capacities for each species. Henry's Law, as shown in Equation 1.2, assumes a dilute solution, which is not always the case for atmospheric aerosol, depending on the liquid water content and concentrations of the ionic species present in the aerosol particle. To account for the nonideality in a concentrated solution, the chemical potential of species A (μ_A), is calculated as shown in Equation 1.4 (Nenes, 1998) as it relates to the standard chemical potential (μ_A^*). The chemical potential is a function of the ideal gas law constant (R), temperature (T), the activity coefficient (α_i) and the mole fraction of the species (χ_i)

$$\mu_A = \mu_A^*(T,p) + RT \ln(\alpha_i \chi_i) \qquad \text{Equation 1.4}$$

Once a gas phase species is dissolved into aqueous solution, such as in an aerosol particle in the atmosphere, ionic species will dissociate and take some time to reach equilibrium, represented by step (c) in Figure 1.6. This equilibrium, calculated using a thermodynamic dissociation constant, is generally reached quickly and is dependent on the pH of the solution. Strong electrolytes will dissociate completely, while weak electrolytes will only partially dissociate. The dissolution (Figure 1.6b) and dissociation (Figure 1.6c) for compound AB is shown in Equation 1.5 (Clegg et al., 1998b; Wexler and Clegg, 2002) and calculation of the thermodynamic dissociation constant (K_{AB}) is shown in Equation 1.6. K_{AB} is calculated using the product of the mole fraction (χ) and mole fraction activity (f) for each of the reactants and products.

$$AB \leftrightarrow A^+_{(aq)} + B^-_{(aq)} + H_2O_{(l)} \qquad \text{Equation 1.5}$$
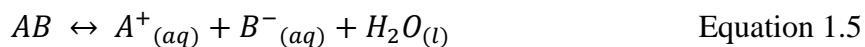
$$K_{AB} = \frac{(\chi_{A^+} f_A^*)(\chi_{B^-} f_B^*)(\chi_{H_2O} f_{H_2O}^*)}{\chi_{AB} f_{AB}^*} \qquad \text{Equation 1.6}$$

The equilibrium between the aqueous and solid phases within the aerosol particle is represented by step (d) in Figure 1.6. In E-AIM, solubility data is used to constrain the equilibrium between aqueous and solid phases. Depending on model settings, solids can be allowed to form when the species reaches saturation with respect to solid phase. The formation of solids from ionic compounds A and B is shown in Equation 1.7. The thermodynamic solubility product (K_S) is calculated using the mole fractions and mole fraction activities of each species. The term for the solid species is not included in the denominator because it is equal to one. Saturation occurs when the ratio of the activity products to K_s in Equation 1.7 equals one (Wexler and Clegg, 2002).

$$K_S = (\chi A^+ f_A^*)(\chi B^- f_B^*)(\chi H_2 O f_{H_2O}^*)$$
Equation 1.7

Alternatively, when run in metastable mode, the model can allow aqueous species to remain dissolved in the aerosol particle in a supersaturated state. The presence of supersaturated aqueous species in aerosol particles was found to be common in laboratory studies (Clegg et al., 1998a, 1998b). Some atmospheric aerosol components exhibit a unique behavior when taking up water over a range of relative humidity (RH) values.

The metastable state of aerosol particles also relates to how the aqueous and solid phases of aerosol particles vary as a function of RH. Wet particle size has a complex dependence on RH for aerosol salt particles. When starting at a low RH, the aerosol particle remains as a dry solid until the deliquescence relative humidity (DRH), when it is first hydrated to form saturated solution and will subsequently grow by additional water condensation as RH increases, following the deliquescence or stable curve. Conversely, when a wet aerosol particle starts at a high RH, it will gradually lose water following the metastable curve until it crystallizes when reaching the efflorescence relative humidity (ERH), following the metastable curve. The aerosol

particles exist solely in the aqueous phase above the DRH and solely in the crystalline phase below the ERH. A hysteresis region exists between the relative humidities of efflorescence and deliquescence, with greater wet particle diameter and water content on the upper, metastable branch of the water content curve.

In regions of O&G development, enhanced emissions of NO_x can potentially enhance inorganic particle formation based on concentrations of other inorganic precursor species, such as NH_3 and SO_2, and the meteorological conditions. NO_x will oxidize to form HNO_3 in the atmosphere and can form inorganic aerosol as described above. It is important to measure the concentrations of each inorganic precursor gas species and the meteorological conditions to understand formation of inorganic aerosol. Thermodynamic models can be used to understand chemical and physical properties of the aerosol formed, such as pH, and can also be used to predict how $PM_{2.5}$ concentrations will change as O&G development impacts air quality. National trends in emissions have led to changes in aerosol composition and thermodynamic properties across the U.S. Regulations on vehicle and power plant emissions have reduced both the emissions of NO_x and SO_2 and the concentrations (Hand et al., 2012) and deposition (Sickles II and Shadwick, 2014) of oxidized nitrogen species and sulfate. The latter study also found that NH_3 emissions have remained relatively constant, but only NH_4^+ in deposition is monitored regularly, so the changes in total reduced nitrogen deposition are not known. Analysis of long-term deposition measurements show a shift from oxidized nitrogen being the dominant species in wet deposition from 1990-1992 to reduced nitrogen being the predominant species in 2010-2012 (Li et al., 2016). While national trends showed decreasing amounts of oxidized nitrogen in wet deposition, only one state, North Dakota, observed an increase in oxidized nitrogen. In addition to changes in national trends in emissions and speciation of wet deposition, regional trends in

aerosol acidity have not changed substantially despite the decreasing concentrations of sulfur

dioxide and sulfate (Weber et al., 2016). In areas of O&G development, local and regional

emissions are reversing this general trend in decreasing emissions. Increases in NO_x and

potentially SO_2 can add inorganic aerosol precursors and other emissions such as VOCs that can

change the aerosol formation pathways as described here.

1.4.2 Organic Aerosol formation processes

Atmospheric organic aerosol (OA), representative of its complex chemical composition,

can form from a variety of chemical and physical processes. OA can be directly emitted as a

primary pollutant (POA) and have predominantly anthropogenic sources (Zhang et al., 2009),

although natural sources such as wildfires are also major contributors to primary OA worldwide.

Secondary OA (SOA) can form from gas phase compounds, either by gas to particle conversion

(or nucleation) or by condensation of low volatility species on preexisting aerosols (Lee and

Allen, 2012; Prather et al., 2008). SOA can originate from biogenic or anthropogenic emissions

and like the chemical composition of precursor VOCs, the formation processes for SOA are

complex, as represented in Figure 1.7, which only represents OA formation by the oxidation of

VOCs.
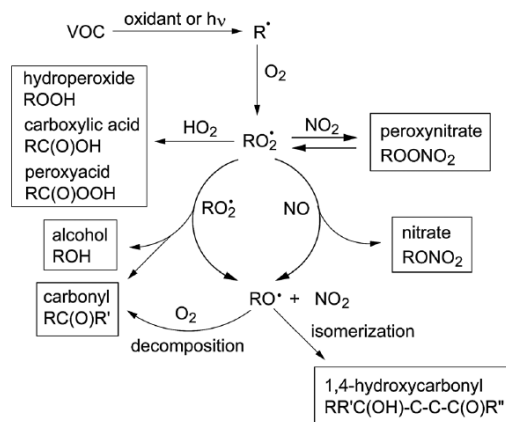
Figure 1.7: A summary of formation pathways for OA by VOC oxidation (Ziemann and Atkinson, 2012)

Ambient VOCs include carbonyls, organic acids, alcohols, and other compounds (Shen et al., 2013). In addition to SOA with similar functional groups to these VOC reactants, reactions with NO_x can form organic nitrates or peroxynitrates. SOA also forms by isomerization or decomposition reactions (Figure 1.7). Biogenic SOA formation can be significant, especially in rural sites that do not have much anthropogenic influence (e.g. Sjostedt et al., 2011). The formation of SOA from biogenic VOCs can also be enhanced in polluted areas, but the mechanisms are not entirely understood (Hoyle et al., 2011). Finally, anthropogenic VOCs come from a wide range of activities. For example, a study in China identified and quantified VOC source emissions from vehicle exhaust, domestic combustion, fossil fuel distribution, food industry, oil refinery, cooking, food industry, pharmaceutical industry, painting, and smoking (Wu et al., 2017).

Limited studies have investigated the effects of O&G emissions on OA formation. A study in the Marcellus Shale basin indicated that significant SOA formation was likely based on organic carbon to elemental carbon ratios larger than six (Pekney et al., 2014). A study downwind of an O&G region in the Barnett shale in the Dallas Fort Worth area of Texas found that about half of the OA identified as hydrocarbon-like could be attributed to VOC emissions from O&G activities (Rutter et al., 2015). These studies suggest a variable but important contribution of O&G to SOA formation in different O&G basins which highlights the importance of continuing to collect field measurements in areas near unconventional O&G development.

1.5. Study Objectives and Chapter Overview

This research study focuses on the analysis of observations obtained in the Bakken O&G Formation Region over the winters of 2013 and 2014 and comparison with long term air quality trends in this region. The study objectives were:

- Using comprehensive air quality measurements of inorganic gases, VOCs, $PM_{2.5}$ composition at high time resolution, and meteorological data, determine if there are elevated levels of air pollution or increased haze formation in the National Parks and other federal units within the Bakken formation region

- Investigate the sources and transport of any elevated pollutants within the Bakken region using chemical tracers and meteorological data, focusing on impacts from O&G activities

- Using the field measurements and thermodynamic models, explore the importance of ammonium nitrate formation in a region impacted by O&G development and the importance to regional haze

- Explore organic aerosol sources and composition to better understand how O&G activities contribute to total $PM_{2.5}$ concentrations

Chapter 1 highlighted the importance of unconventional O&G practices globally and within the U.S. and the environmental impacts from these practices. The methods and air quality instrumentation used in this study are described in detail in Chapter 2. Chapter 3 introduces the Bakken Air Quality Study (BAQS), where comprehensive air quality measurements were collected over two wintertime study periods in the Bakken formation during a period of rapid growth of unconventional O&G extraction. Emissions from the O&G development on the National Parks and other federal lands in that region and how they impact aerosol composition, formation and sources are investigated. Chapter 4 focuses on inorganic aerosol and Chapter 5

covers organic aerosol. Using BAQS measurements, Chapter 6 explores the use of

thermodynamic models to predict aerosol composition and concentrations in this unique region.

The research study conclusions and recommendations for future work are presented in Chapter 7.

2.0 METHODS

A variety of instrumentation to measure both ambient aerosol particles and gases was used in the MARGA comparison study, Bakken Air Quality Studies (BAQS I and BAQS II) and Rocky Mountain National Park (RMNP) study. Information on aerosol composition (inorganic, organic or elemental composition), total aerosol mass, and aerosol scattering was collected. Gaseous species that contribute to aerosol formation, are tracers for anthropogenic or biogenic sources, are regulated as harmful pollutants, and that form by photochemical processes were measured. Instrumentation was chosen to balance short duration high-resolution measurements and long duration low-resolution measurements and depended on instrument availability, financial resources, and feasibility. Duplicate measurements of the same species were often collected using two or more different instruments for measurement validation. Each instrument and measurement technique used in the MARGA comparison (Appendix B), BAQS I (Chapter 3), BAQS II (Chapters 4 and 5) and RMNP (Appendix C) studies are described in this chapter.

2.1 URG

A University Research Glassware (URG) Corporation annular denuder/filter-pack sampler is used to capture both inorganic gases and aerosol particles (Lee et al., 2008; Yu et al., 2005, 2006). Figure 2.1 shows the URG sampling system set up for field sampling (a) and a modified diagram from Yu et al., 2005 of the denuder and filter pack sampling train (b). The sampler first draws ambient air through a Teflon-coated $PM_{2.5}$ cyclone to remove particles with aerodynamic diameters greater than 2.5 µm. Next, a sodium bicarbonate coated glass annular denuder captures nitric acid (HNO_3) and sulfur dioxide (SO_2) and a phosphorous acid coated denuder captures ammonia (NH_3). A filter pack with a 37 mm diameter nylon filter (Pall

Nylasorb, 1.0 µm pore size) captures $PM_{2.5}$. Finally, an additional phosphorous acid coated

denuder is placed after the filter to capture any NH_3 volatilized from ammonium nitrate initially

captured on the filter. Any volatilized HNO_3 from collected particulate ammonium nitrate is

retained on the nylon filter (Yu et al., 2005). Samples are collected between one and seven days

duration with flow control at a nominal flow rate of 10 L min^{-1}. Total sample air volume is

monitored with a dry gas meter downstream of the sampling components and corrected for the

pressure drop through the sample train.
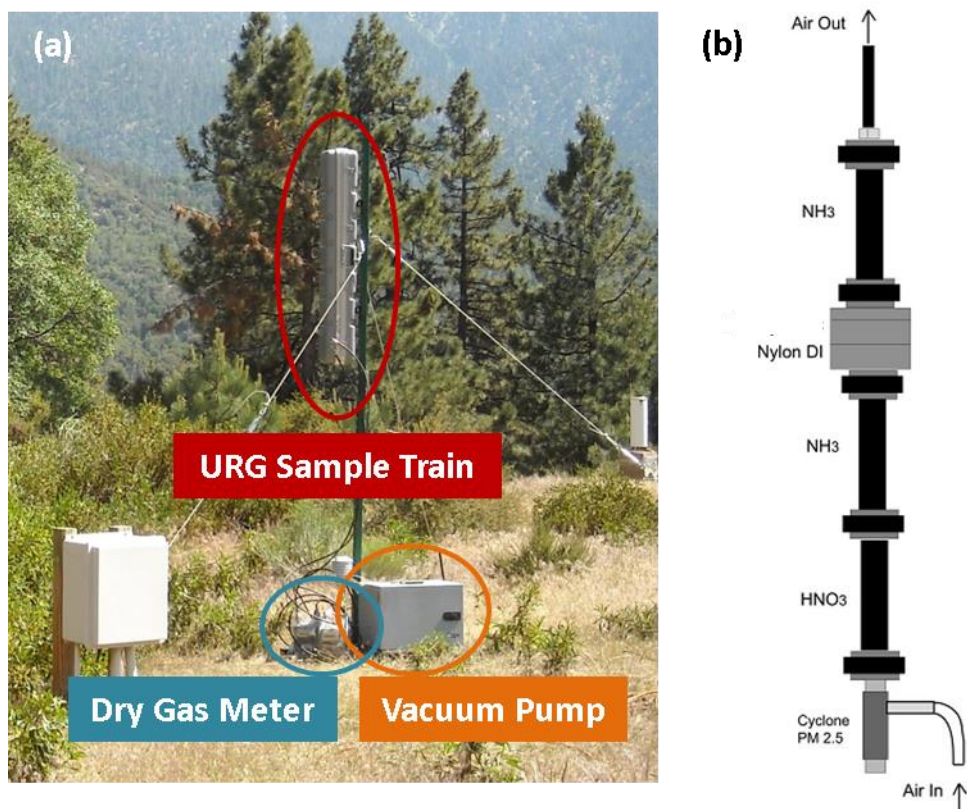
Figure 2.1: The URG sampling system set up in the field (a) identifies the vacuum pump, dry gas meter and the protective case for the sampling train. The order of the cyclone, denuders and nylon filter in the URG sample train is represented in (b), which is modified from a diagram in (Yu et al., 2005).

Denuder and filter samples are extracted in 18.2 MΩ deionized water and analyzed using

ion chromatography to quantify ammonia (NH_3), nitric acid (HNO_3), and sulfur dioxide (SO_2)

20

and PM$_{2.5}$ sodium (Na$^+$), ammonium (NH$_4^+$), potassium (K$^+$), magnesium (Mg^{2+}), calcium (Ca^{2+}), chloride (Cl$^-$), nitrite (NO$_2^-$), nitrate (NO$_3^-$) and sulfate (SO$_4^{2-}$). A Dionex DX-500 ion chromatograph (IC) was used. The anion IC used a Dionex IonPac AS14A 4x150 mm column and Dionex AERS 500 4 mm suppressor with 17 mM sodium carbonate \ 18mM sodium bicarbonate eluent at a flow rate of 1.0 mL min^{-1}. The cation IC used a Dionex IonPac CS12A 5 μm 3x120 mm column and Dionex CERS 500 2 mm suppressor with 0.02 M methanesulfonic acid eluent at a flow rate of 0.5 mL min^{-1}. Calibration curves were prepared using eight different concentrations of a multi-component standard solution and were generated before and after every batch of samples. Purchased Dionex standards were also used to validate the IC analysis. Replicate and blank IC samples were analyzed after every 10 ambient samples.

The limit of detection (LOD) for each species was calculated for the URG samples collected in BAQS I, BAQS II and RMNP; values are listed in Tables 2.1, 2.2 and 2.3. The LOD for a single, blank-corrected sample analysis, calculated at the 95% confidence level, is calculated according to Equation 2.1 using the average standard deviation of the sample blank concentrations (s_b) which were collected throughout each study, the number of blank samples (N_b) and the student's t-value (t). The LODs are presented in μN and also converted to μg m^{-3} using the average daily and 48-hour sample volumes from each study. The LODs for each aerosol species are comparable between the BAQS and RMNP studies with the exception of much higher LOD for NH$_3$ during the RMNP study. This high LOD can be attributed to three high denuder blank values during the first three weeks of the study; 13, 22 and 32 μN. The blank values from the remainder of the study were significantly lower with an average NH$_3$ of 1.43 μN. Using the blanks for the remainder of the study, the LOD is 1.26 μN or 0.011 μg m^{-3}, which is comparable to the LOD measured in BAQS.

$$LOD = s_b * t * \sqrt{\frac{N_b + 1}{N_b}}$$
<div align="right">Equation 2.1</div>

Table 2.1: The average blank values (μN), standard deviations, and LOD calculated from BAQS II URG samples. A t-value of 2.36 was used to determine the LOD for all species except NH_3 (t-value = 2.16). The LOD for daily and 48-hour samples were calculated using a study average sample volume of 11.7 and 23.6 m^3.

	Average Blank (μN)	Number of Samples	Standard Deviation	LOD (μN)	LOD daily (μg m⁻³)	LOD 48-hour (μg m⁻³)
Na^+	0.20	8	0.12	0.30	0.003	0.001
NH_4^+	0.36	8	0.18	0.46	0.004	0.002
K^+	0.06	8	0.06	0.15	0.003	0.001
Mg^{2+}	0.12	8	0.07	0.17	0.002	0.001
Ca^{2+}	0.75	8	0.65	1.63	0.028	0.014
Cl^-	0.58	8	0.30	0.74	0.011	0.006
NO_2^-	0.15	8	0.25	0.63	0.012	0.006
NO_3^-	0.26	8	0.07	0.17	0.004	0.002
SO_4^{2-}	0.15	8	0.14	0.35	0.014	0.007
NH_3	1.53	14	1.11	2.47	0.036	0.018
HNO_3	0.03	8	0.05	0.13	0.007	0.004
SO_2	0.48	8	0.38	0.96	0.053	0.026

Table 2.2: The average blank values (μN), standard deviations, and LOD (μN) calculated from BAQS II URG samples. A t-value of 2.18 was used to determine the LOD for all species except NH_3 (t-value = 1.96). The LOD for daily and weekly samples were calculated using a study average sample volume of 12.7 and 79.4 m^3.

	Average Blank (μN)	Number of Samples	Standard Deviation	LOD (μN)	LOD daily (μg m⁻³)	LOD weekly (μg m⁻³)
Na^+	0.74	13	0.94	2.13	0.019	0.003
NH_4^+	0.22	13	0.10	0.24	0.002	0.0003
K^+	0.11	13	0.07	0.15	0.002	0.0004
Mg^{2+}	0.40	13	0.55	1.24	0.012	0.002
Ca^{2+}	1.98	13	1.71	3.86	0.061	0.010
Cl^-	0.37	13	0.34	0.76	0.011	0.002
NO_2^-	0.23	13	0.33	0.76	0.014	0.002
NO_3^-	0.20	13	0.20	0.44	0.011	0.002
SO_4^{2-}	0.18	13	0.25	0.56	0.021	0.003
NH_3	1.14	27	0.59	1.19	0.016	0.003
HNO_3	0.06	13	0.22	0.49	0.024	0.004
SO_2	0.02	13	0.04	0.08	0.004	0.001

Table 2.3: The average blank values (μN), standard deviations, and LOD calculated from RMNP URG samples. Various t-values were used based on the degrees of freedom of each species; Na^+, NH_4^+, K^+, Cl^-, NO_3^-, HNO_3 and SO_2 used t-value = 2.14, Mg^{2+}, Ca^{2+}, SO_4^{2-} used t-value = 2.16, NO_2^- used t-value = 2.57 and NH_3 used t-value = 2.05. The modified NH_3 row excludes the three high blank samples as discussed in text.

	Average Blank (μN)	Number of Samples	Standard Deviation	LOD (μN)	LOD daily (μg m^{-3})
Na$^+$	1.01	15	1.66	3.66	0.022
NH$_4$$^+$	0.15	15	0.21	0.46	0.002
K$^+$	0.45	15	0.72	1.59	0.016
Mg^{2+}	0.70	14	0.16	0.37	0.002
Ca^{2+}	2.75	14	0.61	1.28	0.013
Cl$^-$	0.83	15	0.70	1.54	0.014
NO$_2$$^-$	0.11	6	0.12	0.34	0.004
NO$_3$$^-$	0.29	15	0.15	0.32	0.005
SO$_4$$^{2-}$	0.35	14	0.18	0.37	0.009
NH$_3$	3.54	29	7.00	14.96	0.134
Modified NH$_3$	1.37	26	0.71	1.49	0.013
HNO$_3$	0.22	15	0.52	1.15	0.038
SO$_2$	0.19	15	0.65	1.43	0.048

Replicate URG samples were collected during BAQS II to determine precision. The percent relative standard deviation (RSD) was calculated using the standard deviations of the replicate measurements and the average concentration (Table 2.4). The replicate samples were used in the calculation only if the ambient concentration was above the LOD. The RSD is reported only if five or more replicate samples above the LOD were collected. The RSD was less than 15% for all reported species, indicating good precision for the URG measurements, especially given the low concentrations sampled under challenging winter conditions.

Table 2.4: The relative standard deviation of replicate BAQS II URG samples analyzed by ion chromatography.

	Average Concentration of Replicates ($\mu g\ m^{-3}$)	Number of Replicates	RSD
Na^+	0.04	5	13.4%
NH_4^+	0.62	6	6.2%
K^+	0.01	5	11.1%
Mg^{2+}	0.01	3	-
Ca^{2+}	0.04	1	-
Cl^-	0.01	2	-
NO_2^-	0.003	0	-
NO_3^-	0.87	6	5.8%
SO_4^{2-}	0.78	6	7.6%
NH_3	1.57	6	10.1%
HNO_3	0.09	5	13.3%
SO_2	0.21	6	14.1%

2.2 MARGA

A MARGA, or Monitor for AeRosol and Gases in ambient Air (Makkonen et al., 2014; Rumsey et al., 2014) makes hourly measurements of the same inorganic precursor gases and PM$_{2.5}$ inorganic species as the URG measurement plus nitrous acid (HONO). The MARGA (Metrohm/Applikon) uses a wet-rotating glass denuder (WRD) to capture inorganic gases (Trebs et al., 2004; Wyers et al., 1993) and a steam jet aerosol collector (SJAC; Khlystov et al., 1995; Slanina et al., 2001) to collect water-soluble inorganic aerosol components. For the inlet, a 1.6m Teflon coated PM$_{2.5}$ cyclone is used with polyethylene tubing that was kept as short as possible to minimize loss of sampled gases. The sample first passes between two concentric glass cylinders of the WRD that are partially filled with absorption solution. As the WRD rotates, the inside walls are coated with the absorption solution onto which the sampled gases diffuse and dissolve into the gas sample solution. The sampled particles pass through the WRD where they enter a humidified chamber of the SJAC. The captured particles grow and settle into the aqueous

aerosol sample solution at the bottom of the SJAC. The MARGA is shown in Figure 2.2 as set up in a shelter for field sampling.

Figure 2.2: The MARGA set up in the shelter during BAQS II.

The MARGA incorporated Metrohm ICs with conductivity detection. The anion IC uses a Metrohm Metrosep A Supp10 75x4.0 mm column and phosphoric acid regenerated suppressor. The cation IC uses a Metrohm Metrosep C 4 100x4.0 mm column and no suppressor. The anion eluent was 7.0 mmol L^{-1} sodium carbonate monohydrate and 8.0 mmol L^{-1} sodium bicarbonate

and the cation eluent was 3.2 mmol L^{-1}. Both anion and cation sample flow rates are 0.7 mL

min^{-1}. The sample loop volumes are 250 µL for the anion IC and 500 µL for the cation IC.

The absorption solution contains 1% hydrogen peroxide which acts as a biocide and oxidizes

collected SO_2 to sulfate for analysis. Internal standards bromide and lithium are measured in the

anion and cation IC analyses, respectively, to account for variations in sample volume. Blank

samples and external standards are analyzed regularly and are used to verify the internal

MARGA calibration. When possible, MARGA measurements are verified with URG

measurements and the linear regression analysis is used to correct MARGA concentrations when

necessary. The accuracy of MARGA measurements is investigated in detail in Chapter 3.

Thorough descriptions of MARGA data analysis methods and instrument modifications for each

study are provided in Appendix A.

2.3 PILS

A particle-into-liquid sampler with ion chromatography (PILS-IC) was operated during

the MARGA comparison study. The PILS utilizes a steam injector and mixing chamber to grow

and capture water soluble $PM_{2.5}$. The enlarged $PM_{2.5}$ is collected onto an impaction plate which

is washed with fluid and runs into a sampling line that is directed towards both an anion and

cation IC (Orsini et al., 2003; Weber et al., 2001). Similar to the URG and MARGA, the PILS

ICs quantify Na^+, NH_4^+, K^+, Mg^{2+}, Ca^{2+}, Cl^-, NO_2^-, NO_3^- and SO_4^{2-} in $PM_{2.5}$. A calibration curve

using eight concentrations of both anion and cation standards was generated. Lithium and

bromide were used as internal standards for the cation and anion ICs, respectively, to account for

dilution in the liquid carrier solution due to steam condensation. The separations were

performed using an eluent of 1.8 mM sodium bicarbonate 1.7 mM sodium carbonate with a

liquid sample flow rate of 1.0 mL min^{-1} for anion IC and 20 mM methane sulfonic acid with a

liquid sample flow rate of 0.5 mL min^{-1} for cation IC. A Dionex AS14A column was used with a

Dionex ASRS ULTRA II suppressor for the anion IC and a Dionex CS12A-5 column was used

with a Dionex CSRS ULTRA II suppressor for the cation IC. A sample loop was continuously

filled and a sample was injected and analyzed every 17 minutes for both anion and cation ICs.

The ambient sample flow rate of the PILS was 15 L min^{-1}.

2.4 IMPROVE filters

The Interagency for Monitoring Protected Visual Environments (IMPROVE) network is

an air quality monitoring network with sites located in national parks and other protected Class I

areas across the United States. The IMPROVE aerosol sampler consists of four modules to

measure a comprehensive set of aerosol components to understand spatial and temporal trends in

visibility and emission sources impacting Class I areas (Hand, 2011; Solomon et al., 2014). In

the studies presented here, data from Modules A and C are used. In module A, total PM$_{2.5}$ mass

is measured gravimetrically using Teflon filters (Malm et al., 2011). Elemental analysis of the

Teflon filter sample is also performed using X-ray fluorescence (XRF). This technique

quantifies all elements with an atomic number greater than 11 (Na) and less than 82 (Pb). In

module C, quartz filters are analyzed by thermal optical reflectance for organic carbon (OC) and

light-absorbing, or elemental, carbon (EC) (Chow et al., 2007; Malm, 2004). In an inert

atmosphere of ultra-pure helium, quartz filter samples are incrementally heated to volatilize first

OC and then EC in the sample. As the carbon is volatilized, it is then pyrolyzed and passed

through a manganese dioxide oxidizer to convert to carbon dioxide (CO$_2$). Finally, a nickel

catalyst reduces the CO$_2$ to methane which is analyzed by a flame-ionization detector (Chow et

al., 2007).

2.5 TEOM

A tapered element oscillating microbalance (TEOM, Thermo Scientific 1405-DF) measured total $PM_{2.5}$ mass in real-time with six-minute time resolution (Patashnick and Rupprecht, 1991). $PM_{2.5}$ is separated with a virtual impactor and the sample is dried in a Nafion dryer. The TEOM determines total $PM_{2.5}$ mass by converting the changes in oscillations of a filter that continuously captures $PM_{2.5}$ to a mass. The filter is held at a high temperature (30 °C) to minimize the relative humidity and prevent condensation.

2.6 AMS

An Aerodyne High-Resolution Time-of-Flight Aerosol Mass Spectrometer (AMS) measured non-refractory PM_1, providing quantitative measurements of inorganic species Cl^-, NO_3^-, SO_4^{2-} and NH_4^+, total organic mass and organic aerosol fragments (Decarlo et al., 2006; Drewnick et al., 2005; Jayne et al., 2000). Five-minute average particle mass spectra were collected using the high sensitivity V mode and high resolution W mode. The ionization efficiency was calibrated using 300 nm ammonium nitrate particles weekly and verified with an in-line condensation particle counter (TSI model 3010). A co-located CO_2 monitor (LiCOR 820) was used to determine the contribution of ambient CO_2 to the AMS *m/z* 44 signal. Data analysis was performed in Igor Pro v6.37 (Wavemetrics Inc, Lake Oswego, OR) using SQUIRREL (v1.54B), PIKA (v1.13B, using updated fragmentation table; Aiken et al., 2008a), and the PMF2 algorithm (Paatero and Tapper, 1994) in PMF Analysis Tool (PET v2.06; Ulbrich et al., 2009). The AMS operation and preliminary data analysis was performed by Dr. Misha Schurman.

The PMF algorithm (Paatero and Tapper, 1994) was used to deconvolve the time series of AMS mass spectra into unique source factors while minimizing the reconstructed mass residual (Schurman et al., 2015; Ulbrich et al., 2009). PMF is a positively-constrained receptor-

based multivariate factor analysis method that can separate unique organic factors from time series of AMS organic mass spectra. Fragments are down-weighted if the signal to noise ratios was less than 2.0 and were removed if the signal to noise ratio was less than 0.2. The factors related to m/z 44 (16, 17, 18, 19, 20, 28 and 44 which correspond to O, HO, H_2O, CO, and CO_2) were also down-weighted, following standard AMS PMF analysis techniques (Jimenez, 2016). The uniqueness of each factor was ensured by establishing differences in the factor timelines and factor profiles. The analysis of the residuals shows limited variability across the range of m/z values analyzed and each fragment follows a normal distribution, suggesting no major biases exist in this interpretation of the factor analysis.

Two and three factor solutions for Fpeak values between -1 and 1 in 0.2 increments were explored (Ulbrich et al., 2009). Fpeak is a parameter that allows the exploration of the rotational freedom in the solutions. The value of Q, a parameter describing the quality of fit of the solution, was also considered when deciding the most appropriate PMF solution. Equation 2.2 shows the value of Q, which for the $m \times n$ data matrix incorporates the standard deviations of the points in the data matrix (σ_{ij}) and the residuals not fit by the model (e_{ij}). This value is compared to the expected Q (Q_{exp}) to determine how well the data is fit within the PMF analysis. If Q/Q_{exp} is much larger than 1, the errors have been overestimated and if Q/Q_{exp} is much less than 1 the errors have been underestimated. Considering both Fpeak and Q/Q_{exp}, a two factor solution was chosen with an Fpeak value of -0.2. This solution produced only a slight change in Q/Q_{exp}. The Q/Q_{exp} value was 0.41.

$$Q = \sum_{i=1}^{m} \sum_{j=1}^{n} \left(e_{ij} / \sigma_{ij} \right)^2$$

Equation 2.2

The amounts of elemental hydrogen (H), nitrogen (N), oxygen (O) and carbon (C) are determined from the major ionic fragments formed from the electrospray ionization in the AMS. Concentrations of H, N, O and C are estimated using multiple calibration standards of a range of compounds and used to determine H/C, N/C and O/C ratios. The organic matter to organic carbon (OM/OC) ratio is then calculated from these ratios (Aiken et al., 2007, 2008).

2.7 Aethalometer

A Magee Scientific 7-wavelength dual-spot aethalometer (Drinovec et al., 2015; Hansen et al., 1984) measured $PM_{2.5}$ black carbon (BC). Ambient air is continuously sampled onto a filter and the light attenuation is measured using 370, 470, 520, 590, 660, 880, and 950 nm wavelengths. Two different sample spots are collected simultaneously on the filter at different flow rates so that the ambient concentration can be corrected for particle loading effects. The light attenuation of a reference spot on the filter with no sample is also measured and used for blank correction. Concentrations are presented as the means of the BC concentration derived from all wavelengths. The other wavelengths allow for the analysis of mineral dust, climate forcing and the direct effects of BC (Drinovec et al., 2015), which are not investigated as part of these studies.

2.8 Nephelometer

Nephelometers (Heintzenberg et al., 2006; Müller et al., 2009) directly measure light extinction due to scattering by particles (b_{sp}). An NGN-2 Optec nephelometer was operated in an open-air configuration with a wavelength of 550 nm. Radiance Research M903 and Ecotech M9003 nephelometers used a $PM_{2.5}$ inlet and measured scattering at 530 nm and 520 nm, respectively. Each nephelometer was calibrated weekly with span gas and zero air and collected data at five minute time resolution. The NGN-2 and Ecotech instruments were operated at

ambient conditions. The Radiance Research instrument was housed indoors (~15°C) throughout BAQS I and BAQS II, and so the samples experienced significant warming and associated reductions in humidity for the measurements.

2.9 Precipitation Analysis

Wet deposition was collected using a NCON Atmospheric Deposition Sampler or a Yankee Environmental TPC 3000. In both samplers, a bucket with an area of 25.3 cm^2 was used to capture both rain and snow samples. Before each sample, the bucket was rinsed five times with 18 MΩ deionized (DI) water and covered with clean aluminum foil until placed in the sampler. The bucket is only open when precipitation is falling, making it a wet-only deposition sample. The mass of the sample and pH measurements were taken as soon as possible after the collection of the sample bucket. The pH meters, equipped with a combination semi-micro electrode, were calibrated with two calibration points of pH 4 and 7 and the average of three replicate pH measurements was reported for each sample. Precipitation samples were frozen after pH analysis until ion chromatography (IC) could be performed. Samples were allowed to thaw completely before pH or IC analysis. The same IC method as the URG filter and denuder samples was used. The average blank for each species measured and limit of detection for ion chromatography analysis are listed in Table 2.5 for BAQS I and 2.6 for BAQS II.

Table 2.5: The average blank values, standard deviations, and LOD (μN) calculated from BAQS I precipitation samples. A t-value of 2.36 was used to determine the LOD for the cations and t-value of 2.31 for the anions.

	Average Blank (μN)	Number of Samples	Standard Deviation	LOD (μN)
Na^+	0.27	7	0.21	0.54
NH_4^+	5.61	7	4.34	10.94
K^+	0.05	7	0.05	0.13
Mg^{2+}	0.45	7	0.26	0.66
Ca^{2+}	2.09	7	1.17	2.96
Cl^-	0.10	9	0.07	0.17
NO_2^-	0.00	9	0.00	0.00
NO_3^-	0.06	9	0.09	0.22
SO_4^{2-}	0.17	9	0.18	0.43

Table 2.6: The average blank values (μN), standard deviations, and LODs calculated from BAQS II precipitation samples. A t-value of 2.26 was used to determine the LOD for all species.

	Average Blank (μN)	Number of Samples	Standard Deviation	LOD (μN)
Na^+	1.09	10	1.03	2.43
NH_4^+	4.38	10	2.17	5.13
K^+	0.08	10	0.07	0.16
Mg^{2+}	0.32	10	0.27	0.64
Ca^{2+}	1.00	10	0.72	1.72
Cl^-	0.02	10	0.04	0.09
NO_2^-	0.45	10	0.55	1.30
NO_3^-	0.01	10	0.02	0.04
SO_4^{2-}	0.02	10	0.04	0.09

2.10 Gas Rack Measurements

2.10.1 Nitrogen containing Gases

Depending on the goals of the study, various gas instruments were included in a gas rack. The measurement of nitrogen-containing gases include nitrogen oxide (NO), nitrogen dioxide (NO_2), nitrogen oxides (NO_x), and total reactive oxidized nitrogen species (NO_y). This gas rack configuration, which has been used in previous studies (Prenni et al., 2014), includes a Teledyne 201E chemiluminescence instrument for NO_x and a Teledyne 200EU instrument for NO_y. NO_x

is the sum of NO and NO_2 and NO_y is the sum of reactive nitrogen compounds including NO_x, HNO_3, HONO, dinitrogen pentoxide (N_2O_5), alkyl nitrates, peroxyacyl nitrates, and particulate nitrate (Dunlea et al., 2007). Both NO_x and NO_y instruments operate on the same principle of converting the more oxidized NO_x and NO_y species to NO with a molybdenum converter (Dickerson, 1984; Fehsenfeld et al., 1987). NO is reacted with ozone (O_3), forming electronically excited NO_2 and the resulting fluorescence is detected optically. The main differences from the NO_x instrument are that the molybdenum converter in the NO_y instrument is located at the inlet and the sample is not filtered to minimize loss of HNO_3 and capture particulate nitrate. The conversion of nitrogen species to NO is not exclusive to NO_2 in the NO_x instrument, so there is a possibility for interferences from additional nitrogen species being detected as NO_x (Dunlea et al., 2007).

High time resolution NH_3 measurements were collected with a Picarro G1103 NH_3 instrument which uses cavity ring down spectroscopy (CRDS; Berden et al., 2000). CRDS is an absorption spectroscopy technique in which a light source is introduced as a pulse into a cavity containing the ambient NH_3 sample and reflects back and forth between two mirrors. The NH_3 absorbs the light as it makes passes through the cavity and the signal decreases over time creating a "ring-down time." The rate at which the light intensity decreases is proportional to the amount of NH_3 in the sample that absorbs the light signal. The sample signal is corrected by the light lost in the cavity when no sample is present. CRDS is very sensitive compared to many other NH_3 instruments due to the long sample path length created by the many passes made in the reflective sample cavity (von Bobrutzki et al., 2010).

2.10.2 Other Gases

In addition to nitrogen-containing gases, gas rack instruments also include carbon monoxide (CO) and sulfur dioxide (SO_2) analyzers. CO was detected using a Teledyne 300EU analyzer which uses the absorption of infrared radiation. A pulsed fluorescence analyzer, Thermo Scientific model 43C, was used to measure SO_2.

2.11 Passive Samplers

Four different Radiello passive samplers were used in the first BAQS to collect weekly measurements of NH_3, NO_2 and SO_2, O_3 and VOCs at all five measurements sites. The passive samplers were deployed 1.5 to 2.0 m above the ground in an upside-down bucket to protect the sampler from precipitation. The passive samplers collect samples by diffusion which is driven by the concentration gradient that exists between the absorbing sample cartridge and ambient air. The passive sample cartridge is placed in a cylindrical diffusive body of which the specific porosity, along with ambient temperature and pressure, determines the average flow rate of the weekly sample. The sampling rate of each compound is specified at a standard temperature of 289 K and corrected based on the ambient temperature recorded for each sample. The total mass of the sample measured on each cartridge is converted to an ambient concentration using the total sampling time and corrected sampling rate (*Radiello Manual*, 2006; http://www.radiello.com/english/index_en.html).

The sample flow rate for NO_2 was corrected for ambient temperature (Equation 2.3), but SO_2 was not, according to the methods recommended by the manufacturer. The sampling rate at 298 K ($Q_{298,NO2}$) for NO_2 is 0.141 ± 0.007 ng ppb^{-1} min^{-1}. The sampling rate at 298 K (Q_{298}) for SO_2 is 0.466 ± 0.022 ng ppb^{-1} min^{-1}. Ambient concentrations were calculated according to Equation 2.4, where the mass (m) is input as ng of NO_2 or SO_2 and the sampling time (t) in

minutes. Similar to NO₂, the sample flow rate for ozone is corrected for ambient temperature (Equation 2.5) where the sample flow rate at a temperature of 298 K is 24.6 ml min^{-1} ($Q_{298,O3}$). The calculation for ambient ozone is shown in Equation 2.6.

$$Q_{K,NO_2} = Q_{298,NO_2} \times \left(\frac{T(K)}{298}\right)^{7.0} \qquad \text{Equation 2.3}$$

$$C_{NO_2 \text{ or } SO_2}(ppb) = \frac{m(ng)}{Q(ng\ ppb^{-1}\ min^{-1}) \times t(min)} \qquad \text{Equation 2.4}$$

$$Q_{K,O_3} = Q_{298,O_3} \times \left(\frac{T(K)}{298}\right)^{1.5} \qquad \text{Equation 2.5}$$

$$C_{O_3}(\mu g\ m^{-3}) = \frac{m(\mu g)}{Q_{K,O_3}(ml\ min^{-1}) \times t(min)} \times 10^6 \qquad \text{Equation 2.6}$$

Weekly blanks and replicates of each passive sampler were collected at the main sampling site at the north unit of Theodore Roosevelt National Park (THRO-N). Additional replicates of NO₂/SO₂ passives were collected at the remaining four sampling sites. The NO₂/SO₂ passives and O₃ passives were extracted and analyzed according to the Radiello manual (*Radiello Manual*, 2006). For the analysis of SO₂, the aqueous passive extract was analyzed using IC in the same method as the URG filters. For the analysis of NO₂, sulfanilamide and N-(1-naphthyl)ethylendiamine dihydrochloride (NEDA) were added to the passive extract to convert the aqueous NO₂ to nitrite. Using a calibration curve of known nitrite concentrations, the nitrite in the samples was measured at 537 nm wavelength in an absorbance spectrophotometer. Measurements were blank corrected using the nitrite measured from the blank passives. In addition, the NO₂ passive extracts were analyzed using ion chromatography for nitrite concentrations according to the IC method used for the URG filter and precipitation samples. The ozone passive cartridges contain 4,4'-dipyridylethylene which undergoes acid-catalyzed ozonolysis in the presence of the adsorbed ozone to form 4-pyridylaldehyde. When the ozone passives are extracted in a solution of sulfuric acid and 3-methyl-2-benzothiazolinone

hydrazine (MBTH), the 4-pyridylaldehyde is condensed to form MBTH-azide yellow. The samples are analyzed in a spectrophotometer at a wavelength of 430 nm to measure the absorbance. The concentration of ozone is determined using a calibration curve and the known conversion factor of 1 µg 4-pyridylaldehyde equaling 0.224 µg ozone.

A previously developed analysis method for the NH_3 passives was used in lieu of the method in the Radiello manual (Day et al., 2012). To prepare the samplers, the intake filter of a laminar flow hood was sprayed with 15% citric acid solution to remove NH_3 from the work area. The NH_3 cartridges were loaded into the blue Radiello diffusive body which is made of 1.7 mm thick microporous polyethylene with an average porosity of 25 ± 5 µm and diffusive path length of 18 mm. The loaded samples were wrapped in clean aluminum foil and placed in polyethylene centrifuge tubes for transport to the field. After collection, the samples were stored in the refrigerator or cold room until the sample could be extracted. The cartridge was removed from the diffusive body and placed in its original plastic vial with 10 mL DI water and sonicated for 45 minutes. The extract was immediately analyzed using the cation IC or transferred into a 15 mL Nalgene tube and stored in the cold room at 4°C. The blue diffusive bodies were rinsed and soaked in DI water between sampling.

The temperature and pressure corrected sample flow rate (Equation 2.7) are calculated following previously developed methods (Day et al., 2012). The standard flow rate at standard temperature and pressure (Q_{std}) is 168 ml min^{-1} for the NH_3 passive samplers (Radiello, 2006) is corrected for ambient temperature (T_o) and ambient pressure (p_o). The ambient pressure at each site was estimated using elevation. The ambient concentration is then calculated using Q(T,P), the mass of NH_3 collected on the cartridge (m, µg) and the sample time (t, min; Equation 2.8).

$$Q(T,P; ml\ min^{-1}) = Q_{std}(ml\ min^{-1}) \left(\frac{p_o(atm)}{p(atm)}\right)\left(\frac{T(K)}{T_0(K)}\right)^{1.81} \qquad \text{Equation 2.7}$$

$$C_{NH_3}(\mu g\ m^{-3}) = \frac{m(\mu g)}{Q(ml\ min^{-1}) \times t(min)} \times 10^6 \qquad\qquad \text{Equation 2.8}$$

2.12 Real-time Ozone

Real-time ozone instruments used in these studies include a Teledyne 400E

(http://www.teledyne-api.com/manuals/04316f_400e.pdf) and 2B Technologies Model 202

(http://www.twobtech.com/model-202-ozone-monitor.html) ozone monitors. Measurement

precision is better than 0.5% for the Teledyne and 1.5ppb or 2% of the reading (whichever is

greater) for the 2B Technologies O_3 monitors. The recommended operating temperature of the

Teledyne is 5 – 40 °C for the Teledyne and 2B Technologies O_3 monitor is 0 – 50 °C, which

were often above the temperatures observed in the BAQS field campaign.

To validate the measurements of the 2B Technologies O_3 monitors operated at ambient

temperatures, O_3 measurements from the CASTNET monitoring station at THRO-S were used

for comparison. CASTNET ozone monitors are operated in shelters maintained between 20 – 30

°C or within the temperature range in the ozone monitor specifications (US EPA, 2016a). The

CASTNET THRO-S site uses a Thermo Scientific Model 491 O_3 monitor.

2.13 VOC canisters

Whole air grab samples for VOC analysis are collected in clean and evacuated 2 L

stainless steel canisters. Canisters were cleaned by evacuating and refilling with ultra-pure

nitrogen eight times while heated to 100°C. When sampling, the canister inlet tubing was

uncapped and inverted at least three times to replace the old air in the inlet tubing with ambient

air. The canister was held above the head of the sample taker and pointed towards the wind.

The canister valve was opened slowly and remained open for 30 seconds to one minute. The

canister valve was closed securely and the inlet tubing was capped. A suite of VOCs was

analyzed on a custom 5-channel gas chromatography system utilizing three flame ionization

detectors, an electron capture detector and a mass spectrometer. VOCs characterized include light hydrocarbons, alkyl nitrates, aromatics and some biogenic compounds. A complete list of the VOCs detected by this method is listed in Table 2.7. This analytical method, conducted in these studies by Dr. Yong Zhou, has been used in several previous studies (Russo et al., 2010b; Swarthout et al., 2013; Zhou et al., 2010).

Table 2.7: The precision, accuracy, and LOD from every VOC species detected from canister samples during BAQS II. The units for the LOD measurements are listed in parenthesis next to the species name.

VOCs	Precision (%)	Accuracy (%)	LOD
ethane (ppt)	1.30	1	10
ethene (ppt)	4.35	5	10
propane (ppt)	1.66	1	3
propene (ppt)	1.81	5	3
t-2-Butene (ppt)	1.90	5	2
1-butene (ppt)	2.14	5	2
i-butene (ppt)	2.15	5	2
c-2-Butene (ppt)	1.97	5	2
i-butane (ppt)	1.61	3	2
n-butane (ppt)	1.59	3	2
ethyne (ppt)	1.72	3	2
cyclopentane (ppt)	2.76	3	2
i-pentane (ppt)	1.52	3	2
n-pentane (ppt)	1.59	3	2
n-hexane (ppt)	2.54	5	2
n-heptane (ppt)	2.26	5	2
n-octane (ppt)	1.43	5	2
n-nonane (ppt)	2.92	5	2
benzene (ppt)	2.32	5	2
toluene (ppt)	2.86	5	2
ethylbenzene (ppt)	2.36	5	1
m+p-xylene (ppt)	1.46	5	1
styrene (ppt)	2.31	5	1
i-propylbenzene (ppt)	4.90	5	1
n-propylbenzene (ppt)	2.21	5	1
3-ethyltoluene (ppt)	4.02	5	1
2-ethyltoluene (ppt)	3.10	5	1
1,3,5-trimethylbenzene (ppt)	3.36	5	1

VOCs	Precision (%)	Accuracy (%)	LOD
1,2,4-trimethylbenzene (ppt)	3.14	5	1
1,2,3-trimethylbenzene (ppt)	3.03	5	1
1,3-diethylbenzene (ppt)	3.41	5	1
1,4-diethylbenzene (ppt)	2.82	5	1
1,2-diethylbenzene (ppt)	3.15	5	1
OCS (ppt)	1.72	5	5
DMS (ppt)	3.77	10	2
C2Cl4 (ppt)	1.81	5	0.01
MeONO2 (ppt)	2.43	10	0.01
EtONO2 (ppt)	2.19	10	0.01
i-PrONO2 (ppt)	3.70	10	0.01
n-PrONO2 (ppt)	4.86	10	0.01
2-BuONO2 (ppt)	3.51	10	0.01
3-PenONO2 (ppt)	3.88	10	0.01
2-PenONO2 (ppt)	3.59	10	0.01
acetaldehyde (ppb)	4.91	15	0.05
ethanol (ppb)	6.16	15	0.05
acetone (ppb)	4.34	15	0.05

3.0 BAKKEN AIR QUALITY STUDY: PILOT STUDY

3.1 Oil and Gas Development in the Bakken Region

The Bakken Formation, a subsurface of the Williston Basin, spans an area of 520,000 km^2 over western North Dakota and eastern Montana in the United States (U.S.) and extends into the Canadian provinces of Manitoba and Saskatchewan. This basin has been actively drilled since the 1950s, but production of oil drastically increased since 2006 due to improvements in horizontal drilling and hydraulic fracturing techniques. An estimated 7.38 billion barrels of oil is recoverable in the U.S. portion of the Williston Basin (Gaswirth and Marra, 2015), which includes both the Bakken formation and the underlying Three Forks formation often included with the Bakken formation. During the Bakken Air Quality Study (BAQS) period, over one third of the captured natural gas was burned off in flaring (U.S. Energy Information Administration, 2014b) because the region lacked the infrastructure or pipelines to safely store and transport natural gas. More recently North Dakota state regulations have led to the completion of natural gas infrastructure which resulted in sharp reductions in natural gas flaring (U.S. Energy Information Administration, 2016b). In parallel to increases in oil production and flaring, other anthropogenic activities associated with the oil and gas industry increased. These include increases in vehicle emissions and generation of road dust (Choi and Roberts, 2015) from diesel truck traffic, greater numbers of diesel engines used during drilling operations, and an increased population needed to support the expanded oil industry. The development of the oil sands in eastern Alberta, Canada, which is just over 1,000 km from the Bakken, is a major source of particulate matter (PM) and aerosol precursors (Liggio et al., 2016; McLinden et al., 2012; Wiklund et al., 2012) which also might impact the Bakken region by long range transport. The

effect these anthropogenic sources have on the regional PM has not been previously studied in detail.

Different processes and activities associated with oil and natural gas extraction can emit PM directly or emit gaseous precursors that can later form secondary PM if favorable conditions exist for particle formation. Emissions inventories from the Bakken (Grant et al., 2014b) and several other U.S. natural gas basins (e.g. Bar-Ilan et al., 2008; Grant et al., 2014b) have been developed for unconventional drilling techniques, providing estimates for emissions of methane and other volatile organic compounds (VOCs), nitrogen oxides (NO_x), ozone, other hazardous air pollutants, and PM which are emitted from different sources associated with oil and gas development. However, detailed aerosol composition measurements are lacking in the Bakken region. Methane and other VOCs from oil and gas operations have been measured at many field locations outside the Bakken (Field et al., 2015; Helmig et al., 2014; Moore et al., 2014; Swarthout et al., 2015; Yuan et al., 2015) and by remote sensing (Schneising et al., 2014). Some VOCs can oxidize and condense or react with other compounds to create secondary organic aerosol. For example, VOCs can react with NO_x to form particulate organic nitrate, which has been observed in the Uintah Basin in Utah (Lee et al., 2014). Black carbon (BC) can also be emitted from diesel trucks and industrial stationary diesel engines (Khalek et al., 2015; U.S. Environmental Protection Agency, 2012) or from flaring (Giwa et al., 2014; Stohl et al., 2013). Additionally, inorganic particle formation from the precursor gases ammonia, nitrogen oxides and sulfur dioxide from local or regional sources can create inorganic ammonium nitrate (AN) and ammonium sulfate (AS) particles (Seinfeld and Pandis, 2006). In the Bakken region, local and regional sources of precursor gases and aerosol from coal-fired power plants, agriculture, and increased population and traffic can potentially contribute to elevated concentrations of PM.

Long term measurements of PM less than 2.5 µm in aerodynamic diameter ($PM_{2.5}$) by the Interagency Monitoring of Protected Visual Environments (IMPROVE) program have shown increases in $PM_{2.5}$ sulfate and nitrate in the Bakken region in the winter (Hand et al., 2012), contrasting decreasing trends across much of the U.S. The trends presented by Hand et al. focused on 2000-2010 while oil production did not rapidly accelerate until 2007 when the Parshall Field was discovered (U.S. Energy Information Administration, 2014a) as shown in Figure 3.1. To better understand wintertime aerosol concentrations and composition in the Bakken region and how they are evolving with regional changes in oil and gas production, BAQS was conducted over two wintertime periods in 2013 and 2014. In this Chapter, the results from the BAQS I pilot study are summarized and the motivation for conducting BAQS II is discussed.
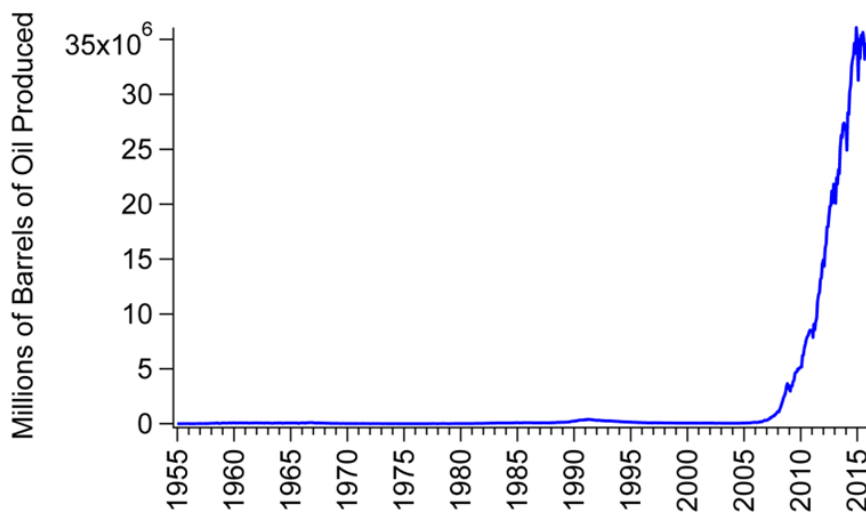
Figure 3.1: The production of oil (millions of barrels produced) in North Dakota from 1955 to 2016.

3.2 Study Overview

A pilot study (BAQS I) was conducted between February 15 and April 6, 2013. Figure 3.2 shows four BAQS sampling site locations used in this analysis along with the active oil and gas wells in 2013 in the Bakken formation. Knife River Indian Villages National Historic Site (KNRI) is located to the east of the main area of oil and gas drilling, but close to several major coal-fired power plants. Medicine Lake National Wildlife Refuge (MELA) is located in eastern Montana, to the west of the main area of drilling. Fort Union Trading Post National Historic Site (FOUS) and the North Unit of Theodore Roosevelt National Park (THRO-N) are both located within the most active area of drilling. The South Unit of Theodore Roosevelt National Park (THRO-S) is located towards the southern end of the most intensive oil and gas operations. At KNRI, MELA and FOUS, 48-hour time integrated aerosol ionic composition and inorganic gas measurements were obtained. THRO-N measured daily aerosol ionic composition and inorganic precursor gases. Passive samplers were deployed at all five sampling sites. All measurements presented from BAQS I are summarized in Table 3.1.
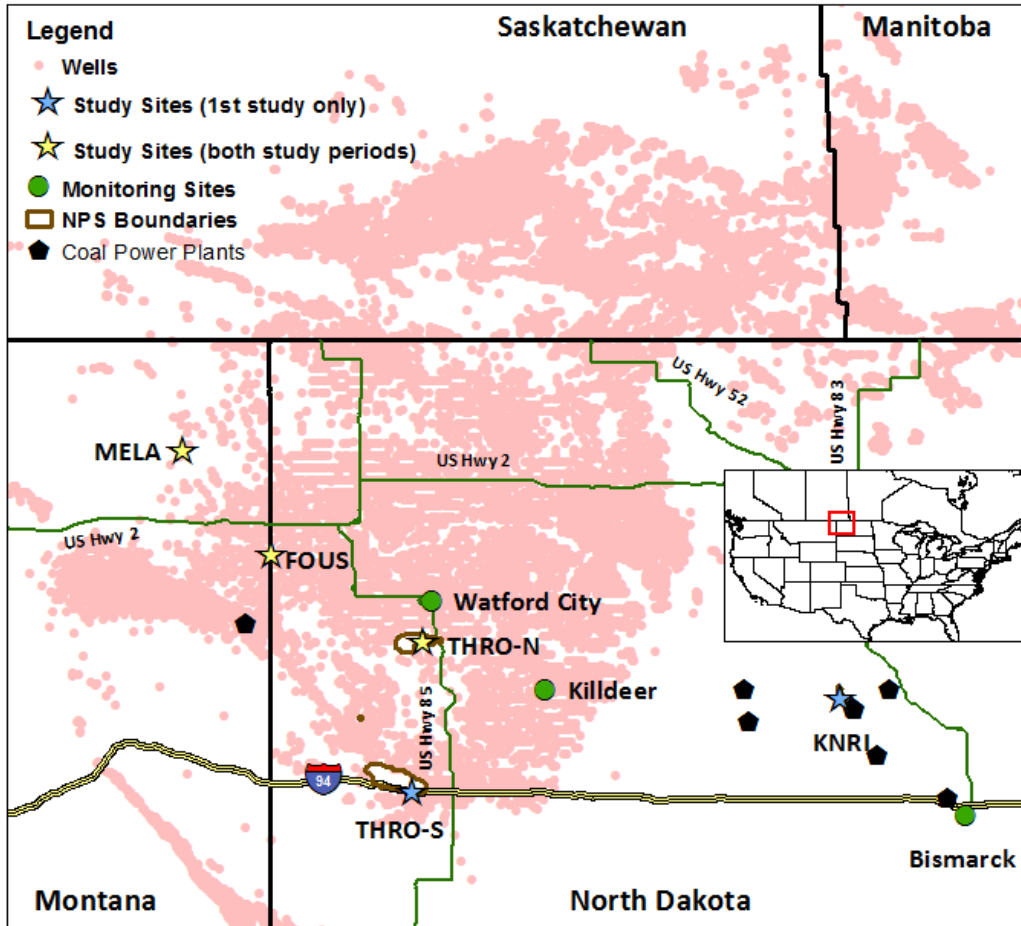
Figure 3.2: A map of eastern Montana and western North Dakota in the United States and southern Manitoba and Saskatchewan in Canada shows the locations of sampling sites during BAQS and active oil wells. See text for full site names. All study sites were used in BAQS I study from February – April 2013 (yellow and blue stars). BAQS II, from November 2013 – March 2014, focused on MELA, FOUS and THRO-N (yellow stars). National park lands are outlined in brown. Active gas and oil wells through the year 2014 are labeled with pink circles. Meteorological data were taken from three additional monitoring sites (green circles). Coal power plants are marked with black pentagons.

Table 3.1: A summary of the measurements and instrumentation used in this analysis for aerosol, gas and VOC concentrations during the first study (BAQS I) from the sampling sites THRO-N, FOUS, MELA and KNRI. The time resolution of each measurement and instrument model, if applicable, is listed in the column.

Measurements During BAQS I						
Sampling Technique	**Measurement**	**THRO-N**	**FOUS**	**MELA**	**KNRI**	**THRO-S**
Aerosol						
URG filter pack	PM$_{2.5}$ ions	Daily	48-hour 3 times per week	48-hour 3 times per week	48-hour 3 times per week	-
IMPROVE Teflon filter	PM$_{2.5}$ mass	Daily	-	-	-	Existing[†]
Aethalometer	PM$_{2.5}$ black carbon	5-minute	-	-	-	-
Nephelometer	PM$_{2.5}$ scattering	5-minute; Radiance Research M903	-	-	5-minute; Ecotech M9003	-
Gases						
URG denuders	inorganic gases	Daily	48-hour 3 times per week	48-hour 3 times per week	48-hour 3 times per week	-
Passive Samplers	NO$_2$/SO$_2$, O$_3$ and NH$_3$	Weekly	Weekly	Weekly	Weekly	Weekly
Real-time O$_3$	O$_3$	1-minute; Teledyne	Hourly, 2B Tech	Hourly, 2B Tech	Hourly, 2B Tech	Existing[‡]
Real-time SO$_2$	SO$_2$	1-minute; Thermo Scientific	-	-	-	-
Nitrogen Oxides	NO, NO$_2$, NO$_x$	1-minute; Teledyne	-	-	-	-
Real-time CO	CO	1-minute; Teledyne	-	-	-	-
Surface Meteorology		1-minute	1-minute	Existing*	Existing*	Existing*

[†]Existing IMPROVE network site

[‡]Existing O$_3$ measurement part of CASTNET network

*Existing surface meteorology measurements were obtained from the Western Regional Climate Center (WRCC) Remote Automated Weather Stations (RAWS).

3.3 Aerosol Measurements

Periods of elevated inorganic aerosol concentrations were observed in the URG filter-pack measurements collected during BAQS I as shown in Figure 3.3. Daily filter samples at THRO-N and 48-hour samples three times each week at MELA, KNRI and FOUS were collected. Data gaps in the KNRI and FOUS timelines were due to power outages. Observations show that increased concentrations occurred regionally across all measurement sites. High concentration episodes were dominated by NH_4^+, SO_4^{2-} and NO_3^-. Concentrations of all other ions measured, including Cl^-, NO_2^-, K^+, Na^+, Ca^{2+}, and Mg^{2+}, were low. The average and maximum concentrations of each aerosol species at all sites for both studies are given in Table 3.2. The highest time-integrated concentration of total inorganic components, 21.3 µg m^{-3} averaged over a 48 hour sample, occurred at FOUS in late March. FOUS is surrounded by a dense area of oil wells (Figure 3.2) and also has the highest average total inorganic aerosol concentration measured in BAQS I (Table 3.2).
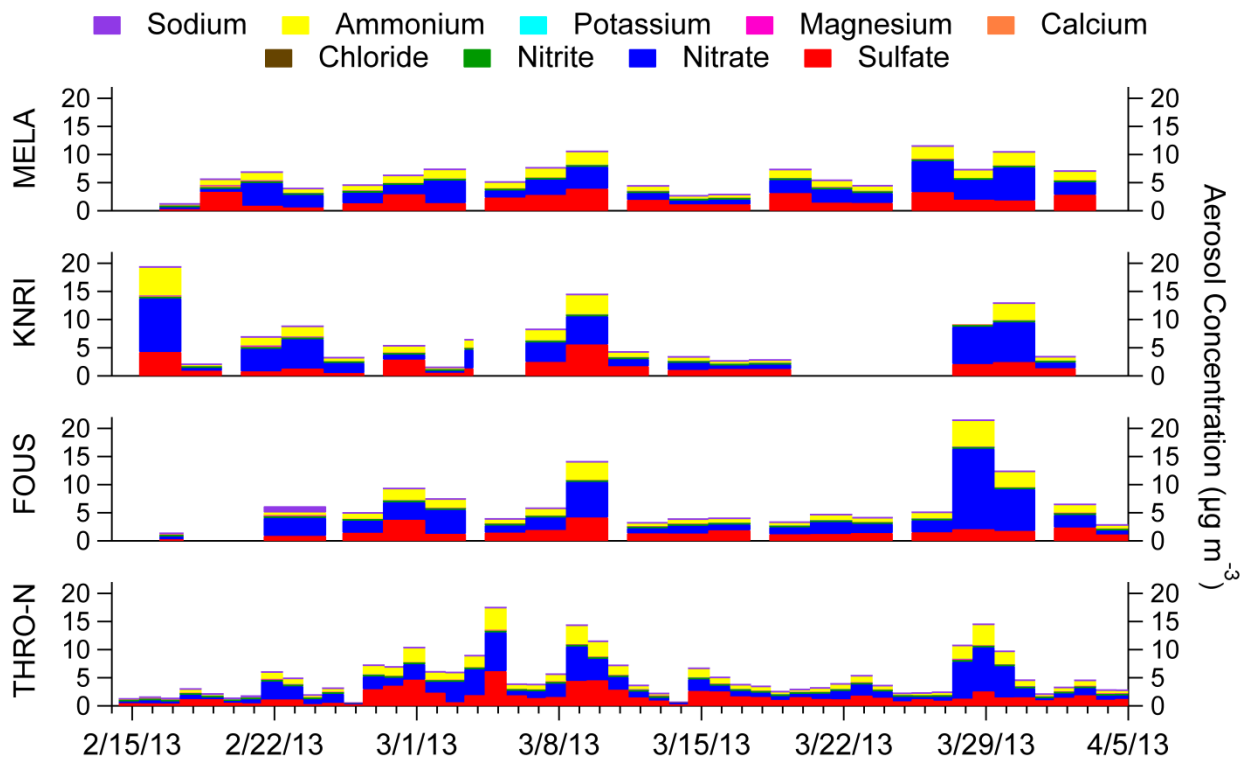
Figure 3.3: Stacked bars representing the contribution of each inorganic species to the total inorganic aerosol from URG filter PM$_{2.5}$ measurements (μg m^{-3}) from BAQS I. The width of the bar signifies the sampling period which varied between daily and 2-day samples.

Table 3.2: The average (bold) and maximum (in parentheses) URG $PM_{2.5}$ species concentrations ($\mu g\ m^{-3}$), total URG inorganic $PM_{2.5}$ from the sum of each listed species, and the $PM_{2.5}$ mass measured from the IMPROVE Teflon filter are listed for BAQS I.

	THRO-N	FOUS	MELA	KNRI
Na^+	**0.03**	**0.09**	**0.05**	**0.06**
	(0.04)	(1.13)	(0.15)	(0.22)
NH_4^+	**1.17**	**1.47**	**1.36**	**1.60**
	(4.04)	(4.73)	(2.50)	(5.08)
K^+	**0.02**	**0.04**	**0.04**	**0.04**
	(0.06)	(0.08)	(0.14)	(0.11)
Mg^{2+}	**0.01**	**0.01**	**0.01**	**0.01**
	(0.02)	(0.02)	(0.02)	(0.03)
Ca^{2+}	**0.05**	**0.04**	**0.04**	**0.05**
	(0.14)	(0.14)	(0.14)	(0.21)
Cl^-	**0.03**	**0.03**	**0.04**	**0.04**
	(0.10)	(0.05)	(0.29)	(0.09)
NO_2^-	**0.004**	**0.01**	**0.01**	**0.01**
	(0.01)	(0.02)	(0.02)	(0.02)
NO_3^-	**1.81**	**3.06**	**2.36**	**3.09**
	(7.84)	(14.3)	(5.86)	(9.51)
SO_4^{2-}	**1.66**	**1.71**	**1.97**	**1.88**
	(6.18)	(4.18)	(3.94)	(5.60)
Total Inorganic	**4.78**	**6.45**	**5.87**	**6.77**
	(17.4)	(21.3)	(11.4)	(19.3)
IMPROVE $PM_{2.5}$	**5.38**	-	-	-
	(14.6)			

Higher time resolution measurements (5-minute) of nephelometer aerosol scattering, b_{sp}, were also obtained at THRO-N and KNRI (Table 3.1). The THRO-N nephelometer operated inside at room temperature and the KNRI nephelometer operated at ambient conditions. At THRO-N, the cooler ambient air was warmed to room temperature inside the nephelometer which significantly decreases the relative humidity. Accounting for the temperature increase, the calculated relative humidity of the sample was 14% on average with a maximum value of 30%. Essentially, the THRO-N nephelometer measured b_{sp} of dry aerosol. The KNRI nephelometer included scattering from the aerosol liquid water content, which was often significant since the range of relative humidity was 40-100%. This is reflected in the higher average b_{sp} observed at

KNRI. Similar to the PM concentrations measured, the b_{sp} shows peaks that generally occur at both sites (Figure 3.4). Differences in b_{sp} between the two sites could be due to differences in aerosol concentrations and/or aerosol liquid water content at both sites. Figure 3.4 shows relative humidity measured at THRO-N, which can be used as a proxy for aerosol liquid water content (assuming similar aerosol composition at the two measurement locations). During the periods where KNRI b_{sp} is much higher than the dry THRO-N b_{sp} measurement, the RH is generally in the upper range of the measurements, indicating that the aerosol liquid water content is a significant contributor to the differences in b_{sp}. However, the discrepancy between b_{sp} at KNRI and THRO-N does not occur at all high RH measurements, indicating that differences in aerosol concentration or other factors are contributing to the differences observed in b_{sp}.
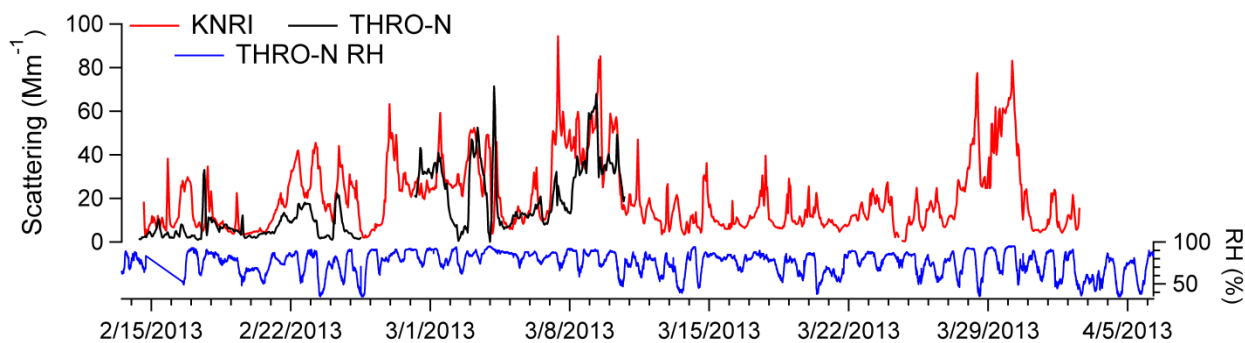
Figure 3.4: The timelines of nephelometer aerosol scattering (b_{sp}; Mm^{-1}) measured at THRO-N and KNRI and relative humidity (RH) measured at THRO-N are shown. The THRO-N nephelometer was operated at room temperature, representing dried aerosol scattering, and the KNRI nephelometer operated at ambient conditions.

3.4 Gas Phase and Primary Aerosol Measurements

Gas phase and black carbon measurements were obtained to better understand the role of aerosol precursor gases, products of photochemical reactions, and direct emissions from oil and gas operations and other anthropogenic activities during BAQS I. Aerosol precursor gas measurements of NH_3, HNO_3 and SO_2 from URG denuder samples are shown in Figure 3.5.

Concentrations of NH_3 were generally very low, with moderate concentrations early in the study at FOUS and slight increases at all sites towards the end of the study period as temperatures increased. HNO_3 concentrations remained low throughout the study at all sites. The highest SO_2 concentrations were observed at KNRI (note the different scale), with smaller peaks observed at the other sampling sites. Unlike the regional episodes of PM observed, the SO_2 trends do not correlate between each sampling site. The high levels of SO_2 likely originate from coal power plants located near KNRI, as shown in Figure 3.2. Back trajectories showing time periods with lower wind speeds and more stagnant air masses correlate with higher SO_2 concentrations, as discussed further in Prenni et al., 2016.
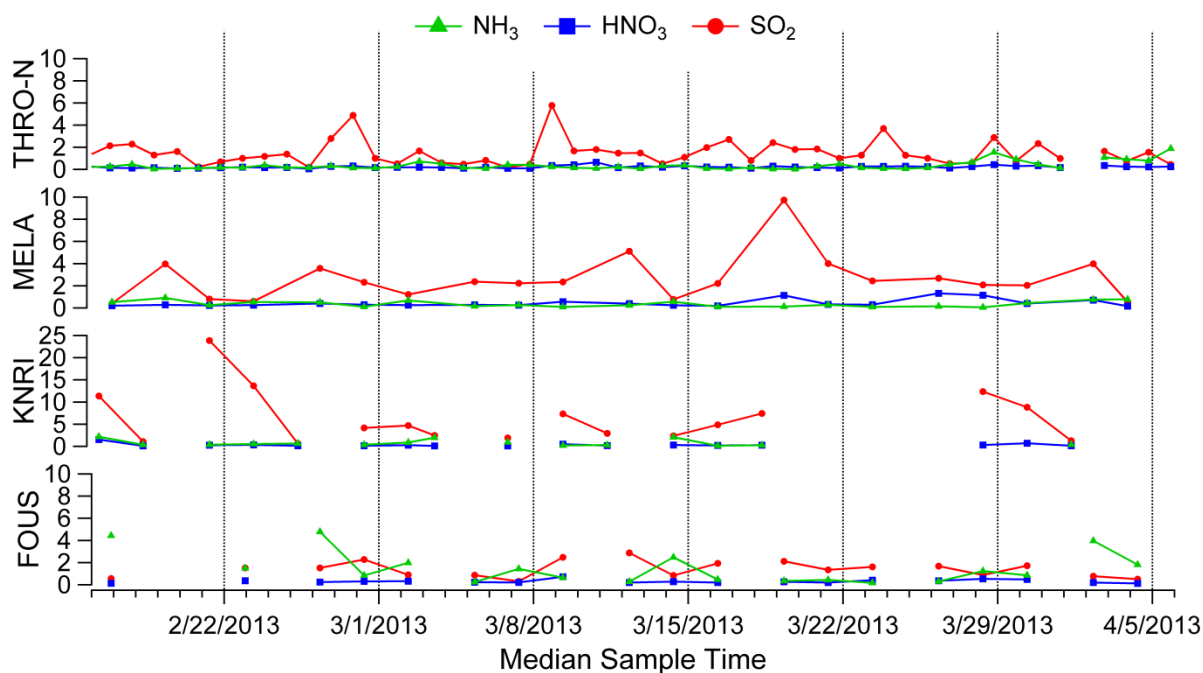
Figure 3.5: Timelines of URG inorganic gas measurements ($\mu g\ m^{-3}$) of NH_3 (green), HNO_3 (blue), and SO_2 (red) from THRO-N, MELA, KNRI and FOUS sampling sites. Daily measurements were made at THRO-N and 2-day samples three times a week at MELA, KNRI, and FOUS. Note the different scale for KNRI.

The gas rack deployed at THRO-N in BAQS I obtained high resolution measurements of SO_2, NO_x, CO and BC. These data were filtered for periodic emissions from the furnace used to heat the sampling shelter. Figure 3.6 shows the daily average timelines of NO_x and BC exhibit similar trends for the entire study. Peaks in CO and SO_2 often coincide with NO_x and BC, but deviations in the trends suggest different sources for these gas phase species. The Pearson correlation coefficients (R^2) shown in Figure 3.7 reinforce the strong correlation between NO_x and BC ($R^2 = 0.81$) and weaker correlations with SO_2 ($R^2 = 0.38$) and CO ($R^2 = 0.36$).
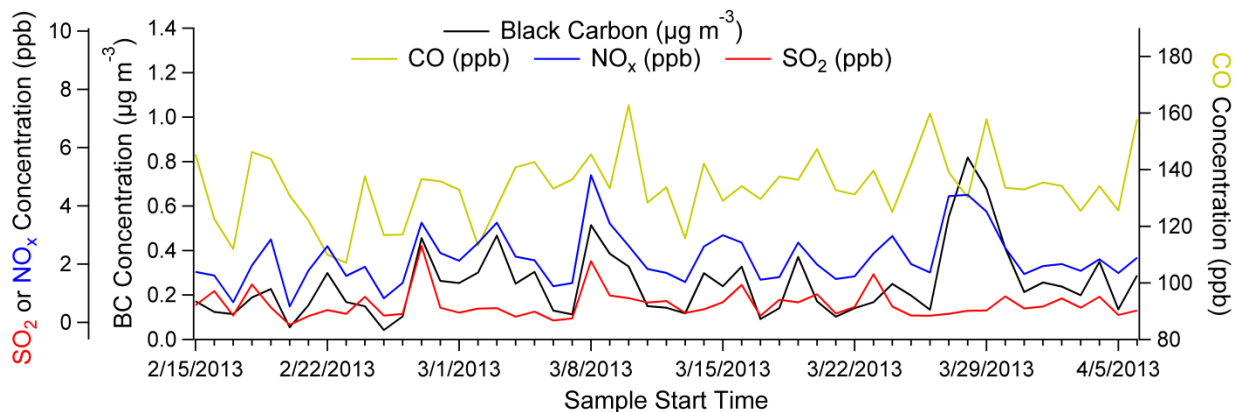
Figure 3.6: Timeline of daily averages of Gas Rack SO_2 (ppb), NO_x (ppb), BC ($\mu g\ m^{-3}$), and CO (ppb) are shown for THRO-N.
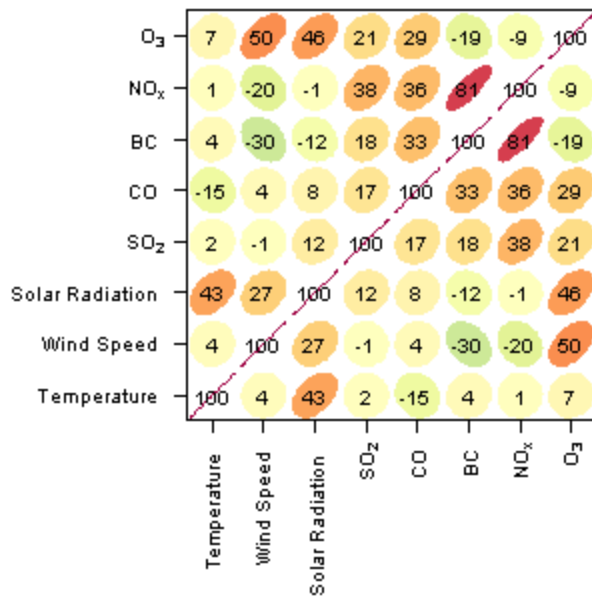
Figure 3.7: Squared correlation coefficients for Gas Rack measurements of NO_x, BC, CO, SO_2 and O_3 and meteorological variables temperature (°C), wind speed (m/s), and solar radiation (KW hr m^{-2}) are listed and color coded so that brighter red colors indicate a strong positive correlation and darker green colors indicate a strong negative correlation.

The timeline of black carbon (BC) measured by an aethalometer at THRO-N shows variable concentrations throughout BAQS I (Figure 3.8), with an average concentration of 0.24 µg m^{-3}. This concentration is much higher than an estimated range of northern hemisphere background black carbon concentration of 0.01 – 0.07 µg m^{-3} determined from measurements taken at Mauna Loa, HI and Point Barrow, AK in 2007 (U.S. Environmental Protection Agency, 2012). The average BC concentration measured at the remote THRO-N site in BAQS I approaches the measured range of urban BC concentrations, 0.3 – 3.0 µg m^{-3}, observed at urban sites within the chemical speciation network in 2007 (U.S. Environmental Protection Agency, 2012). Additionally, long term trends from 2005-2008 measured at rural IMPROVE sites gave an estimated range of 0.14-0.18 µg m^{-3} for the annual mean mass of light absorbing carbon in the upper Midwest (Hand, 2011). These previous long-term BC measurements suggest that BAQS I

concentrations are higher than what would be observed as a background or rural concentration. Considering long-term measurements from IMPROVE sites in or near the Bakken region, an increasing trend in elemental carbon (EC) over time was observed at a site north of THRO-N at Lostwood National Wildlife Refuge (LOST) but no trend was observed at THRO-S which is south of THRO-N (Prenni et al., 2016), suggesting that the impacts from new EC sources can be very localized.
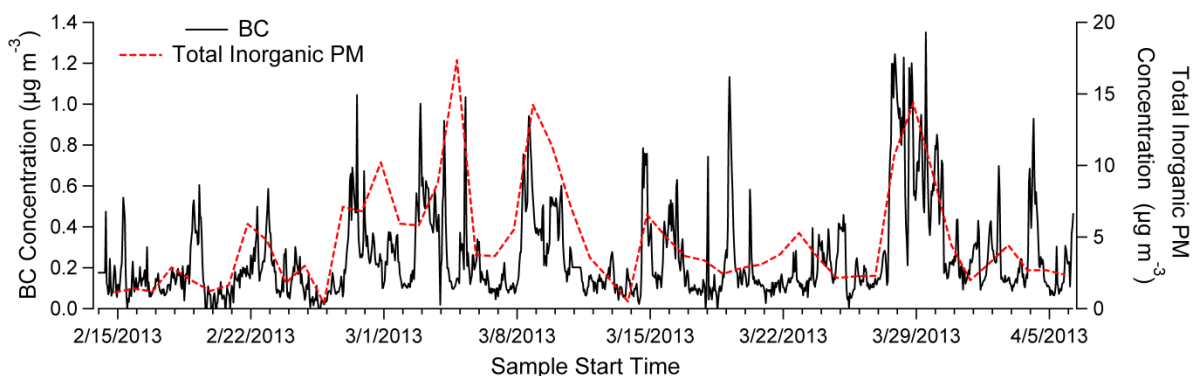
Figure 3.8: Timeline of aethalometer PM$_{2.5}$ black carbon (μg m^{-3}) in solid black and URG total inorganic PM$_{2.5}$ (μg m^{-3}) in dotted red from THRO-N.

Peaks in BC concentrations often match peaks in total inorganic PM$_{2.5}$ conentrations, suggesting similar sources or source regions for these two aerosol types. However, periods occur when the trend deviates, suggesting that there are different sources or regions that impact the measurement site at different times, potentially due to operation schedules and meteorology. This will be discussed in more detail using measurements from BAQS I and BAQS II in the next chapter.

Average O$_3$ concentrations (Table 3.3) show concentrations at all sites were at the higher end of the range of background concentrations. The highest hourly averaged measurement during BAQS I, 68.1 ppb at MELA, is below the National Ambient Air Quality Standard average 8-hour O$_3$ standard of 70 ppb and well below the hourly standard of 120 ppb (US EPA, 2016b).

North American Background O_3 concentrations range from 15 – 35 ppb (Nopmongcol et al., 2016) but have been increasing at a rate of 0.41 ± 0.27 ppb O_3 yr^{-1} as measured between 1995-2011 (Cooper et al., 2012) while more recent studies have estimated that this value is increasing. By these estimates, BAQS ozone levels at all sites were at background level or slightly above. Ozone measurements during BAQS I at all sampling sites show concentrations near background levels (Figure 3.9).

Table 3.3: The average O_3 concentrations (ppb) measured at each site during BAQS I.

	FOUS	KNRI	MELA	THRO-N	THRO-S
O_3 (ppb)	26.8	33.3	33.3	35.1	38.6
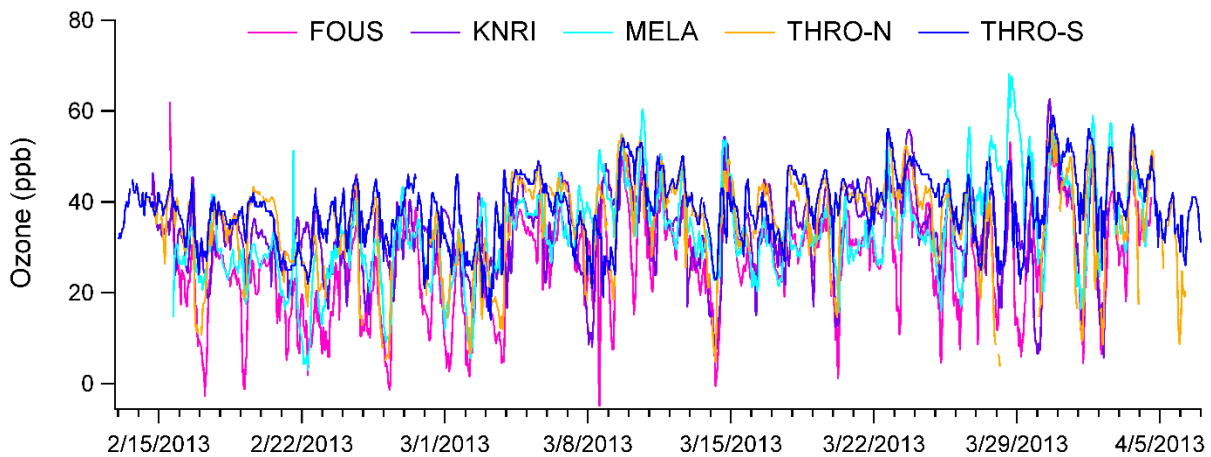
Figure 3.9: Real-time ozone measurements from the five BAQS I sampling sites.

The O_3 measurements in BAQS I contrast observations from other areas of oil and gas development in the Uintah Basin, Utah and the Upper Green River Basin, Wyoming. Measurements from six years in the Uintah Basin gave maximum 8-hour O_3 concentrations over 100 ppb for multiple measurement sites within the basin for 2010, 2011, and 2013 (Stoeckenius, 2015). Peak hourly O_3 concentrations of 143 ppb were observed in 2008 in Boulder, WY (Carter

and Seinfeld, 2012; Schnell et al., 2009).   These studies in wintertime oil and gas development regions have correlated non-methane hydrocarbons (NMHC) with an increase in O_3 (Ahmadov et al., 2014; Field et al., 2015).   VOCs were not measured during BAQS I, but this relationship will be explored further using BAQS II measurements in the next chapter. Being further north and with generally open terrain, limited solar radiation and great ventilation probably help limit wintertime ozone formation in the Bakken.

O_3 has a moderate correlation with wind speed ($R^2 = 0.50$) and with solar radiation ($R^2 = 0.46$; Figure 3.7). The correlation with solar radiation suggests that the O_3 photochemistry is dependent on radiation, as expected. The correlation with wind speed could suggest that higher O_3 concentrations are from long range transport when wind speeds are higher rather than forming locally when wind speeds are light and photochemistry has time to occur during periods of stagnation. Additionally, NO_x concentrations increase as wind speeds decrease ($R^2 = -0.2$; Figure 3. 7) which could lead to a build-up of NO which can act as a sink for O_3 by the oxidation of NO to NO_2.

3.5 Passive Sampler Gas Measurements

3.5.1 Precision of Passive Samplers

Three different passive samplers were deployed during BAQS I and analyzed according to the methods in section 2.11 to test their accuracy and precision in a unique field setting. The three passive sampler types reported here measured NO_2 and SO_2, O_3, and NH_3. To measure precision of the passive samplers, replicates were deployed weekly at THRO-N for the O_3 and NH_3 passives and at all five sites for NO_2/SO_2 passives. The standard deviation and percent relative standard deviation (RSD) are presented in Table 3.3. In addition, the median absolute relative percent difference (MARPD) is shown as an additional measure of precision. The

MARPD and RSD are high for NO_2, SO_2, and NH_3 which can partially be explained by the low concentrations sampled. The limit of detection (LOD) for each gas was calculated using field blank samples, which were lower than the LODs reported by the manufacturer (Table 3.4). LODs reported in $\mu g\ m^{-3}$ (O_3 and NH_3) were converted to ppb using study averaged pressure and sampling period averaged temperature. The average concentration of SO_2 was below the manufacturer's LOD, but above the LOD calculated for this study. The average NO_2 and NH_3 concentrations were low, but above their LODs. O_3 was the only gas substantially higher than the LOD.

Table 3.4: Summary of replicate passive sampler average concentrations (ppb), number of replicates (N), standard deviation, percent relative differences (% RSD), number of replicate samples and the median absolute relative percent difference (MARPD) for each passive. O_3 and NH_3 replicates were collected only at THRO-N and the NO_2/SO_2 passives were collected at all sites. Calculated LODs (Equation 2.1) and manufacturer reported LODs are listed in ppb.

	NO$_2$	SO$_2$	O$_3$	NH$_3$
Average Concentration (ppb)	1.7	0.74	38.2	0.43
N	33	34	7	8
Standard Deviation	0.3	0.15	1.4	0.07
% RSD	21.5%	21.2%	3.5%	17%
# of Replicates	33	34	7	8
MARPD	35%	38%	11%	50%
Calculated LOD (ppb)	0.8	0.2	0.2	0.2
Radiello LOD (ppb)[1]	1.0	1.0	1.0	1.3

1. (Radiello, 2006)

3.5.2 Accuracy of Passive Samplers

Comparison measurements to evaluate passive sampler accuracy included the real-time NO_2 instrument at THRO-N, CASTNET O_3 at THRO-S and daily SO_2 and NH_3 measurements from denuders at THRO-N, FOUS, MELA and KNRI. All comparison measurements were averaged to the weekly passive sampler schedule. The summary of the accuracy of the passive samples is summarized in Table 3.5 which shows the linear regression analysis of the passive samplers versus the comparison measurement.

Table 3.5: A summary of the linear regression analysis between passive sampler and corresponding comparison measurements lists the average concentration (ppb), number of samples (N), slope, y-intercept and Pearson's correlation coefficient (R^2). O_3 comparison measurements are from THRO-S and NO_2 comparison measurements are from THRO-N. SO_2 and NH_3 were compared with denuder measurements at THRO-N, FOUS, KNRI and MELA.

	NO_2	SO_2	O_3	NH_3
Average Concentration (ppb)	1.15	0.86	42.1	0.72
N	8	29	7	29
Slope	0.01	0.64	1.3	0.64
y-intercept	1.12	0.58	-7.6	0.32
R^2	0.00	0.71	0.52	0.79

Measurements of NH_3 from URG denuder samples collected at FOUS, MELA, KNRI and THRO-N are compared with passive measurements in Figure 3.10. The calculation of passive sampler concentrations uses a temperature and pressure corrected sample flow rate (Equation 2.7). Using the points from all sampling sites, the linear regression shows a slope of 0.64, indicating an average underestimation of NH_3 concentrations by the passive samplers. This linear regression and RSD were compared to a previous study that compared passive samplers with URG NH_3 concentrations. A field campaign completed in northeastern Colorado over two study periods obtained an average relative standard deviation of 7.5% for replicate measurements and R^2 values of 0.81 and 0.87, slopes of 0.72 and 0.78 and y-intercepts of 1.11 and 1.26 in a linear regression from each study between passive and URG NH_3 concentrations (Day et al., 2012). Despite much colder temperatures observed during the BAQS I study, similar RSD values and linear regressions compared to previous studies indicate good performance of the NH_3 passive samplers used in BAQS I.
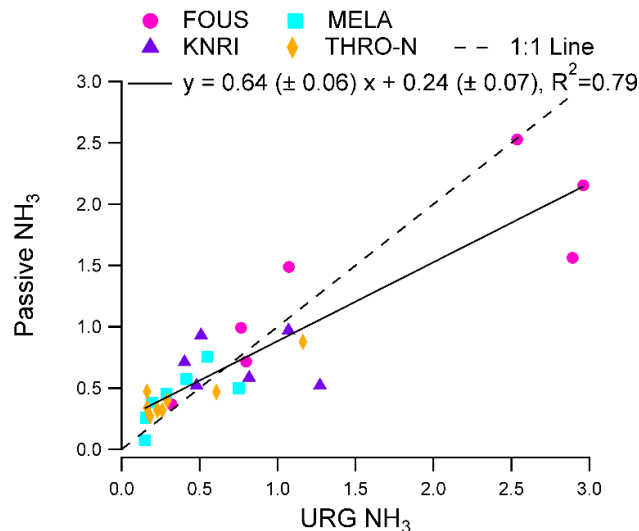
Figure 3.10: Passive sampler measurements of NH_3 (µg m^{-3}) were compared with 24- and 48-hour URG denuder samples from THRO-N, FOUS, KNRI and MELA and colored by average ambient temperature (K). URG samples were combined and averaged to the weekly passive sampling schedule.

Figure 3.11 shows the comparison between O_3 passives and real-time ozone instruments. The comparison from THRO-S shows the closest agreement. Large discrepancies between the different O_3 monitors used at each study site prevents a robust assessment of the passive sampler accuracy. THRO-S is a CASTNET site where the real-time O_3 monitor operates indoors at a controlled room temperature (blue linear fit, Figure 3.11). A Teledyne O_3 monitor was used at THRO-N and operated at ambient temperature. Despite ambient temperatures often falling below the recommended minimum operational temperature (5ºC), good correlation between the Teledyne O_3 and passive sampler concentrations is shown in the orange linear fit (Figure 3.11). The other sites that used 2B technologies O_3 monitors, FOUS, KNRI and MELA, showed much higher concentrations measured by the passive samplers as represented by the pink linear fit (Figure 3.11). This could discrepancy could be due to operating at ambient temperatures often below the acceptable temperature range (details in Section 2.12). The green, blue and purple shaded points in Figure 3.11 are ambient temperatures that fall below the minimum

recommended operating temperature (0ºC). This suggests that the colder ambient temperatures

impacted the instrument calibration.
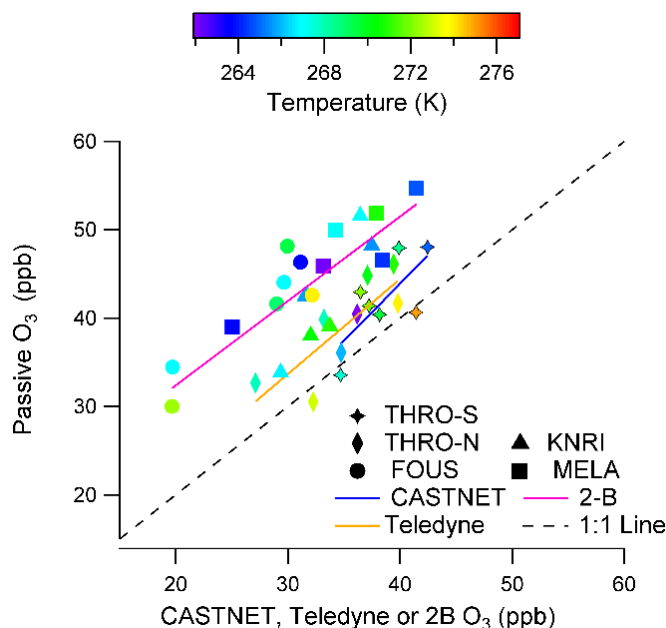
Figure 3.11: Passive sampler measurements of O_3 (ppb) were compared to real-time measurements of O_3 in ppb. Real-time ozone instruments were used at THRO-N (Teledyne), THRO-S (CASTNET station monitor) and KNRI, FOUS and MELA (2B Technologies). The points are colored by average temperature (K).

For the NO_2/SO_2 passive samples, replicates were deployed weekly at all sites and the

comparisons with real-time and denuder measurements are shown in Figure 3.12. Low precision

was calculated for both SO_2 and NO_2 which is likely due to the low concentrations observed in

this study. Greater measurement uncertainty in NO_2 samples with low concentrations and

underprediction of NO_2 compared to a real-time monitor were also observed in a previous study

(Gerboles et al., 2000). The linear regression of passive SO_2 versus URG SO_2 concentrations

gives a slope of 0.64 and y-intercept of 0.58. This low slope, indicating the passive samplers are

underestimating SO_2 is skewed by a few larger concentration values obtained at KNRI (Figure

3.12) with lower concentrations of SO_2 falling along the 1:1 line.
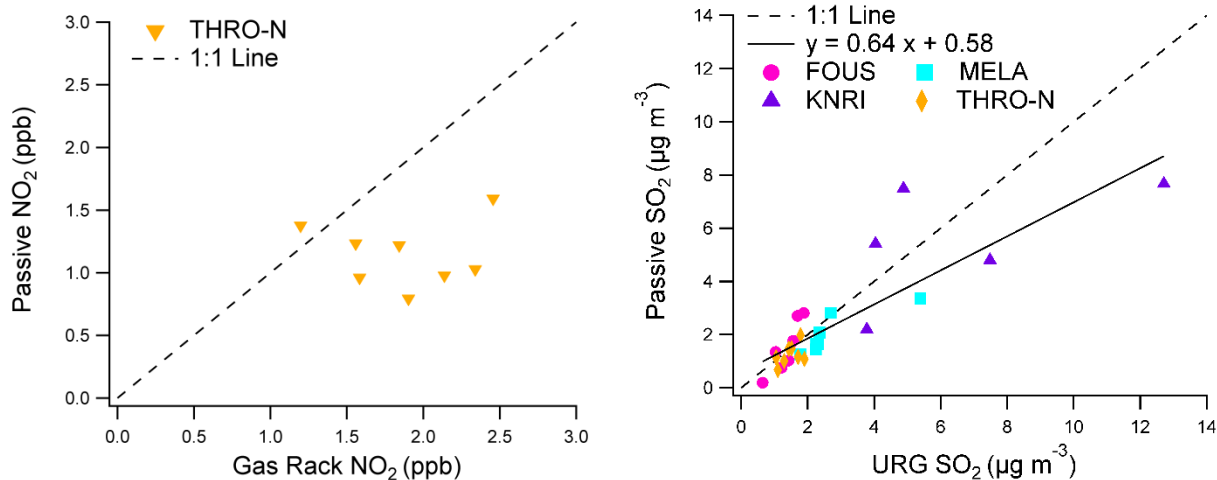
Figure 3.12: Passive sampler measurements of NO_2 (ppb) were compared to real-time measurements of NO_2 (left panel). Passive sampler measurements of SO_2 ($\mu g\ m^{-3}$) were compared with averaged URG denuder samples from four different measurement sites.

The extraction efficiency of NO_2 and SO_2 from the passive samplers was tested by completing the extraction procedure a second time (n=7). These extracts were analyzed in the same method for aqueous concentrations. The average concentration of nitrite in the second extraction was 0.4 μN compared to the original sample extraction concentration of 4.7 μN, indicating that the extraction method is more than 90% efficient.

3.6 Precipitation Measurements

Precipitation samples were obtained from THRO-N, FOUS, KNRI and MELA. THRO-N samples were collected daily when precipitation was present and weekly samples were collected at FOUS, KNRI and MELA. The pH values measured were very similar across the sampling region, with averages of 5.5, 5.6, 5.8 and 5.9 for THRO-N, FOUS, KNRI and MELA, respectively. The timeline of pH and precipitation amount (mm) is shown in Figure 3.13. The pH varies between 4.5 and 6.5 at all sampling sites. In general, MELA and THRO-N received more precipitation than KNRI and FOUS.
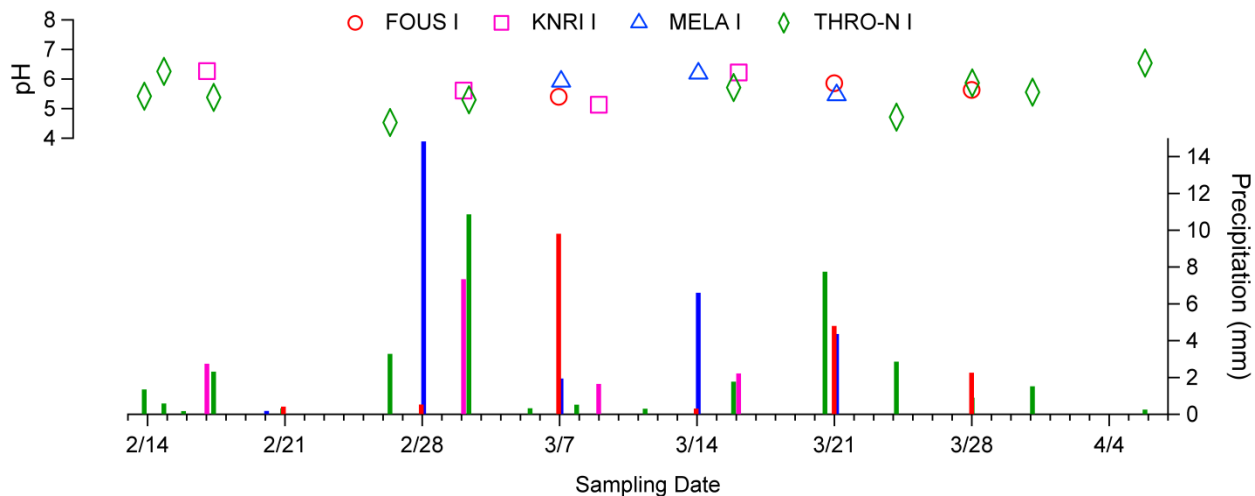
Figure 3.13: The pH and precipitation amount (mm) measured at each sampling site during BAQS I.

3.7 BAQS I Summary and Motivation for BAQS II

Oil and natural gas development in the Bakken region rapidly increased starting in 2007 and continued increasing throughout the BAQS I study period. Emissions from this development can include exhaust from diesel engines powering on-site equipment, evaporation or leaking oil and gas, and flaring. Along with direct emissions from oil and natural gas extraction, additional emissions from vehicle exhaust, generation of road dust and the growing population may also increase. To investigate the impact of the oil and gas development on the Bakken region, the BAQS I field campaign was carried out to measure air quality parameters from national parks and other Federal sites. Aerosol and gas measurements from five different sampling sites throughout the Bakken region have shown elevated regional episodes of inorganic aerosol concentrations which correlated with aerosol scattering measurements. PM$_{2.5}$ BC measurements were also determined to be above background levels and correlated with NO$_x$. Elevated SO$_2$ concentrations were also observed, but the absence of correlations with other species suggested a different source. O$_3$ concentrations were found to be at or near background levels. The impact

61

of the regional elevated aerosol episodes observed in BAQS I motivated the inclusion of organic

aerosol measurements and higher resolution inorganic aerosol measurements in a second study:

BAQS II. The importance of oil and gas development on haze in the national parks is

investigated further in BAQS II.

4.0 INORANIC AEROSOL DURING BAKKEN AIR QUALITY STUDY II

4.1 BAQS II Study Overview

A second Bakken Air Quality Study (BAQS II) was conducted the winter following BAQS I between November 23, 2013 and March 28, 2014. Shown previously in Figure 3.2, only three of the BAQS I sampling sites were used in this second study; the north unit of Theodore Roosevelt National Park (THRO-N), Fort Union Trading Post National Historical Park (FOUS) and Medicine Lake National Wildlife Refuge (MELA). THRO-N, the main site, featured a comprehensive suite of instrumentation to measure VOCs and high-resolution aerosol composition and inorganic precursor gas concentrations. In addition to inorganic aerosol species, organic aerosol was also collected during BAQS II. All instrumentation and measurement time resolution used in BAQS II are listed in Table 4.1.

Table 4.1: A summary of the measurements and instrumentation used during the second study (BAQS II) from the sampling sites THRO-N, FOUS, and MELA. The time resolution of each measurement and model, if applicable, is listed in the column.

	Measurements During BAQS II			
Sampling Technique	**Measurement**	**THRO-N**	**FOUS**	**MELA**
Aerosol				
URG filter pack	$PM_{2.5}$ ions	Daily	Daily	Weekly
IMPROVE Teflon filter	$PM_{2.5}$ mass	Daily	-	-
IMPROVE quartz filter	$PM_{2.5}$ OC/EC	Daily	-	-
AMS	Non-refractory PM_1 ions and total organics	5-minute	-	-
MARGA	$PM_{2.5}$ ions	Hourly	-	-
Aethalometer	$PM_{2.5}$ black carbon	5-minute	-	-
Nephelometer	$PM_{2.5}$ scattering	5-minute; Radiance Research M903	5-minute; Optec NGN-2	5-minute; Ecotech M9003
TEOM	$PM_{2.5}$ mass	6-minute		
Gases				
URG denuders	inorganic gases	Daily	Daily	Weekly
MARGA	inorganic gases	Hourly	-	-
VOCs				
Canister	whole air grab sample	Twice daily	4 times per week	1 time per week
Surface Meteorology		1-minute	1-minute	Existing*

*Existing surface meteorology measurements were obtained from the Western Regional Climate Center (WRCC) Remote Automated Weather Stations (RAWS).

Here we focus on the development and characteristics of winter fine particle haze episodes. Wintertime haze episodes are investigated using aerosol scattering and meteorological variables. Analysis of back trajectories gives insight into the transport patterns associated with observed $PM_{2.5}$ episodes. VOC measurements will be examined to characterize timescales of haze formation and to assess the impact from oil and natural gas operations. A detailed analysis of the aerosol composition, including both inorganic and carbonaceous components, will be discussed. This will include the general characteristics of the $PM_{2.5}$ and contributions of each

species to total PM$_{2.5}$ mass. Finally, gas to particle partitioning of the inorganic species will be explored using a thermodynamic aerosol model. The model is used to analyze sensitivities of aerosol formation to concentrations of inorganic precursor gases.

4.2 Results

Periods of elevated inorganic aerosol concentrations were observed in the URG filter-pack measurements collected during BAQS II as shown in Figure 4.1. Observations show that increased concentrations occurred regionally across all measurement sites. High concentration episodes were dominated by ammonium (NH$_4^+$), sulfate (SO$_4^{2-}$) and nitrate (NO$_3^-$). Concentrations of all other ions measured, including chloride (Cl$^-$), nitrite (NO$_2^-$), potassium (K$^+$), sodium (Na$^+$), calcium (Ca^{2+}), and magnesium (Mg^{2+}), were low. The sample number, mean, standard deviation and maximum concentrations of each aerosol species at all sites for both studies are given in Table 4.2. The highest time-integrated concentrations of total inorganic components measured during BAQS II, which were 7.87 and 7.90 µg m^{-3} for 24 hour samples measured at FOUS and THRO-N. FOUS, which was surrounded by a dense area of oil wells, also had the highest average inorganic aerosol concentration during BAQS I in late March, which was 21.3 µg m^{-3} for a 48 hour sample. MELA, a study background site located west and often upwind of the Bakken production region, had the lowest average inorganic aerosol concentration during both studies. For the three sites used in both studies (THRO-N, FOUS, and MELA), average inorganic PM$_{2.5}$ concentrations were over two times greater for the entire first study period compared to the entire second study period. This difference was found to be significant using the Student's t-test (Table 4.3). The mean aerosol scattering (b$_{sp}$) at THRO-N was also over two times greater during BAQS I compared to BAQS II: 15.3 Mm^{-1} vs 7.1 Mm^{-1}. BC in PM$_{2.5}$ concentrations in BAQS II averaged 0.2 µg m^{-3} with a maximum hourly

concentration of 1.9 µg m^{-3}. For BAQS I, BC concentrations averaged 0.2 µg m^{-3} with a

maximum hourly concentration of 1.4 µg m^{-3}. Timelines of nephelometer and BC measurements

from BAQS II are presented in Figures 4.2 and 4.3.
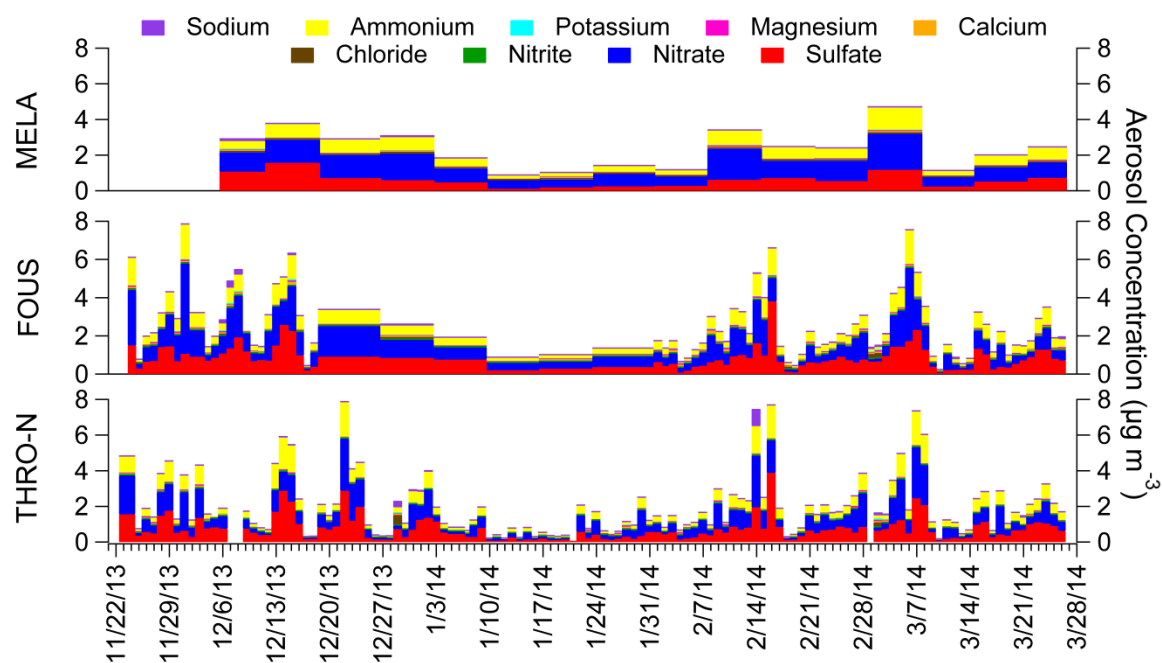
Figure 4.1: Stacked bars representing the contribution of each inorganic species to the total
inorganic aerosol from URG filter PM$_{2.5}$ measurements (µg m^{-3}) from the second study. The
width of the bar signifies the sampling period which varied between daily or weekly samples.

Table 4.2: The average and standard deviation (bold) and maximum (in parenthesis) URG concentrations are listed for each study in units of $\mu g\ m^{-3}$. The number of filter samples collected for each site (N) is listed in the heading of each column. The site locations are labeled with a 1 for measurements collected during the first study and with a 2 during the second study.

	THRO-N N=120	FOUS N=84	MELA N=16
Na^+	**0.04±0.10** (0.97)	**0.05±0.06** (0.38)	**0.05±0.04** (0.17)
NH_4^+	**0.48±0.43** (1.93)	**0.57±0.38** (1.83)	**0.60±0.28** (1.29)
K^+	**0.02±0.02** (0.10)	**0.03±0.02** (0.12)	**0.02±0.01** (0.03)
Mg^{2+}	**0.01±0.01** (0.08)	**0.01±0.01** (0.07)	**0.01±0.01** (0.03)
Ca^{2+}	**0.02±0.03** (0.10)	**0.05±0.03** (0.19)	**0.03±0.01** (0.06)
Cl^-	**0.02±0.06** (0.59)	**0.04±0.05** (0.29)	**0.03±0.03** (0.11)
NO_2^-	**0.001±0.004** (0.02)	**0.01±0.01** (0.08)	**0.003±0.001** (0.005)
NO_3^-	**0.70±0.68** (2.93)	**0.93±0.82** (4.7)	**1.01±0.47** (2.02)
SO_4^{2-}	**0.70±0.68** (3.88)	**0.84±0.61** (3.80)	**0.61±0.39** (1.57)
Total Inorganic	**1.99±1.70** (7.90)	**2.52±1.68** (7.87)	**2.36±1.11** (4.75)
IMPROVE PM$_{2.5}$	**3.27±** (11.1)	-	-

Table 4.3: The Student T-test was used to determine that there was a significant difference between total inorganic $PM_{2.5}$ between BAQS I (x_1) and BAQS II (x_2) at THRO-N, FOUS, and MELA.

	THRO-N	FOUS	MELA
Difference in Mean $\overline{x}_1 - \overline{x}_2$ **(µg m^{-3})**	2.81	3.93	3.51
t value	1.97	1.98	2.03
S$_{pooled}$	2.49	2.54	2.19
N$_1$	51	19	21
N$_2$	120	84	16
t*S$_{pooled}$* $\sqrt{\dfrac{(N_1+N_2)}{(N_1 N_2)}}$	0.82	1.28	1.48
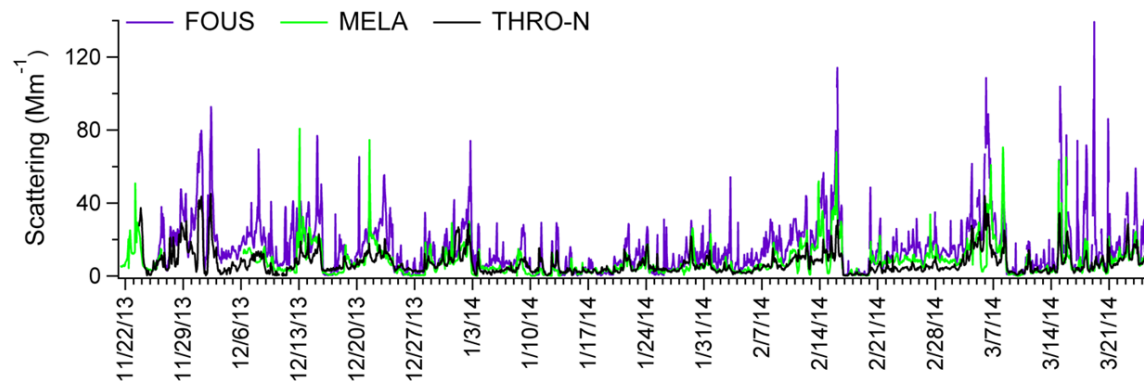
Figure 4.2: Timelines of Nephelometer PM$_{2.5}$ scattering (Mm^{-1}) from the the second study at THRO-N, FOUS, and MELA.
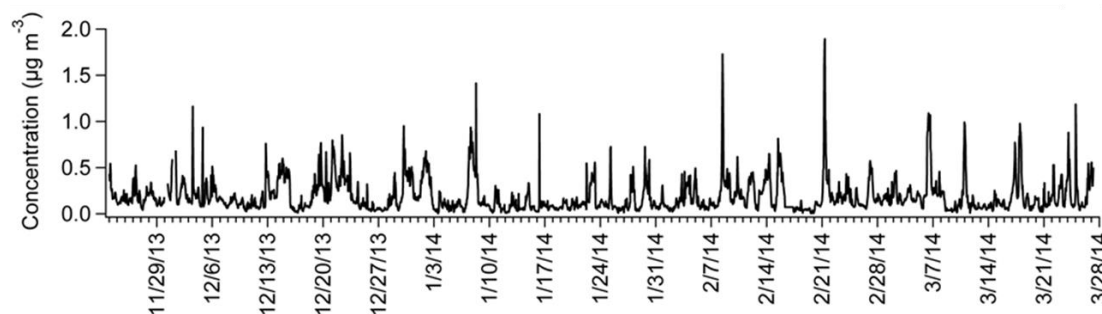
Figure 4.3: Timelines of aethalometer black carbon concentrations in PM$_{2.5}$ from the second study at THRO-N.

During BAQS II, additional instrumentation was added to THRO-N to measure organic aerosol and inorganic aerosol at higher time resolution. AMS organic aerosol in PM$_1$ during BAQS II averaged 1.08 ± 0.66 µg m^{-3} with a maximum hourly concentration of 4.94 µg m^{-3}. The total inorganic aerosol in PM$_{2.5}$ measured by MARGA averaged 2.39 ± 2.32 µg m^{-3} with a maximum hourly concentration of 19.5 µg m^{-3}. The sample number, mean, standard deviation and maximum concentrations of each aerosol species for the MARGA and AMS during BAQS II are given in Table 4.4. Timelines of hourly averaged AMS and hourly MARGA measurements are presented in Figures 4.4 and 4.5.

Table 4.4: The average and standard deviation (bold) and maximum (in parenthesis) MARGA and AMS concentrations are listed for each study in units of $\mu g\ m^{-3}$. The number of samples collected (N) is listed in the heading of each column.

	MARGA N=1605	AMS N=11054
Na^+	**0.01±0.03** (0.36)	
NH_4^+	**0.41±0.50** (4.57)	**0.60±0.58** (5.36)
K^+	**0.01±0.03** (0.37)	
Mg^{2+}	**0.05±0.07** (1.20)	
Ca^{2+}	**0.12±0.16** (2.01)	
Cl^-	**-**	**0.01±0.02** (0.18)
NO_3^-	**1.07±1.07** (9.15)	**0.97±1.27** (9.72)
SO_4^{2-}	**0.95±0.96** (9.59)	**0.78±0.70** (9.04)
Organics	**-**	**1.08±0.66** (4.94)
Total Inorganic	**2.39±2.32** (19.5)	
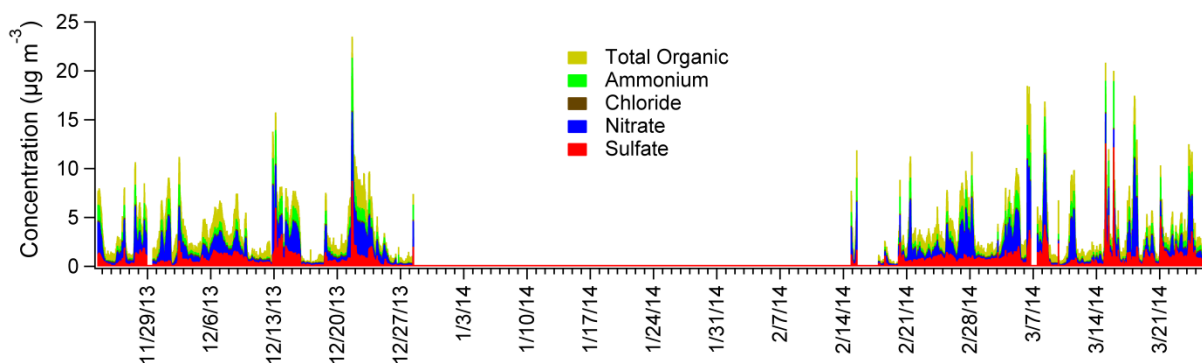
Figure 4.4: The timelines of AMS PM_1 chloride, nitrate, sulfate, ammonium and organics during the second study at THRO-N.
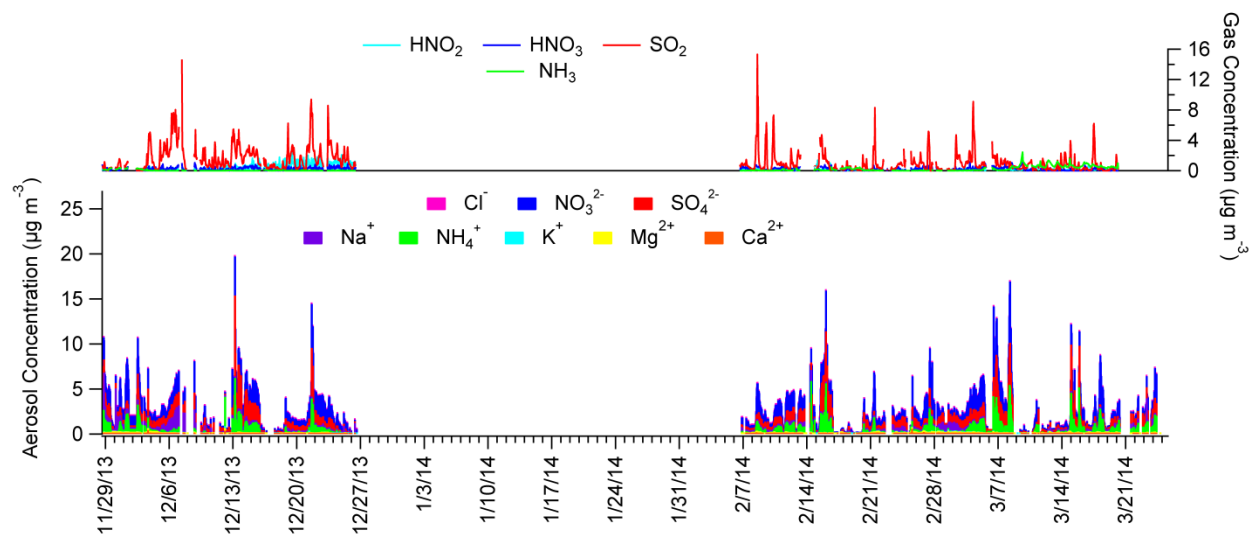
Figure 4.5: Timelines of MARGA measurements show gas concentrations (μg m^{-3}) on the top panel as solid lines and aerosol concentrations (μg m^{-3}) on the bottom panel as stacked bars measured during BAQS II.

The temperature and relative humidity from each study are summarized in Table 4.5. Only similar time periods from both studies are included in this table in order to facilitate comparison between the two studies without a bias from seasonal differences. The temperature varied slightly between sites, with MELA being between 1.7 and 3.1°C colder on average than the other two sites for each study period. THRO-N and FOUS had comparable average temperatures between both studies. Relative humidity was higher at each site during BAQS I compared to BAQS II. Figure 4.6 shows the differences in wind direction and wind speed during the overlapping BAQS I and II time periods. In BAQS I, the wind originated from both the southeast and northwest. BAQS II winds came predominantly from the west northwest, but wind speeds were similar between studies.

Table 4.5: The average (bold), minimum / maximum (in parenthesis) temperature and relative humidity at THRO-N, FOUS and MELA from each study during the overlapping dates; February 13 through March 25.

	BAQS I			BAQS II		
	THRO-N	**FOUS**	**MELA**	**THRO-N**	**FOUS**	**MELA**
Temperature (°C)	**-4.8** (-27.5 / 15.2)	**-4.7** (-22.8 / 15.6)	**-7.8** (-28.3 / 9.4)	**-4.6** (-29.0 / 18.8)	**-5.0** (-29.2 / 22.5)	**-6.7** (-31.1 / 16.1)
Relative Humidity (%)	**77.0** (33.9 / 95.0)	**80.0** (44.2 / 101.2)	**78.0** (64.0 / 95.0)	**67.0** (30.0 / 94.0)	**68.0** (28.0 / 94.0)	**73.5** (22.0 / 100)
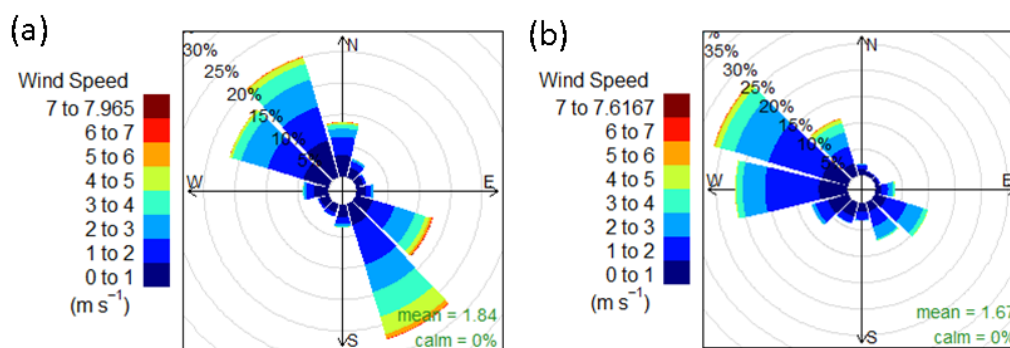
Figure 4.6: Wind roses from February 13 through March 25 from BAQS I in 2013 (a) and BAQS II in 2014 (b) from THRO-N. The percent probability that the wind came from each direction is shown by the length of each wedge and is colored by wind speed (m s^{-1}).

4.3. Discussion

4.3.1 Study Comparison

4.3.1.1 Influence from Meteorology

Comparing overlapping times of year (February 15 through March 28), the average inorganic PM$_{2.5}$ concentrations totaled 5.0 and 2.3 ug m^{-3} at THRO-N in 2013 and 2014, respectively, more than a factor of two difference. Local wind speed and wind direction at THRO-N are plotted in Figure 4.6. The mean wind speed was 1.84 m s^{-1} for 2013, slightly higher than the average 1.67 m s^{-1} for 2014. Both years show strong northwesterly flow, but 2013 also has a significant contribution from southeasterly wind. Increased transport of NH$_3$

from agricultural regions southeast (Pitchford et al., 2009) or north (Carew, 2010) of the Bakken formation might have also helped increase AN formation. No significant differences in average site temperature were observed, but the average relative humidity was lower at all sites during 2014 (Table 4.5), which could impact AN formation. Precipitation measurements during both studies show higher precipitation amounts during BAQS I compared to BAQS II (Figure 4.7), which, in addition to sustained temperatures below freezing, contributed to the more frequent snow cover observed in BAQS I.
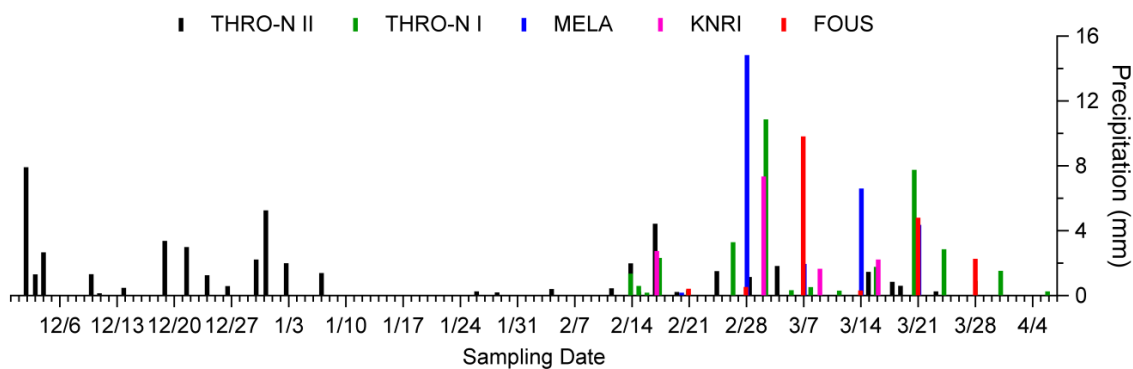
Figure 4.7: Precipitation amount (mm) measured at THRO-N, MELA, KNRI and FOUS during BAQS I (colored lines) and measurements from THRO-N during BAQS II (black lines).

Near THRO-N, average solar radiation at 14:00 decreased from 0.59 to 0.44 KW hr m^{-2} between BAQS I and II (Figure 4.8). Snow cover was present for 89% of BAQS I and only 35% of BAQS II. The presence of snow cover can intensify solar radiation and enhance photochemistry, which has been shown to generate high concentrations of pollutants such as ozone and particulate nitrate in previous studies (Li et al., 2014b; Rappenglück et al., 2014). Snow cover can also strengthen the nighttime inversion layer, trap PM$_{2.5}$ and PM$_{2.5}$ precursor emissions near the surface, and create colder and more humid conditions which are favorable for AN formation (Green et al., 2015). Median atmospheric mixing heights were 293 m and 375 m for 2013 and 2014. Differences in local wind direction, higher relative humidity, higher solar

radiation, more persistent snow cover and lower average mixing height during 2013 may all have contributed to the higher PM$_{2.5}$ concentrations observed.
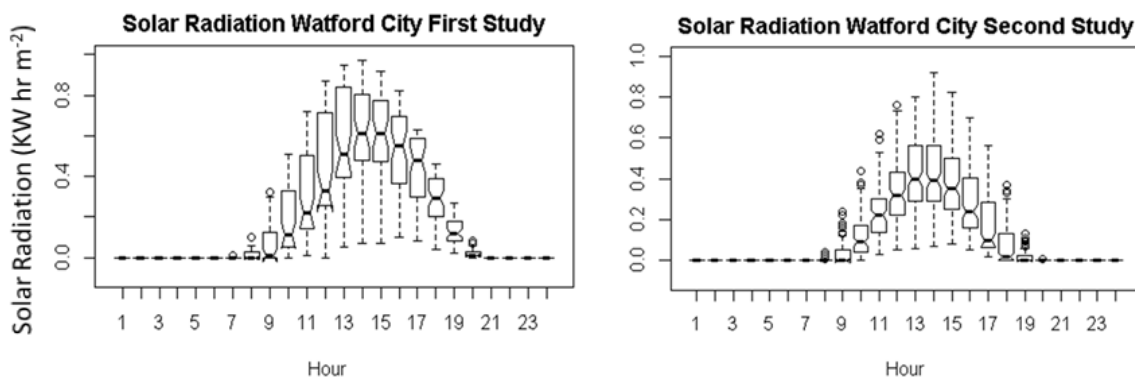
Figure 4.8: The diurnal trends of solar radiation measured in Watford City, ND from the first (top plot) and second (bottom plot) study periods, with measurements in KW hr / m^2. The lines represent the median value, the lower and upper edges of the boxes represent the 1st and 3rd quartiles, the whiskers represent the minimum and maximum values or at most 1.5 times the interquartile range with circles representing any values beyond this range.

4.3.1.2 Aerosol Source Regions and Atmospheric Age

Regional transport patterns were investigated to better understand source regions of observed pollutants. Back trajectories were produced using the hybrid single particle Lagrangian integrated trajectory model (HYSPLIT; Stein et al., 2015) with meteorological input from North American Regional Reanalysis (NARR) data. A residence time analysis was performed to determine the source regions associated with individual aerosol species; each grid cell is colored by the percentage of air masses that resided in that cell. Figure 4.9 shows the residence time of the air masses with the highest 10% of NO$_3^-$ (a and c) and SO$_4^{2-}$ (b and d) concentrations from the daily URG filters for BAQS I (a and b) and MARGA hourly concentrations for BAQS II (c and d). In the first study, the highest concentrations of NO$_3^-$ were associated with transport from southeast of THRO-N while the highest concentrations of SO$_4^{2-}$ are associated with air masses spending time in the Bakken oil patch region as well as in regions to the northwest and northeast. The different patterns suggest that different source regions exist for NO$_3^-$ and SO$_4^{2-}$ precursor

emissions. In the second study, the highest concentrations of NO_3^- and SO_4^{2-} do not show clear

trends in the residence time analysis, with the exception of significant time spent in the Bakken

oil patch region itself. Back trajectories also clearly show patterns of air recirculation and

stagnation in the Bakken region during regional $PM_{2.5}$ episodes (Figure 4.10a). This is similar to

the findings of Prenni et al. (2016), who showed that the highest concentrations of aerosol

precursors (NO_x and SO_2) during the BAQS study corresponded to trajectories that were shorter

(slower speeds) and were more likely to be impacted by closer sources. For comparison, the

residence times of trajectories associated with the lowest 10% of NO_3^- and SO_4^{2-} concentrations

from the second study and representative back trajectories from a period of low $PM_{2.5}$

concentrations show fast transport solely from the west (Figures 4.10b and 4.11). Analysis of the

residence times and local winds from both studies show that the highest concentrations of both

NO_3^- and SO_4^{2-} are associated with emissions from nearby THRO-N, suggesting the importance

of sources local to the oil production region.
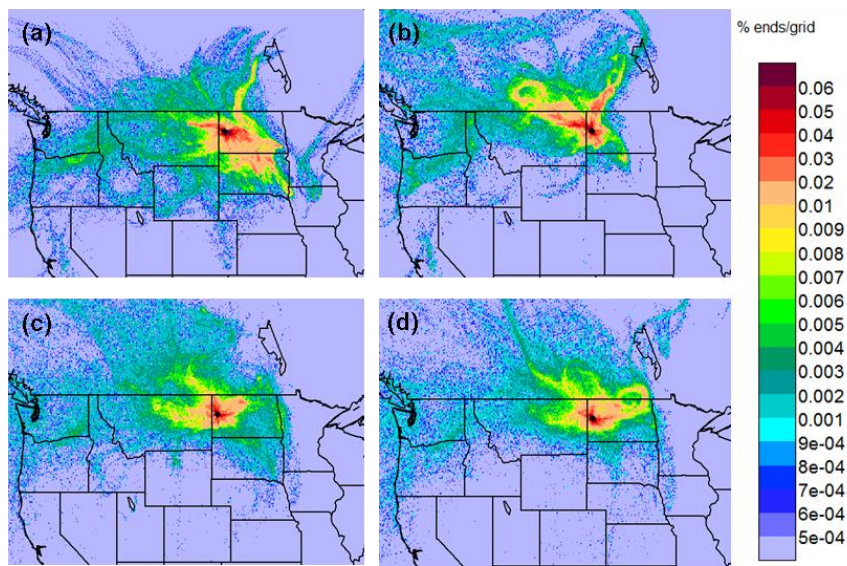
Figure 4.9: The residence times of the highest 10% concentrations using five-day ensemble trajectories of nitrate (panels a and c) and sulfate (panels b and d) using URG measurements during the first study from 2/14/13 – 4/5/13 (top panels) and using MARGA measurements during the second study from 11/30/13 – 3/24/14 (bottom panels).
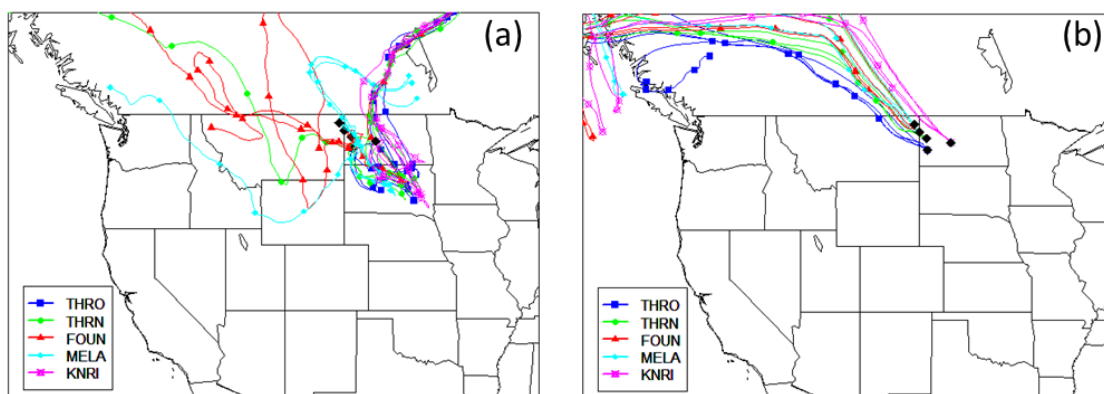
Figure 4.10: Representative two-day back trajectories from five measurement sites from the first study on 3/28/13 (a) and 3/12/13 (b). The five sites were the North Unit of Theodore Roosevelt National Park (THRN), the South Unit of Theodore Roosevelt National Park (THRO), Fort Union (FOUN), Medicine Lake (MELA) and Knife River (KNRI). The back trajectories in (a) are from just one day of a prolonged episode of regional high $PM_{2.5}$ concentrations during which the highest concentrations of URG $PM_{2.5}$ nitrate were observed at all sites. The back trajectories in (b) are representative of days with low regional $PM_{2.5}$ concentrations.
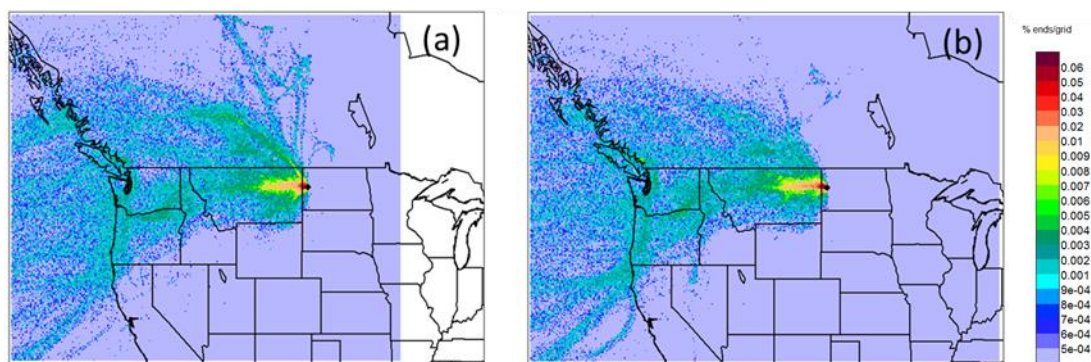
Figure 4.11: Residence time plots show the lowest 10% concentrations of nitrate (a) and sulfate (b) using MARGA measurements from the second study at THRO-N.

Local winds and measured b_{sp} were examined at FOUS to gain insight as to which source regions are important specifically for the degradation of visibility. A wind rose (Figure 4.12a) and conditional probability plot (CPF) showing the 90th percentile b_{sp} concentration (Figure 4.12b) show a clear relationship between the highest values of b_{sp} and easterly local winds and light wind speeds. Easterly winds at FOUS, which is located near the western edge of the Bakken region (Figure 3.2), originate from the densest area of oil and gas operations which

reinforces the importance of local sources on PM$_{2.5}$ concentrations and haze. The major role of local sources also suggests that long range transport, such as from the Alberta oil sands, does not likely significantly contribute to the PM concentrations and haze in the Bakken region.
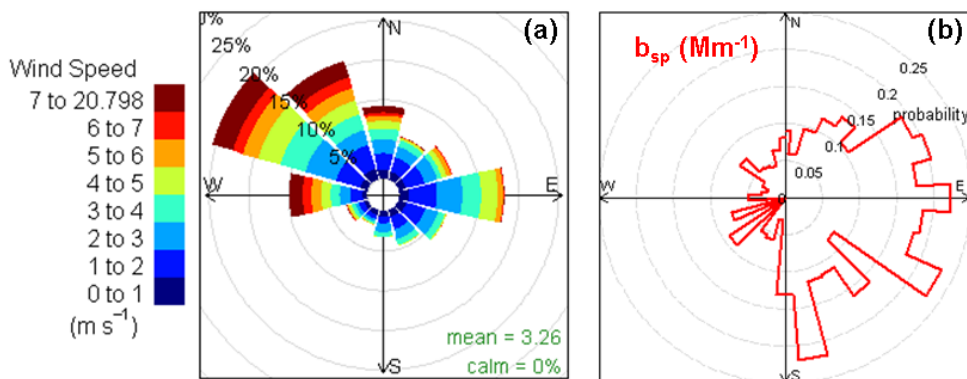
Figure 4.12: A wind rose (a) and conditional probability function plot (CPF, b) are shown from FOUS from the second study. The CPF plot shows the wind directions associated with the 90th percentile concentrations of b$_{sp}$ (31.6 Mm^{-1}) and the probability of occurrence.

To further examine whether the highest inorganic aerosol concentrations are influenced by local emissions, a photochemical clock is used to estimate the atmospheric age of emissions in Figure 4.13. This plot utilizes the concentrations of 2-pentyl nitrate, 2-butyl nitrate and their parent alkanes obtained from VOC canister measurements at THRO-N. The reaction rates of these alkanes with nitrogen oxides and the chemical evolution of the alkyl nitrates are well known, so the ratio of the parent alkane to its alkyl nitrate can be used as a proxy for time or airmass age (Bertman et al., 1995; Russo et al., 2010a). An OH concentration of 5×10^{6} molecules cm^{-3} was used in the calculation which is a recommended average winter concentration (Russo et al., 2010b). Overlaid on this plot are the inorganic aerosol concentration (sum of NH$_4^{+}$, NO$_3^{-}$, and SO$_4^{2-}$) and the calculated airmass age. The airmass age is estimated to be well under one day when the highest inorganic aerosol concentrations are observed. Figure

4.13 also shows i-/n-pentane ratios observed in THRO-N, represented by marker size. The

i-/n-pentane ratios from BAQS are described in detail in Prenni et al. (2016). Briefly, the

i-/n-pentane ratio has been used in previous oil and gas studies as a marker of urban emissions if

the ratio is greater than 1 or oil and gas emissions if the ratio is less than 1 (Gilman et al., 2013;

Swarthout et al., 2013). A smaller marker size in Figure 4.13 represents a smaller i-/n-pentane

ratio, which is indicative of oil and gas emissions. The lower i-/n-pentane ratios correspond with

both higher PM$_{2.5}$ concentrations and younger air mass age. Combined with the preceding

transport analysis, this is compelling evidence that emissions from local sources from oil and gas

operations are large contributors to the high concentration aerosol episodes observed.
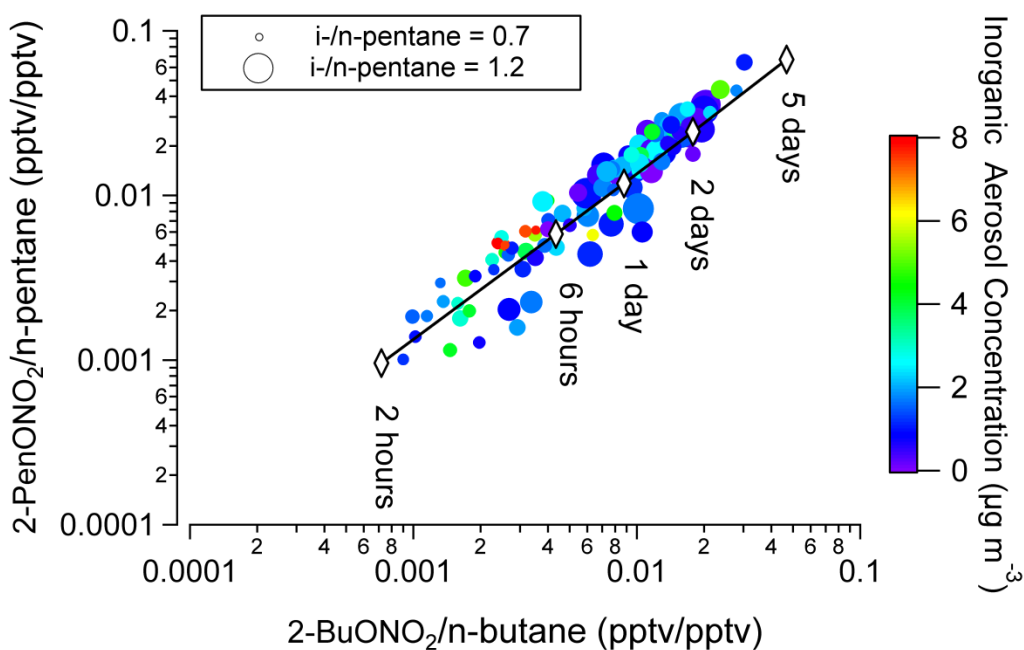
Figure 4.13: The alkyl nitrate chemical clock (see text for description) shows the estimated age of VOC emissions in the sampled air mass and is overlaid with the total inorganic aerosol concentration from URG measurements and the i-/n-pentane ratio.

4.3.2 Aerosol Composition and Formation

4.3.2.1 PM$_{2.5}$ Speciation at THRO-N

An investigation of the higher time resolved aerosol measurements from BAQS II is presented here. Limitations in deployed instrumentation prevent the same analysis for BAQS I. However, similar trends in the episodic nature of the elevated regional PM$_{2.5}$ concentrations, a similar rate of oil production (Figure 4.1), and a similar average ratio of PM$_{2.5}$ nitrate to sulfate were observed in both studies. The comparable emissions and aerosol chemistry in both studies suggests that the speciation results observed for BAQS II are representative of BAQS I. For this analysis, we use hourly reconstructed PM$_{2.5}$ mass which is calculated from the sum of the inorganic species in PM$_{2.5}$ from the MARGA, total organics in PM$_1$ from the AMS (we assume that organic mass is mostly below 1µm) and BC in PM$_{2.5}$ from the aethalometer. To determine that a significant amount of PM$_{2.5}$ organic aerosol was not missing in our PM$_1$ measurement, AMS PM$_1$ organic carbon (OC) and IMPROVE PM$_{2.5}$ OC were compared (Figure 4.14). The average ratio and standard deviation of AMS PM$_1$ OC to IMPROVE PM$_{2.5}$ OC was 1.1 ± 0.6, indicating that the AMS PM$_1$ measurement is similar to the PM$_{2.5}$ organic mass. Additional comparisons of the carbonaceous, inorganic, and total PM measurements are presented in Figures 4.14, 4.15, and 4.16. For further validation, the IMPROVE total PM$_{2.5}$ mass compared to the reconstructed PM$_{2.5}$ mass has a slope of 1.0, y-intercept of -0.41 and a R^2 of 0.92 (Figure 4.16), indicating that the reconstructed PM$_{2.5}$ is representative of the total measured PM$_{2.5}$ mass observed during the study.
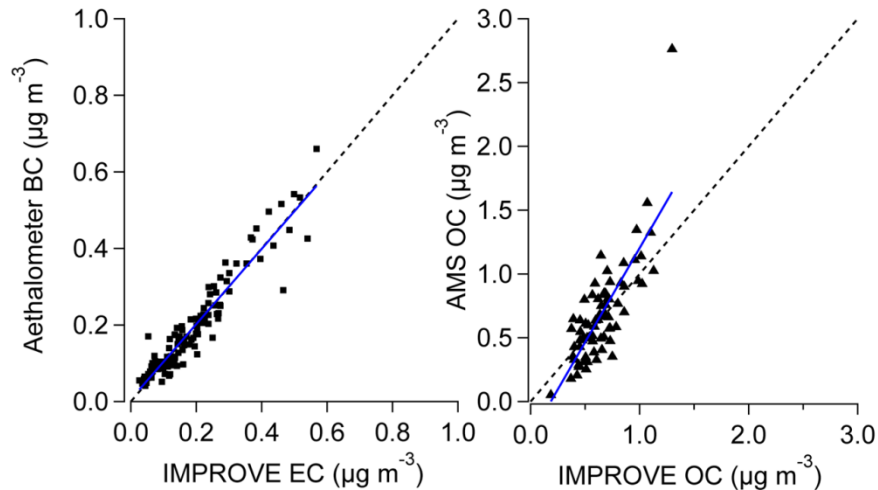
Figure 4.14: Carbonaceous aerosol measurements from the aethalometer (PM$_{2.5}$ BC), AMS (total PM$_1$ OC) and IMPROVE (daily PM$_{2.5}$ OC and EC) are compared. The aethalometer and IMPROVE EC are highly correlated (R^2 = 0.90, y = 0.98x + 0.01). The AMS OC concentrations were calculated using the total organic measurement (OM) in the V mode and the OM/OC ratio generated using W mode measurements. The good correlation between AMS and IMPROVE OC measurements (R^2 = 0.63) suggests that most OC is smaller than 1 µm in aerodynamic diameter. However, the large slope and y-intercept suggests some measurement bias (y = 1.5x – 0.27).
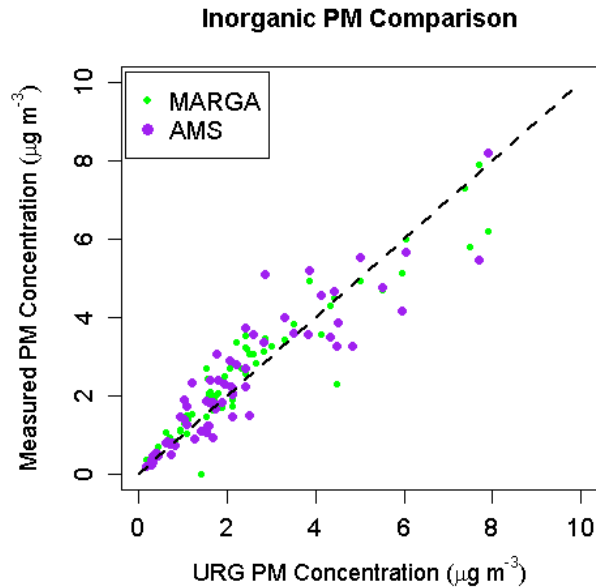
Figure 4.15: The comparison of the URG total inorganic PM$_{2.5}$ with the inorganic component of PM$_{2.5}$ from the MARGA (R^2= 0.9, m = 0.86, y-int = 0.48) and PM$_1$ from the AMS (R^2= 0.82, m = 0.95, y-int = 0.28) during BAQS II at THRO-N.

79

Total PM Comparison
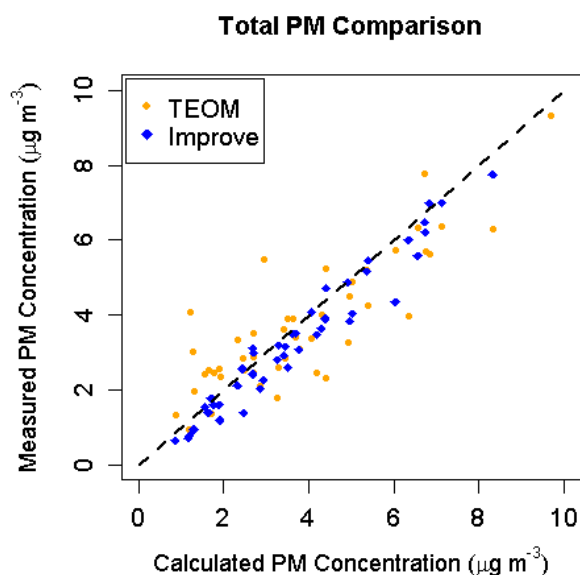
Figure 4.16: The comparison of the reconstructed total PM$_{2.5}$ concentration, as described in section 4.2.1, with the concentration of PM$_{2.5}$ from the TEOM (R^2= 0.74, m = 0.75, y-int = 0.85) and PM$_{2.5}$ from the IMPROVE Teflon filters (R^2= 0.92, m = 1.0, y-int = -0.41) during BAQS II at THRO-N.

The fraction of each aerosol component and reconstructed PM$_{2.5}$ concentration represented as the sum of all measured components are shown in Figure 4.17. On average, inorganics contribute 64.9%, organics contribute 29.7%, and BC contributes 5.4% to the total PM$_{2.5}$ mass. During periods of elevated aerosol concentration, the inorganic species dominate the aerosol fraction and in particular the contribution from NO$_3^-$ increases. Between the lowest and highest PM$_{2.5}$ mass quartiles, the fraction of NO$_3^-$ increases from 15% to 32% while the fraction of SO$_4^{2-}$ only increases from 18 to 22% (Figure 4.18) indicating a greater importance of AN formation at higher total PM$_{2.5}$ concentrations. Differences between NO$_3^-$ and SO$_4^{2-}$ source regions will be discussed below. Figure 4.17 also shows that b$_{sp}$ measured by the nephelometer tracks closely with total PM$_{2.5}$ mass.
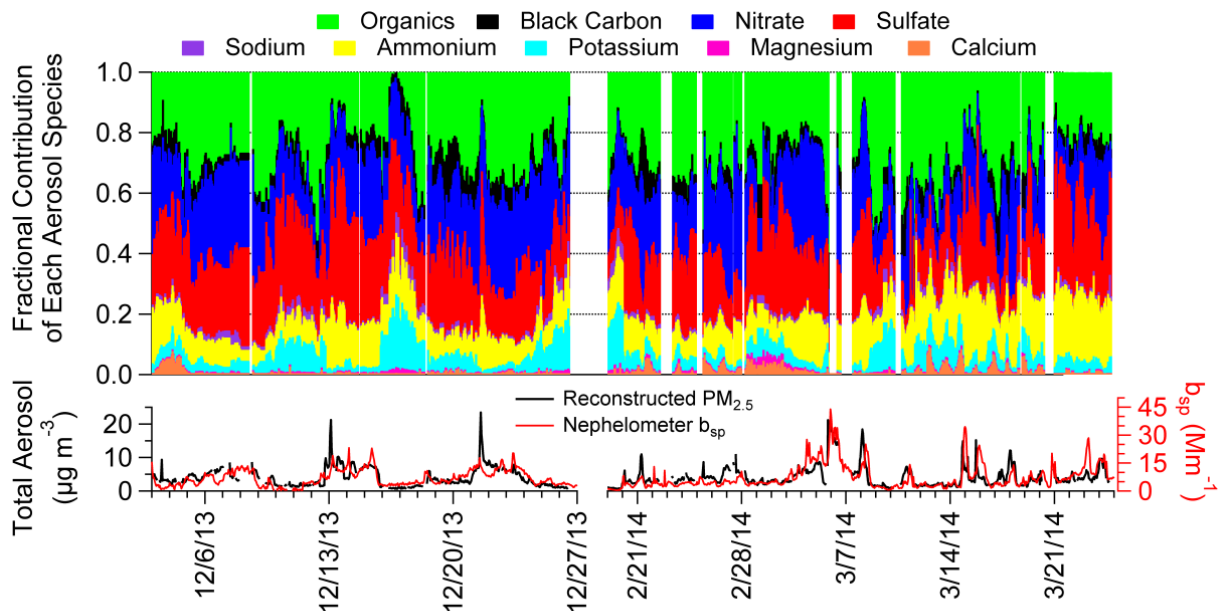
Figure 4.17: The top panel is a timeline of the fraction of each inorganic species, total organics and black carbon that contribute to total hourly reconstructed PM$_{2.5}$ mass. The bottom timeline shows the reconstructed PM$_{2.5}$ mass (μg m^{-3}) and the total light extinction due to particle scattering (b$_{sp}$) from nephelometer measurements (Mm^{-1}).
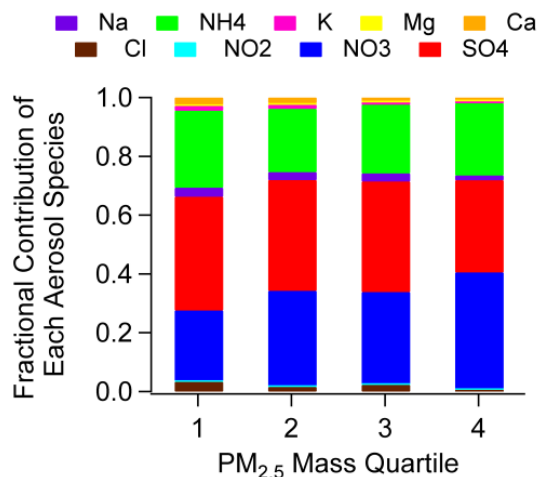
Figure 4.18: Fractional contribution of each chemical species to the total inorganic PM$_{2.5}$ mass separated by mass quartile. Bar 1 represents the 25% lowest PM$_{2.5}$ mass concentrations and bar 4 represents the highest 25%.

4.3.2.2 Role of Aerosol Precursor Gases in Inorganic Particle Formation

Concentration timelines of total N(-III) species and total N(V) species are plotted in

Figure 4.19. The color of the line indicates the gas fraction of NH_3 or HNO_3 relative to the total

N(-III) or N(V), ranging from 0 (all N(-III) or N(V) in particulate form) to 1 (all N(-III) or N(V)

in the gas phase). During the majority of periods with high concentrations of N(V) and N(-III),

the gas fractions were low, indicating both N(-III) and N(V) were predominantly in the particle

phase. The NH_3 gas fraction is higher during the beginning and end of the study, when

temperatures were also generally higher. December and March, for example, featured average

NH_3 gas fractions and temperatures of 0.2 and -8 °C and 0.5 and -1 °C, respectively. The

average HNO_3 gas ratio was 0.3 for both December and March. This reveals that periods with

extremely cold temperatures are often limited by NH_3 while throughout the entire winter study

period there is limited HNO_3 available. Increases in excess N(-III) (Equation 1.1) in March may

reflect NH_3 emission from the application of fertilizer or other regional agricultural practices in

combination with warmer temperatures which increases NH_3 volatilization (Balasubramanian et

al., 2015; Gilliland et al., 2006).
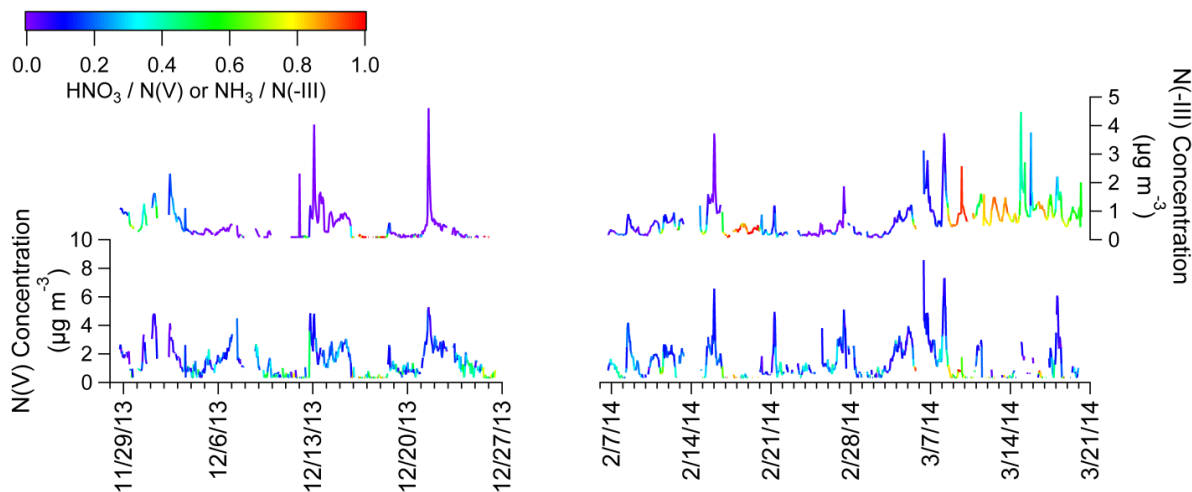
Figure 4.19: N(-III) and N(V) concentrations (μg m^{-3}) observed in the second study at THRO-N using hourly MARGA measurements. The timeline color indicates the N(-III) gas ratio (NH$_3$ / N(-III)) and N(V) gas ratio (HNO$_3$ / N(V)).

The sensitivity of AN and PM$_{2.5}$ formation to sulfate, N(-III), and N(V) concentrations investigated using ANISORROPIA is summarized in Table 4.6. Understanding how further growth in regional NO$_x$ emissions, which are likely to yield increases in HNO$_3$ concentrations, might impact AN formation is of particular interest in contemplating possible effects from future growth in Bakken oilfield development on regional haze. The average sensitivities of inorganic NO$_3^-$ formation, for example, to changes in total N(-III) and N(V) concentrations are listed in Table 4.6 as 0.36 and 0.13, respectively. These values indicate that, on average, a one mole increase in total N(-III) would yield a 0.36 mole increase in PM$_{2.5}$ NO$_3^-$, while a one mole increase in total N(V) would yield a smaller, 0.13, mole increase in PM$_{2.5}$ NO$_3^-$. This suggests that the formation of particulate matter is more sensitive to increases in NH$_3$ than to increases in NO$_x$ during the winter months, when the input data were collected. The average sensitivities of PM$_{2.5}$ NH$_4^+$ to changes in N(-III) and N(V) are 0.76 and 0.11 mole/mole. Concentrations of SO$_4^{2-}$, by contrast, are seen to be relatively insensitive to changes in N(-III) or N(V), due to the low volatility of SO$_4^{2-}$ which keeps it predominantly in the aerosol phase. The sensitivities of

inorganic $PM_{2.5}$ concentrations to changes in N(-III) and N(V) (µg/µg) are explored in more

detail in Figure 4.20. Here we see that the sensitivity of total $PM_{2.5}$ concentrations to N(-III) is

typically greater during colder periods when excess N(-III) is low, indicating the strong

limitation of fine particle formation imposed by NH_3 during these times. At warmer

temperatures during late winter, excess N(-III) increases and the sensitivity of $PM_{2.5}$ formation to

N(-III) is generally low. Not surprisingly, a contrasting trend is seen for $PM_{2.5}$ sensitivity to

N(V). Figure 4.20b shows that $PM_{2.5}$ is not very sensitive to N(V) concentrations at extremely

low temperatures and low excess N(-III) concentrations, but that the sensitivity sharply increases

above -10°C when excess N(-III) concentrations tend to be higher. These findings suggest that

effects of additional future NO_x emissions from additional oil development activities in the

region are likely to exert the strongest effects on haze formation during later parts of winter when

temperatures and NH_3 concentrations increase.

Table 4.6: Study averaged model sensitivities (bold) and standard deviation (in parentheses) for the formation of particulate species H^+, NO_3^-, NH_4^+, SO_4^{2-}, HSO_4^- and total $PM_{2.5}$. Sensitivities to individual species are given as a molar ratio of the model predicted aerosol species over the input of total N(-III), N(V) or SO_4^{2-}. The sensitivity of predicted total $PM_{2.5}$ was calculated by summing the sensitivities of each predicted aerosol species to the three different input species and is given in mass units (µg / µg).

δ predicted / δ input	δH^+	δNO_3^-	δNH_4^+	δSO_4^2	δHSO_4^-	$\delta PM_{2.5}$
			(mole / mole)			(µg / µg)
δN(-III)	**-0.37**	**0.36**	**0.76**	**0.02**	**-0.02**	**1.99**
	(0.44)	(0.42)	(0.40)	(0.05)	(0.05)	(1.64)
δN(V)	**0.02**	**0.13**	**0.11**	**-0.002**	**0.001**	**0.17**
	(0.04)	(0.25)	(0.25)	(0.01)	(0.006)	(0.32)
δSO_4^{2-}	**0.81**	**-0.60**	**0.51**	**0.96**	**0.04**	**0.72**
	(0.85)	(0.78)	(0.84)	(0.11)	(0.11)	(0.59)

Figure 4.20: The sensitivities of PM$_{2.5}$ to N(-III) and N(V) concentrations (µg/µg) calculated by ANISORROPIA. Panel (a) shows the sensitivity of PM$_{2.5}$ to N(-III) and panel (b) shows the sensitivity of PM$_{2.5}$ to N(V) compared with temperature in °C on the x-axis; the points are colored by the concentrations of excess N(-III) in nmol m^{-3}.

4.4 BAQS Inorganic Aerosol Summary and Conclusions

Intensive ground-based aerosol measurements over two consecutive winters in the Bakken oil and gas region showed periods of regionally elevated concentrations of PM$_{2.5}$, with a maximum 48-hour average PM$_{2.5}$ inorganic aerosol concentration of 21.3 µg m^{-3} observed at Fort Union in the heart of the Bakken oil patch. The lowest concentrations were typically found at Medicine Lake, outside and often upwind of the oil patch. Concentrations across the region were found to be highest during periods of air mass stagnation and recirculation; the lowest concentrations were typically associated with fast transport of air from the west or northwest. Both average and peak PM$_{2.5}$ concentrations were higher in early 2013 than in early 2014. Differences in snow cover, atmospheric stability, solar illumination, and transport directions might be associated with the differing fine particle concentrations and aerosol scattering measurements. Use of a chemical clock revealed that periods with the highest PM$_{2.5}$ concentrations tended to be associated with VOC emissions aged less than a day and a VOC

signature more indicative of oil and gas contributions than from urban centers. This reinforces the importance of local Bakken region sources in formation of regional haze episodes.

Inorganic species made up the majority of the total $PM_{2.5}$ mass, with both ammonium sulfate and ammonium nitrate having significant contributions. We observed increases in NO_x emitted from oil and gas operations (Prenni et al., 2016), which formed HNO_3 and combined with available NH_3 to form ammonium nitrate aerosol and contributed to haze episodes. It was shown using meteorological conditions, gas and aerosol measurements, and thermodynamic modeling, that conditions in the Bakken were favorable for ammonium nitrate formation for the majority of the sampling period. $PM_{2.5}$ concentrations were typically more sensitive to the availability of N(-III) during the coldest part of the winter; sensitivity to available N(V) grew as temperatures increased along with N(-III) availability in the later part of winter.

5.0 ORGANIC AEROSOL DURING BAKKEN AIR QUALITY STUDY II

Non-refractory PM_1 measurements were obtained in December 2013 and February – March 2014 using an Aerodyne high resolution time-of-flight aerosol mass spectrometer (AMS) at THRO-N during BAQS II. IMPROVE quartz filters were analyzed for daily organic carbon concentration. See Chapter 2 for detailed methods on the operation of the AMS and IMPROVE filter collection and Chapter 4 and 5 for field study details. Basic AMS organics and IMPROVE OC results from BAQS II were presented in Chapter 4 to complete the discussion on total aerosol, but this chapter provides a much more detailed look at the organic component of the aerosol. In addition to total organic aerosol (OA), the analysis of the AMS measurements also provides detail on important elemental ratios including oxygen to carbon (O/C), organic matter to organic carbon (OM/OC), nitrogen to carbon (N/C) and hydrogen to carbon (H/C). These ratios can be used to investigate properties of the aerosol such as aging and oxidation. Positive Matrix Factorization (PMF) analysis was conducted with the AMS organic aerosol measurements to gain further insight on the sources and characteristics of the organic aerosol measured during BAQS II. Finally, the OM/OC ratio and organic aerosol measurements were included into a calculation of aerosol scattering, to investigate the contribution of organic aerosol to total aerosol scattering and the presence of haze.

New emissions associated with oil and gas development in the Bakken region could impact local organic aerosol (OA) concentrations and composition. Understanding the characteristics of the OA at the North Unit of Theodore Roosevelt National Park (THRO-N) is important for investigating sources, aerosol aging and contributions to aerosol scattering (b_{sp}) in the Bakken region. Analysis techniques such as positive matrix factorization (PMF) are used to

investigate air pollution source apportionment (Paatero and Tapper, 1994; Ulbrich et al., 2009; Zhang et al., 2011b) which is commonly used for determining the source factors of OA as measured by an aerosol mass spectrometer (e.g. Lanz et al., 2007). Multiple measurements obtained during BAQS II used to validate the OA factors include concentrations of other pollutants, AMS derived organic mass to organic carbon (OM/OC) ratios (Aiken et al., 2008), and other estimates of oxidation and airmass lifetimes. The importance of OA in aerosol scattering (b_{sp}) is determined by calculating the reconstructed b_{sp} and comparing with measured b_{sp}. The variables used in calculating reconstructed b_{sp} are examined to gain insight into how OA impacts visibility in the Bakken region.

5.1 Organic Aerosol Trends in the Bakken Region

5.1.1 Regional Organic Aerosol Trends

Long term OA measurements at THRO-N are not available, but organic carbon (OC) measurements are available at three surrounding IMPROVE sites: Medicine Lake National Wildlife Refuge, MT (MELA), Lostwood National Wildlife Refuge, ND (LOST) and the South Unit of Theodore Roosevelt National Park, ND (THRO-S; Figure 5.1a). OC is converted to OA by multiplying by a factor of 1.8, which is a recommended OM/OC ratio for a remote location (Pitchford et al., 2007). Significant decreasing OA trends from 1999 - 2014 were observed at all sites (all Kendall tau p-values < 0.01). To compare with BAQS II OA measurements, the average winter (December, January and February) concentrations for each IMPROVE site are shown in Figure 5.1b. Over the BAQS II study period, the organic aerosol (OA) concentrations calculated from every third day 24-hour filter samples were found to be higher at THRO-N, the field site most centrally located within the region of oil and gas development, when compared with concurrent measurements made at surrounding national monitoring sites (purple circle in

Figure 5.1b). The sharp increase in oil production in North Dakota (Figure 5.1b; U.S. Energy

Information Administration, 2014) contrasts the decreasing trend in OA from the IMPROVE

measurement sites surrounding the dense area of oil wells in the Bakken. The elevated

concentrations measured at THRO-N during BAQS II will be investigated further.
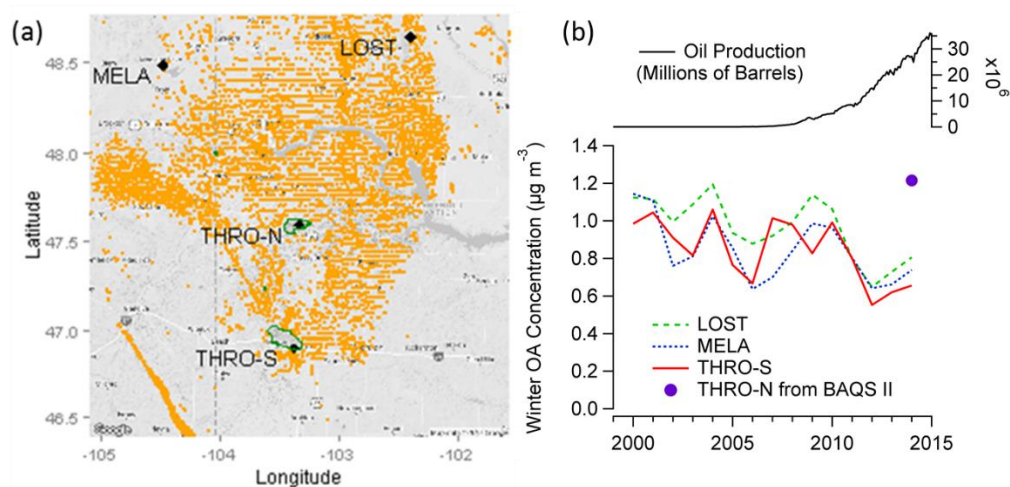
Figure 5.1: The map (a) shows the measurement sites and their proximity to active oil and gas wells (orange dots) and national park lands (green outline). Long-term trends of average winter organic aerosol concentrations ($\mu g\ m^{-3}$) from December, January and February as calculated from 24-hour IMPROVE filters that sampled every three days collected at THRO-N (purple circle), MELA (blue dotted line), LOST (green dashed line) and THRO-S (red solid line) are shown in the timeline compared with oil produced in North Dakota (black line) represented in millions of barrels of oil (b).

5.2.2 Organic Aerosol Summary from BAQS II

At THRO-N, measurements of hourly averaged AMS OA in PM_1 and daily organic

carbon (OC) in $PM_{2.5}$ from IMPROVE filters were obtained during BAQS II (Table 5.1).

Collection methods for organic aerosol measurements using the AMS and IMPROVE OC/EC

filters are described in detail previously in Sections 2.6 and 2.4. The organic mass concentration

(OMC) is estimated by multiplying the measured OC by a factor of 1.8. Despite the difference

in PM size measured, good agreement between AMS OA and IMPROVE OMC is observed

throughout the study (Figure 5.2).
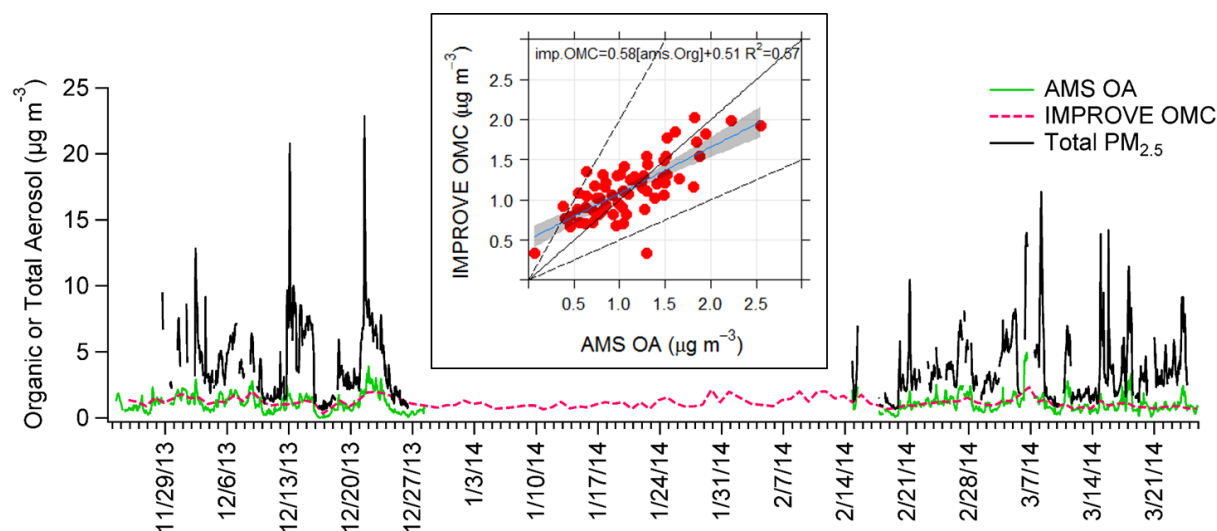
Figure 5.2: Timelines of total reconstructed PM$_{2.5}$ (black solid line; see Chapter 5 for description), AMS OA (green solid line) and IMPROVE OMC (pink dashed line) are shown. The inset shows the linear regression (blue solid line with gray shading for the 95% confidence interval) between IMPROVE OMC and daily averaged AMS OA concentrations (µg m^{-3}, red circles) with the 1:1 line (solid black line) and 1:2 and 1:0.5 lines (dashed black line).

The total reconstructed PM$_{2.5}$ timeline is plotted in Figure 5.2 with the two different organic aerosol measurements. This shows consistently low organic aerosol throughout the time period with small elevations in concentrations corresponding with increases in total PM$_{2.5}$. The highest fractions of OA are observed when PM$_{2.5}$ concentrations are low. This is consistent with the observations described in the previous chapter that indicated the highest episodes of PM$_{2.5}$ were dominated by inorganic species. The study average AMS OA in PM$_1$ and standard deviation was 1.1 ± 0.66 µg m^{-3} for the operational period between 11/23/13 - 12/28/13 and 2/14/14 - 3/26/14. During the same time period, IMPROVE OMC averaged 1.15 ± 0.39 µg m^{-3}. This average is representative of the entire study period (11/22/13 – 3/26/14) in which the average OMC was 1.16 ± 0.39 µg m^{-3}.

90

5.2 Organic Aerosol Characteristics

5.2.1 Organic Aerosol Sources

The average O/C and H/C ratios were 0.45 ± 0.18 and 1.30 ± 0.28, respectively. The average OM/OC was 1.72 ± 0.23 with minimum and maximum values of 0.57 and 2.4. The average N/C ratio was 0.012 ± 0.04. A PMF two factor solution identifying a hydrocarbon like organic aerosol (HOA) factor and a low volatility oxidized organic (LVOOA) factor was determined. The factor profiles are shown in Figure 5.3. The classification of each factor was verified by comparing with previously established common organic aerosol factors (Zhang et al., 2011a). The HOA factor was identified by having strong signals from fragments at *m/z* 43 ($C_2H_3O^+$) and 57 (mostly $C_4H_9^+$; Canagaratna et al., 2007; Lanz et al., 2007), a marker for diesel combustion. In addition, the HOA factor had higher signals for *m/z* 41, 55, 69, 71, 83, 85, which are tracers for hydrocarbons (series of $C_nH_{2n+1}^+$ and $C_nH_{2n-1}^+$; Ng et al., 2010; Zhang et al., 2005a) and *m/z* 91 and 95 which are tracers for combustion (Zhang et al., 2005c). The oxidized organic aerosol factor is dominated by fragments at *m/z* 44 (CO_2^+) and 43 (Canagaratna et al., 2007; Zhang et al., 2005b). A higher amount of *m/z* 44 relative to *m/z* 43 was observed (Figure 5.3), suggesting higher levels of oxidation and low volatility (Aiken et al., 2008; Zhang et al., 2011a). This two factor solution, among various PMF solutions explored, also had the most complete separation of *m/z* 55 and 57 in the HOA factor and *m/z* 44 in the LVOOA factor.
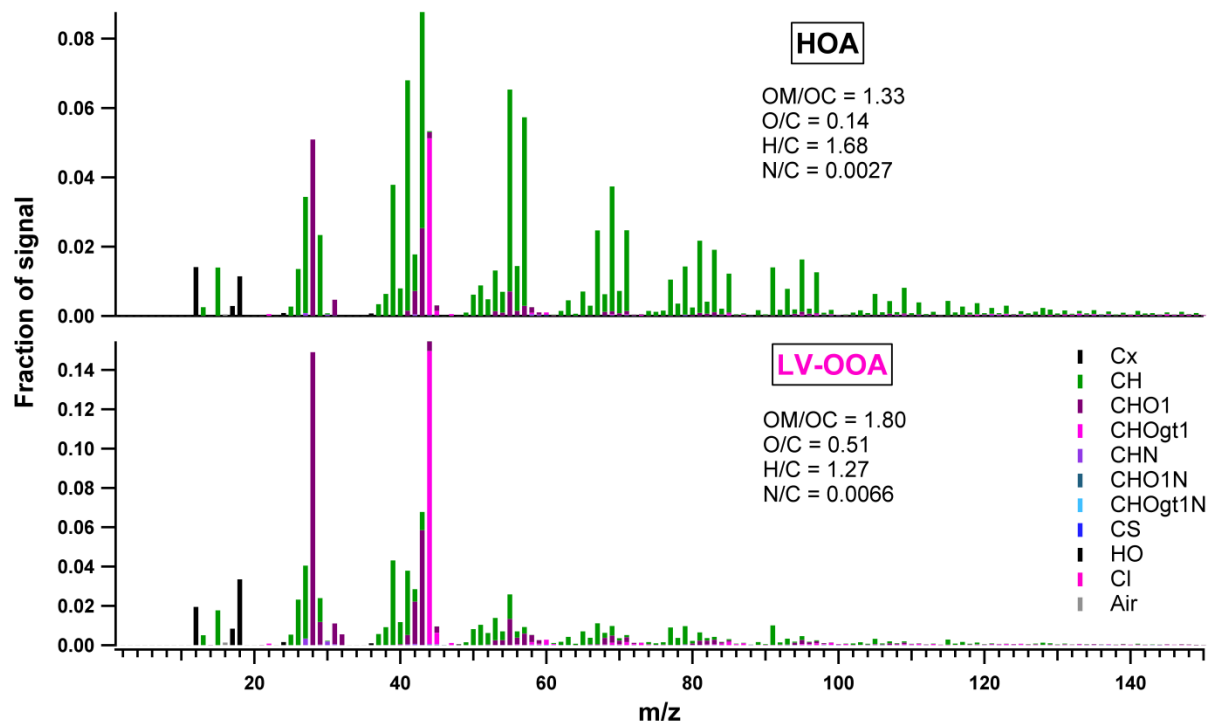
Figure 5.3: The AMS organic aerosol factor profiles of HOA and LVOOA showing the fraction of *m/z* signal with each bar colored by the AMS fragment. Elemental ratios for each factor are also shown.

A three factor solution was explored (see Appendix D for details), but the two factor solution produced the most unique factor separation of factor profiles and timeline dissimilarities (Figure 5.4). HOA averaged 0.20 µg m^{-3} and made up 20.5 % of the total OA and LVOOA averaged 0.78 µg m^{-3} and made up 79.5% of the total OA. For HOA, the average O/C and H/C ratios were 0.14 and 1.68 and for LVOOA were 0.51 and 1.27 (Figure 5.3).
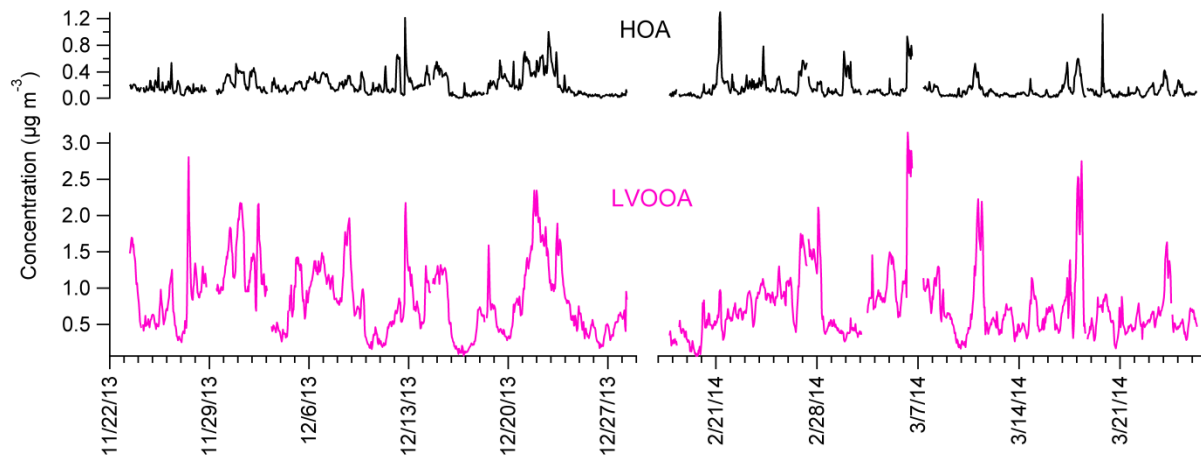
Figures 5.4: Timelines of HOA (black) and LVOOA (pink) concentrations derived from the AMS PMF two factor solution.

The PMF solution identifying HOA and LVOOA as the only two factors during BAQS II is consistent with previous studies that have found only one oxidized organic aerosol factor in field studies conducted in the winter, while the semi-volatile oxidized organic aerosol factor is more commonly found in summer time measurements (Jimenez et al., 2009). HOA originates from primary sources so would be expected to come from anthropogenic activities such as mobile or stationary diesel or gasoline engine combustion (Lanz et al., 2007; Rutter et al., 2015) or flaring (Stohl et al., 2013) in the Bakken region. BAQS HOA correlates positively with BC concentrations and with NO_x, which could also be generated by diesel combustion and flaring sources, as shown in Figure 5.5a. Positive correlations between HOA and NO_x or BC have been observed in other studies performed in urban locations impacted by traffic emissions (e.g. Brown et al., 2012; Lanz et al., 2010; Xu et al., 2016).
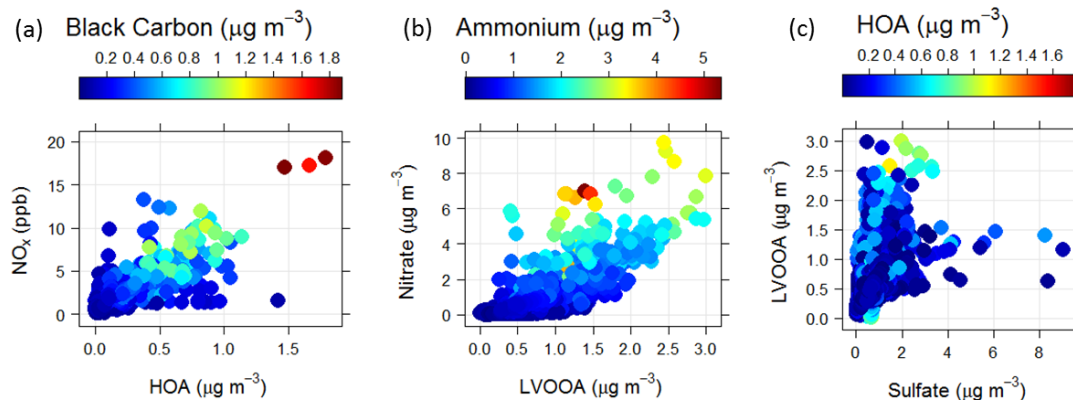
Figure 5.5: Scatter plots showing the comparison between (a) HOA with NO_x (ppb) and black carbon ($\mu g\ m^{-3}$) and (b) LVOOA with nitrate and ammonium ($\mu g\ m^{-3}$), (c) sulfate ($\mu g\ m^{-3}$) with HOA or LVOOA factors ($\mu g\ m^{-3}$).

BAQS HOA also correlated with VOC tracers for oil and gas, including light hydrocarbons ethane, propane, i-butane, and i-pentane. This correlation contrasts observations from a previous study, in the Barnett Shale in Texas, where the HOA factor did not correlate with VOC tracers of oil and gas operations (Armendariz, 2009). Armendariz et al. suggested that the stationary diesel engines at oil and gas extraction sites were not a significant contribution to the HOA in that region. Figure 5.6a shows the Pearson correlation coefficients for hourly averaged concentrations of each PMF factor corresponding with the concentrations of various VOCs collected as grab canister samples. Strong correlations between HOA and the light hydrocarbons, benzene, toluene, ethylbenzene, and xylenes (BTEX) further reinforce that HOA is directly correlated with activities associated with oil and gas operations. For comparison, the VOC correlation with LVOOA are also listed in Figure 5.6a. Very low correlations are observed between LVOOA with the light hydrocarbons and with BTEX.
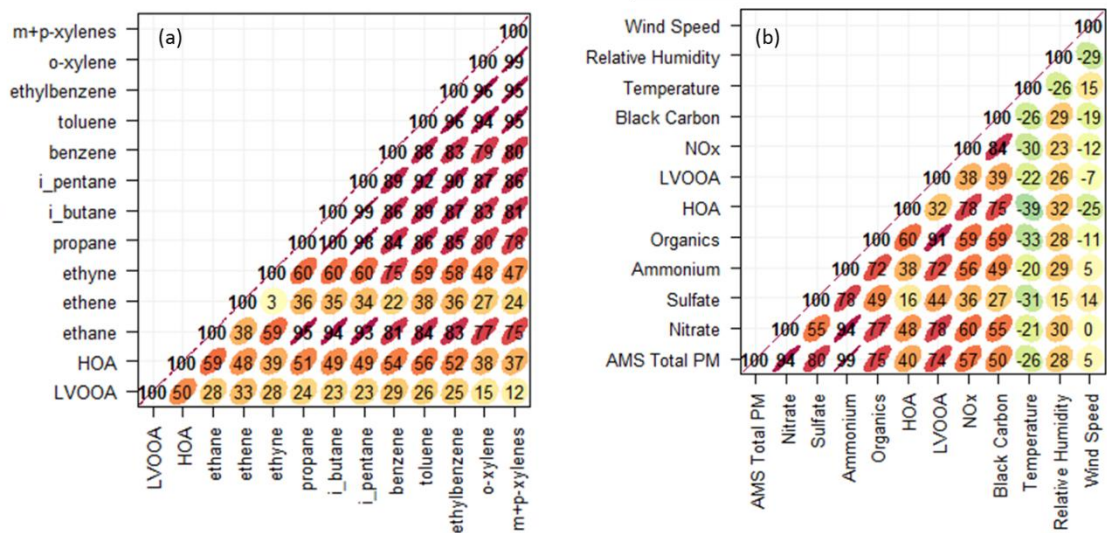
Figure 5.6: Pearson correlation coefficients for AMS PMF factors with (a) VOCs (ppt) and (b) with AMS aerosol species, total PM ($\mu g\ m^{-3}$), black carbon ($\mu g\ m^{-3}$), nitrogen oxides (ppb) temperature (^{o}C), relative humidity (%) and wind speed (m s^{-1}).

LVOOA results from atmospheric aging processes which can be associated with the production of inorganic PM$_{2.5}$ (Zhang et al., 2005b). High correlation is observed between LVOOA and NO$_3^-$ and NH$_4^+$ (Figures 5.5b and 5.6b). By contrast, SO$_4^{2-}$ concentrations do not correlate well with LVOOA or HOA, suggesting that SO$_4^{2-}$ has different sources than ammonium nitrate aerosol or OA (Figure 5.5c and 5.6b). Weak but negative correlations between OA and wind speed or temperature support the trends observed in the previous section that showed the inorganic aerosol in this region correlated with higher total aerosol concentrations, lower temperatures, and more stagnant air masses with allow emissions from the oil and natural gas drilling region to build up higher concentrations of aerosol (Chapter 4). The diurnal plots in Figure 5.7 show that as wind speeds increase during mid-day, HOA concentrations decrease. To relate this to the inorganic concentrations, the diurnal trends of NH$_4^+$, NO$_3^-$, and SO$_4^{2-}$ are also shown. The concentrations of NO$_3^-$ also decrease as wind speeds increase. This suggests that the average daily pattern of a build-up of inorganic NO$_3^-$ and HOA concentrations are enhanced

by low wind speeds. LVOOA, NH_4^+, SO_4^{2-} and total organics do not have a clear diurnal trend which suggests that the concentrations are likely not as impacted by wind speed and local sources are not a significant contributor to total concentration.
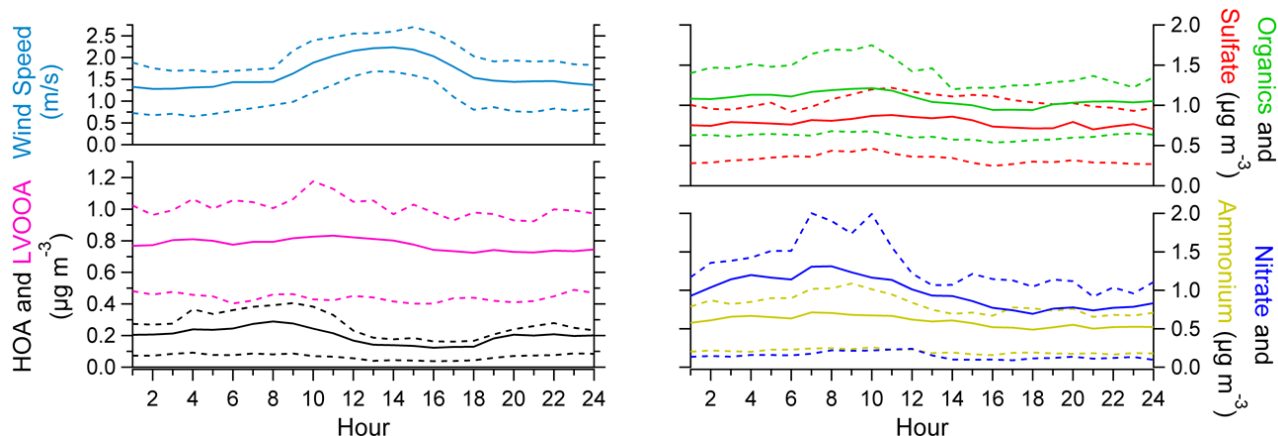
Figure 5.7: The diurnal trends of average HOA (black), LVOOA (pink), nitrate (blue), sulfate (red), ammonium (yellow), total organics (green) and wind speed (light blue) are plotted in the solid lines with dotted lines representing the 25% and 75% percentiles.

5.2.2 Organic Aerosol Aging

Aerosol oxidation and aging characteristics can be further investigated using elemental ratios H:C and O:C as displayed in a van Krevelen diagram (Heald et al., 2010). This plot shows the oxidation states of the bulk atmospheric organic aerosol particles, where aerosol measurements towards the upper left of the diagram are less aged aerosol and become more oxidized as they move down and to the right within the triangle. The BAQS AMS elemental ratios are plotted in Figure 5.8 and colored by the ratio of HOA to LVOOA. The higher ratio of HOA, indicated by the cooler colors, appear in the less oxidized section of the triangle which reinforces the results of the two factor PMF solution.

96
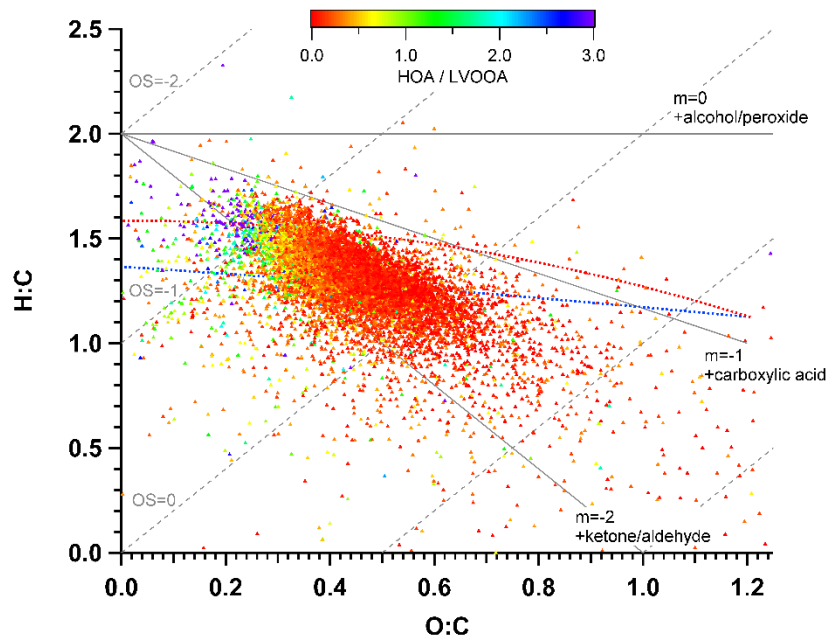
Figure 5.8: A Van Krevelen diagram showing H:C versus O:C using AMS measurements. The points are colored by the ratio of HOA/LVOOA.

Figure 5.9 shows the f43-f44 triangle diagram (Ng et al., 2011), another common tool for understanding aerosol oxidation levels. The values of f43 and f44 represent the fraction of AMS OA comprised by *m/z* 43 and *m/z* 44, respectively. Most points fall within the triangle, which represents the area where typical observed atmospheric ratios of f44/f43 are found. In the plot, aerosol at lower oxidation level appear at the bottom of the triangle and points move up and to the left as the aerosol becomes more oxidized. The circles highlight where the HOA (black), SVOOA (semi-volatile oxidized organic aerosol; orange) and LVOOA (pink) PMF factors usually fall within this plot (Schurman et al., 2015). Most of the aerosol falls within the typical LVOOA and SVOOA regions, with the highest concentrations of organic aerosol falling within the SVOOA region. The absence of points within the HOA region is not surprising since HOA only comprised 20% of the total organic aerosol and was generally mixed with LVOOA. The

scatter outside of the triangle in Figure 5.9 is correlated with the lowest measured concentrations of OA and could reflect higher uncertainty in those measurements.
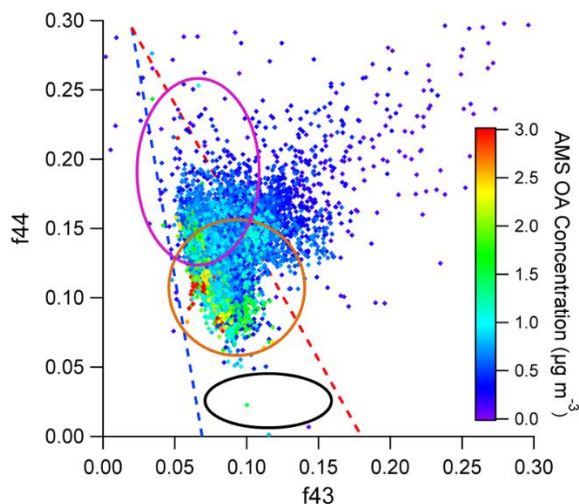
Figure 5.9: f44 versus f43 diagram colored by OA concentration (µg m^{-3}). The circles represent where the typical PMF factors fall; HOA (black), SV-OOA (orange), and LV-OOA (pink).

The OM/OC ratio can be used as an indicator of aging or more oxidized aerosol (Aiken et al., 2008). A lower OM/OC indicates the presence of more aliphatic carbon groups and urban OA signatures. A higher OM/OC indicates the presence of more oxygenated and functionalized groups and OA from rural sources. Many studies have measured OM/OC ratios and assigned different ranges of values for urban versus rural sources of OA. When comparing with previous studies in both urban and rural areas (Table 5.1), the average OM/OC of 1.72 measured during BAQS II suggests influence from fresh sources.

In addition to OM/OC, other aging metrics that can be estimated from atmospheric measurements can be used. This study provides the opportunity to compare the OM/OC ratios to the OC/EC ratio, NO_x/NO_y, and the estimated age of emissions in an airmass from an alkyl nitrate chemical clock. Lower OC/EC ratios typically indicate more primary sources and higher ratios more secondary organic aerosol (SOA) formation (Kanakidou et al., 2005). A lower

NO_x/NO_y indicates the aerosol is more aged and a higher ratio suggests the mass is dominated by fresh emissions (Dingle et al., 2016). The alkyl nitrate chemical clock, described in detail in Section 5.3.1.2, uses known reaction rates of measured VOCs to estimate airmass age (Russo et al., 2010a). A summary of these ratios measured during other field studies in a variety of urban and rural locations is presented in Table 5.1 for comparison.

Table 5.1: Average and standard deviations (when available) for OM/OC, OC/EC and NO_x/NO_y ratios from field studies at rural and urban field sites.

Ratio	BAQS Average ± Standard Deviation	Measurements from Other Studies
OM/OC	**1.72 ± 0.23**	Rural Sites 2.1 ± 0.2: Average from multiple rural sites (Turpin and Lim, 2001) 1.5-1.9: Rural New York site (Bae et al., 2006) Urban Sites 1.5-1.7: Multiple urban sites (Zhang et al., 2005c) 1.54 ± 0.20: Las Vegas (Brown et al., 2013a) 1.3-1.6: Urban New York site (Bae et al., 2006) 1.71: Mexico City (Aiken et al., 2008)

OC/EC	**4.56 ± 2.50**	Rural Sites
		1.63-2.23: Duke Forest, NC (Khan et al., 2012)
		Agricultural site in Netherlands:
		   4.0 ± 2.0: Winter
		   8.8 ± 3.7: Spring
		   3.2 ± 1.0: Summer
		   2.9 ± 1.1: Fall
		   (Dusek et al., 2017)
		Urban Sites
		1.4-2.4: Los Angeles (Turpin et al., 1991)
		1.0-3.0: Average in Asian Cities (Fang et al., 2008)
		0.80-1.12: Nairobi, Kenya (Khan et al., 2012)

NO_x/NO_y	**0.87 ± 0.64**	Rural Sites < 0.5: Colorado Front Range (Dingle et al., 2016) 0.25: Jungfraujoch (Zellweger et al., 2000) Urban Sites > 0.8 Boston, New York City (Warneke et al., 2007) > 0.5: Denver, Colorado Front Range (Dingle et al., 2016)

Hourly averaged measurements of each ratio are plotted in Figure 5.10. Higher levels of oxidation are represented by higher ratios of OM/OC and OC/EC and by lower ratios of NO_x/NO_y. Scatter plots show the comparisons between NO_x/NO_y and the two organic aerosol based ratios do not have good agreement. A much better correlation is observed between OM/OC and OC/EC. Even though all ratios indicate levels of oxidation, the poor agreement is not surprising because of the expected differences in sources of organic aerosol and NO_x.
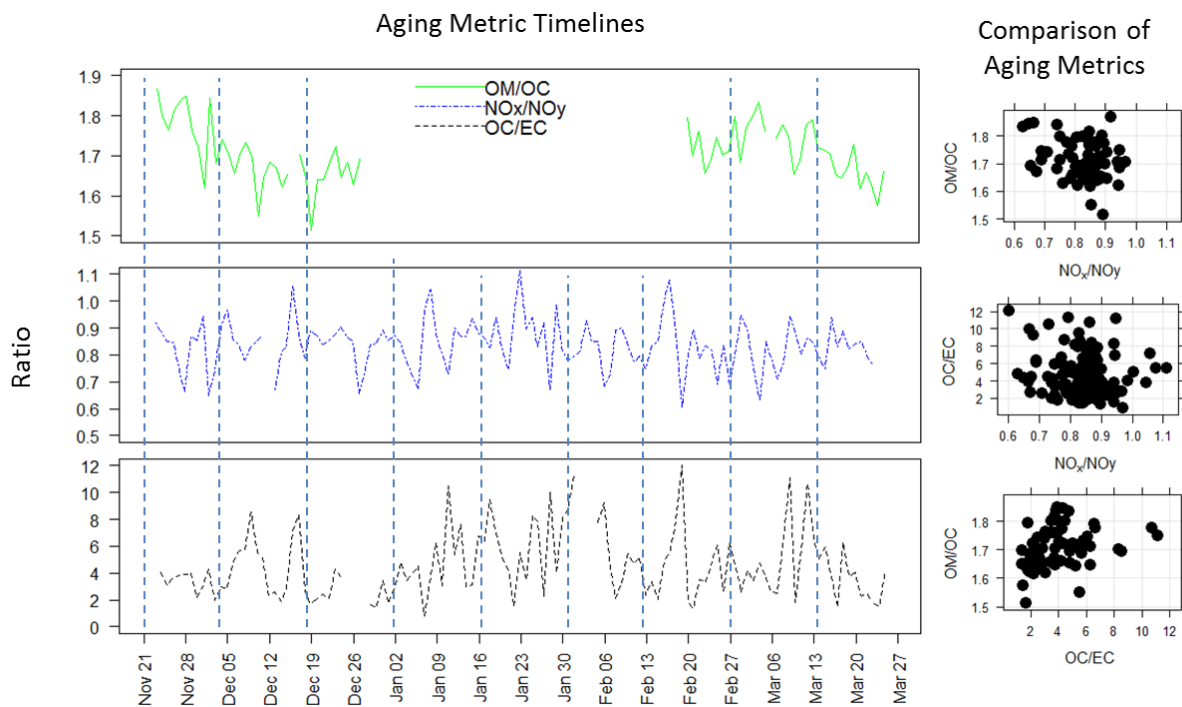
Figure 5.10: Timelines of daily averaged OM/OC (green), NO_x/NO_y (blue), and OC/EC (black) on the left and scatter plots comparing each ratio on the right.

In Chapter 4, the alkyl nitrate chemical clock utilized VOC measurements to estimate an air mass age and found that fresher emissions of VOCs corresponded with higher concentrations of $PM_{2.5}$. Compared here are an estimate of air mass age using the alkyl nitrate chemical clock with OC/EC and OM/OC (Figure 5.11). The markers are both sized and colored according to the elemental ratio. The highest OC/EC and OM/OC ratios, indicating more aged emissions, are

associated with longer air mass ages, while the lowest ratios are associated with the shortest air mass ages. This comparison validates the use of these three methods for understanding oxidation and aerosol aging.
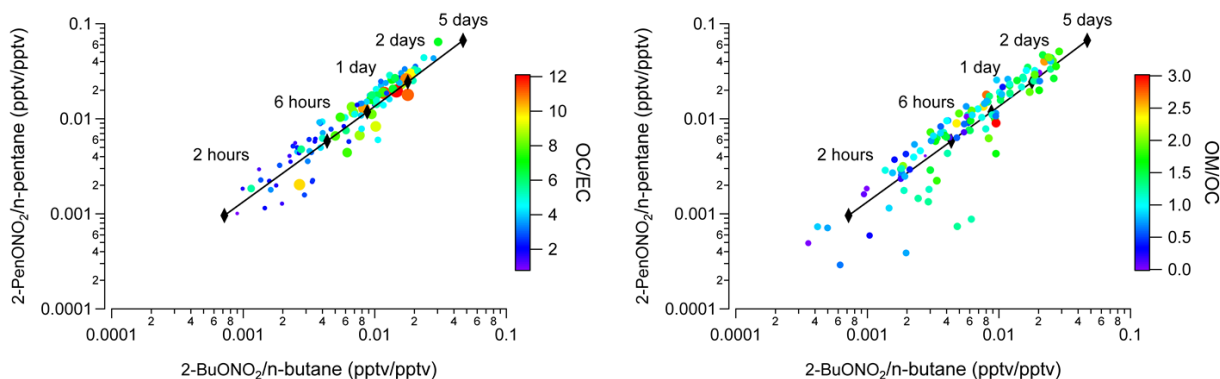
Figure 5.11: Alkyl nitrate chemical clock showing airmass age compared to estimates of organic aerosol aging from IMPROVE filter OC/EC (left) and AMS estimated OM/OC (right).

The diurnal trend of average OM/OC (Figure 5.12) shows that it peaks in the afternoon and follows a similar trend in the diurnal trends in wind speed (Figure 5.8). On average, higher OM/OC corresponds with the time of day when wind speeds are elevated, suggesting that there is more influence from background regional OA that would be more oxidized. However, the diurnal trend for OM/OC is weak, which is similar to trends observed in other studies (Zhang et al., 2005b), which suggested that the dominance of background aged aerosol reduced the variation in OM/OC throughout the day.
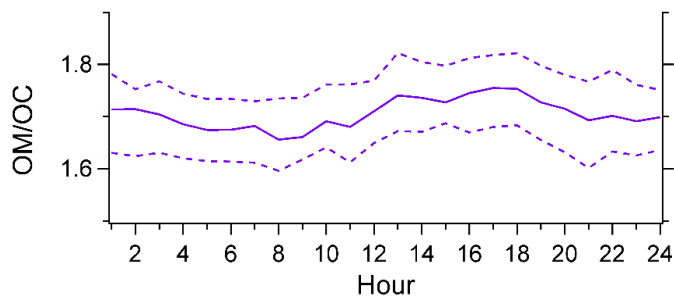
Figure 5.12: The diurnal trend in average OM/OC (solid line) with the 25th and 75th percentile ratios (dashed lines).

5.3 Role of Organic Aerosol in Light Scattering

5.3.1 Reconstructed Aerosol Scattering (b_{sp})

Reconstructed fine aerosol mass (RCFM) was calculated according to the IMPROVE method (Malm et al., 2000). Daily RCFM is calculated from the sum of ammonium sulfate (AS), ammonium nitrate (AN), OMC, crustal materials (SOIL) and chloride to represent sea salt (SALT) in $PM_{2.5}$. The equations to calculate the mass of each aerosol component are shown in Equations 5.1-5.5. Measurements of daily URG SO_4^{2-} and NO_3^- from nylon filters were used to calculate concentrations of AS and AN. URG Cl^- was multiplied by 1.8 to get the concentration of the SALT component. The calculated concentration of aerosol from SOIL uses the concentrations of aluminum (Al), silicon (Si), calcium (Ca), iron (Fe) and titanium (Ti) from the IMPROVE Module A Teflon filter samples. Daily measurements of OC from IMPROVE and an OM/OC of 1.8 were used to calculate OMC (Equation 5.3).

$$AS = (NH_4)_2SO_4 = 4.125[S] = 1.375[SO_4^{2-}] \qquad \text{Equation 5.1}$$

$$AN = NH_4NO_3 = 1.29[NO_3^-] \qquad \text{Equation 5.2}$$

$$OMC = \frac{OM}{OC} * [OC] \qquad \text{Equation 5.3}$$

$$SOIL = 2.2[Al] + 2.49[Si] + 1.63[Ca] + 2.42[Fe] + 1.94[Ti] \quad \text{Equation 5.4}$$

$$SALT = 1.8[Cl^-] \qquad \text{Equation 5.5}$$

Hourly RCFM was also calculated using hourly MARGA $PM_{2.5}$ measurements of inorganic species and hourly averaged AMS total organic PM_1 measurements (methods described in 2.2 and 2.6). The components for the estimation of soil (Equation 5.4) were not measured hourly and the majority of the measurements of chloride from the MARGA were below the instrument detection limit, so the daily concentrations of SOIL and SALT components from the daily reconstructed $PM_{2.5}$ were expanded to the hourly data set.

The average contribution of each aerosol component to the total daily and hourly RCFM as represented by the pie chart in Figure 5.13a and b shows that on average, OMC is a dominant species in the total RCFM, along with AS and AN. Contributions from SOIL and SALT are small. Similar RCFM contributions are seen for the daily and hourly measurement sets.
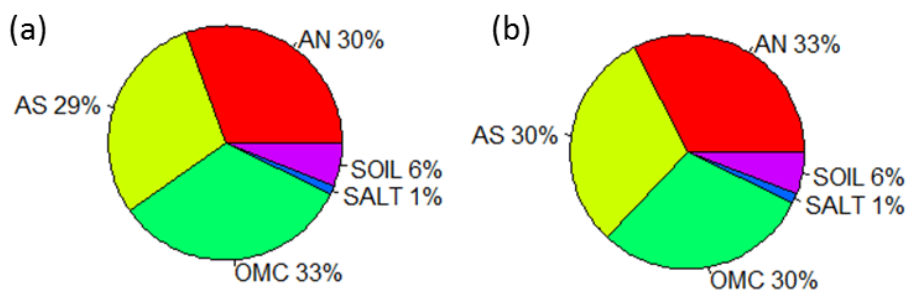
Figure 5.13: The pie charts represents the average RCFM composition using daily filter measurements (a) and hourly MARGA and AMS measurements (b). Only the overlapping time period (11/23/13 - 12/28/13 and 2/14/14 - 3/26/14) was selected to enable direct comparison of the two methods. See text for abbreviations.

The equation used to calculate reconstructed aerosol scattering (b_{sp}) was modified from the revised IMPROVE equation (Pitchford et al., 2007), shown in Equation 5.6. For comparison, the b_{sp} was also calculated using the PM$_{2.5}$ species in the old IMPROVE equation (Hand, 2011), shown in Equation 5.7. The b_{sp} equations include scattering from each component of the above RCFM (Equations 5.1-5.5) multiplied by a dry mass extinction term (m^2 g^{-1}). Relative humidity factors for both the small ($f(RH)_s$) and large fractions ($f(RH)_l$) of AN and AS (Equation 5.6) or for total AN and AS ($f(RH)$; Equation 5.7) and relative humidity factors for sea salt ($f(RH)_{ss}$) are included in both equations.

$$b_{sp} = 2.2 \times f(RH)_s \times [Small\ AS] + 4.8 \times f(RH)_l \times [Large\ AS] +$$

$$2.4 \times f(RH)_s \times [Small\ AN] + 5.1 \times f(RH)_l \times [Large\ AN] +$$

$$2.8 \times [Small\ OMC] + 6.1 \times [Large\ OMC] +$$

$$1 \times [SOIL] +$$

$$1.7 \times f(RH)_{ss} \times [SALT] \qquad\qquad\qquad\qquad \text{Equation 5.6}$$

$$b_{sp} = 3 \times f(RH) \times [AS] +$$

$$3 \times f(RH) \times [AN] +$$

$$4 \times [OMC] +$$

$$1 \times [SOIL] +$$

$$1.8 \times f(RH)_{ss} \times [SALT] \qquad\qquad\qquad\qquad \text{Equation 5.7}$$

5.3.2 Comparison with Measured Aerosol Scattering

At THRO-N, b_{sp} (Mm^{-1}) was calculated using dry RCFM to compare with the PM$_{2.5}$ scattering measurements, so the relative humidity factors were not included in Equations 5.6 and 5.7. The nephelometer was inside a shelter and operated at room temperature, effectively drying the much cooler, ambient air that was sampled. The nephelometer measured an average internal relative humidity of 14% and maximum value of 30%. When using the improved equation in Pitchford et al., 2007, no RH factor is needed when RH is below 35%, the efflorescence relative humidity for ammonium sulfate (Seinfeld and Pandis, 2006).

The RCFM species as described above were used in the revised IMPROVE reconstructed b_{sp} equation (Equation 5.6) and the old reconstructed b_{sp} equation (Equation 5.7). The nephelometer measurements were averaged to 24-hours starting and ending at 8:00 am to compare with the time scale of the daily filter measurements used to calculate reconstructed b_{sp}

(Figure 5.14). On average, the reconstructed b_{sp} compares well with the measured b_{sp}. However, the old equation tends to overestimate b_{sp} during lower periods, especially during January. The revised equation also overestimates b_{sp}, but is in closer agreement with the measured b_{sp}. The b_{sp} calculated using the revised equation will be used for the remainder of this analysis.
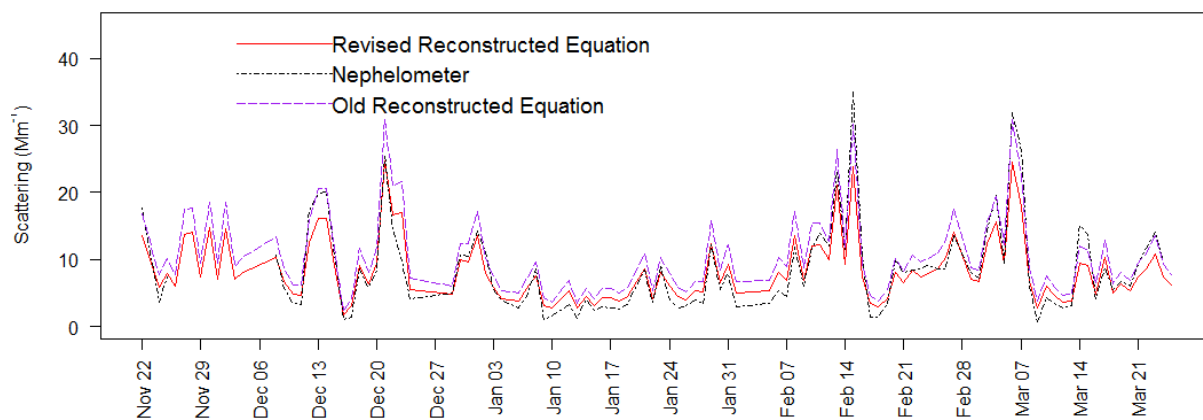
Figure 5.14: Timeline of daily averaged nephelometer measurements (black dashed line) and reconstructed b_{sp} using the revised IMPROVE equation (red solid line) and the old IMPROVE equation (purple dashed line).

Hourly averages of the nephelometer measurements were also used to compare with the hourly reconstructed b_{sp} (Figure 5.15). Both the daily and hourly measurements show that, in general, reconstructed b_{sp} is overestimated at lower scattering values and when there is a higher fraction of the total $PM_{2.5}$ composed by organic aerosol. Conversely, reconstructed b_{sp} is underestimated at the higher values and correspond with low fractions of organic aerosol (Figure 5.16).
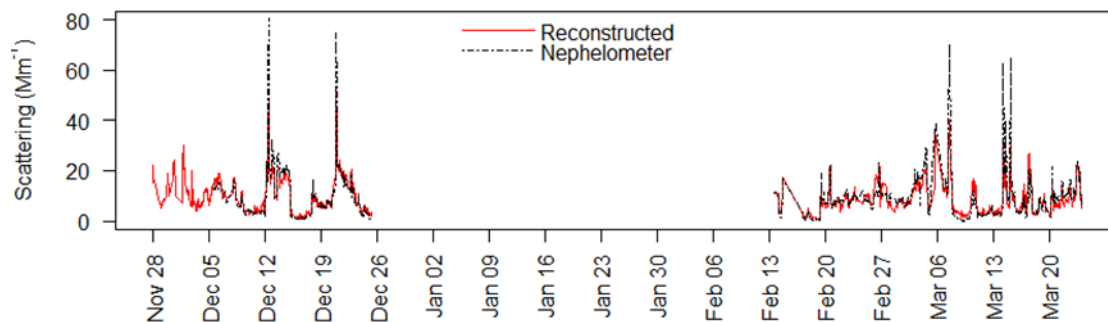
Figure 5.15: Timeline of hourly averaged nephelometer measurements (black dashed line) and hourly reconstructed b_{sp} (red solid line).
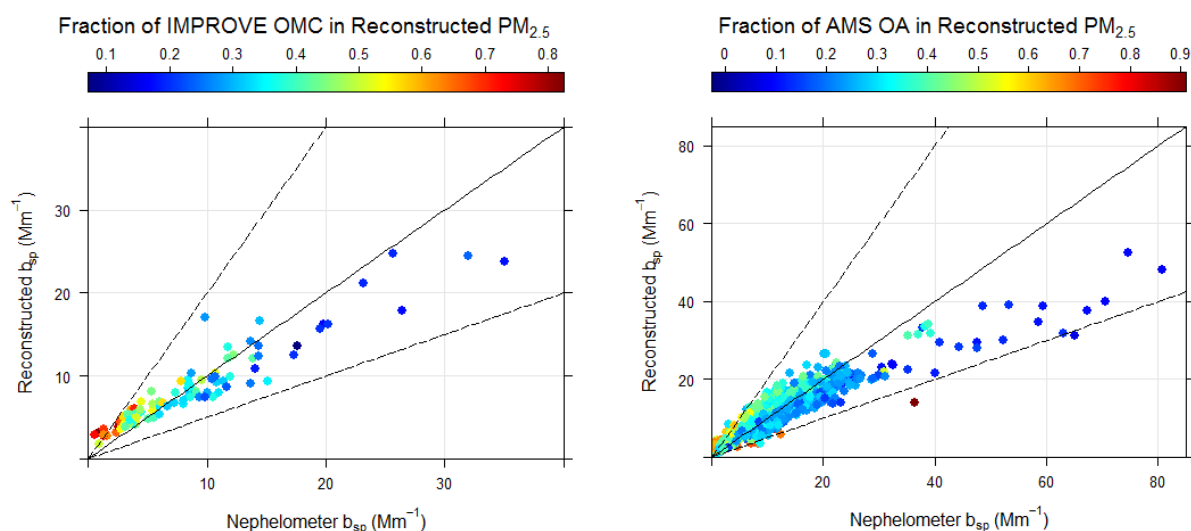
Figure 5.16: Comparison of calculated and measured b_{sp} (Mm^{-1}) colored by the fraction of OMC in the total reconstructed PM$_{2.5}$ mass using daily measurements (left panel) and hourly measurements (right panel) with the 1:1 line (solid) and 1:2 and 1:0.5 lines (dashed).

To better understand the overestimation of reconstructed b_{sp} at lower values and underestimation of b_{sp} at higher values (Figure 5.17), the contribution of OA to the b_{sp} is investigated further. Here we only use the time period the AMS and MARGA were operating (11/23/13 - 12/28/13 and 2/14/14 - 3/26/14). First the use of the constant OM/OC of 1.8 is considered, which has been identified in previous studies as a potential source of error in estimated reconstructed b_{sp} (Lowenthal et al., 2015; Lowenthal and Kumar, 2016). Previous measurements of OM/OC in a range of studies have shown that the ratio can vary over location,

time of day (Aiken et al., 2008; Brown et al., 2013a), and time of year (Simon et al., 2011). The

mean calculated OM/OC ratio was 1.72 ± 0.12 with significant variability as shown in Figure

5.17. To check the validity using the estimated OM/OC ratio of 1.8, the AMS derived OM/OC is

applied to the calculation of OMC shown in Equation 5.3 and used to calculated reconstructed

b_{sp}. When using the OM/OC values from the AMS, the average reconstructed b_{sp} is lower than

the average nephelometer measurements (Table 5.2). In addition, a constant OM/OC of 1.72,

was used as the input in the calculation for reconstructed b_{sp}, which was very similar to using the

OM/OC of 1.8 or the daily averaged AMS derived OM/OC (Table 5.2).
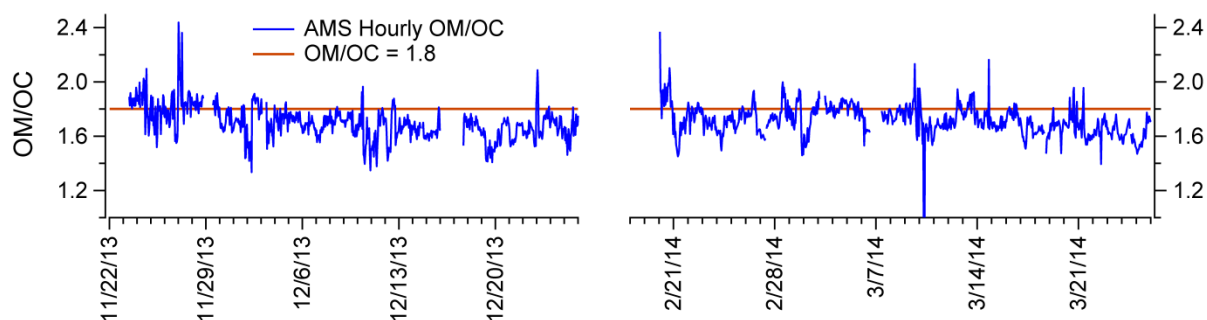
Figure 5.17: Timeline of hourly averaged OM/OC derived from AMS organic aerosol measurements (blue) compared with OM/OC ratio used in the IMPROVE revised reconstructed aerosol scattering equation (orange line).

Table 5.2: The average and standard deviations for b_{sp} as measured by the nephelometer and as calculated using a constant OM/OC of 1.8 or 1.72 and the daily averaged OM/OC as derived from AMS measurements. Averages were calculated during the time period when the AMS was operational (11/23/13 - 12/28/13 and 2/14/14 - 3/26/14).

	b_{sp} (Mm^{-1})
Nephelometer	9.68 ± 5.87
OM/OC = 1.8	9.17 ± 4.34
OM/OC = 1.72	9.02 ± 4.31
OM/OC from AMS	9.00 ± 4.32

When b_{sp} is low, OMC comprises a larger fraction of the total RCFM. This could suggest

that the linear regression analysis between the measured and calculated b_{sp} would improve at

lower b_{sp} values when using the AMS derived OM/OC values. To test this, the same plot as

107

shown in Figure 5.16 was generated using calculated b_{sp} using daily averaged AMS OM/OC values to estimate OMC concentration (Figure 5.18). The linear regression did not improve when using the AMS measured OM/OC ratio in place of the averaged value or the standard value of 1.8 at lower b_{sp} values. The same trend of overestimated reconstructed b_{sp} at lower scattering was observed in the previous analysis as well as other studies (Lowenthal and Kumar, 2016). Additionally, when only considering the lower b_{sp} values, the R^2 or slope do not improve significantly when using the AMS OM/OC values.
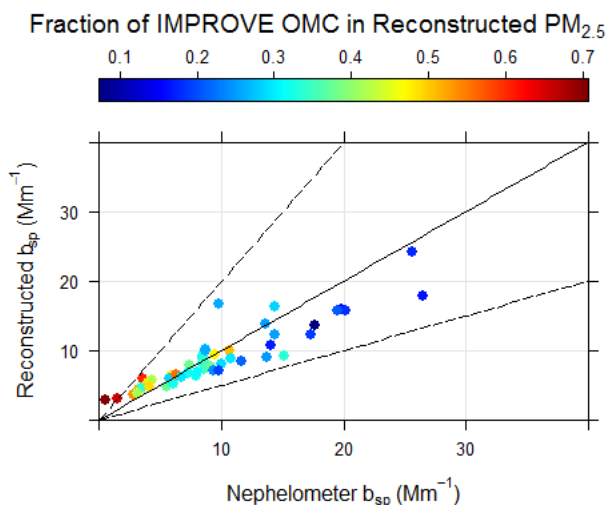
Figure 5.18: Comparison of daily calculated and measured b_{sp} (Mm^{-1}) colored by the fraction of OMC in the total reconstructed PM$_{2.5}$ mass using an OM/OC ratio of 1.72 with the 1:1 line (solid) and 1:2 and 1:0.5 lines (dashed).

The next factors considered in the reconstructed b_{sp} equation are the dry mass extinction coefficients used in Equation 5.6 or 5.7 for each species. To investigate how representative the extinction coefficients are, a multivariate linear regression is performed on the daily and hourly BAQS II reconstructed PM$_{2.5}$ measurements compared to the nephelometer measurements. For simplicity, the old IMPROVE method (Equation 5.7) is used, which only considers one extinction coefficient for each species regardless of particle size. For the linear regression, the y-

intercept was forced through 0. The terms for SOIL and SALT were removed since they had

very small contributions to the total b_{sp} and higher uncertainty due to their low ambient

concentrations. Table 5.3 shows the results from the linear regression analysis of both hourly

and daily measurements.

Table 5.3: Multiple linear regression analysis of daily and hourly measurements fitting them to
the nephelometer measurements. The dry mass extinction coefficients (m^2/g) and standard
deviations from Equation 5.7 for the small and large fractions of $PM_{2.5}$ are also listed for
comparison (Pitchford et al., 2007).

	AS	AN	OMC
Daily	4.4 ± 0.30	2.7 ± 0.33	1.5 ± 0.26
Hourly	4.8 ± 0.08	2.7 ± 0.10	1.0 ± 0.11
Small Fraction	2.2	2.4	2.8
Large Fraction	4.8	5.1	6.1

The estimated extinction coefficients and standard deviations for the large and small

fractions of AS, AN and Org from the revised IMPROVE reconstructed b_{sp} equation are also

shown in Table 5.3. Small standard deviations in the estimated extinction coefficients gives

confidence to the results. If the extinction coefficients in the revised b_{sp} calculation were

representative for the aerosol measurements used in this analysis, the multivariate linear

regression coefficients should fall somewhere in between the coefficients for the small and large

fractions. We see that the hourly coefficient calculated for AS (4.8 ± 0.08) is more similar to the

large size fraction (4.8) and the calculated AN coefficient (2.7 ± 0.10) is more similar to the

small fraction (2.4). This could suggest that in the $PM_{2.5}$ sampled during BAQS, more AS

resided in larger particles sizes and more AN resided in smaller particle sizes. For OMC, the

calculated coefficient is smaller than the estimated coefficient for the small fraction of OMC.

This shows that the scattering contribution from OMC is lower than predicted in the revised b_{sp}

equation and suggests that OMC is associated with smaller particle sizes.

5.3.3 Importance of Organics in Total Scattering

The contributions of each species to the total b_{sp}, Table 5.4, show that OMC has the most significant average contribution to total b_{sp}, 41.3%, when considering dry aerosol. When relative humidity is considered in the reconstructed b_{sp}, both AN and AS have larger contributions than OMC. This calculation assumes OMC is not hygroscopic, which previous studies have shown is not always a valid assumption (Brock et al., 2016; Lowenthal and Kumar, 2016). Total average reconstructed b_{sp} with and without relative humidity factors are 8.38 and 15.16 Mm^{-1}, respectively for the daily RCFM.

Table 5.4: Calculated using the IMPROVE reconstructed $PM_{2.5}$ mass equations, the average concentration of each species is shown and dry aerosol scattering (b_{sp}).

	AN	AS	OMC	SALT	SOIL
RCFM Concentration ($\mu g\ m^{-3}$)	0.93	1.00	1.16	0.037	0.19
Contribution to b_{sp} (dry, %)	28	28	41	1	2
Contribution to b_{sp} (with RH, %)	37	37	23	1	1

Figure 5.19 shows the contribution of each RCFM species to total of each b_{sp} quartile measurement. In the lowest 25% of b_{sp} measurements, OMC dominates the aerosol scattering. In the fourth quartile, corresponding with the haziest conditions, OMC comprises less than 25% of the total scattering. During the haziest conditions, the inorganic components AS and AN dominant the scattering. This reinforces that the majority of wintertime haze is due to the inorganic species AS and AN, but these results also suggest an important contribution from the organic component of the $PM_{2.5}$.
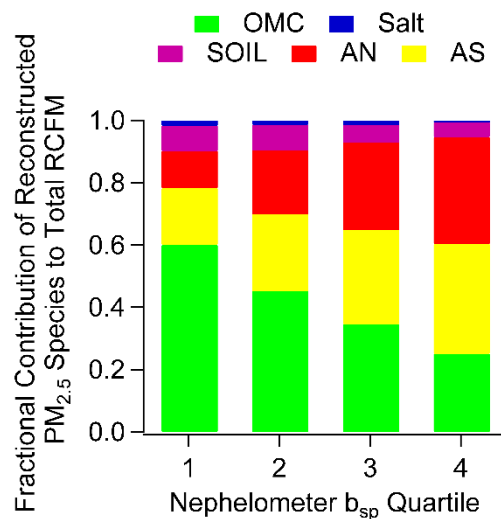
Figure 5.19: A stacked bar plot showing, for measured b_{sp} (Mm^{-1}) quartiles, the contribution of each RCFM component to the total scattering.

Finally, all scattering and absorbing components are considered in order to calculate total extinction (Hand et al., 2014), which is shown in Figure 5.20. Scattering by RCFM components AS, AN, OMC, SALT and SOIL were included as described above. Coarse particulate matter ($PM_{10} - PM_{2.5}$) concentrations were not measured during BAQS, so measurements of PM_{10} and $PM_{2.5}$ from the nearby IMPROVE site at THRO-S (Figure 5.1) were used to calculate a ratio to estimate coarse PM concentrations at THRO-N. The average coarse PM at THRO-S was 3.3 μg m^{-3} and the ratio of coarse to fine PM was found to be 1.20. This gave an average coarse PM concentration at THRO-N of 2.2 μg m^{-3}. This assumption may not be robust, due to the strong influence of local emission sources to coarse PM, but since it is found to be a small contributor to total light extinction it should not strongly influence the total light extinction calculated. Absorbtion by NO_2 and EC were calculated using measurements from the Teledyne 201E chemiluminescence instrument and IMPROVE EC filter measurements. An estimated value of 11 Mm^{-1} for Rayleigh scattering was used.

111
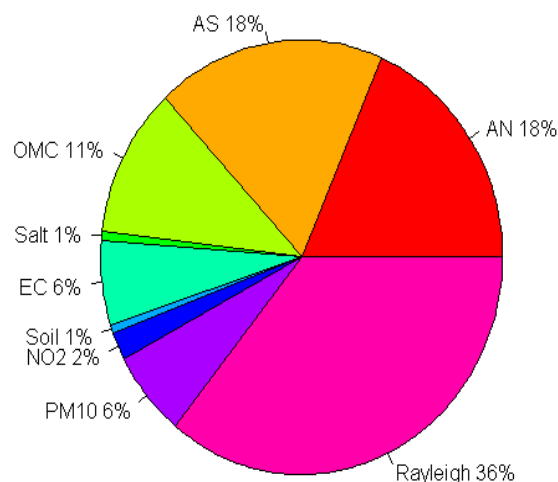
Figure 5.20: Reconstructed b_{ext} including all species in $PM_{2.5}$ (AN, AS, OMC, Salt, Soil and EC), absorption from NO_2, scattering from PM_{10} and Rayleigh scattering and including relative humidity factors.

AS and AN make up the majority of the anthropogenic contribution to total extinction at THRO-N. OMC also contributes a significant fraction on average and, as shown previously, is more significant when b_{sp} is lower. Absorption from elemental carbon and scattering from coarse PM contribute small but non-negligible fraction. Contributions from salt, soil, and NO_2 to total light extinction are very low.

5.4 Conclusions

Regional long-term OA measurements near the Bakken oil and gas development region suggest concentrations have been decreasing. Measurements of OA during BAQS II at THRO-N show elevated concentrations compared to the concentrations observed at the long-term measurement sites. PMF analysis of the OA at THRO-N found an HOA factor is influenced by local anthropogenic sources, strongly correlating with NO_x and BC concentrations, likely from the sources associated with the oil and gas development. An LVOOA factor was correlated with aerosol nitrate and ammonium which was previously found to be associated with local emissions that build up during stagnations events (Chapter 4). Van Krevelen and f44 versus f43 plots both indicated that the LVOOA factor was associated with a more aged and oxidized aerosol, while

112

the HOA factor was associated with more fresh emissions. Higher OM/OC, higher OC/EC and longer airmass lifetimes estimated by an alkyl nitrate clock were used to gain an understanding of the bulk atmospheric OA characteristics, which suggested that OA at THRO-N included important contributions from long-range transport of oxidized aerosol and from more local sources. The role of OMC in contributing to total light scattering was found to be significant, ranging from 60% in the least hazy quartile to 25% in the most hazy quartile. This analysis suggests that the OA in the Bakken oil and gas extraction region has unique characteristics, which is important to consider as OA in other oil and gas extraction regions is studied in more detail.

6.0 AEROSOL THERMODYNAMIC MODELING USING HOURLY MARGA DATA

To better understand the formation of inorganic atmospheric aerosol, thermodynamic aerosol models can be used to represent the chemical properties of atmospheric aerosol and predict gas to particle partitioning. Thermodynamic aerosol models, using the mathematical framework as described in Chapter 1, provide detail on the partitioning of each chemical species between gas, aqueous and solid phases. They are also useful tools to simulate physical properties that are difficult to measure, such as liquid water content and pH. Two different thermodynamic models, E-AIM and ISORROPIA, will be used in this analysis.

The use of hourly data to validate thermodynamic equilibrium models, as investigated in previous studies (Schaap et al., 2011), offers significant advantage in understanding how variable meteorological conditions and concentrations of atmospheric constituents impact how the model treats the gas and aerosol composition and concentrations. A comprehensive review of thermodynamic models for inorganic aerosol (Zhang et al., 2000) suggests that model predictions are sensitive to temperature especially when there are higher nitrate concentrations present, but did not test model predictions at low ambient temperatures. The work presented here will utilize a data set obtained during the Bakken Air Quality Study (BAQS) to explore the lower temperature performance of the models.

6.1 Model Descriptions

6.1.1 E-AIM

The extended aerosol inorganic model (E-AIM; http://www.aim.env.uea.ac.uk) is a thermodynamic model that has been developed for a variety of aerosol chemical systems to study gas to particle partitioning as well as chemical properties such as liquid water content and pH

(Clegg et al., 1998b; Wexler and Clegg, 2002). Solving for the minimization of Gibbs free energy, the model predicts the equilibrium composition of gas, aqueous and solid phases of each chemical species. The model can be run in two different modes: forward and reverse. In the forward mode, the total gas and aerosol components of each species (i.e. $NH_{3(g)} + NH_4^+{}_{(p)}$) are input into the model along with ambient temperature and relative humidity (RH). This model requires electroneutrality, so the input of H^+ or OH^- must be adjusted to balance the anions and cations. The forward model will partition the gas, aqueous and solid phases of each species based on chemical properties such as chemical activity. In the reverse mode of the model, the input of each species consists of only the aerosol component. The model predicts the gas partial pressures based on the gas phase equilibrium of each species.

The web interface of the E-AIM Model II used in this analysis, represents the chemical system of H^+- NH_4^+ - SO_4^{2-} - NO_3^- - H_2O and is valid from a temperature range of 200 to 330 K. Only inorganic species were considered since detailed organic speciation measurements were not collected. The model was run in forward mode treating the aerosol in a metastable thermodynamic state. In the metastable state, the model generates supersaturated aqueous aerosol and prevents the partitioning of any species into a solid phase.

6.1.2 ISORROPIA

ISORROPIA (http://isorropia.eas.gatech.edu) is another thermodynamic aerosol model which operates according to the same principles as E-AIM, but more assumptions are included to increase the computational efficiency (Nenes, 1998). ISORROPIA version II was used in a forward and metastable mode using N(-III), N(V), SO_4^{2-}, temperature, and relative humidity as inputs. The improved computational efficiency allows ISORROPIA (ISO) to be used in numerous global and regional models including CAMx (http://www.camx.com/), CHIMERE

(http://www.lmd.polytechnique.fr/chimere/), CMAQ (https://www.cmascenter.org/cmaq/),

COSMO-ART (http://www.imk-tro.kit.edu/3509.php), GEOS-Chem

(http://acmg.seas.harvard.edu/geos/), and LOTOS-EUROS (http://www.lotos-euros.nl/).

6.2 Model Comparison Results

Hourly measured N(-III) and N(V) concentrations from the MARGA were input and run

in the forward mode to partition into the gas, aqueous, and solid phases. SO_4^{2-} is also provided

as input to the model, but remains predominantly in the particle phase due to the low vapor

pressure of $H_2SO_{4(g)}$. The model allows partitioning between $H_2SO_{4(g)}$, $SO_4^{2-}{}_{(aq)}$, $HSO_4^{-}{}_{(aq)}$, and

the formation of sulfate salts. The model output gas and aerosol concentrations were compared

to the measurements, which are shown in Figures 6.1 and 6.2. To enable a direct comparison

between models, both were run with metastable conditions which prevented the formation of any

solid species including ice. The metastable state treats the aerosol as being on the efflorescence

branch of the aerosol water uptake curves, which prevents crystallization of the species in the

aerosol phase (Ansari and Pandis, 2000).
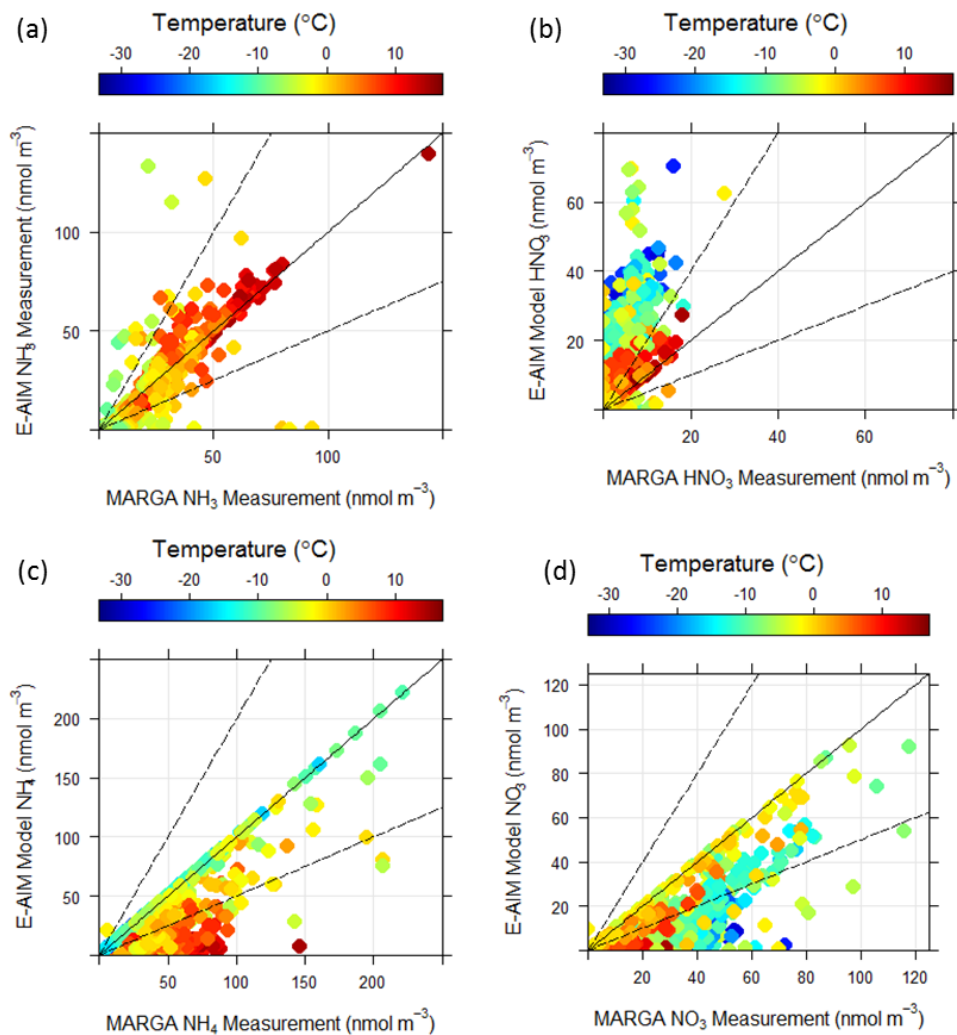
Figure 6.1: Comparison of MARGA measurements and E-AIM model output of (a) NH_3, (b) HNO_3, (c) NH_4^+ and (d) NO_3^- using the forward mode of the E-AIM Model II. Points are colored by temperature (ºC). The 1:1 line (solid black line) and the 1:2 and 1:0.5 lines (black dashed lines) are also shown.
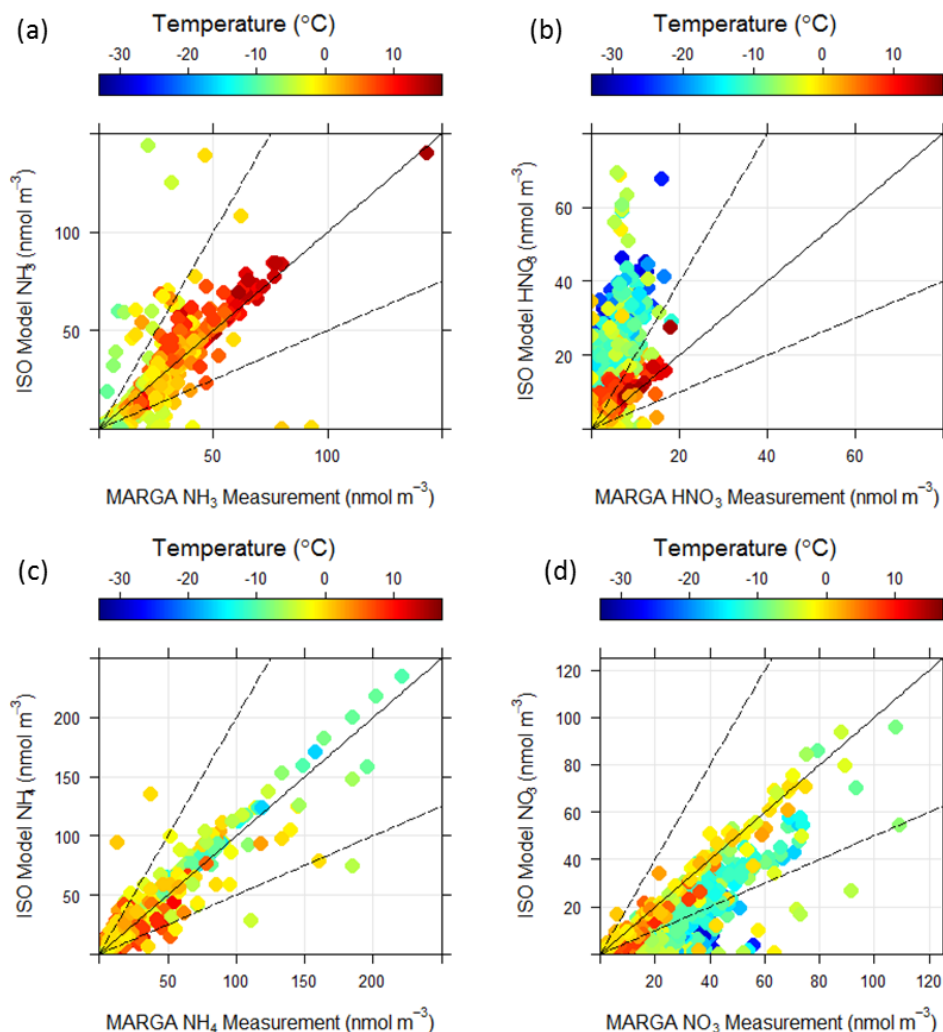
Figure 6.2: Comparison of MARGA measurements and ISORROPIA (ISO) model output of (a) NH_3, (b) HNO_3, (c) NH_4^+ and (d) NO_3^- using the forward mode of the E-AIM Model II. Points are colored by temperature (ºC). The 1:1 line (solid black line) and the 1:2 and 1:0.5 lines (black dashed lines) are also shown.

The model outputs for all species of N(-III) and N(V) from E-AIM and ISORROPIA (ISO) show similar trends. Overall, the model partitions more HNO_3 into the gas phase than what is seen in the measurements. Correspondingly, the model partitions less N(V) into the particulate phase as NO_3^-. Good agreement in modeled NH_4^+ concentrations is observed with MARGA measurements in ISO, but E-AIM shows an underestimation in modeled NH_4^+ when temperatures are higher and when NH_3 concentrations are elevated (Figure 6.3).
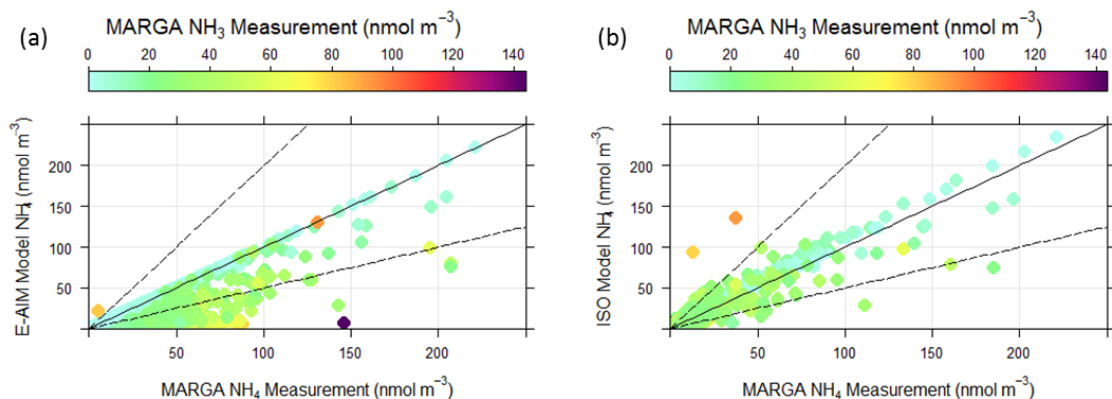
Figure 6.3: Comparison of MARGA NH_4^+ measurements with E-AIM (a) and ISORROPIA (b) model output colored by MARGA NH_3 (nmol). The 1:1 line (solid black line) and the 1:2 and 1:0.5 lines (black dashed lines) are also shown.

To validate the importance of using hourly MARGA data in the E-AIM model, daily URG measurements of the same species and daily averaged temperature and relative humidity were input into the model using the same model settings and compared with measurements (Figure 6.4). The comparison for each species show similar trends to the E-AIM results between the hourly MARGA and daily URG measurements. A comparison of the MARGA and URG measurements (Figure 6.5) shows good agreement in NH_3, HNO_3, NH_4^+, NO_3^-, and SO_4^{2-}, verifying good accuracy in MARGA measurements for all species. As expected, much less scatter exists in the comparison with the daily URG measurements. When using daily measurements, a much larger range of thermodynamic conditions are present compared to the hourly measurements, so trends in the model comparison are dampened after averaging over a longer time period. This is shown clearly in the comparison of daily HNO_3 (Figure 6.3b), which does not show as large of an overestimation in model concentrations and diminishes the trend with temperature. This validates the importance of using the hourly data to be able to identify trends in model disparities at different ambient conditions.
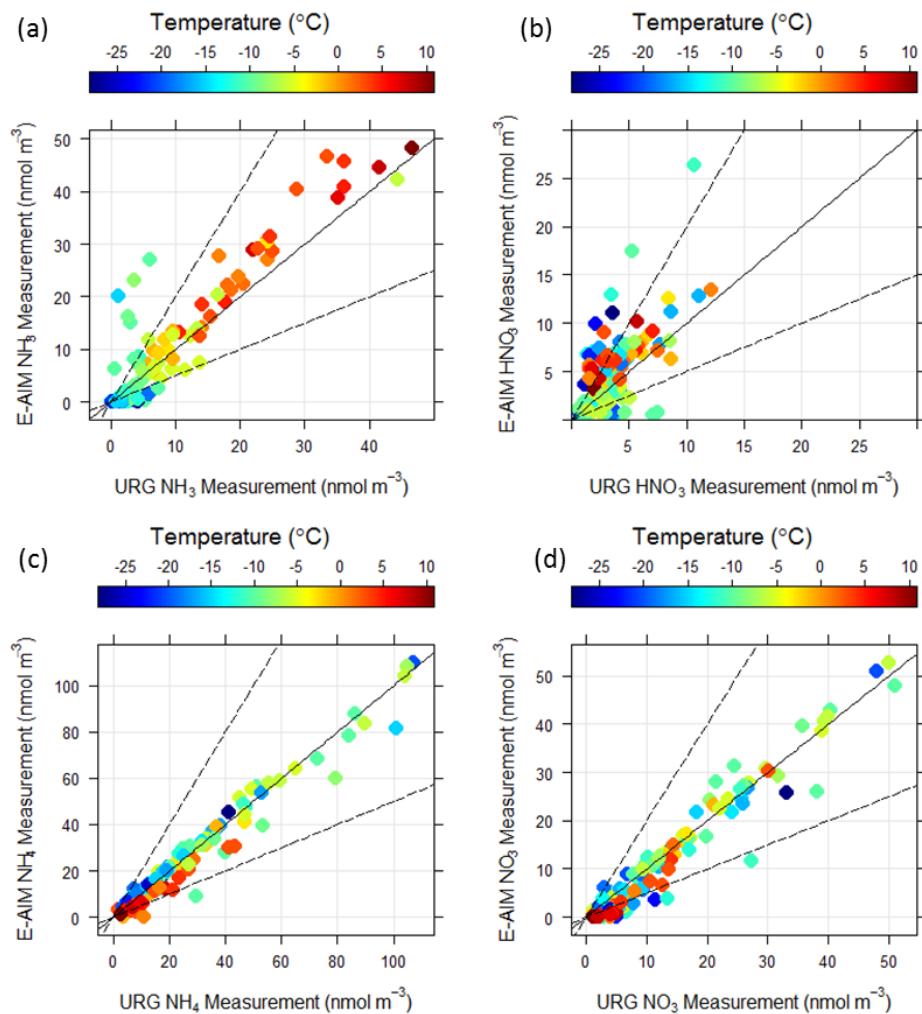
Figure 6.4: Comparison of URG measurements from THRO-N and E-AIM model output of (a) NH₃, (b) HNO₃, (c) NH₄⁺ and (d) NO₃⁻ using the forward mode of the E-AIM Model II. Points are colored by temperature (°C). The 1:1 line (solid black line) and the 1:2 and 1:0.5 lines (black dashed lines) are also shown.
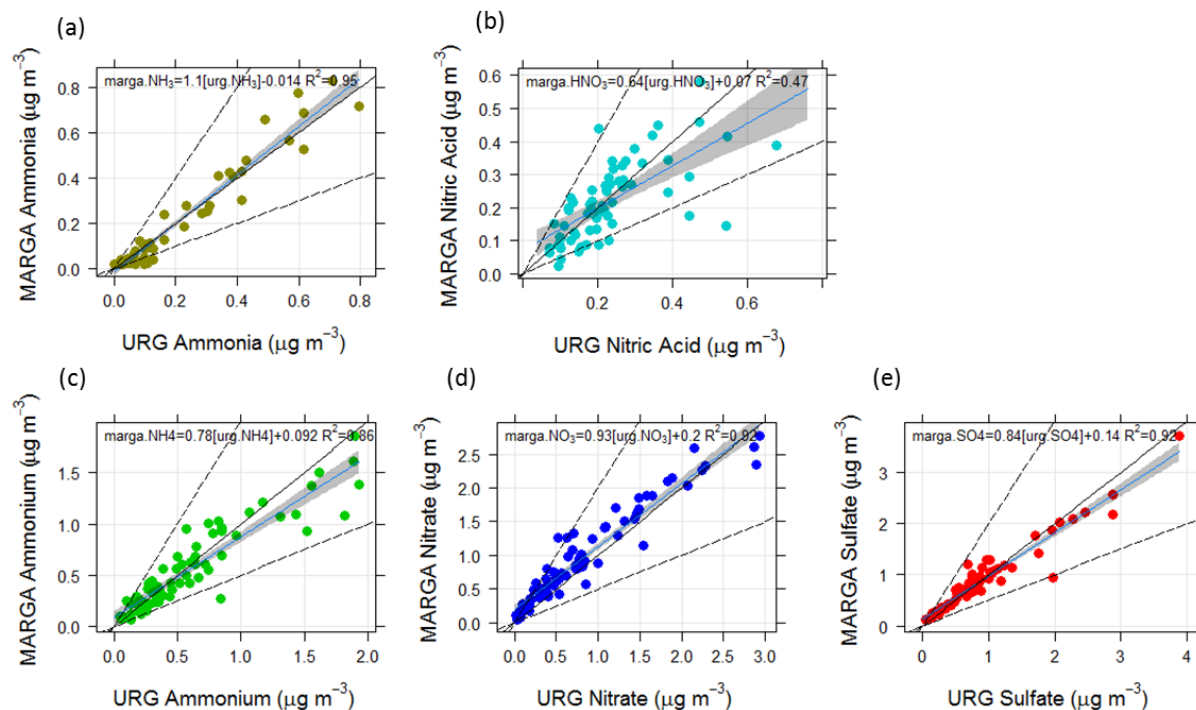
Figure 6.5: Comparison of BAQS daily averaged MARGA measurements and URG measurements of NH_3 (a), HNO_3 (b), NH_4^+ (c), NO_3^- (d), and SO_4^{2-}.

Table 6.1 shows the slopes (m), y-intercepts (y), and Pearson correlation coefficients (R^2) from each model comparison using BAQS II data from THRO-N. The linear regressions for NH_3, HNO_3, and NO_3^- are very similar between models. However, for NH_4^+, the slope and R^2 were much better for ISORROPIA compared to E-AIM. This can be seen in Figures 6.2c, which shows that the E-AIM model tends to under predict the concentration of NH_4^+, particularly at higher temperatures and lower concentrations. Figures 6.1b and 6.2b show that both E-AIM and ISORROPIA tend to over predict HNO_3 at the coldest temperatures. This is compensated by both models under predicting particulate NO_3^-.

Table 6.1: Linear regression analysis of modeling versus measurement concentrations of NH_3, NH_4^+, HNO_3, and NO_3^-. The slope (m), y-intercept (y) and Pearson correlation coefficient (R^2) are shown for each species for the E-AIM and ISORROPIA (ISO) comparisons shown in Figures 6.2 and 6.3.

	NH₃	NH₄	HNO₃	NO₃
E-AIM with MARGA	m = 1.0 y = -0.9 R^2 = 0.79	m = 0.68 y = 0.6 R^2 = 0.65	m = 2.1 y = 5.6 R^2 = 0.38	m = 0.58 y = -4.9 R^2 = 0.63
ISO	m = 1.0 y = -0.9 R^2 =0.79	m = 0.97 y = 2.5 R^2 =0.9	m = 2.0 y = 5.3 R^2 = 0.36	m = 0.67 y = -3.7 R^2 = 0.68
E-AIM with URG	m = 1.1 y = 0.049 R^2 = 0.87	m = 0.96 y = -0.23 R^2 = 0.96	m = 1.0 y = 1.1 R^2 = 0.35	m = 1.0 y = -1.7 R^2 = 0.94

6.3 Model Comparison Discussion

6.3.1 Model Settings

Both ISORROPIA and E-AIM modeling results gave similar poor results for the linear regression analysis with hourly measured HNO_3 and NO_3^- (Table 6.1). Much better agreement was observed for hourly measurements of NH_3 and NH_4^+ and daily measurements of all four species. Only E-AIM results for HNO_3 and NO_3^- will be discussed here in detail to focus on understanding the model discrepancies with partitioning N(V) over a range of ambient temperatures. The previously shown results were obtained by using the model in the metastable mode, which prevented the formation of solids. To test if preventing the formation of solid species, including ice, is impacting our model comparison, the model is run in the deliquescence, or stable, state allowing the formation of solids. The slopes and R^2 for the two model conditions are shown in Table 6.2. Including the formation of ice did not change the slopes or R^2 for HNO_3 of NO_3, indicating that including the formation of solid species or ice does not impact the

partitioning between gas and particle phase of N(V) in this environment. The linear regression

analysis for NH_3 and NH_4^+ also did not change after varying the model conditions (not shown).

Table 6.2: The slope (m) and Pearson correlation coefficient (R^2) from a linear regression analysis of modeled vs. measured HNO_3 and NO_3 under metastable and stable thermodynamic states as described in the text.

	HNO_3	NO_3
Metastable	m = 2.1	m = 0.58
	$R^2 = 0.38$	$R^2 = 0.63$
Stable	m = 2.2	m = 0.57
	$R^2 = 0.37$	$R^2 = 0.6$

Despite the similarities in the linear regression from the different thermodynamic states,

the formation of solids contributed a significant fraction of total N(V) in the model when run in

the stable state. The average fraction of solid NH_4^+, NO_3^-, and SO_4^{2-} in the total aerosol (solid

and aqueous) are 0.49 ± 0.48, 0.26 ± 0.43, and 0.43 ± 0.48, respectively. For 24% of the

measurements, all NO_3^- was partitioned into the solid phase with only 3% of measurements

having a mixture of solid and aqueous phases. Considering only the measurements where the

model partitioned all NO_3^- into the solid phase, the linear regression analysis shows slightly

better slope for HNO_3 but overall worse correlation with measurements for both HNO_3 (m = 1.8,

$R^2 = 0.26$) and NO_3^- (m = 0.46, $R^2 = 0.49$). This suggests that running the model in the stable state

does not improve the model performance. Only the metastable state without ice formation is

explored further.

6.3.2 NH_3 Availability

Based on previous studies, the measurements in this study can be divided into two

regimes: NH_3 limited and NH_3 rich (Bassett and Seinfeld, 1983). The NH_3 limited regime

occurs when there is not enough NH_3 and NH_4^+ to fully neutralize sulfate, or when [N(-III)] is

less than two times [SO_4^{2-}]. In the NH_3 rich regime, sulfate is fully neutralized and [N(-III)] is

greater than two times $[SO_4^{2-}]$. Of the measurements used in this study, about 1/3 of the sampling times were NH_3 limited and 2/3 were NH_3 rich. Figure 6.6 shows how these two regimes impacted the modeling and measurement comparison of HNO_3 and NO_3^- partitioning. The most underestimated modeled NO_3^- is when the aerosol is NH_3 limited.
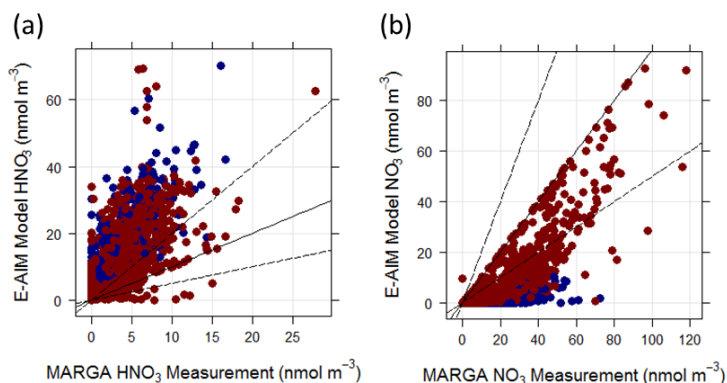
Figure 6.6: The same comparison of modeled and measured HNO_3 (a) and NO_3^- (b) as in Figure 6.2 but points are colored blue if NH_3 limited and maroon if NH_3 rich. The 1:1 line (solid black line) and the 1:2 and 1:0.5 lines (black dashed lines) are also shown.

Correspondingly, over predicted HNO_3 also occurs in the NH_3 limited regime. This trend is not as robust, however, as over predicted HNO_3 also frequently exists in the NH_3 rich regime as well. This suggests that predicting correct partitioning of HNO_3 may be more dependent on temperature (Figure 6.1c) than on the availability of NH_3.

6.3.3 Thermodynamic Equilibrium

The thermodynamic models assume equilibrium is reached in the ambient gas – aerosol system, which previous laboratory and field studies have found is not always the case. It has been shown that at cooler temperatures and higher RH, reaching thermodynamic equilibrium can slow down and be longer than characteristic transport times of emissions (Allen et al., 1989; Wexler and Seinfeld, 1990). The favorability of volatile species such as NH_3 and HNO_3 to exist

at colder temperatures produces higher gas concentrations which takes longer to condense into the aerosol phase and slows down reaching equilibrium (Meng and Seinfeld, 1996).

E-AIM has built in checks to test that the system is in equilibrium based on physical constraints of the thermodynamic parameters generated. In the modeling results presented here, two thermodynamic error codes were generated. The "R" code indicates that the aqueous and hydrophobic liquid phase are not in equilibrium with one another. This error code can be disregarded because the hydrophobic phase only applies to organic compounds, which are not included in these model analyses. The "G" code indicates that the measured RH and calculated partial pressures of the trace gases did not agree with the gas – liquid equilibrium value calculated from the liquid phase activities. A "G" error code was generated for 0.2% of the measurements while in the stable state and for 1% of the measurements in the metastable state. The measurements that generated errors, both "R" and "G", were removed from the model measurement comparison to see if the agreement improved. The slopes and correlation coefficients for the linear regression analysis are shown in Table 6.3. Compared to the regression analysis including measurements that generated an error, shown in Table 6.2, the slopes and correlation coefficients are nearly identical. This indicates that the errors generated did not affect the overall modeling results.

Table 6.3: Similar to Table 6.2, the slope (m) and Pearson correlation coefficient (R^2) from a linear regression analysis of modeled vs. measured HNO_3 and NO_3 under metastable and stable thermodynamic states but with model generated errors removed.

	HNO_3	NO_3
Metastable	m = 2.1	m = 0.58
	$R^2 = 0.38$	$R^2 = 0.62$
Stable	m = 2.2	m = 0.57
	$R^2 = 0.37$	$R^2 = 0.6$

E-AIM Model II was developed to use with environments that experience extremely cold temperatures, particularly for studying aerosol in the stratosphere (Wexler and Clegg, 2002). The trend in increasing model disagreement with N(V) partitioning at colder ambient temperatures, as shown in Figure 6.1b and 6.1d. Figure 6.7 shows that more than 75% of the measurements observed during this field study were obtained at ambient temperatures below freezing. The RH was generally high during this study, with the median RH of 0.74 and lower quartile of 0.63.
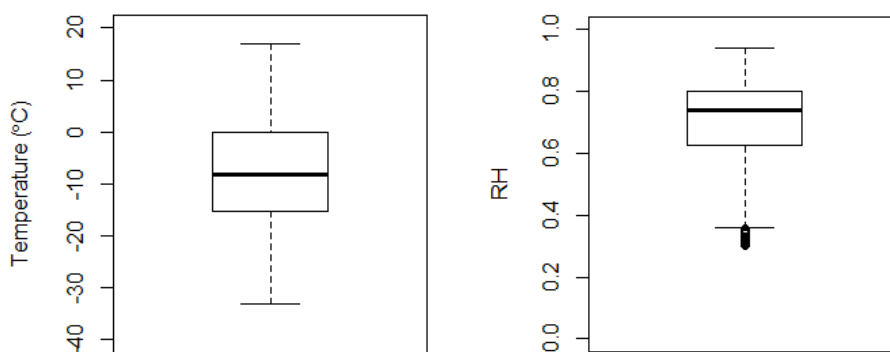
Figure 6.7: Boxplots showing the temperature (ºC) and relative humidity (RH, fraction). The lines in the boxes represent the median and the quartiles. The whiskers extend to the most extreme data but not more than the range times the interquartile range. Outliers are plotted as circles.

Figure 6.8 shows that ambient temperature and RH are negatively correlated above freezing but are much more scattered below freezing. The trends with model partitioning of N(-III) and N(V) species with ambient RH is investigated next. The same four comparison plots for NH$_3$, HNO$_3$, NH$_4^+$, and NO$_3^-$ are shown for the ISORROPIA model comparison (Figure 6.9). For the N(V) species, the best agreement for particulate NO$_3^-$ are at the highest RH values and conversely the best agreement with HNO$_3$ are at the lowest RH measurements. This result contrasts with the trends with temperature, when better agreement with both HNO$_3$ and NO$_3^-$ was

observed at higher temperatures, reflecting the negative correlation between temperature and relative humidity at temperatures above freezing. For the N(-III) species, the model tends to under predict NH_4^+ and over predict NH_3 at lower RH values. An updated study (Meng and Seinfeld, 1996) showed that thermodynamic equilibrium was not sensitive to RH, contrary to previous findings, suggesting that temperature is a stronger contributor to the model disagreement compared to RH when running the model in metastable mode.
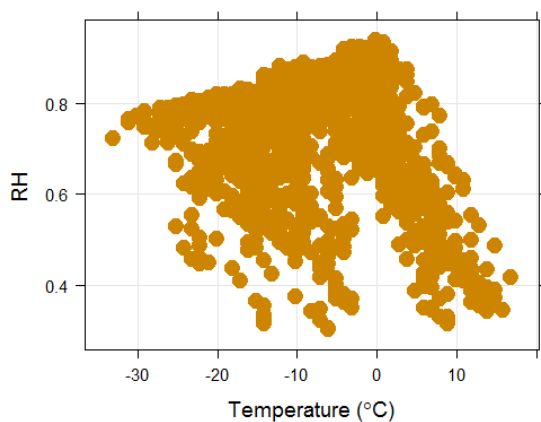
Figure 6.8: Ambient RH (fraction) versus ambient temperature (°C) measured during BAQS II for the measurements used in the thermodynamic modeling comparison.
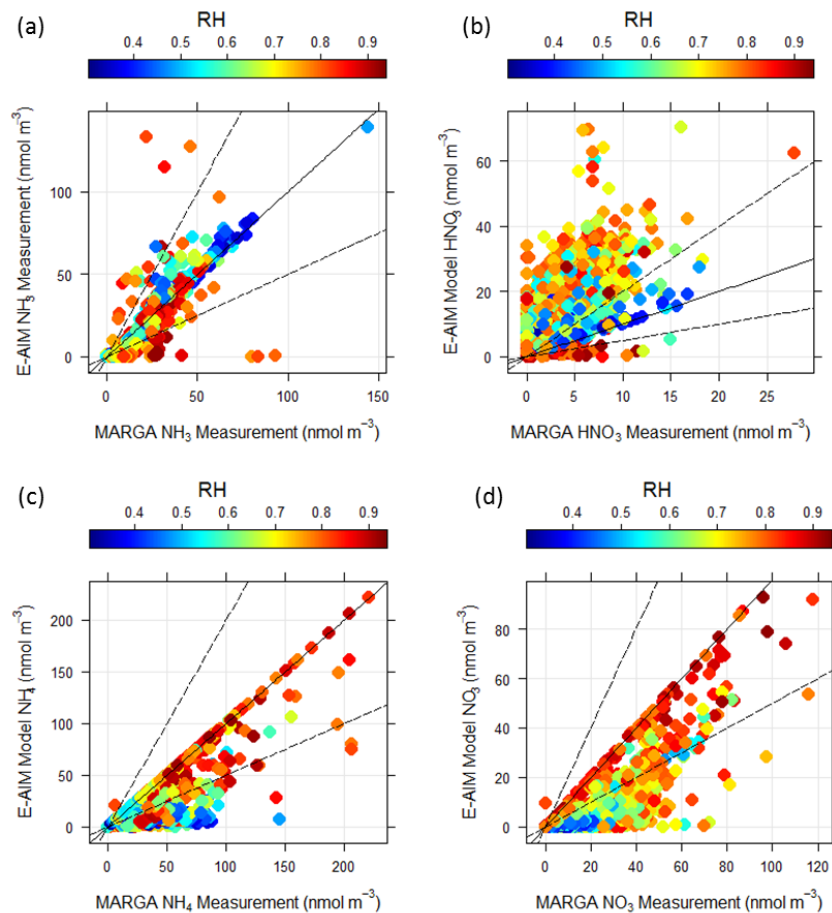
Figure 6.9: The comparison of E-AIM predicted NH_3 (a), HNO_3 (b), NH_4^+ (c), and NO_3^- with MARGA measurements and are colored by ambient RH. The 1:1 line (solid black line) and the 1:2 and 1:0.5 lines (black dashed lines) are also shown.

To further consider the effect of the ambient RH on the thermodynamic state of the gas-aerosol system, the deliquescence relative humidity (DRH) and efflorescence relative humidity (ERH) of the major species in our gas-aerosol system are considered. Table 6.4 shows the DRH for a $(NH_4)_2SO_4$ (AS) and NH_4NO_3 (AN) single component aerosol particle. Multicomponent aerosol, which is more representative of ambient aerosol, will generally have a DRH that is lower than either of the single component aerosol DRHs but follow the same trend of increasing DRH as temperature decreases. The DRH of a mixture of AS and AN, measured at 30 °C (Table 6.4), is one example where the multicomponent DRH is only lower than the DRH of one single

component (Wexler and Seinfeld, 1991). It is also worth noting that the DRH for AN varies over a much wider range than AS. The formation of AN is much more sensitive to both RH and temperature than AS (Stelson and Seinfeld, 1982), which is reflected in the differences in the range of DRH for both compounds. For the temperature and RH of the measurements used in this comparison study (Figure 6.8) and considering the measured DRH at $0°C$ or a lower temperature, the majority of the measurements will likely be below the DRH.

Table 6.4: DRH and ERH of ammonium sulfate and ammonium nitrate (Seinfeld and Pandis, 2006; Wexler and Seinfeld, 1991).

	DRH			ERH
Salt	0°C	15°C	30°C	25°C
$(NH_4)_2SO_4$	81.8%	80.6%	79.5%	35%
NH_4NO_3	76.6%	68.1%	58.5%	Not observed
Mixture			62.3%	

To understand if the temperature and RH effects on the model results from the BAQS data set is unique to this environment, E-AIM modeling results using MARGA measurements obtained in Fort Collins, Colorado (FOCO) in the winter of 2015 will be investigated. The average temperature, RH and input species needed for E-AIM from BAQS and FOCO are compared in Table 6.5. Overall, the temperature and RH measured during the two studies are similar, but concentrations were higher in FOCO, particularly $NH_{3(g)}$. SO_4^{2-} was the only species with a lower average concentration in FOCO. All measurements during the FOCO study were in the NH_3 rich regime, as previously described in Section 6.4.2, which is unsurprising given the high NH_3 and low SO_4^{2-} concentrations observed.

Table 6.5: The average values for measured temperature (Temp, ºC), relative humidity (RH, fraction), and hourly MARGA concentrations input into E-AIM ($\mu g\ m^{-3}$).

	Temp	**RH**	**HNO$_3$**	**NO$_3^-$**	**NH$_3$**	**NH$_4^+$**	**SO$_4^{2-}$**
BAQS	-7.8	0.70	0.25	1.3	0.18	0.60	0.96
FOCO	-1.3	0.63	0.58	3.1	3.1	0.98	0.60

Better model agreement is shown in the FOCO measurements for NH_3, NH_4^+, and NO_3^- at higher concentrations (>100 nmol) which are generally not observed at BAQS (Figure 6.10). When comparing to the same concentration ranges as measurements during BAQS (outlined in pink), discrepancies with the model are observed. The trends in temperature for HNO_3 and NO_3^- are opposite, where modeled concentrations in FOCO are lower for HNO_3 and higher for NO_3^- at lower temperatures. The model agreement for HNO_3 for both BAQS and FOCO measurements show a lot of scatter, but very low concentrations with higher uncertainty were observed at both locations. Additionally, the different NH_3 regime between the two locations likely plays a role in the model performance of partitioning N(V).
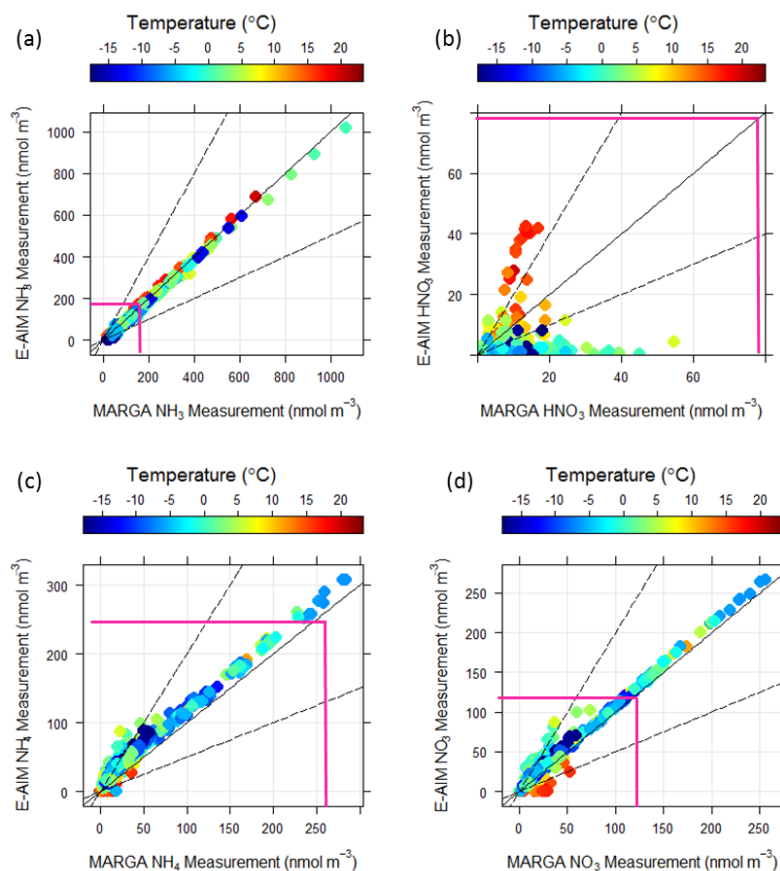
Figure 6.10: Comparison of FOCO MARGA measurements and E-AIM model output of (a) NH_3, (b) HNO_3, (c) NH_4^+ and (d) NO_3^- using the forward mode of E-AIM. Points are colored by temperature (°C). The 1:1 line (solid black line) and the 1:2 and 1:0.5 lines (black dashed lines) are shown. The pink outline represents the concentration range observed during BAQS.

6.3.4 Predicted Aerosol Water and pH

Figure 6.11 shows the relationship between aerosol water and RH. As expected, aerosol liquid water content (LWC) increases sharply as RH increases. The figure also shows that the highest temperatures correspond with low RH and aerosol water concentrations, but cooler temperatures exist throughout the range of RH and aerosol water concentrations observed. The highest LWC values were predicted when temperatures fell between freezing and -10°C.
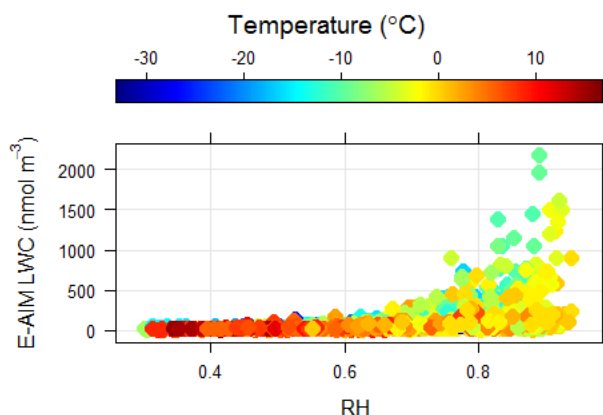
Figure 6.11: E-AIM predicted aerosol liquid water concentration (LWC, nmol) is compared with the measured relative humidity and temperature in °C (color bar).

To understand the differences in how pH can be calculated, model output from both E-AIM and ISO are explored in this section. In E-AIM, the model predicts the mole fraction, $xH^+_{(aq)}$, and activity coefficient as a mole fraction, $fH^+_{(aq)}$, for the aqueous hydrogen ion, $H^+_{(aq)}$. The pH can then be calculated using Equation 6.1 (Hennigan et al., 2015; Squizzato et al., 2013). In ISO, the amount of predicted H^+, in moles, and the predicted mass of liquid water, in liters, was used to calculate the molar concentration of $H^+_{(aq)}$. These values were then used to solve for pH using Equation 6.2.

$$pH = -\log(xH^+_{(aq)} \times fH^+_{(aq)})$$
Equation 6.1

$$pH = -\log([H^+_{(aq)}])$$
Equation 6.2

The comparison of pH between models (Figure 6.12) shows a tendency for ISO to usually predict more acidic aerosol than E-AIM. ISO does also predict some high outliers (pH > 8) compared to the E-AIM predications. Although low LWC values are found at all pH values, the lowest pH values correspond only with low LWC, represented by the cool colors in Figure 6.10. Low pH values are predicted since low RH can limit the amount of aerosol water present in the aerosol, causing the pH to decrease as the amount of $H^+_{(aq)}$ becomes more concentrated.
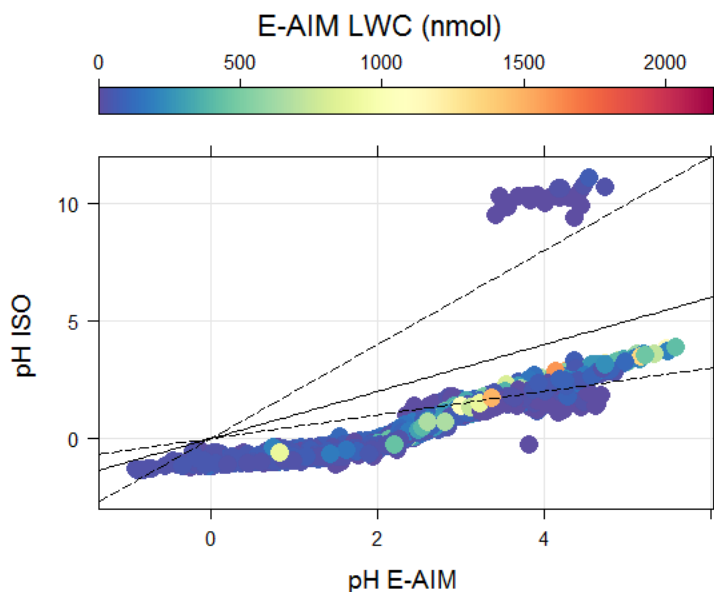
Figure 6.12: Comparison of pH calculated from the ISORROPIA (ISO) and E-AIM models colored by aerosol liquid water content (LWC, nmol) predicted by E-AIM. The 1:1 line (solid black line) and the 1:2 and 1:0.5 lines (black dashed lines) are also shown.

The modeled differences in pH from E-AIM and ISO can arise from the difference in calculations of pH, as shown in Equations 6.1 and 6.2. E-AIM takes into account the water activity and mole fraction of H^+ in the aerosol when calculating pH. ISO only uses the molar concentration of H^+ in the aerosol, which neglects the effects of ionic strength and ionic charge. Equation 6.1, which is used in E-AIM, is more accurate at predicting pH at low aerosol water concentrations when the aerosol has higher ionic strength. This difference in predicting pH can be seen in Figure 6.12, especially when LWC is near zero. The extremely high pH predicted by

ISO are also correlated with very low LWC. This suggests that the assumptions used in the ISO model can generate unrealistic pH values. Also important to note is that the predicted pH could be biased low when the cations Na^+, K^+, Mg^{2+} and Ca^{2+} are excluded from the model input, which is the case for the ISO model (Guo et al., 2015) and the E-AIM analysis presented here. E-AIM was used to investigate three different ways to run the model to calculate pH. The pH values presented in Figure 6.13 (x-axis) have been determined by running the model in the forward mode with total N(-III) and N(V) measurement inputs. Other studies have recommended calculating pH by running the model in the reverse mode or in the forward with just aerosol inputs (Guo et al., 2015; Weber et al., 2016). The forward model is much less sensitive to measurement errors than the reverse model (Hennigan et al., 2015), suggesting it is a more robust method to calculate pH. Figure 6.14 shows very high pH values predicted from the reverse mode and forward mode with no gas input.
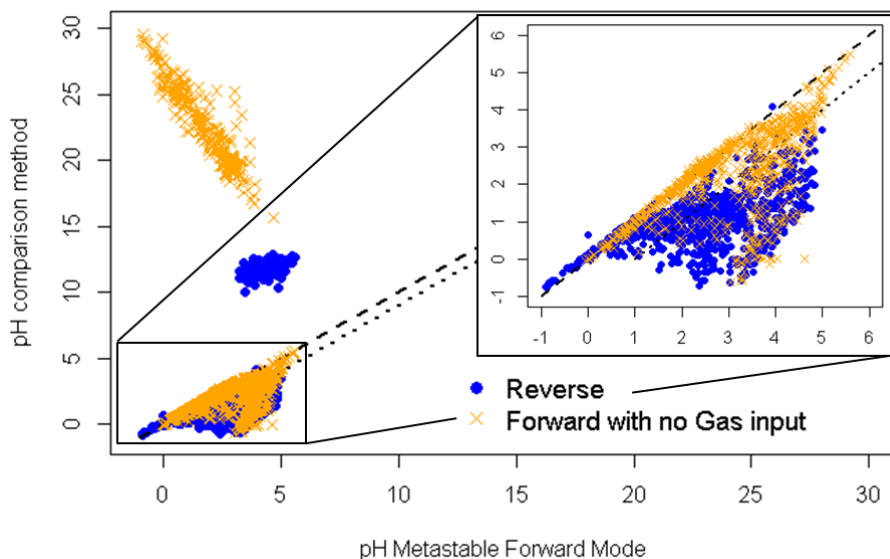
Figure 6.13: Predicted pH using E-AIM from three different model configurations. The pH range of -1 to 6 was enlarged and inset in the top right of the plot. The forward mode with metastable conditions with total gas and aerosol inputs (x-axis) are compared with the model run in reverse mode (blue) and in the forward mode with no gas input (orange). A 1:1 line is represented by the dashed line and the dotted line is a 1:1 line shifted down one pH unit towards the x-axis.

Relating this back to the original model comparison presented in Figure 6.1, it is unsurprising that the disparity in model predicted HNO_3 and NO_3^- correlates with predicted pH (Figure 6.14). The over predicted HNO_3 and underpredicted NO_3^- concentrations predicted by E-AIM correlated with lower pH.
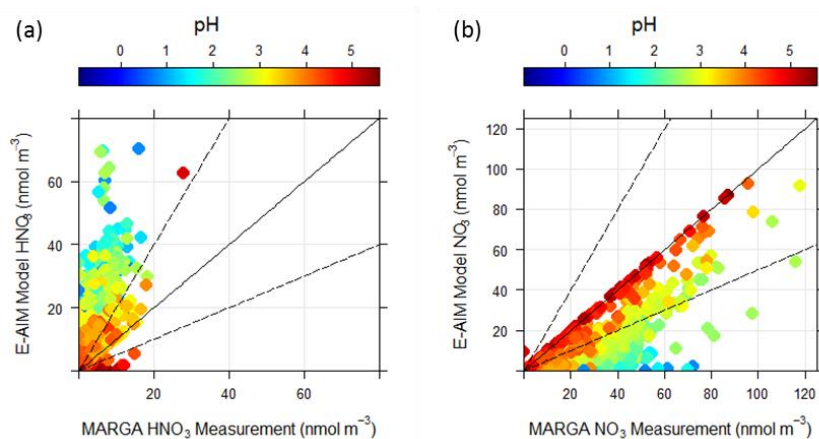
Figure 6.14: Comparison of MARGA measurements and E-AIM model output of (a) NH_3, (b) HNO_3, (c) NH_4^+ and (d) NO_3^- using the forward mode of the E-AIM Model II. Points are colored by pH. The 1:1 line (solid black line) and the 1:2 and 1:0.5 lines (black dashed lines) are also shown.

6.4 Conclusions

Hourly gas and aerosol measurements collected during the BAQS field study which was conducted during the winter in North Dakota, a location that experiences cold temperatures and elevated aerosol concentrations, was used to assess two thermodynamic models. This unique data set allowed for a detailed comparison of the temperature sensitivity of model predicted gas and aerosol partitioning of inorganic species. Both E-AIM and ISO over predicted HNO_3 and under predicted NO_3^- for a significant fraction of the hourly MARGA measurements. E-AIM showed a strong correlation between model bias and decreasing temperature. This bias could stem from the longer times for aerosol-gas partitioning to reach equilibrium at colder temperatures. The model bias was also weakly correlated with RH, which is corroborated with

the weak correlation between ambient temperature and RH measured during BAQS.   Model

predicted pH is explored and results suggest that running the model in a metastable forward

mode with inputs of total gas and aerosol species gives the most realistic pH values. Model

predictive bias was also found to correlate strongly with decreasing pH.

7.0 CONCLUSIONS AND FUTURE WORK

7.1 Summary and Conclusions

The recent rapid expansion of unconventional oil and gas drilling in the United States has brought up concerns on how these activities are impacting local and regional air quality around the drilling locations. Previous field studies have focused on emissions of greenhouse gases such as methane and compounds hazardous to human health such as benzene and other volatile organic compounds. Limited research has been done concerning how oil and gas activities impact $PM_{2.5}$ and haze. In this work, measurements and modeling analysis from a comprehensive air quality field study in the Bakken formation region during a period of rapid growth in oil production by unconventional techniques linked elevated $PM_{2.5}$ concentrations with oil and gas development. Measurements were collected in National Parks and other federally protected lands in remote locations with minimal influence from urban emissions.

An initial study in the Bakken region included multiple measurements of inorganic aerosol, total $PM_{2.5}$, aerosol scattering and meteorology at five sampling sites across the region. Regionally elevated concentrations of $PM_{2.5}$ were observed across all sites, with ammonium nitrate being the dominant species measured. The highest concentrations observed were at Fort Union National Historic Site, a sampling site centrally located within the densest area of oil wells. The lowest concentrations were observed at Medicine Lake National Wildlife Refuge, which is located to the west and often upwind of the main area of oil drilling. High aerosol scattering measurements were also observed, reinforcing the anthropogenic impacts on haze in these remote federal lands. BC measurements above background levels correlated with NO_x, suggesting influence from combustion processes, including both stationary and mobile diesel

engines and flaring. Especially during periods of elevated $PM_{2.5}$ concentrations, inorganic ammonium nitrate and ammonium sulfate dominated the total PM mass. These observations motivated a second, more comprehensive study including measurements of organic aerosol, VOCs, and higher time resolved measurements of inorganic $PM_{2.5}$ species.

Much lower average $PM_{2.5}$ concentrations were observed during BAQS II, consistent with differences in meteorological conditions experienced during each study period. When concentrations were lower during BAQS II, less snow cover, reduced atmospheric stability and lower solar illumination were measured. Additionally, local wind direction at THRO-N was predominantly from the northwest during BAQS II and from both the northwest and southeast during BAQS I. Even though the drilling of new oil wells and oil production increased from BAQS I to BAQS II, suggesting a potential increase in emissions, the different meteorology and transport patterns contributed to lower average $PM_{2.5}$ concentrations.

During both studies, higher concentrations of $PM_{2.5}$ were associated with recirculating or stagnant air masses as determined with HYSPLIT backwards trajectory analysis. Use of a VOC chemical clock (based on the ratios of alkyl nitrate to parent alkane concentration ratios) indicated that the highest $PM_{2.5}$ concentrations were associated with recent emissions, pointing to the important contributions of local and regional emissions to haze formation. Further reinforcing the contribution of oil and gas development to elevated $PM_{2.5}$ concentrations, a well-documented oil and gas tracer, the i-/n-pentane ratio, indicated that air quality in the locations sampled were influenced more by oil and gas emissions than by urban emissions.

Observations of organic aerosol during BAQS II at THRO-N were also used to associate the increased $PM_{2.5}$ concentrations observed in the Bakken region with the regional oil and gas drilling activities. PMF analysis of the organic aerosol identified a two factor solution. An HOA

137

factor, associated with fresh emissions, correlated with NO_x and BC. These primary emissions likely originate from combustion processes associated with activities surrounding the oil and gas operations. An LVOOA factor correlated with inorganic $PM_{2.5}$ species, which is also enhanced by the regional oil and gas drilling activities as described above. Using the IMPROVE reconstructed aerosol scattering equation, organic aerosol was calculated to have a significant contribution to the formation of haze, though inorganic species dominate at the highest $PM_{2.5}$ concentrations.

As the future of unconventional oil and gas extraction is uncertain and dependent on economics and other complex factors, it is insightful to investigate how $PM_{2.5}$ concentrations may respond if future emissions increase. Increases in local NO_x and available NH_3, along with favorable thermodynamic conditions, support the formation of ammonium nitrate aerosol. Using the available meteorological data, gas and aerosol measurements, and thermodynamic modeling results, it was observed that ammonium nitrate formation was highly favorable during the majority of the study period. The formation of additional $PM_{2.5}$ was found to generally be more sensitive to the availability of N(-III) during colder temperatures with increasing sensitivity to the availability of N(V) during warmer temperatures. This data set was also used to investigate thermodynamic aerosol model performance for ammonium nitrate formation in this cold environment. Both E-AIM and ISORROPIA models showed a strong correlation between model bias and decreasing temperature. Decreased model performance was also correlated with decreasing predicted pH.

7.2 Recommendations for Future Work

Here we revisit the initial study objectives proposed in the Introduction and discuss the limitations associated with this work and potential avenues for further research within the

Bakken and in other regions of O&G development. The observations and analysis presented in this work significantly contribute to understanding how unconventional O&G techniques contribute to PM$_{2.5}$, particularly within the Bakken formation region.

- The first objective was to determine if elevated levels of air pollution or increased haze formation were occurring in the Bakken formation region. This was accomplished using a variety of air quality instrumentation over two winter time periods. However, the large differences in total PM$_{2.5}$ concentrations observed indicate the importance making similar measurements over a longer measurement period to include how concentrations change across a variety of meteorological conditions. Previous studies in other O&G basins also show large annual variations in numerous pollutants, including inorganic PM$_{2.5}$ species in the Upper Green River basin (Li et al., 2014b) and ozone in the Uinta basin (e.g. Edwards et al., 2013) which were correlated with year to year differences in meteorology. Long term monitoring networks, such as IMPROVE, provide information on annual differences in some species, but measurements are limited. More intensive field studies such as BAQS provide the detailed information needed to understand local transport, sources of pollutants and diurnal variability.

- Determining the impacts of O&G activities on elevated pollutants, the second objective, was thoroughly explored in the Bakken formation region during BAQS. This objective was completed using a variety of measurements and different analysis techniques, which all suggested influence of O&G emissions on increases in both inorganic and organic aerosol. Additional analysis techniques such as source apportionment could help identify the relative importance of specific emission sources associated with the different activities involved in O&G operations. For example, the VOC measurements collected at

THRO-N were used to do a PMF analysis, but limited measurements prevented any definitive conclusions. A PMF analysis was also performed using VOCs and other measurements collected at RMNP, a site impacted by anthropogenic activities including O&G drilling operations when upslope winds are observed. Limited measurements during upslope events were collected during the study period, which again prevented completing a robust analysis. Both PMF analyses are described in Appendix E. PMF analyses using VOCs have been effective in previous field studies to identify specific sources within O&G regions (Field et al., 2015; Rutter et al., 2015).

- The third objective of this work was to investigate ammonium nitrate formation and the importance to regional haze formation. This was accomplished by measuring hourly concentrations of HNO_3, NH_3, NO_3^-, NH_4^+, and meteorological variables and using thermodynamic aerosol modeling. By using the model, insight was gained on how meteorological conditions change the favorability of ammonium nitrate formation, the sensitivity of $PM_{2.5}$ formation to the addition of N(-III) and N(V) species, and model bias over a range of conditions. On average, it is predicted that $PM_{2.5}$ will increase by 1.99 ± 1.64 or 0.17 ± 0.32 µg m^{-3} with a 1 µg m^{-3} increase in N(-III) or N(V), respectively. The causes of the increased model bias at lower temperatures were not resolved and is an interesting issue for future investigation. Additional thermodynamic modeling analysis using high time resolution data sets across a range of temperatures should be completed to fully understand the model performance in a variety of conditions.

    o The measurements and modeling results also highlight the consistent availability of ammonia during the BAQS study. This contrasts a previous study in the Jonah-Pinedale region of Wyoming, a rural O&G production area similar to the

Bakken region, where the complete depletion of ammonia during the winter was observed (Li et al., 2014b). The major sources of ammonia in the Bakken region are unknown, but possible important sources include the transport of ammonia from intensive agricultural operations in the midwestern U.S. or from livestock and crop production in southern Manitoba and Saskatchewan in Canada, fertilizer plants in North Dakota, the operation of selective catalytic reduction systems at low temperatures, or regional winter fertilizer applications. Further work is needed to elucidate the sources of the excess ammonia observed in this region.

- Understanding organic aerosol sources and composition and their role in total $PM_{2.5}$ concentrations was the fourth objective. Measurements from the AMS gave a detailed look at the organic aerosol during the second study. However, this relatively short analysis period is limited in fully understanding the characterization of the organic aerosol in the Bakken region. OA formation could also be important during warmer times of the year when biogenic sources of OA are more important. Using techniques to determine aerosol aging using AMS measurements, including OM/OC, the van Krevelen diagram, and the f44 versus f43 plot, the potential for secondary OA formation was found. Previous work investigating the formation of SOA in other O&G regions is limited. In the Uinta basin, the formation of organic nitrates was found to be important (Lee et al., 2014). Future measurements of VOCs, alkyl nitrates and oxidants including ozone are needed to investigate the possibility of organic nitrate formation in the Bakken or other regions.

8.0 REFERENCES

Ahmadov, R., McKeen, S., Trainer, M., Banta, R., Brewer, A., Brown, S., Edwards, P. M., de Gouw, J. a., Frost, G. J., Gilman, J., Helmig, D., Johnson, B., Karion, A., Koss, A., Langford, A., Lerner, B., Olson, J., Oltmans, S., Peischl, J., Pétron, G., Pichugina, Y., Roberts, J. M., Ryerson, T., Schnell, R., Senff, C., Sweeney, C., Thompson, C., Veres, P., Warneke, C., Wild, R., Williams, E. J., Yuan, B. and Zamora, R.: Understanding high wintertime ozone pollution events in an oil and natural gas producing region of the western US, Atmos. Chem. Phys., 14(14), 20295–20343, doi:10.5194/acpd-14-20295-2014, 2014.

Aiken, A. C., Decarlo, P. F., Kroll, J. H., Worsnop, D. R. and Huffman, J. A.: O/C and OM/OC Ratios of Primary, Secondary, and Ambient Organic Aerosols with High Resolution Time-of-Flight Aerosol Mass Spectrometry, Environ. Sci. Technol., 42(12), 4478–4485, 2008.

Allen, A. G., Harrison, R. M. and Erisman, J. W.: Field Measurements of the Dissociation of Ammonium Nitrate and Ammonium Chloride Aerosols, Atmos. Environ., 23(7), 1591–1599, 1989.

Ansari, A. S. and Pandis, S. N.: The effect of metastable equilibrium states on the partitioning of nitrate between the gas and aerosol phases, Atmos. Environ., 34(1), 157–168, doi:10.1016/S1352-2310(99)00242-3, 2000.

Armendariz, A.: Emissions from Natural Gas Production in the Barnett Shale Area and Opportunities for Cost-Effective Improvements, Dallas, TX., 2009.

Bae, M. S., Demerjian, K. L. and Schwab, J. J.: Seasonal estimation of organic mass to organic carbon in PM2.5 at rural and urban locations in New York state, Atmos. Environ., 40(39), 7467–7479, doi:10.1016/j.atmosenv.2006.07.008, 2006.

Balasubramanian, S., Koloutsou-vakakis, S., Mcfarland, D. M. and Rood, M. J.: Reconsidering emissions of ammonia from chemical fertilizer usage in Midwest USA, J. Geophys. Res. Atmos., 1–15, doi:10.1002/2015JD023219.Received, 2015.

Bar-Ilan, A., Friesen, R., Grant, J., Pollack, A., Henderer, D., Pring, D., Sgamma, K. and Moore, T.: A Comprehensive Oil and Gas Emissions Inventory for the Denver-Julesburg Basin in Colorado, Novato, CA., 2008.

Bassett, M. E. and Seinfeld, J. H.: Atmospheric equilibrium model of sulfate and nitrate aerosols, Atmos. Environ., 17(11), 2237–2252, doi:10.1016/0004-6981(84)90147-1, 1983.

Berden, G., Peeters, R. and Miejer, G.: Cavity Ring-Down Spectroscopy: Experimental Schemes and Applications, Int. Rev. Phys. Chem., 19(4), 565–607, 2000.

Bertman, S. B., Roberts, J. M., Parrish, D. D., Buhr, M. P., Goldan, P. D., Kuster, W. C., Fehsenfeld, F. C., Montzka, S. A. and Westberg, H.: Evolution of alkyl nitrates with air mass age, J. Geophys. Res., 100(D11), 22805, doi:10.1029/95JD02030, 1995.

Blake, U.: The Unconventional Oil and Gas Process, and an Introduction to Exposure Pathways, Elsevier Inc., 2016.

von Bobrutzki, K., Braban, C. F., Famulari, D., Jones, S. K., Blackall, T., Smith, T. E. L., Blom, M., Coe, H., Gallagher, M., Ghalaieny, M., McGillen, M. R., Percival, C. J., Whitehead, J. D., Ellis, R., Murphy, J., Mohacsi, A., Pogany, A., Junninen, H., Rantanen, S., Sutton, M. A. and Nemitz, E.: Field inter-comparison of eleven atmospheric ammonia measurement techniques, Atmos. Meas. Tech., 3, 91–112, doi:10.5194/amt-3-91-2010, 2010.

Brock, C. A., Wagner, N. L., Anderson, B. E., Attwood, A. R., Beyersdorf, A., Campuzano-Jost, P., Carlton, A. G., Day, D. A., Diskin, G. S., Gordon, T. D., Jimenez, J. L., Lack, D. A., Liao, J., Markovic, M. Z., Middlebrook, A. M., Ng, N. L., Perring, A. E., Richardson, M. S., Schwarz, J. P., Washenfelder, R. A., Welti, A., Xu, L., Ziemba, L. D. and Murphy, D. M.: Aerosol optical properties in the southeastern United States in summer - Part 1: Hygroscopic growth, Atmos. Chem. Phys., 16(8), 4987–5007, doi:10.5194/acp-16-4987-2016, 2016.

Brown, D. R., Lewis, C. and Weinberger, B. I.: Human exposure to unconventional natural gas development: A public health demonstration of periodic high exposure to chemical mixtures in ambient air, J. Environ. Sci. Heal. Part A, 50(5), 460–472, doi:10.1080/10934529.2015.992663, 2015.

Brown, S. G., Lee, T., Norris, G. a., Roberts, P. T., Collett, J. L., Paatero, P. and Worsnop, D. R.: Receptor modeling of near-roadway aerosol mass spectrometer data in Las Vegas, Nevada, with EPA PMF, Atmos. Chem. Phys., 12(1), 309–325, doi:10.5194/acp-12-309-2012, 2012.

Brown, S. G., Lee, T., Roberts, P. T. and Collett Jr., J. L.: Variations in the OM/OC ratio of urban organic aerosol next to a major roadway, J. Air Waste Manage. Assoc., 63(12), 1422–1433, doi:10.1080/10962247.2013.826602, 2013a.

Brown, S. S., Thornton, J. a., Keene, W. C., Pszenny, A. a. P., Sive, B. C., Dubé, W. P., Wagner, N. L., Young, C. J., Riedel, T. P., Roberts, J. M., VandenBoer, T. C., Bahreini, R., Öztürk, F., Middlebrook, A. M., Kim, S., Hübler, G. and Wolfe, D. E.: Nitrogen, Aerosol Composition, and Halogens on a Tall Tower (NACHTT): Overview of a wintertime air chemistry field study in the front range urban corridor of Colorado, J. Geophys. Res. Atmos., 118(14), 8067–8085, doi:10.1002/jgrd.50537, 2013b.

CAMx: Comprehensive Air Quality Model with Extensions, Ramboll Env. [online] Available from: http://www.camx.com/ (Accessed 27 April 2017), 2016.

Canagaratna, M. R., Jayne, J. T., Jimenez, J. L., Allan, J. D., Alfarra, M. R., Zhang, Q., Onasch, T. B., Drewnick, F., Coe, H., Middlebrook, A., Delia, A., Williams, L. R., Trimborn, A. M., Northway, M. J., Decarlo, P. F., Kolb, C. E., Davidovits, P. and Worsnop, D. R.: Chemical and Microphysical Characteriztion of Ambient Aerosol with the Aerodyne Aerosol Mass Spectrometer, Mass Spectrom. Rev., 26, 185–222, doi:10.1002/mas, 2007.

Carew, R.: Ammonia emissions from livestock industries in Canada: Feasibility of abatement strategies, Environ. Pollut., 158(8), 2618–2626, doi:10.1016/j.envpol.2010.05.004, 2010.

Carter, W. P. L. and Seinfeld, J. H.: Winter ozone formation and VOC incremental reactivities in the Upper Green River Basin of Wyoming, Atmos. Environ., 50(x), 255–266, doi:10.1016/j.atmosenv.2011.12.025, 2012.

Chimere: A multi-scale chemistry-transport model for atmospheric composition analysis and forecast, Lab. Dyn. Meteorol. [online] Available from: http://www.lmd.polytechnique.fr/chimere/ (Accessed 27 April 2017), 2017.

Choi, J. and Roberts, D. C.: Impacts of Air Pollution on Productivity Growth in the Air and Truck Transportation Industries in the US: an Application of the Data Envelopment Analysis Malmquist Environmental Productivity Index, Open J. Soc. Sci., 3(February), 120–129, 2015.

Chow, J. C., Watson, J. G., Chen, L.-W. A., Chang, M. C. O., Robinson, N. F., Trimble, D. and Kohl, S.: The IMPROVE_A Temperature Protocol for Thermal/Optical Carbon Analysis: Maintaining Consistency with a Long-Term Database, J. Air Waste Manage. Assoc., 57(9), 1014–1023, doi:10.3155/1047-3289.57.9.1014, 2007.

Clegg, S. L., Brimblecombe, P. and Wexler, A. S.: Thermodynamic Model of the System H^+ - NH_4^+ - Na^+ - SO_4^{2-} - NO_3^- - Cl^- - H_2O at 298.15 K, J. Phys. Chem. A, 102, 2155–2171, 1998a.

Clegg, S. L., Brimblecombe, P. and Wexler, A. S.: Thermodynamic Model of the System H^+ - NH_4^+ - SO_4^{2-} - NO_3^- - H_2O at Tropospheric Temperatures, J. Phys. Chem. A, 102(12), 2137–2154, doi:10.1021/jp973042r, 1998b.

Clegg, S. L., Brimblecombe, P. and Wexler, A. S.: Extended AIM Aerosol Thermodynamics Model, [online] Available from: http://www.aim.env.uea.ac.uk/aim/aim.php (Accessed 27 April 2017), 2016.

CMAQ: Community MultiScale Air Quality Modeling System, Univ. North Carolina [online] Available from: https://www.cmascenter.org/cmaq/ (Accessed 27 April 2017), 2017.

Cooper, J., Stamford, L. and Azapagic, A.: Shale Gas: A Review of the Economic, Environmental, and Social Sustainability, Energy Technol., 1–22, doi:10.1002/ente.201500464, 2016.

Cooper, O. R., Gao, R.-S., Tarasick, D., Leblanc, T. and Sweeney, C.: Long-term ozone trends at rural ozone monitoring sites across the United States, 1990-2010, J. Geophys. Res. Atmos., 117(D22), n/a-n/a, doi:10.1029/2012JD018261, 2012.

COSMO-ART: Consortium for Small-scale Modeling, Karlsruhe Inst. Technol. [online] Available from: http://www.imk-tro.kit.edu/3509.php (Accessed 27 April 2017), 2014.

Day, D. E., Chen, X., Gebhart, K. A., Carrico, C. M., Schwandner, F. M., Benedict, K. B., Schichtel, B. A. and Collett, J. L.: Spatial and temporal variability of ammonia and other inorganic aerosol species, Atmos. Environ., 61, 490–498, doi:10.1016/j.atmosenv.2012.06.045, 2012.

Decarlo, P. F., Kimmel, J. R., Trimborn, A., Northway, M. J., Jayne, J. T., Aiken, A. C., Gonin, M., Fuhrer, K., Horvath, T., Docherty, K. S., Worsnop, D. R. and Jimenez, J. L.: Field-Deployable, High-Resolution, Time-of-Flight Aerosol Mass Spectrometer, Anal. Chem., 78(24), 8281–8289, doi:8410.1029/2001JD001213, 2006.

Dickerson, R. R.: Measurements of Reactive Nitrogen Compounds in the Free Troposphere, Atmos. Environ., 18, 2585–2593, 1984.

Dingle, J. H., Vu, K., Bahreini, R., Apel, E. C., Campos, T. L., Flocke, F., Fried, A., Herndon, S., Hills, A. J., Hornbrook, R. S., Huey, G., Kaser, L., Montzka, D. D., Nowak, J. B., Reeves, M., Richter, D., Roscioli, J. R., Shertz, S., Stell, M., Tanner, D., Tyndall, G., Walega, J., Weibring, P. and Weinheimer, A.: Aerosol optical extinction during the front range air pollution and photochemistry Éxperiment (FRAPPÉ) 2014 summertime field campaign, Colorado, USA, Atmos. Chem. Phys., 16(17), 11207–11217, doi:10.5194/acp-16-11207-2016, 2016.

Drewnick, F., Hings, S. S., DeCarlo, P., Jayne, J. T., Gonin, M., Fuhrer, K., Weimer, S., Jimenez, J. L., Demerjian, K. L., Borrmann, S. and Worsnop, D. R.: A new time-of-flight aerosol mass spectrometer (TOF-AMS) - Instrument description and first field deployment, Aerosol Sci. Technol., 39(7), 637–658, doi:10.1080/02786820500182040, 2005.

Drinovec, L., Močnik, G., Zotter, P., Prévôt, A. S. H., Ruckstuhl, C., Coz, E., Rupakheti, M., Sciare, J., Müller, T., Wiedensohler, A. and Hansen, A. D. A.: The "dual-spot" Aethalometer: an improved measurement of aerosol black carbon with real-time loading compensation, Atmos. Meas. Tech., 8(5), 1965–1979, doi:10.5194/amt-8-1965-2015, 2015.

Dunlea, E. J., Herndon, S. C., Nelson, D. D., Volkamer, R. M., San Martini, F., Sheehy, P. M., Zahniser, M. S., Shorter, J. H., Wormhoudt, J. C., Lamb, B. K., Allwine, E. J., Gaffney, J. S., Marley, N. a., Grutter, M., Marquez, C., Blanco, S., Cardenas, B., Retama, a., Ramos Villegas, C. R., Kolb, C. E., Molina, L. T. and Molina, M. J.: Evaluation of nitrogen dioxide chemiluminescence monitors in a polluted urban environment, Atmos. Chem. Phys., 7(2), 2691–2704, doi:10.5194/acpd-7-569-2007, 2007.

Dusek, U., Hitzenberger, R., Kasper-giebl, A., Kistler, M., Meijer, H. A. J., Szidat, S., Wacker, L., Holzinger, R. and Röckmann, T.: Sources and formation mechanisms of carbonaceous aerosol at a regional background site in the Netherlands: Insights from a year-long radiocarbon study, Atmos. Chem. Phys., 17(September), 3233–3251, doi:10.5194/acp-2016-624, 2017.

Edwards, P. M., Young, C. J., Aikin, K., deGouw, J. a., Dubé, W. P., Geiger, F., Gilman, J. B., Helmig, D., Holloway, J. S., Kercher, J., Lerner, B., Martin, R., McLaren, R., Parrish, D. D., Peischl, J., Roberts, J. M., Ryerson, T. B., Thornton, J., Warneke, C., Williams, E. J. and Brown, S. S.: Ozone photochemistry in an oil and natural gas extraction region during winter: simulations of a snow-free season in the Uintah Basin, Utah, Atmos. Chem. Phys. Discuss., 13(3), 7503–7552, doi:10.5194/acpd-13-7503-2013, 2013.

Edwards, P. M., Brown, S. S., Roberts, J. M., Ahmadov, R., Banta, R. M., deGouw, J. a., Dubé, W. P., Field, R. a., Flynn, J. H., Gilman, J. B., Graus, M., Helmig, D., Koss, A., Langford, A. O., Lefer, B. L., Lerner, B. M., Li, R., Li, S.-M., McKeen, S. a., Murphy, S. M., Parrish, D. D., Senff, C. J., Soltis, J., Stutz, J., Sweeney, C., Thompson, C. R., Trainer, M. K., Tsai, C., Veres,

P. R., Washenfelder, R. a., Warneke, C., Wild, R. J., Young, C. J., Yuan, B. and Zamora, R.: High winter ozone pollution from carbonyl photolysis in an oil and gas basin, Nature, 514(7522), 351–354, doi:10.1038/nature13767, 2014.

Estrada, J. M. and Bhamidimarri, R.: A review of the issues and treatment options for wastewater from shale gas extraction by hydraulic fracturing, Fuel, 182, 292–303, doi:10.1016/j.fuel.2016.05.051, 2016.

Fang, G. C., Wu, Y. S., Chou, T. Y. and Lee, C. Z.: Organic carbon and elemental carbon in Asia: A review from 1996 to 2006, J. Hazard. Mater., 150(2), 231–237, doi:10.1016/j.jhazmat.2007.09.036, 2008.

Fawole, O. G., Cai, X. M. and Mackenzie, A. R.: Gas flaring and resultant air pollution: A review focusing on black carbon, Environ. Pollut., 216, 182–197, doi:10.1016/j.envpol.2016.05.075, 2016.

Fehsenfeld, F. C., Dickerson, R. R., Hobler, G., Luke, W. T., Nunnermacker, L. J., Roberts, J. M., Curran, C. M., Eubank, C. S., Fahey, D. W., Mindplay, P. C. and Pickering, K. E.: A Ground-Based Intercomparison of NO, NOx, and NOy Measurement Techniques, J. Geophys. Res., 92(7), 710–722, doi:10.1029/JD092iD12p14710, 1987.

Field, R. A., Soltis, J., McCarthy, M. C., Murphy, S. and Montague, D. C.: Influence of oil and gas field operations on spatial and temporal distributions of atmospheric non-methane hydrocarbons and their effect on ozone formation in winter, Atmos. Chem. Phys., 15(6), 3527–3542, doi:10.5194/acp-15-3527-2015, 2015.

Frac Focus Chemical Disclosure Registry: Chemical Use In Hydraulic Fracturing, [online] Available from: http://fracfocus.org/water-protection/drilling-usage (Accessed 9 May 2017), 2017.

Gaswirth, S. B. and Marra, K. R.: U.S. Geological Survey 2013 assessment of undiscovered resources in the Bakken and Three Forks Formations of the U.S. Williston Basin Province, Am. Assoc. Pet. Geol. Bull., 99(4), 639–660, 2015.

GEOS-Chem: Goddard Earth Observing System Model - Chemistry, Harvard Univ. Dalhousie Univ. [online] Available from: http://acmg.seas.harvard.edu/geos/ (Accessed 27 April 2017), 2017.

Gerboles, M., Detimmerman, F., Amantini, L. and De Saeger, E.: Validation of Radiello Diffusive Sampler for Monitoring NO2 in Ambient Air, Italy., 2000.

Gilliland, A. B., Wyat Appel, K., Pinder, R. W. and Dennis, R. L.: Seasonal NH3 emissions for the continental united states: Inverse model estimation and evaluation, Atmos. Environ., 40(26), 4986–4998, doi:10.1016/j.atmosenv.2005.12.066, 2006.

Gilman, J. B., Lerner, B. M., Kuster, W. C. and de Gouw, J. A.: Source signature of volatile organic compounds from oil and natural gas operations in northeastern Colorado., Environ. Sci. Technol., 47(3), 1297–305, doi:10.1021/es304119a, 2013.

Giwa, S. O., Adama, O. O. and Akinyemi, O. O.: Baseline black carbon emissions for gas flaring in the Niger Delta region of Nigeria, J. Nat. Gas Sci. Eng., 20, 373–379, doi:10.1016/j.jngse.2014.07.026, 2014.

Grant, J., Parikh, R., Bar-Ilan, A. and Morris, R.: Development of Baseline 2011 and Future Year 2015 Emissions from Oil and Gas Activity in the Great Plains Basin, Novato, CA., 2014a.

Grant, J., Parikh, R., Bar-Ilan, A. and Morris, R.: Development of Baseline 2011 and Future Year 2015 Emissions from Oil and Gas Activity in the Williston Basin, Novato, CA. [online] Available from: http://www.wrapair2.org/pdf/2011_2015_Williston_Basin_14Aug2014.pdf, 2014b.

Green, M. C., Chow, J. C., Watson, J. G., Dick, K. and Inouye, D.: Effects of Snow Cover and Atmospheric Stability on Winter PM $_{2.5}$ Concentrations in Western U.S. Valleys, J. Appl. Meteorol. Climatol., 54(6), 1191–1201, doi:10.1175/JAMC-D-14-0191.1, 2015.

Guo, H., Xu, L., Bougiatioti, A., Cerully, K. M., Capps, S. L., Hite, J. R., Carlton, A. G., Lee, S. H., Bergin, M. H., Ng, N. L., Nenes, A. and Weber, R. J.: Fine-particle water and pH in the southeastern United States, Atmos. Chem. Phys., 15(9), 5211–5228, doi:10.5194/acp-15-5211-2015, 2015.

Hand, J. L.: Spatial and Seasonal Patterns and Temporal Variability of Haze and its Constituents in the United States, Fort Collins, CO., 2011.

Hand, J. L., Gebhart, K. A., Schichtel, B. A. and Malm, W. C.: Increasing trends in wintertime particulate sulfate and nitrate ion concentrations in the Great Plains of the United States (2000–2010), Atmos. Environ., 55, 107–110, doi:10.1016/j.atmosenv.2012.03.050, 2012.

Hand, J. L., Schichtel, B. A., Malm, W. C., Copeland, S., Molenar, J. V., Frank, N. and Pitchford, M.: Widespread reductions in haze across the United States from the early 1990s through 2011, Atmos. Environ., 94, 671–679, doi:10.1016/j.atmosenv.2014.05.062, 2014.

Hansen, A. D. A., Rosen, H. and Novakov, T.: The aethalometer — An instrument for the real-time measurement of optical absorption by aerosol particles, Sci. Total Environ., 36, 191–196, doi:10.1016/0048-9697(84)90265-1, 1984.

Heald, C. L., Kroll, J. H., Jimenez, J. L., Docherty, K. S., Decarlo, P. F., Aiken, a. C., Chen, Q., Martin, S. T., Farmer, D. K. and Artaxo, P.: A simplified description of the evolution of organic aerosol composition in the atmosphere, Geophys. Res. Lett., 37(8), doi:10.1029/2010GL042737, 2010.

Heintzenberg, J., Wiedensohler, A., Tuch, T. M., Covert, D. S., Sheridan, P., Ogren, J. A., Gras, J., Nessler, R., Kleefeld, C., Kalivitis, N., Aaltonen, V., Wilhelm, R. T. and Havlicek, M.: Intercomparisons and aerosol calibrations of 12 commercial integrating nephelometers of three manufacturers, J. Atmos. Ocean. Technol., 23(7), 902–914, doi:10.1175/JTECH1892.1, 2006.

Helmig, D., Thompson, C. R., Evans, J., Boylan, P., Hueber, J. and Park, J. H.: Highly elevated atmospheric levels of volatile organic compounds in the uintah basin, Utah, Environ. Sci.

Technol., 48(9), 4707–4715, doi:10.1021/es405046r, 2014.

Hennigan, C. J., Izumi, J., Sullivan, A. P., Weber, R. J. and Nenes, A.: A critical evaluation of proxy methods used to estimate the acidity of atmospheric particles, Atmos. Chem. Phys., 15(5), 2775–2790, doi:10.5194/acp-15-2775-2015, 2015.

Hoyle, C. R., Boy, M., Donahue, N. M., Fry, J. L., Glasius, M., Guenther, A., Hallar, A. G., Huff Hartz, K., Petters, M. D., Petäjä, T., Rosenoern, T. and Sullivan, A. P.: A review of the anthropogenic influence on biogenic secondary organic aerosol, Atmos. Chem. Phys., 11(1), 321–343, doi:10.5194/acp-11-321-2011, 2011.

ISORROPIA: aerosol thermodynamic model & adjoint, Georg. Inst. Technol. [online] Available from: http://isorropia.eas.gatech.edu/index.php?title=Main_Page (Accessed 27 April 2017), 2013.

Jayne, J. T., Leard, D. C., Zhang, X., Davidovits, P., Smith, K. A., Kolb, C. E. and Worsnop, D. R.: Development of an Aerosol Mass Spectrometer for Size and Composition Analysis of Submicron Particles, Aerosol Sci. Technol., 33(1–2), 49–70, doi:10.1080/027868200410840, 2000.

Jimenez, J. L.: PMF-AMS Analysis Guide, Jimenez Res. Gr. Wiki [online] Available from: http://cires1.colorado.edu/jimenez-group/wiki/index.php/PMF-AMS_Analysis_Guide (Accessed 13 December 2016), 2016.

Jimenez, J. L., Canagaratna, M. R., Donahue, N. M., Prevot, A. S. H., Zhang, Q., Kroll, J. H., DeCarlo, P. F., Allan, J. D., Coe, H., Ng, N. L., Aiken, A. C., Docherty, K. S., Ulbrich, I. M., Grieshop, A. P., Robinson, A. L., Duplissy, J., Smith, J. D., Wilson, K. R., Lanz, V. A., Hueglin, C., Sun, Y. L., Tian, J., Laaksonen, A., Raatikainen, T., Rautiainen, J., Vaattovaara, P., Ehn, M., Kulmala, M., Tomlinson, J. M., Collins, D. R., Cubison, M. J., Dunlea, E. J., Huffman, J. A., Onasch, T. B., Alfarra, M. R., Williams, P. I., Bower, K., Kondo, Y., Schneider, J., Drewnick, F., Borrmann, S., Weimer, S., Demerjian, K., Salcedo, D., Cottrell, L., Griffin, R., Takami, A., Miyoshi, T., Hatakeyama, S., Shimono, A., Sun, J. Y., Zhang, Y. M., Dzepina, K., Kimmel, J. R., Sueper, D., Jayne, J. T., Herndon, S. C., Trimborn, A. M., Williams, L. R., Wood, E. C., Middlebrook, A. M., Kolb, C. E., Baltensperger, U. and Worsnop, D. R.: Evolution of Organic Aerosols in the Atmosphere, Science (80), 326 (December), 1525–1529, 2009.

Kanakidou, M., Seinfeld, J. H., Pandis, S. N., Barnes, I., Dentener, F. J., Facchini, M. C., Van Dingenen, R., Ervens, B., Nenes, A., Nielsen, C. J., Swietlicki, E., Putaud, J. P., Balkanski, Y., Fuzzi, S., Horth, J., Moortgat, G. K., Winterhalter, R., Myhre, C. E. L., Tsigaridis, K., Vignati, E., Stephanou, E. G. and Wilson, J.: Organic aerosol and global climate modelling: a review, Atmos. Chem. Phys., 5, 1053–1123, doi:10.5194/acp-5-1053-2005, 2005.

Khalek, I. A., Blanks, M. G., Merritt, P. M. and Zielinska, B.: Regulated and unregulated emissions from modern 2010 emissions-compliant heavy-duty on-highway diesel engines, J. Air Waste Manage. Assoc., 65(8), 987–1001, doi:10.1080/10962247.2015.1051606, 2015.

Khan, B., Hays, M. D., Geron, C. and Jetter, J.: Differences in the OC/EC Ratios that Characterize Ambient and Source Aerosols due to Thermal-Optical Analysis, Aerosol Sci.

Technol., 46(2), 127–137, doi:10.1080/02786826.2011.609194, 2012.

Khlystov, A., Wyers, G. P. and Slanina, J.: The steam-jet aerosol collector, Atmos. Environ., 29(17), 2229–2234, doi:1352-2310(95) 00180-8, 1995.

Korfmacher, K., Hawker, J. S. and Winebrake, J.: Transportation Activities Associated with High-Volume Hydraulic Fracturing Operations in the Marcellus Shale Formation, Anal. Environ. Infrastruct. Impacts, (2503), 70–80, 2015.

Lanz, V. A., Alfarra, M. R., Baltensperger, U., Buchmann, B., Hueglin, C. and Prévôt, A. S. H.: Source apportionment of submicron organic aerosols at an urban site by factor analytical modelling of aerosol mass spectra, Atmos. Chem. Phys., 7(6), 1503–1522, doi:10.5194/acp-7-1503-2007, 2007.

Lanz, V. A., Prevot, A. S. H., Alfarra, M. R., Weimer, S., Mohr, C., DeCarlo, P. F., Gianini, M. F. D., Hueglin, C., Schneider, J., Favez, O., D'Anna, B., George, C. and Baltensperger, U.: Characterization of aerosol chemical composition with aerosol mass spectrometry in Central Europe: an overview, Atmos. Chem. Phys., 10, 10453–10471, doi:10.5194/acp-10-10453-2010, 2010.

Lee, L., Wooldridge, P. J., Gilman, J. B., Warneke, C., de Gouw, J. and Cohen, R. C.: Low temperatures enhance organic nitrate formation: evidence from observations in the 2012 Uintah Basin Winter Ozone Study, Atmos. Chem. Phys., 14(22), 12441–12454, doi:10.5194/acp-14-12441-2014, 2014.

Lee, S.-H. and Allen, H. C.: Analytical measurements of atmospheric urban aerosol., Anal. Chem., 84(3), 1196–201, doi:10.1021/ac201338x, 2012.

Lee, T., Yu, X. Y., Ayres, B., Kreidenweis, S. M., Malm, W. C. and Collett, J. L.: Observations of fine and coarse particle nitrate at several rural locations in the United States, Atmos. Environ., 42(11), 2720–2732, doi:10.1016/j.atmosenv.2007.05.016, 2008.

Li, R., Warneke, C., Graus, M., Field, R., Geiger, F., Veres, P. R., Soltis, J., Li, S.-M., Murphy, S. M., Sweeney, C., Pétron, G., Roberts, J. M. and de Gouw, J.: Measurements of hydrogen sulfide (H2S) using PTR-MS: calibration, humidity dependence, inter-comparison and results from field studies in an oil and gas production region, Atmos. Meas. Tech. Discuss., 7(6), 6205–6243, doi:10.5194/amtd-7-6205-2014, 2014a.

Li, Y., Schwandner, F. M., Sewell, H. J., Zivkovich, A., Tigges, M., Raja, S., Holcomb, S., Molenar, J. V., Sherman, L., Archuleta, C., Lee, T. and Collett, J. L.: Observations of ammonia, nitric acid, and fine particles in a rural gas production region, Atmos. Environ., 83(3), 80–89, doi:10.1016/j.atmosenv.2013.10.007, 2014b.

Li, Y., Schichtel, B. A., Walker, J. T., Schwede, D. B., Chen, X., Lehmann, C. M. B., Puchalski, M. A., Gay, D. A. and Collett, J. L.: Increasing importance of deposition of reduced nitrogen in the United States, Proc. Natl. Acad. Sci., 113(21), 5874–5879, doi:10.1073/pnas.1525736113, 2016.

Liggio, J., Li, S.-M., Hayden, K., Taha, Y. M., Stroud, C., Darlington, A., Drollette, B. D., Gordon, M., Lee, P., Liu, P., Leithead, A., Moussa, S. G., Wang, D., O'Brien, J., Mittermeier, R. L., Brook, J. R., Lu, G., Staebler, R. M., Han, Y., Tokarek, T. W., Osthoff, H. D., Makar, P. A., Zhang, J., L. Plata, D. and Gentner, D. R.: Oil sands operations as a large source of secondary organic aerosols, Nature, 534, 91–94, doi:10.1038/nature17646, 2016.

LOTOS-EUROS: Long Term Ozone Simulation (LOTOS) European Operational Smog (EUROS) Model, Organ. Appl. Sci. Res. [online] Available from: http://www.lotos-euros.nl/ (Accessed 27 April 2017), 2017.

Lowenthal, D., Zielinska, B., Samburova, V., Collins, D., Taylor, N. and Kumar, N.: Evaluation of assumptions for estimating chemical light extinction at U.S. national parks, J. Air Waste Manage. Assoc., 65(3), 249–260, doi:10.1080/10962247.2014.986307, 2015.

Lowenthal, D. H. and Kumar, N.: Evaluation of the IMPROVE Equation for estimating aerosol light extinction, J. Air Waste Manage. Assoc., 66(7), 726–737, doi:10.1080/10962247.2016.1178187, 2016.

Lyman, S., Shorthill, H. and Utah State University: Final Report: 2012 Uintah Basin Winter Ozone and Air Quality Study., 2013.

Lyon, D. R.: Methane Emissions from the Natural Gas Supply Chain, Elsevier Inc., 2016.

Makkonen, U., Virkkula, A., Mäntykenttä, J., Hakola, H., Keronen, P., Vakkari, V. and Aalto, P. P.: Semi-continuous gas and inorganic aerosol measurements at a Finnish urban site: comparisons with filters, nitrogen in aerosol and gas phases, and aerosol acidity, Atmos. Chem. Phys., 12(12), 5617–5631, doi:10.5194/acp-12-5617-2012, 2012.

Makkonen, U., Virkkula, A., Hellén, H., Hemmilä, M., Sund, J., Äijälä, M., Ehn, M., Junninen, H., Keronen, P., Petäjä, T., Worsnop, D. R., Kulmala, M. and Hakola, H.: Semi-continuous gas and inorganic aerosol measurements at a boreal forest site: Seasonal and diurnal cycles of NH3, HONO and HNO3, Boreal Environ. Res., 19(September), 311–328, 2014.

Malm, W. C.: Spatial and monthly trends in speciated fine particle concentration in the United States, J. Geophys. Res., 109(D3), doi:10.1029/2003JD003739, 2004.

Malm, W. C., Pitchford, M. L., Scruggs, M., Sisler, J. F., Ames, R., Copeland, S., Gebhart, K. A. and Day, D. E.: IMPROVE III: Spatial and Seasonal Patterns and Temporal Variability of Haze and its Constituents in the United States, Fort Collins, CO., 2000.

Malm, W. C., Schichtel, B. A. and Pitchford, M. L.: Uncertainties in PM2.5 Gravimetric and Speciation Measurements and What We Can Learn from Them, J. Air Waste Manage. Assoc., 61(11), 1131–1149, doi:10.1080/10473289.2011.603998, 2011.

Maloney, K. O., Baruch-Mordo, S., Patterson, L. A., Nicot, J.-P., Entrekin, S. A., Fargione, J. E., Kiesecker, J. M., Konschnik, K. E., Ryan, J. N., Trainor, A. M., Saiers, J. E. and Wiseman, H. J.: Unconventional oil and gas spills: Materials, volumes, and risks to surface waters in four states of the U.S., Sci. Total Environ., 581–582, 369–377, doi:10.1016/j.scitotenv.2016.12.142, 2017.

McLinden, C. A., Fioletov, V., Boersma, K. F., Krotkov, N., Sioris, C. E., Veefkind, J. P. and Yang, K.: Air quality over the Canadian oil sands: A first assessment using satellite observations, Geophys. Res. Lett., 39(4), n/a-n/a, doi:10.1029/2011GL050273, 2012.

Meng, Z. and Seinfeld, J. H.: Time scales to achieve atmospheric gas-aerosol equilibrium for volatile species, Atmos. Environ., 30(16), 2889–2900, doi:10.1016/1352-2310(95)00493-9, 1996.

Metrohm Applikon: MARGA 1S Manual, Schiedam, Netherlands., 2011.

Moore, C. W., Zielinska, B., Pétron, G. and Jackson, R. B.: Air impacts of increased natural gas acquisition, processing, and use: A critical review, Environ. Sci. Technol., 48(15), 8349–8359, doi:10.1021/es4053472, 2014.

Müller, T., Nowak, A., Wiedensohler, A., Sheridan, P., Laborde, M., Covert, D. S., Marinoni, A., Imre, K., Henzing, B., Roger, J.-C., Martins dos Santos, S., Wilhelm, R., Wang, Y.-Q. and de Leeuw, G.: Angular Illumination and Truncation of Three Different Integrating Nephelometers: Implications for Empirical, Size-Based Corrections, Aerosol Sci. Technol., 43(6), 581–586, doi:10.1080/02786820902798484, 2009.

Nenes, A.: ISORROPIA : A New Thermodynamic Equilibrium Model for Multiphase Multicomponent Inorganic Aerosols, Aquat. Geochemistry, 4, 123–152, 1998.

Ng, N. L., Canagaratna, M. R., Zhang, Q., Jimenez, J. L., Tian, J., Ulbrich, I. M., Kroll, J. H., Docherty, K. S., Chhabra, P. S., Bahreini, R., Murphy, S. M., Seinfeld, J. H., Hildebrandt, L., Donahue, N. M., Decarlo, P. F., Lanz, V. A., Prévôt, A. S. H., Dinar, E., Rudich, Y. and Worsnop, D. R.: Organic aerosol components observed in Northern Hemispheric datasets from Aerosol Mass Spectrometry, Atmos. Chem. Phys., 10(10), 4625–4641, doi:10.5194/acp-10-4625-2010, 2010.

Ng, N. L., Canagaratna, M. R., Jimenez, J. L., Chhabra, P. S., Seinfeld, J. H. and Worsnop, D. R.: Changes in organic aerosol composition with aging inferred from aerosol mass spectra, Atmos. Chem. Phys., 11(13), 6465–6474, doi:10.5194/acp-11-6465-2011, 2011.

Nopmongcol, U., Jung, J., Kumar, N. and Yarwood, G.: Changes in US background ozone due to global anthropogenic emissions from 1970 to 2020, Atmos. Environ., 140, 446–455, doi:10.1016/j.atmosenv.2016.06.026, 2016.

Norris, G., Duvall, R., Brown, S. and Bai, S.: EPA Positive Matrix Factorization (PMF) 5.0 Fundamentals and User Guide., 2014.

Nowak, J. B., Neuman, J. a., Kozai, K., Huey, L. G., Tanner, D. J., Holloway, J. S., Ryerson, T. B., Frost, G. J., McKeen, S. a. and Fehsenfeld, F. C.: A chemical ionization mass spectrometry technique for airborne measurements of ammonia, J. Geophys. Res., 112, 1–12, doi:10.1029/2006JD007589, 2007.

Paatero, P. and Tapper, U.: Positive Matrix Factorization: A Non-negative Factor Model with Optimal Utilization of Error Estimates of Data Values, Environmetrics, 5, 111–126, 1994.

PacWest Consulting Partners: Tight Gas Fracturing Technology and Patent Report, [online] Available from: http://dolcera.com/wiki/index.php?title=Tight_Gas_Fracturing_Technology_and_Patent_Report (Accessed 9 May 2017), 2012.

Parrish, D. D. and Fehsenfeld, F. C.: Methods for gas-phase measurements of ozone, ozone precursors and aerosol precursors, Atmos. Environ., 34(12–14), 1921–1957, doi:10.1016/S1352-2310(99)00454-9, 2000.

Patashnick, H. and Rupprecht, E. G.: Continuous PM-10 Measurements Using the Tapered Element Oscillating Microbalance, J. Air Waste Manag. Assoc., 41, 1079–1083, 1991.

Patterson, L. A., Konschnik, K. E., Wiseman, H., Fargione, J., Maloney, K. O., Kiesecker, J., Nicot, J.-P., Baruch-Mordo, S., Entrekin, S., Trainor, A. and Saiers, J. E.: Unconventional Oil and Gas Spills: Risks, Mitigation Priorities, and State Reporting Requirements, Environ. Sci. Technol., 51, 2563–2573, doi:10.1021/acs.est.6b05749, 2017.

Pekney, N. J., Veloski, G., Reeder, M., Tamilia, J., Rupp, E. and Wetzel, A.: Measurement of atmospheric pollutants associated with oil and natural gas exploration and production activity in Pennsylvania's Allegheny National Forest., J. Air Waste Manag. Assoc., 64(9), 1062–1072, doi:10.1080/10962247.2014.897270, 2014.

Pitchford, M. L., Malm, W. C., Schichtel, B. A., Kumar, N., Lowenthal, D. H. and Hand, J. L.: Revised Algorithm for Estimating Light Extinction from IMPROVE Particle Speciation Data, J. Air Waste Manage. Assoc., 57(11), 1326–1336, doi:10.3155/1047-3289.57.11.1326, 2007.

Pitchford, M. L., Poirot, R. L., Schichtel, B. a, Malm, W. C. and Maim, W. C.: Characterization of the Winter Midwestern Particulate Nitrate Bulge, J. Air Waste Manage. Assoc., 59(9), 1061–1069, doi:10.3155/1047-3289.59.9.1061, 2009.

Prather, K. A., Hatch, C. D. and Grassian, V. H.: Analysis of Atmospheric Aerosols, Annu. Rev. Anal. Chem., 1, 485–514, doi:10.1146/annurev.anchem.1.031207.113030, 2008.

Prenni, A. J., Levin, E. J. T., Benedict, K. B., Sullivan, A. P., Schurman, M. I., Gebhart, K. A., Day, D. E., Carrico, C. M., Malm, W. C., Schichtel, B. A., Collett, J. L. and Kreidenweis, S. M.: Gas-phase reactive nitrogen near Grand Teton National Park: Impacts of transport, anthropogenic emissions, and biomass burning, Atmos. Environ., 89, 7490–7756, doi:10.1016/j.atmosenv.2014.03.017, 2014.

Prenni, A. J., Day, D. E., Evanoski-Cole, A. R., Sive, B. C., Hecobian, A., Zhou, Y., Gebhart, K. A., Hand, J. L., Sullivan, A. P., Li, Y., Schurman, M. I., Desyaterik, Y., Malm, W. C., Schichtel, B. A. and Collett Jr., J. L.: Oil and gas impacts on air quality in federal lands in the Bakken region: an overview of the Bakken Air Quality Study and first results, Atmos. Chem. Phys., 16, 1401–1416, doi:doi:10.5194/acpd-15-28749-2015, 2016.

Radiello: Radiello Manual, Padova, Italy. [online] Available from: www.radiello.com, 2006.

Rappenglück, B., Ackermann, L., Alvarez, S., Golovko, J., Buhr, M., Field, R. A., Soltis, J.,

Montague, D. C., Hauze, B., Adamson, S., Risch, D., Wilkerson, G., Bush, D., Stoeckenius, T. and Keslar, C.: Strong wintertime ozone events in the Upper Green River basin, Wyoming, Atmos. Chem. Phys., 14(10), 4909–4934, doi:10.5194/acp-14-4909-2014, 2014.

Rester, E. and Warner, S. D.: Environmental and Health Issues in Unconventional Oil and Gas Development, Elsevier Inc., 2016.

Roberts, J. M., Veres, P. R., Yuan, B., Warneke, C., Geiger, F., Peter, M., Wild, R., Dube, W., Petron, G., Kofler, J., Zahn, A., Brown, S. S., Graus, M., Gilman, J., Lerner, B., Peischl, J., De, J. A., Li, R., Bates, T., Quinn, P., Koss, A., Li, S., David, D., Senff, C. J., Langford, A. O., Banta, R., Martin, R., Murphy, S., Soltis, J. and Field, R.: Chapter 5.0 INTENSIVE CHEMICAL MEASUREMENTS AT HORSE POOL, UBOS 2013 Synth. Rep., (March) [online] Available from: http://www.deq.utah.gov/locations/U/uintahbasin/ozone/strategies/studies/UBOS-2013.htm, 2014.

Rodriguez, M. A., Barna, M. G. and Moore, T.: Regional Impacts of Oil and Gas Development on Ozone Formation in the Western United States, J. Air Waste Manage. Assoc., 59(9), 1111–1118, doi:10.3155/1047-3289.59.9.1111, 2009.

Roy, A. A., Adams, P. J. and Robinson, A. L.: Air pollutant emissions from the development, production, and processing of Marcellus Shale natural gas., J. Air Waste Manag. Assoc., 64(1), 19–37, doi:10.1080/10962247.2013.826151, 2014.

Rumsey, I. C., Cowen, K. A., Walker, J. T., Kelly, T. J., Hanft, E. A., Mishoe, K., Rogers, C., Proost, R., Beachley, G. M., Lear, G., Frelink, T. and Otjes, R. P.: An assessment of the performance of the Monitor for AeRosols and GAses in ambient air (MARGA): A semi-continuous method for soluble compounds, Atmos. Chem. Phys., 14(3), 5639–5658, doi:10.5194/acp-14-5639-2014, 2014.

Russo, R. S., Zhou, Y., White, M. L., Mao, H., Talbot, R. and Sive, B. C.: Multi-year (2004–2008) record of nonmethane hydrocarbons and halocarbons in New England : seasonal variations and regional sources, Atmos. Chem. Phys., 10, 4909–4929, doi:10.5194/acp-10-4909-2010, 2010a.

Russo, R. S., Zhou, Y., Haase, K. B., Wingenter, O. W., Frinak, E. K., Mao, H., Talbot, R. W. and Sive, B. C.: Temporal variability, sources, and sinks of C1 -C5 alkyl nitrates in coastal New England, Atmos. Chem. Phys., 10, 1865–1883, 2010b.

Rutter, A. P., Griffin, R. J., Cevik, B. K., Shakya, K. M., Gong, L., Kim, S., Flynn, J. H. and Lefer, B. L.: Sources of air pollution in a region of oil and gas exploration downwind of a large city, Atmos. Environ., 120, 89–99, doi:10.1016/j.atmosenv.2015.08.073, 2015.

Schaap, M., Otjes, R. P. and Weijers, E. P.: Illustrating the benefit of using hourly monitoring data on secondary inorganic aerosol and its precursors for model evaluation, Atmos. Chem. Phys., 11(21), 11041–11053, doi:10.5194/acp-11-11041-2011, 2011.

Schneising, O., Burrows, J. P., Dickerson, R. R., Buchwitz, M. and Bovensmann, H.: Remote sensing of fugitive methane emissions from oil and gas production in North American tight

geologic formations, Earth's Futur., 2, 1–11, doi:10.1002/2014EF000265, 2014.

Schnell, R. C., Oltmans, S. J., Neely, R. R., Endres, M. S., Molenar, J. V. and White, A. B.: Rapid photochemical production of ozone at high concentrations in a rural site during winter, Nat. Geosci., 2(2), 120–122, doi:10.1038/ngeo415, 2009.

Schurman, M. I., Lee, T., Desyaterik, Y., Schichtel, B. A., Kreidenweis, S. M. and Collett, J. L.: Transport, biomass burning, and in-situ formation contribute to fine particle concentrations at a remote site near Grand Teton National Park, Atmos. Environ., 112, 257–268, doi:10.1016/j.atmosenv.2015.04.043, 2015.

Schwarz, J. P., Holloway, J. S., Katich, J. M., McKeen, S., Kort, E. A., Smith, M. L., Ryerson, T. B., Sweeney, C. and Peischl, J.: Black Carbon Emissions from the Bakken Oil and Gas Development Region, Environ. Sci. Technol. Lett., 2(10), 281–285, doi:10.1021/acs.estlett.5b00225, 2015.

Seinfeld, J. H. and Pandis, S. N.: Atmospheric chemistry and physics: from air pollution to climate change, Second., Wiley, Hoboken, New Jersey., 2006.

Shen, X., Zhao, Y., Chen, Z. and Huang, D.: Heterogeneous reactions of volatile organic compounds in the atmosphere, Atmos. Environ., 68, 297–314, doi:10.1016/j.atmosenv.2012.11.027, 2013.

Sickles II, J. E. and Shadwick, D. S.: Air quality and atmospheric deposition in the eastern US: 20 years of change, Atmos. Chem. Phys. Discuss., 14(12), 17943–17998, doi:10.5194/acpd-14-17943-2014, 2014.

Silvern, R. F., Jacob, D. J., Kim, P. S., Marais, E. A. and Turner, J. R.: Incomplete sulfate aerosol neutralization despite excess ammonia in the eastern US: a possible role of organic aerosol, Atmos. Chem. Phys. Discuss., 0(June), 1–21, doi:10.5194/acp-2016-315, 2016.

Simon, H., Bhave, P. V., Swall, J. L., Frank, N. H. and Malm, W. C.: Determining the spatial and seasonal variability in OM/OC ratios across the US using multiple regression, Atmos. Chem. Phys., 11(6), 2933–2949, doi:10.5194/acp-11-2933-2011, 2011.

Sjostedt, S. J., Slowik, J. G., Brook, J. R., Y.-W. Chang, R., Mihele, C., Stroud, C. A., Vlasenko, A. and Abbatt, J. P. D.: Diurnally resolved particulate and VOC measurements at a rural site: Indication of significant biogenic secondary organic aerosol formation, Atmos. Chem. Phys., 11(12), 5745–5760, doi:10.5194/acp-11-5745-2011, 2011.

Slanina, J., ten Brink, H. M., Otjes, R. P., Even, A., Jongejan, P., Khlystov, A., Waijers-Ijpelaan, A. and Hu, M.: The continuous analysis of nitrate and ammonium in aerosols by the steam jet aerosol collector (SJAC): extension and validation of the methodology, Atmos. Environ., 35(13), 2319–2330, doi:10.1016/s1352-2310(00)00556-2, 2001.

Solomon, P. A., Crumpler, D., Flanagan, J. B., Jayanty, R. K. M., Rickman, E. E. and McDade, C. E.: U.S. National PM2.5 Chemical Speciation Monitoring Networks-CSN and IMPROVE: Description of Networks., J. Air Waste Manage. Assoc., 64(12), 1410–38,

doi:10.1080/10962247.2014.956904, 2014.

Squizzato, S., Masiol, M., Brunelli, a., Pistollato, S., Tarabotti, E., Rampazzo, G. and Pavoni, B.: Factors determining the formation of secondary inorganic aerosol: a case study in the Po Valley (Italy), Atmos. Chem. Phys., 13(4), 1927–1939, doi:10.5194/acp-13-1927-2013, 2013.

Stein, A. F., Draxler, R. R., Rolph, G. D., Stunder, B. J. B., Cohen, M. D. and Ngan, F.: NOAA's hysplit atmospheric transport and dispersion modeling system, Bull. Am. Meteorol. Soc., 96(12), 2059–2077, doi:10.1175/BAMS-D-14-00110.1, 2015.

Stelson, A. W. and Seinfeld, J. H.: Relative humidity and temperature dependence of the ammonium nitrate dissociation constant, Atmos. Environ., 16(5), 983–992, doi:10.1016/0004-6981(82)90184-6, 1982.

Stoeckenius, T.: Final Report 2014 Uinta Basin Winter Ozone Study, Novato, CA. [online] Available from: http://www.deq.utah.gov/locations/U/uintahbasin/ozone/docs/2015/02Feb/UBWOS_2014_Final.pdf, 2015.

Stohl, A., Klimont, Z., Eckhardt, S., Kupiainen, K., Shevchenko, V. P., Kopeikin, V. M. and Novigatsky, A. N.: Black carbon in the Arctic: the underestimated role of gas flaring and residential combustion emissions, Atmos. Chem. Phys., 13(17), 8833–8855, doi:10.5194/acp-13-8833-2013, 2013.

Swarthout, R. F., Russo, R. S., Zhou, Y., Hart, A. H. and Sive, B. C.: Volatile organic compound distributions during the NACHTT campaign at the Boulder Atmospheric Observatory: Influence of urban and natural gas sources, J. Geophys. Res. Atmos., 118(18), 10,614-10,637, doi:10.1002/jgrd.50722, 2013.

Swarthout, R. F., Russo, R. S., Zhou, Y., Miller, B. M., Mitchell, B., Horsman, E., Lipsky, E., McCabe, D. C., Baum, E. and Sive, B. C.: Impact of Marcellus Shale Natural Gas Development in Southwest Pennsylvania on Volatile Organic Compound Emissions and Regional Air Quality, Environ. Sci. Technol., 150212094038000, doi:10.1021/es504315f, 2015.

Trebs, I., Meixner, F. X., Slanina, J., Otjes, R., Jongejan, P. and Andreae, M. O.: Real-time measurements of ammonia, acidic trace gases and water-soluble inorganic aerosol species at a rural site in the Amazon Basin, Atmos. Chem. Phys., 4, 967–987, 2004.

Turpin, B. J. and Lim, H.-J.: Species Contributions to PM2.5 Mass Concentrations: Revisiting Common Assumptions for Estimating Organic Mass, Aerosol Sci. Technol., 35(February), 602–610, doi:10.1080/02786820119445, 2001.

U.S. Energy Information Administration: The Geology of Natural Resources, Today in Energy [online] Available from: https://www.eia.gov/todayinenergy/detail.php?id=110, 2011.

U.S. Energy Information Administration: Bakken fuels North Dakota's oil production growth, Today in Energy [online] Available from: http://www.eia.gov/todayinenergy/detail.cfm?id=17391 (Accessed 5 January 2015a), 2014.

U.S. Energy Information Administration: Nonmarketed natural gas in North Dakota still rising due to higher total production, Today in Energy [online] Available from: http://www.eia.gov/todayinenergy/detail.cfm?id=15511 (Accessed 1 January 2015b), 2014.

U.S. Energy Information Administration: International Energy Outlook 2016., 2016a.

U.S. Energy Information Administration: Natural gas flaring in North Dakota has declined sharply since 2014, Today in Energy [online] Available from: http://www.eia.gov/todayinenergy/detail.cfm?id=26632 (Accessed 3 August 2016b), 2016.

U.S. Environmental Protection Agency: Report to Congress on Black Carbon, Research Triangle Park, NC., 2012.

U.S. Environmental Protection Agency: Hydraulic fracturing for oil and gas: impacts from the hydraulic fracturing water cycle on drinking water resources in the United States, Washington, DC., 2016.

Ulbrich, I. M., Canagaratna, M. R., Zhang, Q., Worsnop, D. R. and Jimenez, J. L.: Interpretation of Organic Components from Positive Matrix Factorization of Aerosol Mass Spectrometric Data., Atmos. Chem. Phys., 9, 2891, 2009.

US EPA: 2016 CASTNET Annual Network Plan., 2016a.

US EPA: Table of Historical Ozone National Ambient Air Quality Standards (NAAQS), [online] Available from: https://www.epa.gov/ozone-pollution/table-historical-ozone-national-ambient-air-quality-standards-naaqs (Accessed 25 August 2016b), 2016.

US Goverment Accountability Office: Information on Shale Resources, Development, and Environmental and Public Health Risks., 2012.

Warneke, C., McKeen, S. A., de Gouw, J. A., Goldan, P. D., Kuster, W. C., Holloway, J. S., Williams, E. J., Lerner, B. M., Parrish, D. D., Trainer, M., Fehsenfeld, F. C., Kato, S., Atlas, E. L., Baker, A. and Blake, D. R.: Determination of urban volatile organic compound emission ratios and comparison with an emissions database, J. Geophys. Res. Atmos., 112(10), doi:10.1029/2006JD007930, 2007.

Weber, R. J., Guo, H., Russell, A. G. and Nenes, A.: High aerosol acidity despite declining atmospheric sulfate concentrations over the past 15 years, Nat. Geosci., 9(April), 1–5, doi:10.1038/NGEO2665, 2016.

Wentworth, G. R., Murphy, J. G., Benedict, K. B., Bangs, E. J. and Collett, J. L.: The role of dew as a night-time reservoir and morning source for atmospheric ammonia, Atmos. Chem. Phys., 16(11), 7435–7449, doi:10.5194/acp-16-7435-2016, 2016.

Wexler, A. S. and Clegg, S. L.: Atmospheric aerosol models for systems including the ions H+, NH4+, Na+, SO42-, NO3-, Cl-, Br- and H2O, J. Geophys. Res., 107(D14), 2002.

Wexler, A. S. and Seinfeld, J. H.: The Distribution of Ammonium-Salts Among a Size and

Composition Dispersed Aerosol, Atmos. Environ., 24(5), 1231–1246, doi:10.1016/0960-1686(90)90088-5, 1990.

Wexler, A. S. and Seinfeld, J. H.: Second-generation inorganic aerosol model, Atmos. Environ. Part A, Gen. Top., 25(12), 2731–2748, doi:10.1016/0960-1686(91)90203-J, 1991.

Wiklund, J. a, Hall, R. I., Wolfe, B. B., Edwards, T. W. D., Farwell, A. J. and Dixon, D. G.: Has Alberta oil sands development increased far-field delivery of airborne contaminants to the Peace-Athabasca Delta?, Sci. Total Environ., 433, 379–82, doi:10.1016/j.scitotenv.2012.06.074, 2012.

Wu, W., Zhao, B., Wang, S. and Hao, J.: Ozone and secondary organic aerosol formation potential from anthropogenic volatile organic compounds emissions in China, J. Environ. Sci., 53, 224–237, doi:10.1016/j.jes.2016.03.025, 2017.

Wyers, G. P., Otjes, R. P. and Slanina, J.: A continuous-flow denuder for the measurement of ambient concentrations and surface-exchange fluxes of ammonia, Atmos. Environ. Part A. Gen. Top., 27(13), 2085–2090, doi:10.1016/0960-1686(93)90280-C, 1993.

Xu, L., Williams, L. R., Young, D. E., Allan, J. D., Coe, H., Massoli, P., Fortner, E., Chhabra, P., Herndon, S., Brooks, W. A., Jayne, J. T., Worsnop, D. R., Aiken, A. C., Liu, S., Gorkowski, K., Dubey, M. K., Fleming, Z. L., Visser, S., Pr??v??t, A. S. H. and Ng, N. L.: Wintertime aerosol chemical composition, volatility, and spatial variability in the greater London area, Atmos. Chem. Phys., 16(2), 1139–1160, doi:10.5194/acp-16-1139-2016, 2016.

Young, A. H., Keene, W. C., Pszenny, A. a. P., Sander, R., Thornton, J. a., Riedel, T. P. and Maben, J. R.: Phase partitioning of soluble trace gases with size-resolved aerosols in near-surface continental air over northern Colorado, USA, during winter, J. Geophys. Res. Atmos., 118(16), 9414–9427, doi:10.1002/jgrd.50655, 2013.

Yu, X., Lee, T., Ayres, B., Kreidenweis, S. M., Collett, J. L. and Malm, W.: Particulate Nitrate Measurement Using Nylon Filters, J. Air Waste Manag. Assoc., 55(8), 1100–1110, 2005.

Yu, X., Lee, T., Ayres, B., Kreidenweis, S., Malm, W. and Collett, J. L.: Loss of fine particle ammonium from denuded nylon filters, Atmos. Environ., 40(25), 4797–4807, doi:10.1016/j.atmosenv.2006.03.061, 2006.

Yuan, B., Kaser, L., Karl, T., Graus, M., Peischl, J., Campos, T. L., Shertz, S., Apel, E. C., Hornbrook, R. S., Hills, A., Gilman, J. B., Lerner, B. M., Warneke, C., Flocke, F. M., Ryerson, T. B., Guenther, A. B. and de Gouw, J. A.: Airborne flux measurements of methane and volatile organic compounds over the Haynesville and Marcellus shale gas production regions, J. Geophys. Res. Atmos., 120, 6271–6289, doi:10.1002/2015JD023242, 2015.

Zellweger, C., Ammann, M., Buchmann, B., Hofer, P., Lugauer, M., Ruttimann, R., Streit, N., Weingartner, E. and Baltensperger, U.: Summertime NOy speciation sea level , Switzerland, J. Environ. Monit., 105(D5), 6655–6667, 2000.

Zhang, Q., Alfarra, M. R., Worsnop, D. R., James, D., Coe, H., Canagaratna, M. R. and Jimenez, J. L.: Deconvolution and Quantification of Hydrocarbon-like and Oxygenated Organic Aerosols

Based on Aerosol Mass Spectrometry Deconvolution and Quantification of Hydrocarbon-like and Oxygenated Organic Aerosols Based on Aerosol Mass Spectrometry, Environ. Sci. Technol., 39(13), 4938–4952, doi:10.1021/es048568l, 2005a.

Zhang, Q., Worsnop, D. R., Canagaratna, M. R. and Jimenez, J.-L.: Hydrocarbon-like and oxygenated organic aerosols in Pittsburgh: insights into sources and processes of organic aerosols, Atmos. Chem. Phys. Discuss., 5(5), 8421–8471, doi:10.5194/acpd-5-8421-2005, 2005b.

Zhang, Q., Canagaratna, M. R., Jayne, J. T., Worsnop, D. R. and Jimenez, J. L.: Time- and size-resolved chemical composition of submicron particles in Pittsburgh: Implications for aerosol sources and processes, J. Geophys. Res. Atmos., 110(7), 1–19, doi:10.1029/2004JD004649, 2005c.

Zhang, Q., Jimenez, J. L., Canagaratna, M. R., Ulbrich, I. M., Ng, N. L., Worsnop, D. R. and Sun, Y.: Understanding atmospheric organic aerosols via factor analysis of aerosol mass spectrometry: A review, Anal. Bioanal. Chem., 401(10), 3045–3067, doi:10.1007/s00216-011-5355-y, 2011a.

Zhang, Q., Jimenez, J. L., Canagaratna, M. R., Ulbrich, I. M., Ng, N. L., Worsnop, D. R. and Sun, Y.: Understanding atmospheric organic aerosols via factor analysis of aerosol mass spectrometry: a review., Anal. Bioanal. Chem., 401(10), 3045–67, doi:10.1007/s00216-011-5355-y, 2011b.

Zhang, Y., Seigneur, C., Seinfeld, J. H., Jacobson, M., Clegg, S. L. and Binkowski, F. S.: A comparative review of inorganic aerosol thermodynamic equilibrium modules: Similarities, differences, and their likely causes, Atmos. Environ., 34(1), 117–137, doi:10.1016/S1352-2310(99)00236-8, 2000.

Zhang, Y., Sheesley, R. J., Schauer, J. J., Lewandowski, M., Jaoui, M., Offenberg, J. H., Kleindienst, T. E. and Edney, E. O.: Source apportionment of primary and secondary organic aerosols using positive matrix factorization (PMF) of molecular markers, Atmos. Environ., 43(34), 5567–5574, doi:10.1016/j.atmosenv.2009.02.047, 2009.

Zhou, Y., Shively, D., Mao, H., Russo, R. S., Pape, B., Mower, R. N., Talbot, R. and Sive, B. C.: Air toxic emissions from snowmobiles in Yellowstone National Park., Environ. Sci. Technol., 44(1), 222–8, doi:10.1021/es9018578, 2010.

Ziemann, P. J. and Atkinson, R.: Kinetics, products, and mechanisms of secondary organic aerosol formation, Chem. Soc. Rev., 41(19), 6582–605, doi:10.1039/c2cs35122f, 2012.

APPENDIX A: ADDITIONAL DETAILS ON MARGA METHODS

A.1 Instrument Operation

The MARGA used for all measurements presented in this work was a 1S unit which was borrowed from the U.S. EPA. The MARGA 1S manual (Metrohm Applikon, 2011) was generally followed for instrument operation with any modifications noted below. The MARGA inlet consisted of an unheated polyethylene tubing with a Teflon-coated cyclone with a size-cut to capture only particulate matter with an aerodynamic diameter less than 2.5 µg m^{-3} (PM$_{2.5}$). The ambient air sample first passes through a wet rotating denuder (WRD, Wyers, 1993; Trebs, 2004) which captures ammonia (NH$_3$), sulfur dioxide (SO$_2$), nitric acid (HNO$_3$) and nitrous acid (HONO). The WRD consists of two horizontal concentric glass tubes that constantly rotate. The sample air passes through between the glass tubes, which is filled partially with the absorbance solution, which is a 10 mg/L hydrogen peroxide solution. The gases are dissolved into the sample solution and the aerosol flows through into a steam-jet aerosol collector (SJAC, Khlystov, 1995; Slanina, 2001). The SJAC is heated and humidified to supersaturated conditions, enabling the growth of the collected aerosol. The aerosol particles then settle into the sample solution. Tubing from both the WRD and SJAC carry the sample to an anion and a cation ion chromatograph. The water-soluble inorganic PM$_{2.5}$ components measured are chloride (Cl$^-$), nitrite (NO$_2^-$), nitrate (NO$_3^-$), sulfate (SO$_4^{2-}$), sodium (Na$^+$), ammonium (NH$_4^+$), potassium (K$^+$), magnesium (Mg^{2+}), and calcium (Ca^{2+}).

The schedule for MARGA maintenance is described in Table 8 of the manual. To reduce operational costs, guard and analytical columns were not replaced until they exceeded their operational lifetime, contrary to the manual recommendation of replacing them at regular time

intervals. Regular cleaning of MARGA components were completed at the recommended frequency or more often. The preparation of cation and anion eluents are also described in the manual. However, previous MARGA users noticed contamination peaks when using HNO_3 solution for the cation eluent, so a 3.2 mmol L^{-1} methanesulfonic acid (MSA) solution was used instead. The anion IC eluent, 7.0 mmol L^{-1} sodium carbonate monohydrate and 8.0 mmol L^{-1} sodium bicarbonate, is described in the manual. The recommended internal standard contains 320 µg L^{-1} lithium and 3680 µg L^{-1} bromide.

During standard MARGA operation, a significant sulfate peak (0.5 – 0.7 µg SO_4^{2-} m^{-3}) was consistently present in the anion IC baseline, which was first noticed after setting it up in the CSU laboratory in September 2013. Extensive laboratory tests were conducted to investigate this source of contamination. The following tests were conducted, eliminating specific components as sources of the high sulfate blank:

- All components of the MARGA were cleaned, including the WRD, SJAC, injection valve, syringes, etc.

- Replaced pump tubing, aspirating filters, o-rings in denuder caps, back-pressure loops, sample loops; anything the sample solution came in contact with

- Ran the MARGA cleaning cycle multiple times, for longer time periods than recommended in the manual

- Installed a new anion column

- Changed or removed the inline filters for WRD and SJAC sample lines

- The MARGA anion analytical column was replaced with a Dionex anion column

- Replaced the suppressor tubing

- Added 2-3mM oxalic acid to phosphoric acid regenerant

160

- Increased flow in suppressor by switching to tubing with a larger inner diameter

- Tried alternate suppressor regenerant solution: 0.1 M oxalic acid and 5% acetone in H_3PO_4 solution (35 mL H_3PO_4, 50 mL acetone and 12.607 g oxalic acid in 915 L DI)

- Tried different cation eluent (the nitric acid eluent described in the manual)

- Used 0.1% peracetic acid as the cleaning solution in the MARGA cleaning program, then ran a few days with standard hydrogen peroxide absorbance solution.

After all of the tests listed were performed, the high sulfate blank persisted. The sulfate contamination peak was finally eliminated after replacing both the Metrohm anion column and suppressor with an anion Dionex column and suppressor, narrowing down the source of sulfate contamination to the Metrohm suppressor.

The MARGA was operated in different configurations during the three main measurement campaigns, which are summarized in Table A.1. During BAQS, the MARGA was operated according to the manual with all the standard Metrohm components. The sulfate blank was characterized and subtracted from the ambient measurements. At RMNP, the Metrohm anion IC system was replaced with a Dionex column and suppressor, as described in the URG sample analysis section, which is the standard anion IC method for the Collett research group. During the NH_3 comparison measurements conducted in the laboratory at CSU, the MARGA was operated with all original Metrohm components. However, the focus for the comparison studies was NH_3, which only used the cation IC system.

Table A.1: Alterations in MARGA anion separation during different studies

	BAQS and Laboratory at CSU	RMNP
Anion Column	Metrohm	Dionex
Suppressor	Metrohm	Dionex
Eluent	7.0 mM sodium carbonate monohydrate and 8.0 mM sodium bicarbonate	17 mM sodium carbonate and 18mM sodium bicarbonate eluent

A.2 Data Analysis Procedures

The first step in determining the ambient concentrations is to integrate the peak areas in the chromatograms. MARGA software automatically integrates the chromatograms but often does a poor job of drawing a good baseline or fully capturing the peak when ambient concentrations are low. The Applikon integration software, MargaTool, is designed to view chromatograms and manually perform reintegration when necessary. The MargaTool was used to visually inspect each chromatogram. The chromatograms were removed if any of the following were observed: baseline abnormality (shift because of eluent change, spikes from air being injected if syringe dries out, etc.), excessive noise, or another obvious problem with the instrument that prevented good analytical separation. If poor integration was observed, peaks were reintegrated. MargaTool was first used, but better agreement with comparison measurements were observed when peaks were reintegrated with other chromatogram integrating software and ambient concentrations were calculated using an external calibration curve.

To have more control over integrating the MARGA chromatograms, the raw data files were output and then input into Dionex Chromeleon, a commercial program for integrating chromatograms. The method to retrieve the MARGA files and input them into Chromeleon was developed by Doris Chen and summarized here. An example of how peak reintegration improves the accuracy of the ambient concentrations, a comparison timeline is shown in Figure

A.1 between URG aerosol measurements, automated MARGA concentrations and reintegrated

MARGA peaks converted to ambient concentrations using an external calibration.

1. Using MARGA tool, either a single .dat file or a batch of selected .dat files will be converted to time series of conductivity data files as .txt format, with a time interval of 0.1s;
2. Within the folder where the .txt files are stored, copy a template (named anion_template.nc) to that particular folder;
3. Double click createNC.jar to open the program and then provide the program with the right path of the folder which has the .txt files.
4. The corresponding .cdf files for each .txt file (the same file name) will be created within the same folder;
5. Create a new folder and copy the generated .cdf files into it;
6. Open Chromeleon, under File→Import→Non-Chromeleon data, there will be a green cross at the lower left side, click on that and choose Folder; provide the path for the folder which has all the .cdf files;
7. Follow the instruction of Chromeleon and press the Import button, the whole folder with .cdf files will be imported to Chromeleon as a sequence.
8. When the new sequence is successfully imported to Chromeleon, right click on the sequence and click "Convert to Chromeleon Processing", manual integrations should be activated.
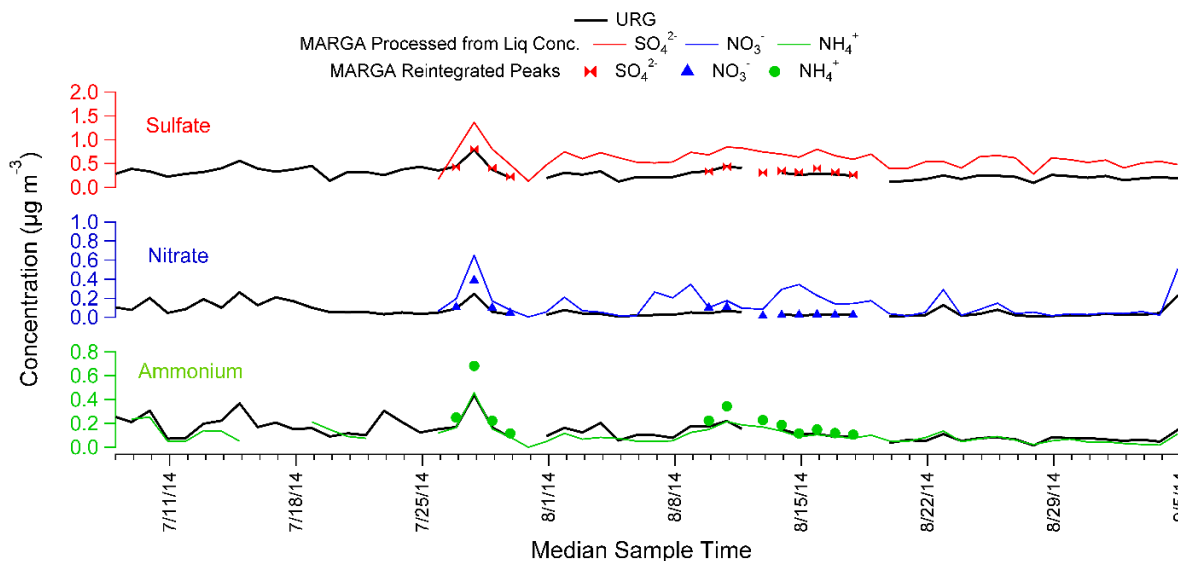
Figure A.1: Timelines of sulfate, nitrate and ammonium comparing URG measurements (solid black lines), automated MARGA concentrations (solid colored lines) and select reintegrated MARGA peaks using Chromeleon (symbols).

163

Once the liquid concentration for each species is determined, as described above, the steps for

processing the MARGA data are as follows:

1. Remove chromatograms with missing, incomplete or asymmetrical peaks
2. Blank correct using measured aqueous blank concentrations
3. Calculate LOD using 4xnoise of the ion chromatography signal
4. Replace values below LOD with ½ LOD
5. Enter a concentration of 0 for samples were no peak was detected
6. For anions, convert liquid concentration to ambient concentration (C_i, µg m^{-3}) using the equation A.1
   a. Correct for internal standard using MARGA measured Br concentration (C_{Br}, µg L^{-1}) and predicted concentration of internal standard (C_{IS}, µg L^{-1}) of 3680 µg L^{-1} Br$^-$.
   b. Convert from MARGA aqueous sample flow (Q_s, mL hr^{-1}) to ambient flow rate (Q_{air}, m^3 hr^{-1}) using the conversion factor $\frac{Q_s}{Q_{air}} = \frac{25.3\frac{mL}{hr}*\frac{1L}{1000mL}}{1\frac{m^3}{hr}} = 0.0253\frac{L}{m^3}$
   c. Correct for the measured flow rate of sample (Q_s, mL hr^{-1}) and flow rate of internal standard (Q_{Br}, mL hr^{-1}), using the factor $\frac{Q_s-Q_{Br}}{Q_s} = \frac{25.3\frac{mL}{hr}-2.53\frac{mL}{hr}}{25.3\frac{mL}{hr}} = 0.9$
   d. Correct sample and internal standard volumes using calculated syringe volumes (sample and IS) corrected with fluctuations in syringe speed using Table A.2 and the following equations
   e. Correct ambient gas concentration with conversion from aqueous concentrations to ambient concentrations using molecular weights (MW) of gas phase ($MW_{i(air)}$) and aqueous phase species ($MW_{i(liq)}$)

$$C_i = C_{liq} * \frac{Q_s-Q_{Br}}{Q_s} * \frac{C_{IS}}{C_{Br}} * \frac{Q_s}{Q_{air}} * \frac{MW_{i(air)}}{MW_{i(liq)}}$$ Equation A.1

7. For cations, convert liquid concentration to ambient concentration (C_i, µg m^{-3}) using the equation A.1, with the following modifications
   a. Replace measured C_{Br} with measured C_{Li}
   b. Use C_{IS} of 320 µg L^{-1} for Li$^+$ internal standard concentration
   c. Q_{Li} is the same as Q_{Br} (2.53 mL hr^{-1})

Correcting for Syringe Pump Speed

Table A.2: Conversion from MARGA measured syringe speed to sample and IS syringe volume (copied from MARGA 1S manual)

Syringe Speed	Sample Syringe Volume	IS Syringe Volume
274	23.6	2.36
276	23.8	2.38
278	24.0	2.40
280	24.1	2.41
282	24.3	2.43
284	24.5	2.45
286	24.7	2.47
288	24.8	2.48
290	25.0	2.50
292	25.2	2.52
294	25.3	2.53
296	25.5	2.55
298	25.7	2.57
300	25.9	2.59
302	26.0	2.60
304	26.2	2.62
306	26.4	2.64

Using the data from Table A.2, the following conversion from syringe speed (x) to sample (Q_s) or internal standard (Q_{IS}) volumes were used:

$$Q_s = 0.0863x - 0.0196 \qquad \text{Equation A.2}$$

$$Q_{IS} = 0.0086x - 0.002 \qquad \text{Equation A.3}$$

To extract the sample flow and air flow rates from the MARGA, java programs were created by Doris Chen were used to extract the data files. Her procedure is summarized below.

Retrieving sample flow rate and air flow rate from instrument log file

1. Open airFlow.jar java program.
2. Find and load the .xml file from MARGA
3. Name the file xxxx.xls and save
4. Rename that file with the appropriate date before extracting more flow data.
5. Open the Java program and change the path to the folder where the .xml files are stored.
6. It will ask where you want to save the extracted information. The file name must be xxxx.xls.

APPENDIX B: MARGA LABORATORY NH$_3$ COMPARISON STUDIES

This study provides a comprehensive comparison of MARGA NH$_3$ with other real-time high resolution NH$_3$ measurements in an environment with relatively low ambient NH$_3$ concentrations. Previous studies have described (Trebs et al., 2004) and compared numerous NH$_3$ instruments (von Bobrutzki et al., 2010; Prenni et al., 2014) and have addressed the challenges to measuring a highly volatile and water soluble gas. Comparison studies of the MARGA performance with other aerosol and gas instrumentation and assessments of the accuracy and precision of the instrument have also been completed. These studies have either lacked NH$_3$ comparison measurements (Makkonen et al., 2012) or used comparison measurements with much lower time resolution (Rumsey et al., 2014). In this study, the MARGA will be operated in the laboratory with other real-time NH$_3$ instruments for a comparison study. The MARGA instrument set-up was altered to determine what conditions are optimal for the collection and measurement of NH$_3$.

In addition to the MARGA, three Air Sentry NH$_3$ monitors and a Picarro NH$_3$ instrument were used for this study to provide real-time high resolution NH$_3$ comparison measurements. A Particle Measuring Systems Air Sentry II instrument uses ion mobility and the Picarro instrument uses cavity ring-down spectroscopy (CRDS) to detect ambient NH$_3$. The instruments were set up in the laboratory with inlets configured to measure ambient air. The standard operating procedure of the Picarro and Air Sentry includes heating the tubing to 100°F by wrapping a heated wire and insulating foam around the Teflon inlet tubing (Prenni et al., 2014). A filter is attached to the inlet to remove particles and potential interferences with particulate ammonium. The Air Sentry and Picarro NH$_3$ instruments were calibrated for each study by

mixing clean air from a zero air generator with ultra pure NH_3 to a steady calculated calibration concentration of NH_3. This calibration standard is also measured using a sodium bicarbonate coated annular denuder for comparison (see URG methods in Section 2.1).

The inlet material and temperature can be varied to minimize NH_3 loss in the sampling line. NH_3 will stick to many surfaces, including tetrafluoroethylene (TFE) Teflon tubing that is commonly used for instrument inlets (Nowak et al., 2007; Parrish and Fehsenfeld, 2000). However, Nowak et al., 2007 found that NH_3 loss was reduced in less common types of Teflon tubing, fluorinated ethylene-propylene (FEP) and perfluoro-alkoxy (PFA) Teflon material. Another way to reduce the loss of NH_3 to the inlet tubing walls is to heat the inlet to minimize the condensation of NH_3 onto cooler surfaces, which has been done in previous studies (Wentworth et al., 2016).

For an initial comparison, the MARGA was operated alongside a Picarro and/or Air Sentry NH_3 instrument which were run according to their standard operating procedures. The MARGA comparison with the Picarro or Air Sentry depended on the availability of the instrumentation and heating units. The first instrument configuration tested was standard operation of the MARGA, Picarro and first two Air Sentries (Normal). Under "Normal" operation of the Picarro and Air Sentry instruments, the inlet tubing is heated to 100°F. The comparison is shown in B.1. The initial comparison measurements, in the "Normal" case, shown in Table B.1, indicate that the MARGA generally overestimates NH_3.
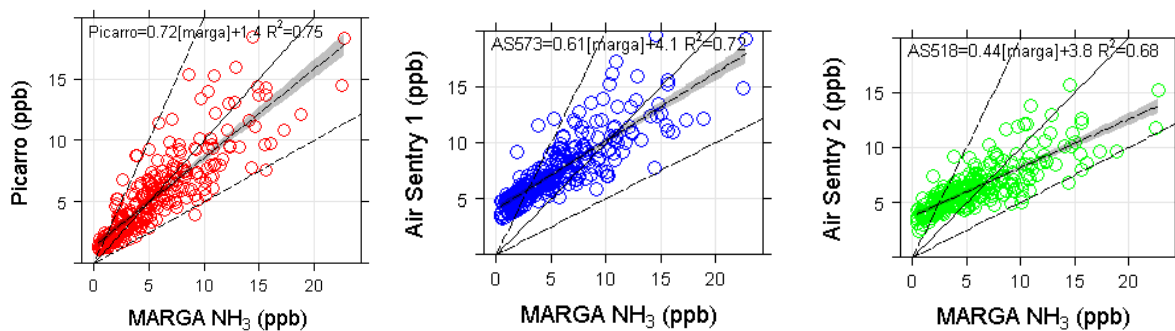
Figure B.1: MARGA NH$_3$ from the "Normal" case compared with NH$_3$ from the Picarro and two Air Sentry instruments. The Picarro and Air Sentry instrument inlets were heated but the MARGA inlet was not. The linear regression (dotted line with gray shading), the 1:1 line (solid black line) and 1:2 and 1:0.5 lines (dashed black line) are shown.

Table B.1: The slope (m), y-intercept (b) and squared Pearson correlation coefficient (R^2) from the comparisons of the MARGA with the Picarro or Air Sentry instruments under normal operation.

	m	b	R^2
Picarro	0.72	1.4	0.75
AS 1	0.61	4.1	0.72
AS 2	0.44	3.8	0.68

Three different tests were performed with the various Air Sentry instruments. For the baseline comparison, neither the MARGA nor Air Sentry inlets were heated ("No Heat"). Two different tests were performed to investigate if the tubing material and inlet configuration was impacting the collection efficiency of NH$_3$ in the MARGA. For the first test ("Heated PE"), the PE tubing of the MARGA was heated to 100°F. For the second test ("Heated Teflon"), Teflon tubing replaced the PE tubing and was also heated to 100°F. For both the "Heated PE" and "Heated Teflon" tests, the comparison measurements were collected with an Air Sentry NH$_3$ instrument with an unheated inlet in order to compare with the "No Heat" measurements. The schedule of the sampling tests and instrument configurations as well as data coverage are depicted in the timeline plot in Figure B.2.
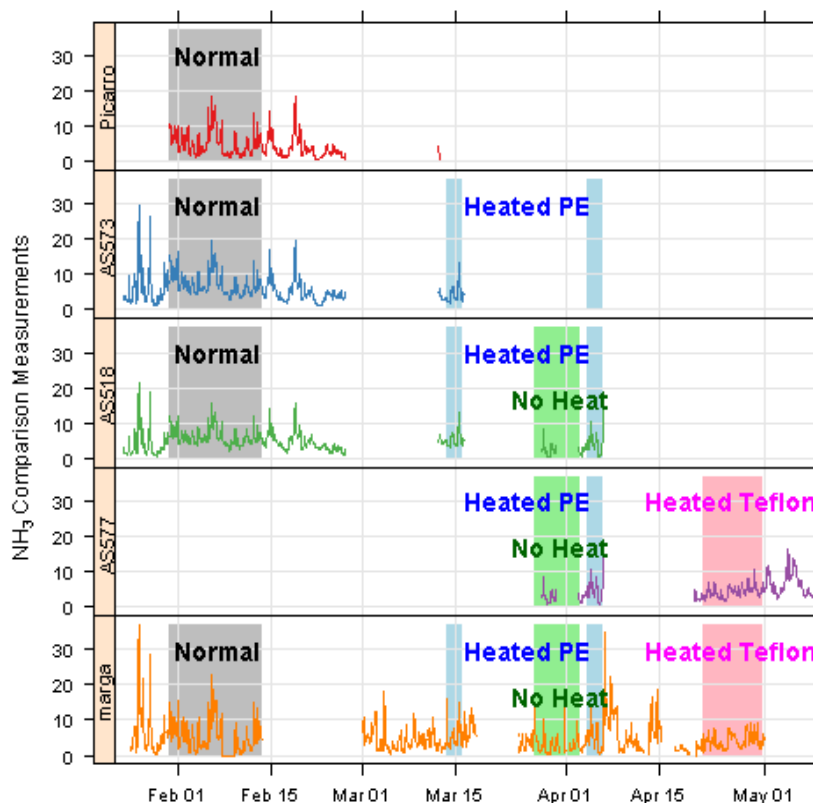
Figure B.2: A timeline of all NH$_3$ measurements collected on 5 different instruments: MARGA, Picarro and three Air Sentries; Air Sentry 1 (AS573), Air Sentry 2 (AS518) and Air Sentry 3 (AS577). The time periods are highlighted according to the four different comparison tests performed.

To compare how heating the inlet and changing the material of the MARGA inlet affected the collection efficiency of NH$_3$, the difference in the slopes of the Air Sentry and MARGA comparison between the inlet tests (Heated PE and Heated Teflon) and the base case (No Heat) in Air Sentry or MARGA) were observed. Only Air Sentry 2 (AS518) and Air Sentry 3 (AS577) were used since they have the most complete data coverage as shown in Figure B.2.
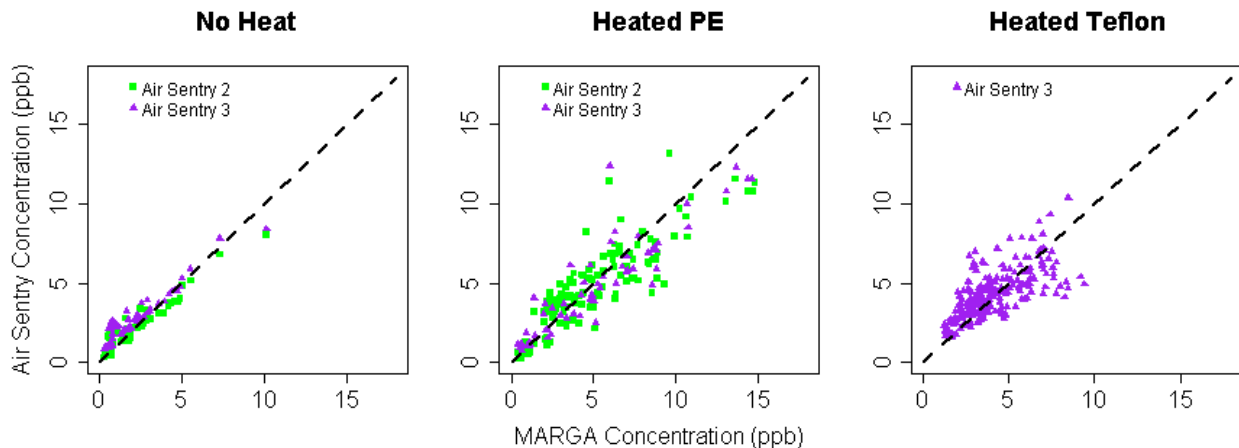
Figure B.3: The comparisons of the Air Sentry and MARGA NH_3 measurements with all MARGA measurements. The NH_3 comparison measurements from the "No Heat" base case, "Heated PE", and "Heated Teflon" cases as compared to the dashed 1:1 line.

For the baseline case, no inlets were heated ("No Heat"). The slope, y-intercept and R^2 for each comparison were 0.76, 0.54 and 0.91 for Air Sentry 2 and 0.79, 1.0, 0.91 for Air Sentry 3. The similar performance between Air Sentry 2 and Air Sentry 3 justifies using either instrument for the MARGA comparison analysis. For the "Heated PE" case, the slope, y-intercept and R^2 for each comparison were 0.71, 1.2 and 0.75 for the Air Sentry 2 and 0.75, 0.9, and 0.83 for the Air Sentry 3. For the "Heated Teflon" case, the slope, y-int and R^2 for the Air Sentry 3 were 0.58, 1.9, and 0.49. The difference in slopes between the inlet tubing material is greater than the differences between the slopes for the heated and unheated PE tubing cases. This suggests that heating the inlet had some impact on the MARGA collection efficiency, but the inlet material was a more important factor. This increase in collection efficiency may be caused by the volatilization of aerosol NH_4^+ in the inlet which is converted to a gas and collected in the instrument as NH_3. The Heated Teflon case generated a very low slope, and at low concentrations, the MARGA overestimated NH_3 concentrations significantly. This result is counter intuitive, since at lower concentrations it could be suggested that the volatilization of

NH_4^+ would have a proportionally larger impact on the NH_3 concentrations the most and result in overestimating the concentrations. This comparison also suggests that when heating the inlet tubing, there is a nonlinear response for different concentrations of NH_3.

The calibration slope can vary by concentration range, so only the measurements in overlapping ranges from each test were compared in the next figure (B.4). A low concentration range was chosen by taking the highest minimum value (from the heated Teflon case) and the lowest average concentration (from the baseline no heated inlet case). For each case, the slopes are higher than the cases when all data was included. For the case with no heating and the heated PE tubing, the slopes were very close to one, however, there was a lot of scatter that prevented good agreement between the two instruments. This suggests that the Air Sentry was not measuring much ammonia from ammonium nitrate volatilizing in the heated inlet. This is also supported by the low concentration of MARGA particulate NH_4^+ measured during this period $(0.07 \ \mu g \ m^{-3})$.
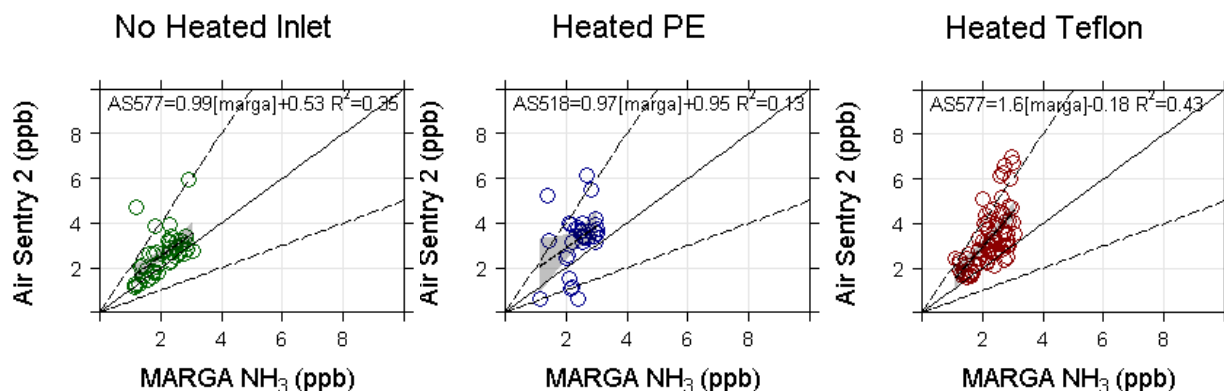
Figure B.4: The comparisons of the Air Sentry and MARGA NH_3 measurements in the MARGA concentration range between 1.12 – 3.08 ppb.

Table B.2: Statistical summary of all MARGA measured NH_3 (ppb) for each comparison test.

Study	Average (stdev)	Median	Min	Max	Count
Normal	4.83 (4.22)	3.89	0.0	22.77	334
No Heat	3.08 (2.84)	2.10	0.32	15.77	143
Heated PE	4.89 (3.01)	4.18	0.43	14.92	123
Heated PTFE	4.09 (1.91)	3.68	1.12	9.40	218

Under normal operation of the MARGA and Picarro, the following figure shows that PILS NH_4^+ compares well with the MARGA NH_4^+. The MARGA slightly overestimates both NH_3 compared to the Picarro and NH_4^+ compared to the PILS. The comparison of total NH_3 and NH_4^+ (NH_x) also shows an overestimation by the MARGA.
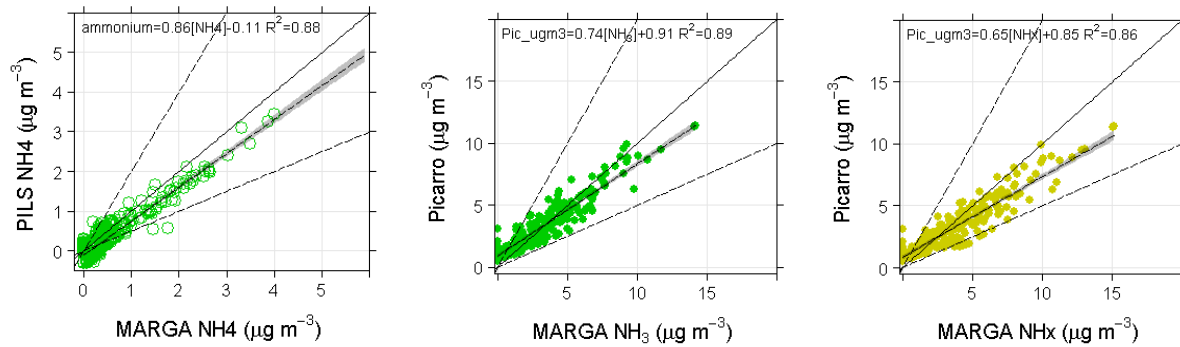
Figure B.5: The comparison of MARGA measurements of NH_4^+ with the PILS, NH_3 with the Picarro, and total NH_x as a sum between the PILS NH_4^+ and Picarro NH_3 measurements.

The MARGA was operated in Rocky Mountain National Park (ROMO), Colorado in summer 2014 and its measurements were compared to URG, Picarro NH_3 and IMPROVE filter measurements. The comparison of MARGA and URG measurements for the major ionic species are shown in Figure C.1.   The MARGA NH_3 measurements were also compared to a Picarro NH_3 instrument (Figure C.2). Very low concentrations of all species were observed during this study as shown by the study averages listed in Table C.1. Comparison NH_3 measurements show much better agreement with MARGA and URG compared to MARGA and Picarro measurements (Figures C.1 and C.2).
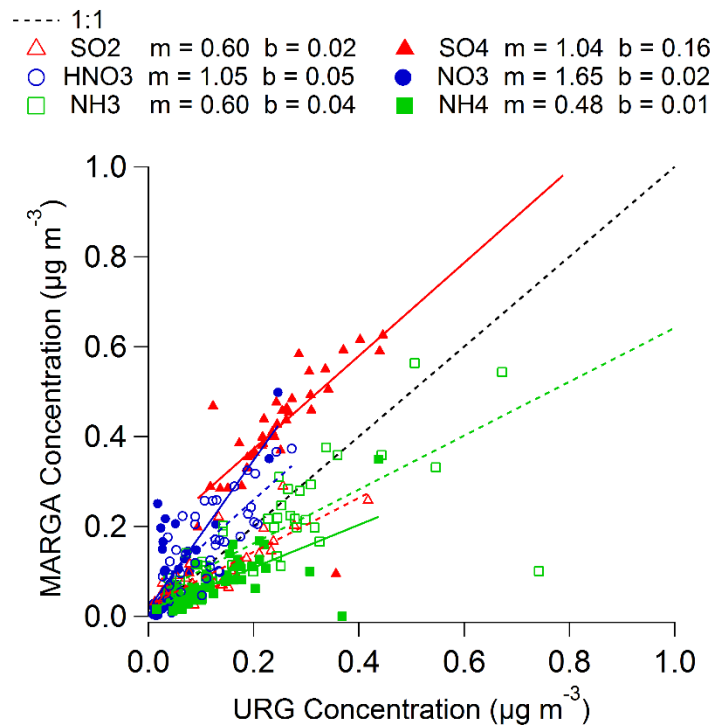
Figure C.1: Comparison measurements of nitric acid (HNO_3), ammonia (NH_3), sulfur dioxide (SO_2), nitrate (NO_3^-), ammonium (NH_4^+), and sulfate (SO_4^{2-}). The gas species are represented by open markers and dotted lines and the particulate species are represented with filled in markers and solid lines as described in the key.
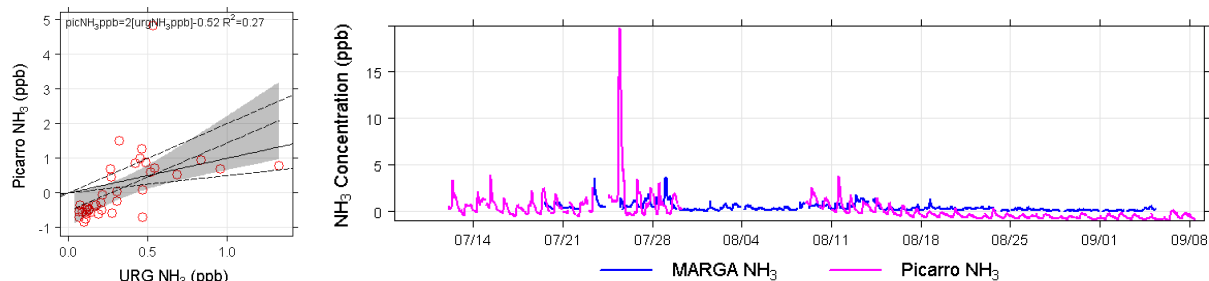
Figure C.2: The URG NH_3 (ppb) and Picarro NH_3 (ppb) plotted as a comparison (left panel) and as timelines (right panel).

Table C.1: The average concentrations for each species as measured by the MARGA and URG ($\mu g\ m^{-3}$), and Pearson correlation coefficient (R^2) from the comparison of MARGA and URG measurements from ROMO.

Species	MARGA Average (standard deviation)	URG Average (standard deviation)	R^2
HNO_3	0.19 (0.17)	0.11 (0.07)	0.45
SO_2	0.12 (0.15)	0.12 (0.08)	0.54
NH_3	0.17 (0.16)	0.18 (0.19)	0.76
NO_3^-	0.12 (0.17)	0.06 (0.06)	0.7
SO_4^{2-}	0.50 (0.21)	0.26 (0.12)	0.9
NH_4^+	0.08 (0.07)	0.11 (0.08)	0.81

Timelines showing the major ionic species measured by the URG, MARGA and IMPROVE filter samples are shown in Figures C.3 (gases) and C.4 (particles). MARGA tends to overestimate HNO_3, NO_3^- and SO_4^{2-}. MARGA slightly underestimates NH_4^+ and SO_2 during some periods. Excellent agreement is shown in NH_3 measurements. To further validate the URG particle measurements, the IMPROVE measurements, also shown in Figure C.4, show good agreement with URG measurements.
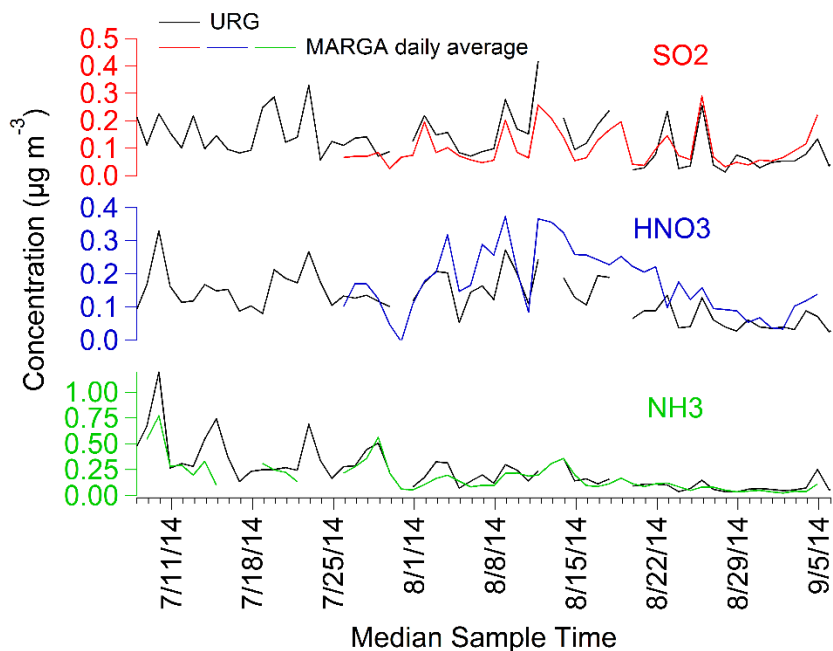
Figure C.3: Timelines of URG and MARGA SO_2, HNO_3, and NH_3 ($\mu g\ m^{-3}$) as measured during ROMO.
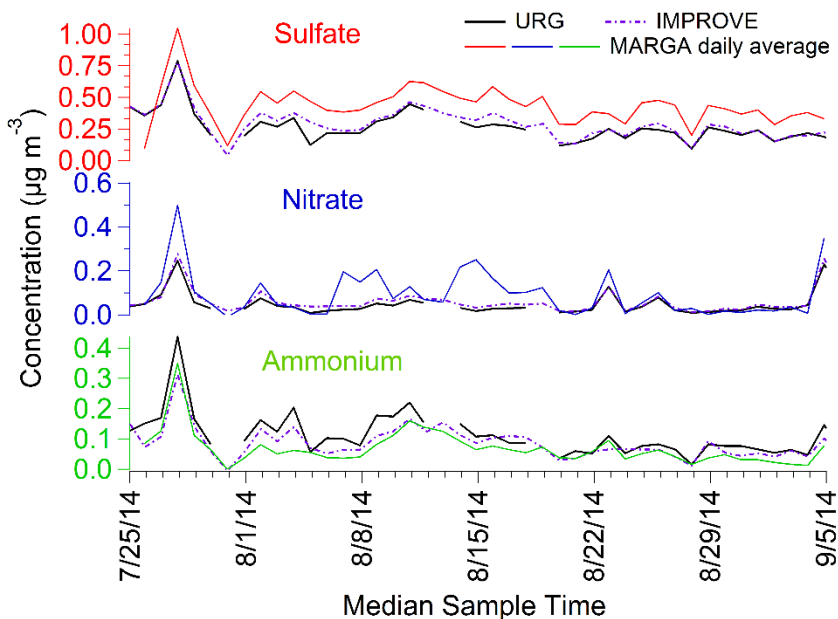
Figure C.4: Timelines of URG, MARGA and IMPROVE SO_4^{2-}, NO_3^-, and NH_4^+ ($\mu g\ m^{-3}$) as measured during ROMO.

According to the AMS PMF analysis as described in Section 2.6, a three factor PMF was also explored. Shown below (Figure D.1) are the factor profiles of the three factors: HOA (green), LVOOA (red) and semi-volatile oxidized OA (SVOOA, black). Only the results for an fpeak value of zero are considered here for simplicity. A clear difference in the ratios of *m/z* 43 and *m/z* 44 are seen in the LVOOA and SVOOA factors. However, the timelines of each factor (Figure D.2) show little difference in the LVOOA and SVOOA factors, which suggest that this solution might be a result of factor splitting and do not represent independent OA factors. Figure D.3 gives the correlation coefficients between the timelines of each factor (tseries) and the factor profiles (profiles). The clustering of these points suggest a lack of significant differences between the time series and factor profiles of the factors in this solution.
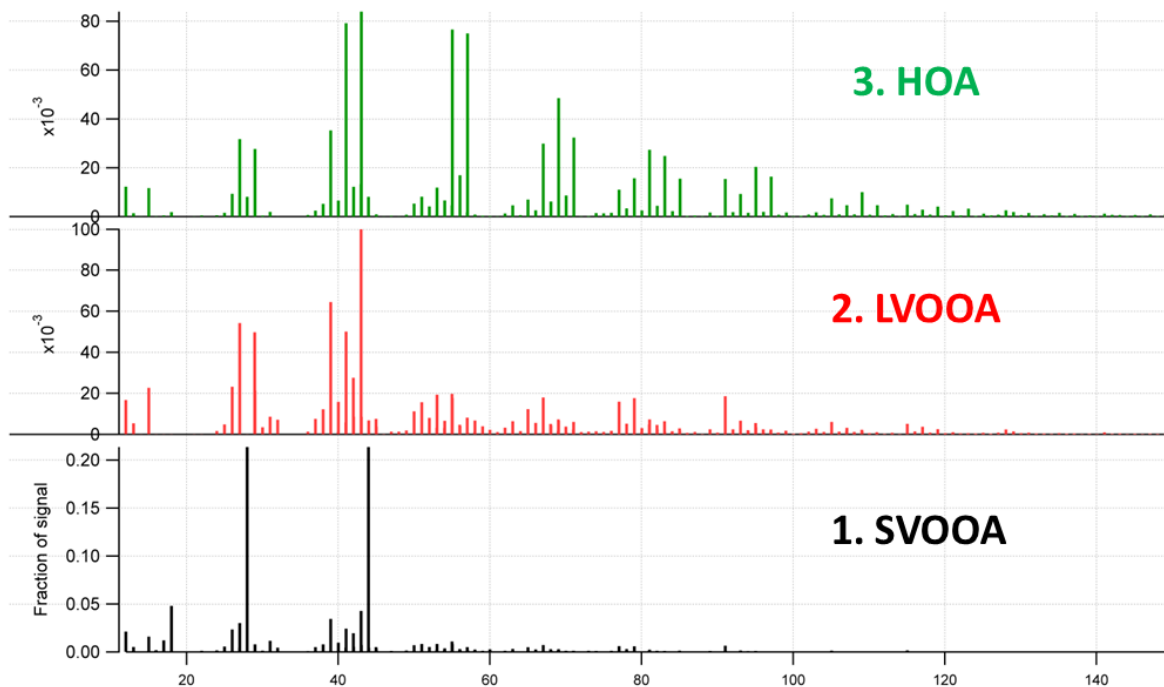
Figure D.1: The AMS organic aerosol factor profiles of HOA, LVOOA, and SVOOA showing the fraction of *m/z* signal with each bar colored by the AMS fragment.
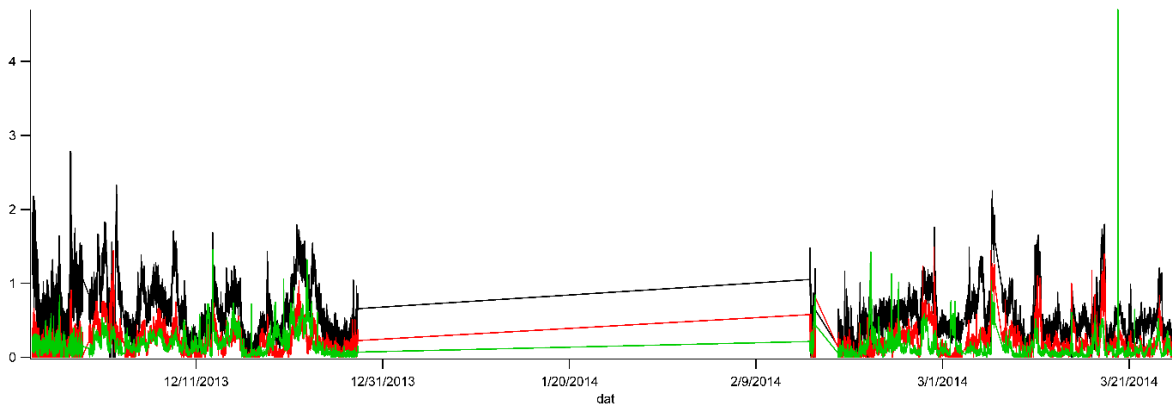
Figure D.2: Timelines of HOA (green), LVOOA (red), and SVOOA (black) concentrations (µg m^{-3}) derived from the AMS PMF three factor solution.
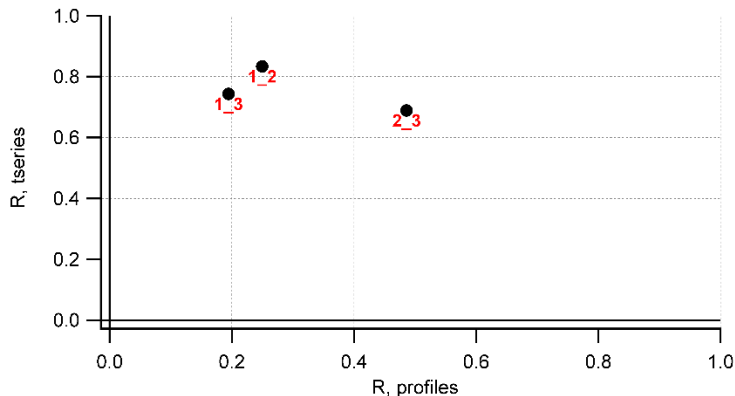
Figure D.3: The correlations between each factor time series (tseries, y-axis) and the factor profiles (profiles, x-axis) for HOA (3), LVOOA (2), and SVOOA (1) factors.

The final analysis of the PMF three factor solution was to compare each factor with other ambient species measured during BAQS (Figure D.4), as was done with the two factor solution described in Section 2.6. The HOA factors shows strong correlation with other primary species including NO_x and black carbon, which was also observed with the HOA from the two factor solution. The LVOOA factor shows moderate correlation with secondary species nitrate ($R^2 = 0.62$) and ammonium ($R^2 = 0.54$), which is not as strong of a correlation as the 2 factor solution LVOOA with nitrate ($R^2 = 0.78$) or ammonium ($R^2 = 0.72$). The SVOOA factor is less oxidized

than LVOOA and has been shown in previous studies to correlate with sulfate. SVOOA does

not correlate well with sulfate ($R^2 = 0.13$), nitrate ($R^2 = 0.52$), or ammonium ($R^2 = 0.40$).
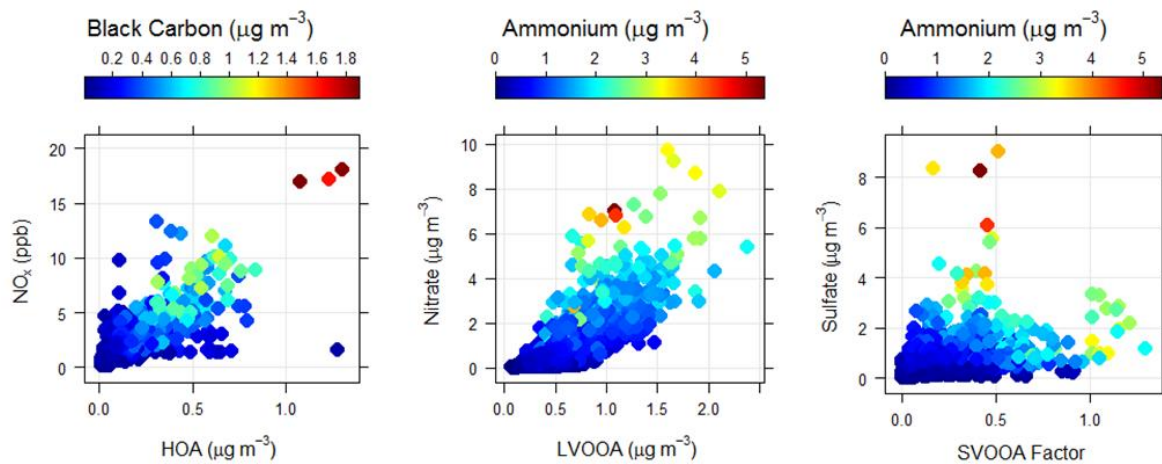
Figure D.4: Scatter plots showing the comparison between (a) HOA with NO_x (ppb) and black carbon ($\mu g\ m^{-3}$), (b) LVOOA with nitrate and ammonium ($\mu g\ m^{-3}$), and (c) SVOOA with sulfate and ammonium ($\mu g\ m^{-3}$).

APPENDIX E: PMF ANALYSIS USING ROMO AND BAQS MEASUREMENTS

Positive matrix factorization (PMF) analysis was conducted using VOC measurements from the BAQS and ROMO field studies. The EPA PMF Model 5.0 was used (Norris et al., 2014), which is a receptor based source apportionment model. For both sites, a 4-factor solution was found to be the most robust. However, both sampling sites were limited in the number of samples used. For BAQS, 197 VOC samples were used and for RMNP 667 samples were used in the PMF analysis.

E.1 BAQS PMF Analysis

VOC canister samples, as described in Section 2.13, used in this PMF analysis were collected at the north unit of Theodore Roosevelt National Park (THRO-N). The site location and proximity to active oil wells (orange dots) are shown in Figure E.1.
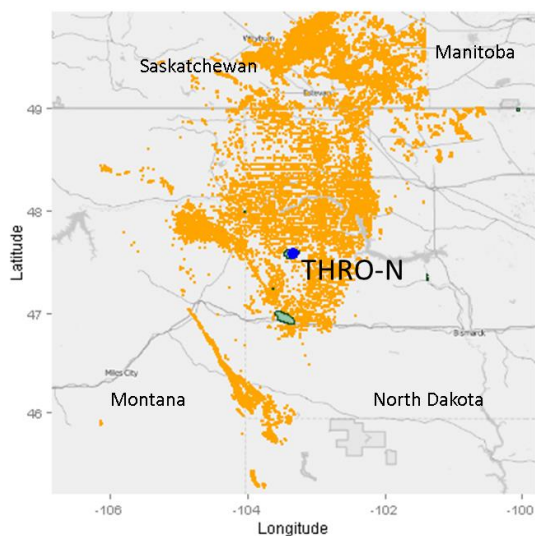
Figure E.1: A map of the BAQS study region showing the site where VOC measurements were collected (blue circle, THRO-N) and active oil wells (orange dots).

Figure E.2 shows timelines of some of the major VOC species, NO_x, NH_3 and the total inorganic $PM_{2.5}$ mass during BAQS. The VOCs chosen are common chemical tracers for

various anthropogenic activities. Ethane is a tracer for O&G extraction, ethyne is a tracer for combustion, and C_2Cl_4 is an urban signature. Timeline dissimilarities between these three species indicate the contributions of different emissions impacting THRO-N. The concentrations of many VOCs observed during BAQS were well above background levels and indicative of anthropogenic emissions.
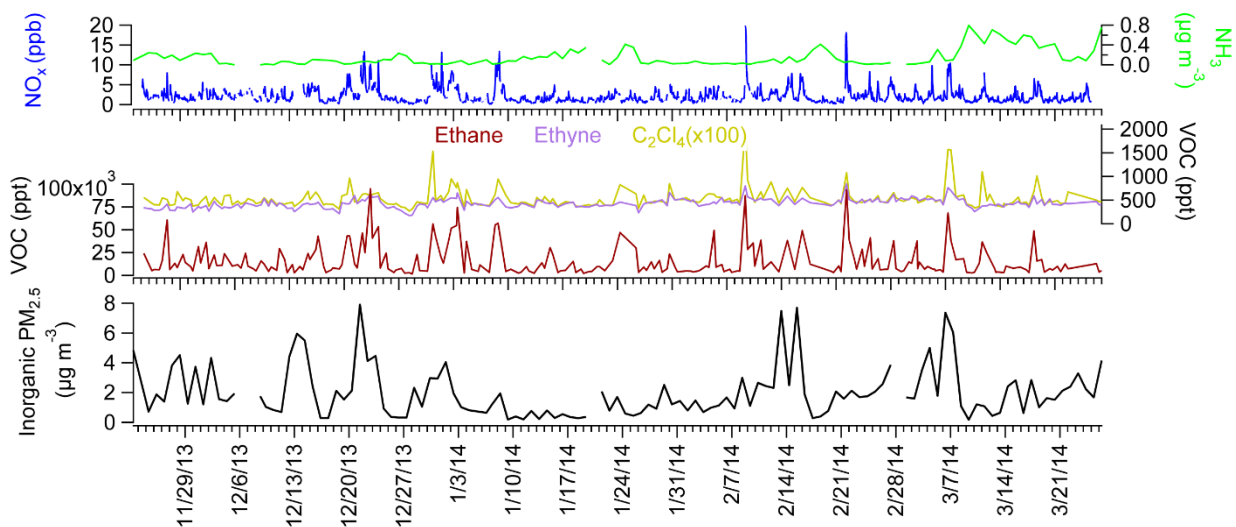
Figure E.2: Timelines of important VOC tracers including ethane (ppt, maroon), ethyne (ppt, purple) and C_2Cl_4 (ppt x100, yellow), and concentrations of NO_x (ppb, blue), NH_3 ($\mu g\ m^{-3}$, green), and total inorganic $PM_{2.5}$ mass ($\mu g\ m^{-3}$, black) are shown.

The PMF four factor solution factor profiles are shown in Figure E.3. The four factor solution provided the most detailed results with meaningful ambient factors and without factor splitting. The factor assignments are still speculative and the limited number of VOC measurements prevents a more robust analysis. The first factor proposed is labeled "Oil and Gas 1" (red). This factor includes substantial contributions from VOCs common from O&G operations, including ethane, butanes and pentanes, as well as NO_x and BC which can be generated from flaring or combustion associated with O&G operations. The "Oil and Gas 2" factor, in green, also includes contributions from the alkanes commonly associated with O&G

181

operations. However, the Oil and Gas 1 factor favors the smaller lighter alkanes (i.e. ethane) and the Oil and Gas 2 factor favors the larger lighter alkanes (i.e. pentane). The third factor is identified as "Regional Background" (blue) because of the signatures of combustion (CO, NO_x, BC, and ethyne), urban emissions (C_2Cl_4) and secondary species that indicate aging (propyl and butyl alkyl nitrates). The fourth and final factor, labeled as "Processed Industrial," is comprised of secondary products of the BTEX compounds, which could originate from industrial processes. A significant contribution from the butyl alkyl nitrate in the processed industrial factor also indicates that this is a more aged factor.
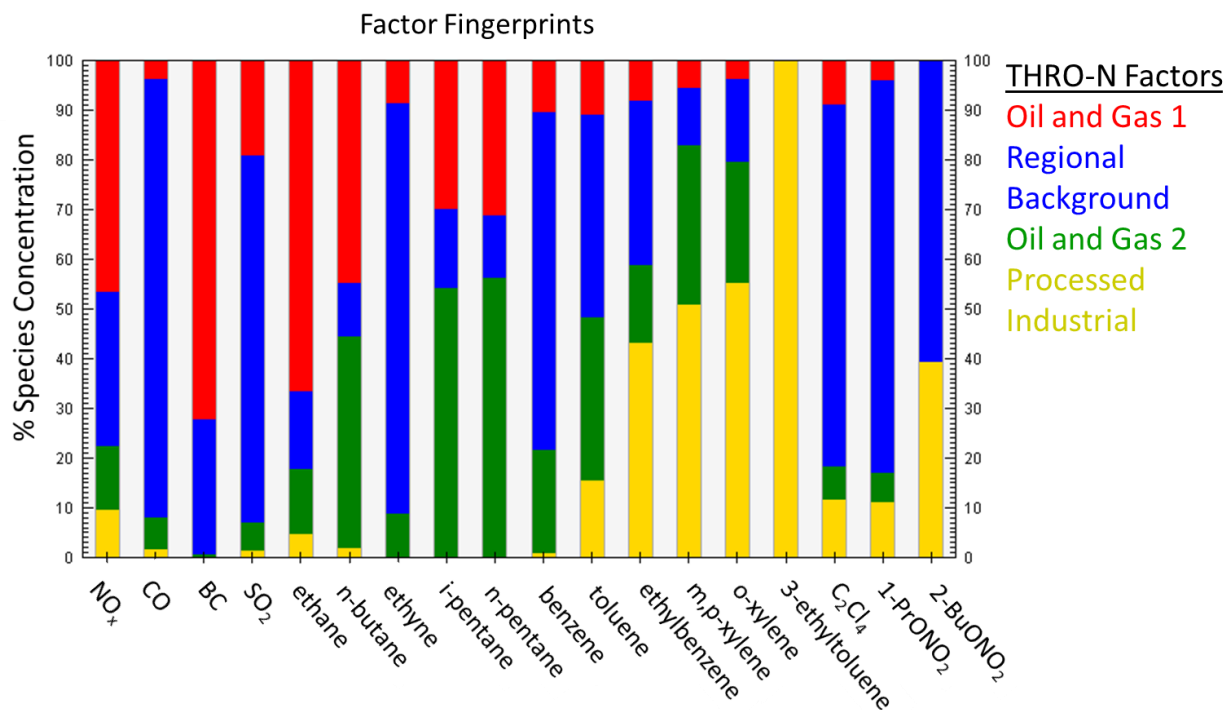
Figure E.3: The factor fingerprints of a four factor solution using VOC and other gas phase measurements collected during BAQS.

To further consider the differences in the four factors identified, the timelines of each factor are plotted in Figure E.4. The lack of peaks in the regional background factor reinforces the assignment as a background source. The other three factors show spikes that often overlap.

To take a closer look at the differences in the Oil and Gas factors, back trajectories from two time periods when each factor dominated the PMF analysis are shown (Figure E.4). The back trajectories show different potential source regions for each factor, suggesting regional differences in the oil and gas factors identified.
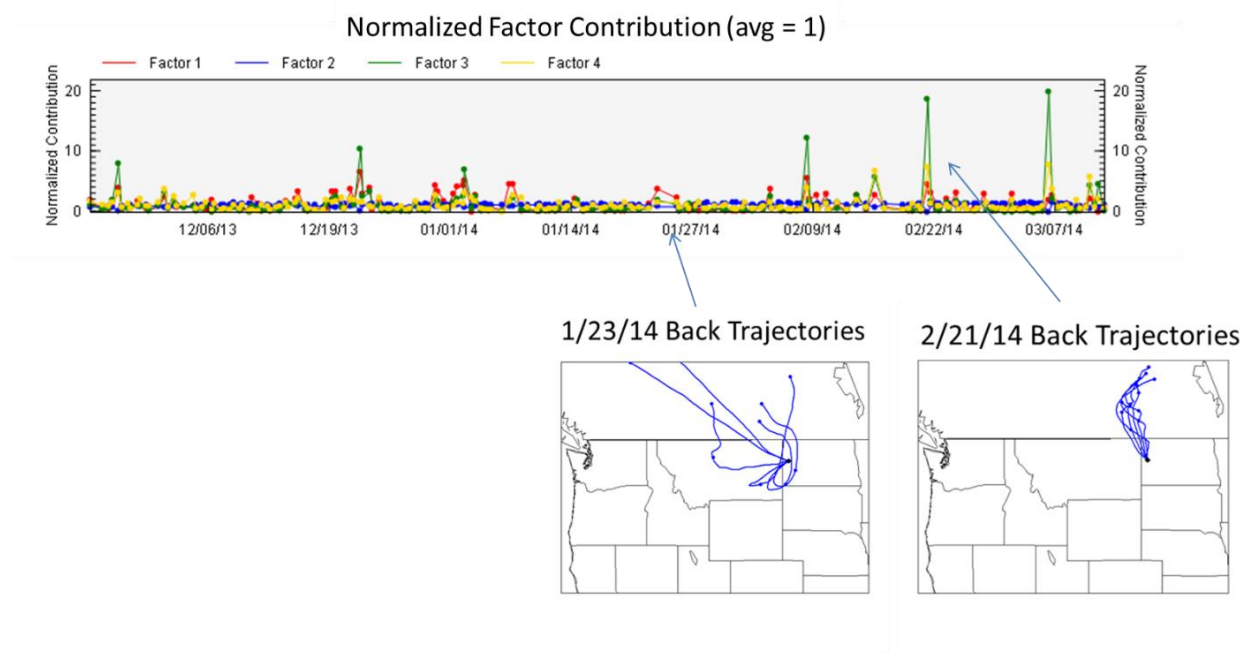
Figure E.4: The timelines of each factor from BAQS are plotted with two back trajectories that correspond the identified spikes in Factor 1 (Oil and Gas 1) and Factor 3 (Oil and Gas 2).

E.2 ROMO PMF Analysis

Real-time hourly VOC measurements during the Rocky Mountain National Park (ROMO) study were obtained. The same 5-channel GC/MS instrument that was described in Section 2.13 for canister analysis was operated in real-time at ROMO. The sampling site location (blue circle) and proximity to active oil wells (orange dots) are shown in Figure E.5.
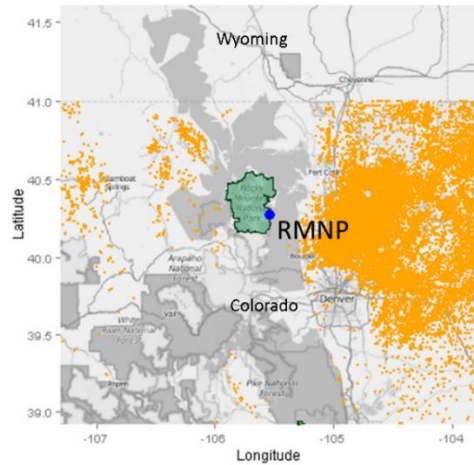
Figure E.5: A map of the ROMO study region showing the sampling site (blue circle; Rocky Mountain National Park, RMNP) where VOC measurements were taken and the locations of active oil wells (orange dots).

The concentrations of major VOC tracers, as described in the previous section, are shown in timelines in Figure E.6. The concentrations of NO_x, NH_3, and total inorganic $PM_{2.5}$ mass are also shown. Differences in the timelines of the VOC tracers indicate different emissions from local and regional sources are impacting the measurement site.
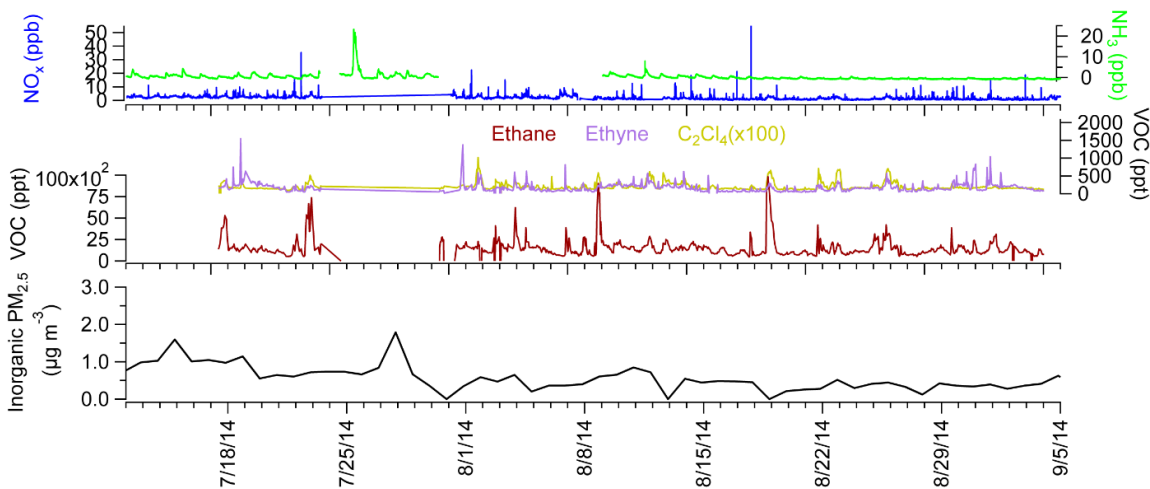
Figure E.6: Timelines of important VOC tracers including ethane (ppt, maroon), ethyne (ppt, purple) and C_2Cl_4 (ppt x100, yellow). Concentrations of NO_x (ppb, blue), NH_3 (ppb, green), and total inorganic $PM_{2.5}$ mass ($\mu g\ m^{-3}$, black) are also shown.

Even though differences in the timelines of the VOC tracers were observed, the factor profiles show significant overlap in the contributions of the VOC tracer species to each factor. The three anthropogenic factors are loosely termed "Upslope," "Combustion CO," and "Combustion NO_x." Each of these factors contains significant contributions from ethane, ethyne and C_2Cl_4, which indicates that the separation of these factors is not clear. The "Upslope" factor was labeled as urban and oil and gas because of the significant contributions from the light alkanes (ethane, butane, pentane) and C_2Cl_4. The two combustion factors had large contributions from NO_x or CO, but also containing the VOC tracers for combustion and urban emissions. The final factor was the biogenic factor (blue), which comprised almost all of the isoprene fingerprint. The biogenic factor also contained contributions from the BTEX species, which could suggest some influence of background concentrations of anthropogenic species associated with the biogenic source or an unidentified anthropogenic source that overlaps with the biogenic emissions.
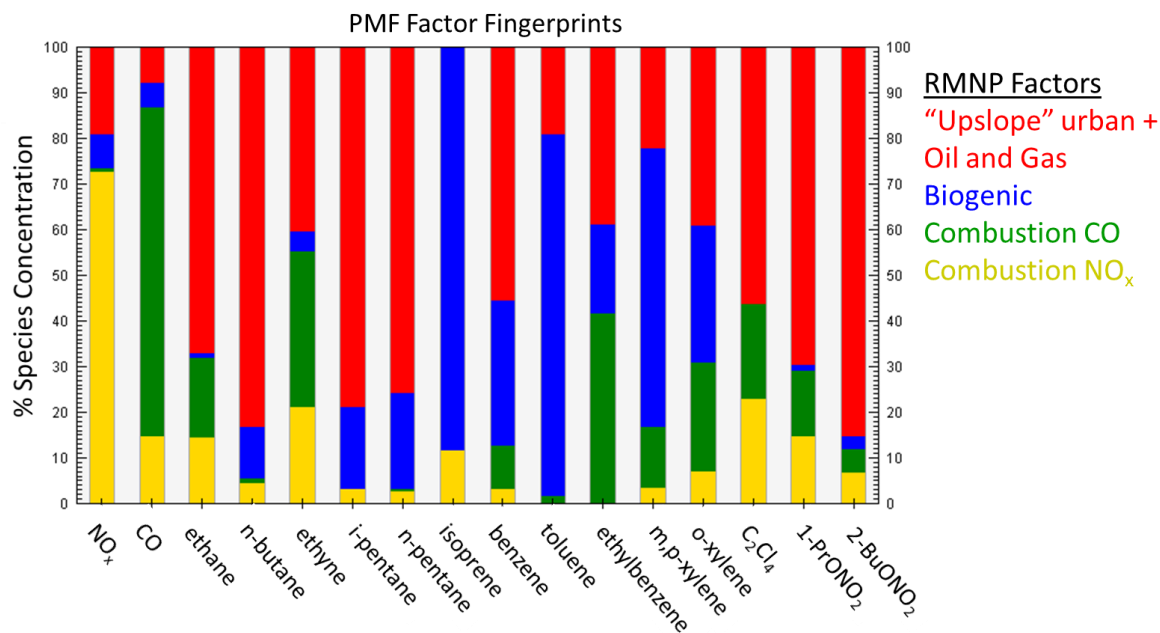
Figure E.7: The factor fingerprints of a four factor solution using VOC and other gas phase measurements collected during ROMO.

The differences in the timelines for each factor (Figure E.8) further suggest the possibility of two different combustion factors. These factors may be due to local traffic or other anthropogenic activities that originate from different source regions. Additionally, the upslope factor is generally low with limited spikes. This reflects the lack of upslope wind events observed during this study period. This limited the differences in the VOC concentrations observed which prevented a robust PMF analysis during this sampling period.
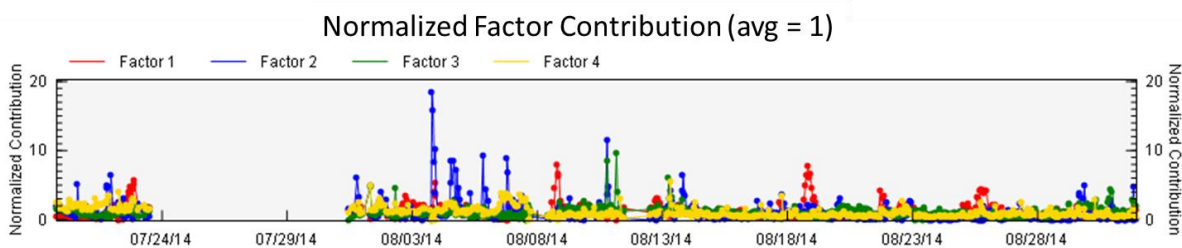
Figure E.8: Timelines of the four factors identified in the ROMO PMF analysis

APPENDIX F: URG, IMPROVE, PRECIPITATION, AND PASSIVE SAMPLER DATA
FROM BAQS I AND BAQS II

F.1 URG Data from BAQS I and II

The calculated ambient concentrations of URG aerosol and gas ionic species from

Theodore Roosevelt National Park, North Unit (THRO-N), Fort Union Trading Post National

Historic Site (FOUS), Medicine Lake National Wildlife Refuge (MELA), and Knife River Indian

Villages National Historic Site (KNRI) are presented in the table below. Three 48-hour samples

were collected each week at FOUS, MELA and KNRI and daily samples were collected at

THRO-N during BAQS I. During BAQS II, daily samples were collected at THRO-N

throughout the entire study. Daily samples were collected at FOUS between 11/23 – 12/18 and

1/31 – 3/26 while weekly samples were collected between 12/18 – 1/31. Weekly samples were

collected at MELA throughout BAQS II. These values are not blank corrected and missing

values are flagged according to the key below. Samples collected that were shorter or longer

than the normal sample duration are also flagged but the concentrations presented are valid for

the sample times listed. The sample volume was calculated at ambient temperature and pressure.

The ambient pressure was estimated using site elevation. Invalid measurements are not included.

Flags:

- Long: Sample was longer than 24 hours
- Short: Sample was shorter than 24 hours
- Ext: There was a problem with the denuder or filter extraction
- Nit: Problem with integrating the nitrate peak
- Pump: Issue with vacuum pump because of power loss or cold temperatures
- Denuder: An issue with the denuder prevented collect of gas or gas and aerosol
  measurements, which include the denuder was broken, the denuders were placed in the
  wrong order, etc.
- Daylight: Daylight Savings Time Started, but the URG continued to operate in Mountain
  Standard Time
- Tubing: Tubing was pinched and prevented proper airflow through instrument

Table F.1: Concentrations of inorganic gas and aerosol species (µg m^{-3}) collected using the URG sampler at THRO-N, FOUS, MELA, and KNRI during BAQS I

Start	Stop	Aerosol Cations (µg m^{-3})					Aerosol Anions (µg m^{-3})				Gases (µg m^{-3})			Flag

Theodore Roosevelt North Unit (THRO-N)

Start	Stop	Na$^+$	NH$_4^+$	K$^+$	Mg$^+$	Ca$^+$	Cl$^-$	NO$_2^-$	NO$_3^-$	SO$_4^{2-}$	NH$_3$	HNO$_3$	SO$_2$	
2/14/13 8:00	2/15/13 8:00	0.014	0.265	0.018	0.004	0.037	0.027	0.004	0.310	0.502	0.164	0.172	1.217	
2/15/13 8:00	2/16/13 8:00	0.018	0.368	0.023	0.006	0.036	0.024	0.005	0.523	0.470	0.220	0.284	1.233	
2/16/13 8:00	2/17/13 7:54	0.011	0.329	0.024	0.007	0.041	0.020	0.009	0.373	0.430	0.278	0.140	2.143	
2/17/13 7:55	2/18/13 8:00	0.023	0.799	0.037	0.007	0.035	0.042	0.006	0.787	1.207	0.468	0.120	2.299	
2/18/13 8:00	2/19/13 8:00	0.033	0.400	0.012	0.009	0.037	0.034	0.008	0.302	1.225	0.059	0.154	1.308	
2/19/13 9:57	2/20/13 8:00	0.029	0.336	0.006	0.005	0.031	0.050	0.003	0.249	0.587	0.116	0.093	1.628	Short
2/20/13 8:00	2/21/13 8:00	0.034	0.338	0.012	0.008	0.057	0.046	0.002	0.713	0.480	0.146	0.103	0.241	
2/21/13 8:00	2/22/13 8:00	0.031	1.376	0.025	0.011	0.123	0.061	0.005	3.186	1.153	0.195	0.149	0.686	
2/22/13 8:00	2/23/13 8:00	0.017	1.179	0.018	0.007	0.071	0.033	0.007	2.335	1.162	0.187	0.195	1.007	
2/23/13 8:00	2/24/13 8:00	0.009	0.574	0.007	0.004	0.033	0.019	0.003	0.876	0.330	0.400	0.157	1.180	
2/24/13 8:02	2/25/13 8:00	0.015	0.778	0.019	0.004	0.052	0.041	0.005	1.579	0.565	0.192	0.178	1.384	
2/25/13 8:00	2/26/13 8:00	0.011	0.093	0.003	0.003	0.038	0.037	0.003	0.044	0.200	0.186	0.060	0.205	

2/26/13 8:00	2/27/13 8:00	0.018	1.762	0.035	0.005	0.037	0.036	0.006	2.299	2.964	0.325	0.266	2.804
2/27/13 8:00	2/28/13 8:00	0.021	1.707	0.036	0.005	0.029	0.024	0.012	1.419	3.603	0.160	0.310	4.888
2/28/13 8:00	3/1/13 8:00	0.014	2.724	0.035	0.003	0.031	0.026	0.012	2.765	4.669	0.143	0.158	1.017
3/1/13 8:00	3/2/13 8:00	0.031	1.537	0.023	0.004	0.037	0.057	0.009	1.923	2.374	0.264	0.187	0.519
3/2/13 8:00	3/3/13 7:53	0.010	1.439	0.009	0.007	0.059	0.039	0.009	3.624	0.665	0.737	0.186	1.681
3/3/13 8:00	3/4/13 8:00	0.012	2.211	0.018	0.003	0.026	0.046	0.007	4.618	1.915	0.524	0.171	0.618
3/4/13 8:00	3/5/13 8:00	0.049	4.062	0.040	0.012	0.072	0.108	0.013	6.889	6.184	0.181	0.113	0.482
3/5/13 8:00	3/6/13 8:00	0.051	0.937	0.030	0.011	0.032	0.028	0.009	0.820	1.885	0.102	0.191	0.822
3/6/13 8:00	3/7/13 8:00	0.032	0.979	0.019	0.005	0.025	0.033	0.003	1.236	1.395	0.427	0.095	0.187
3/7/13 8:00	3/8/13 8:00	0.032	1.416	0.028	0.006	0.051	0.055	0.008	2.372	1.604	0.438	0.099	0.475
3/8/13 8:00	3/9/13 8:00	0.036	3.522	0.030	0.010	0.054	0.026	0.014	6.152	4.441	0.259	0.351	5.789
3/9/13 8:00	3/10/13 7:57	0.044	2.863	0.033	0.005	0.060	0.029	0.015	3.825	4.567	0.169	0.414	1.680
3/10/13 8:01	3/11/13 8:00	0.024	1.840	0.046	0.005	0.045	0.032	0.018	2.245	2.895	0.113	0.647	1.817
3/11/13 8:00	3/12/13 8:00	0.056	0.812	0.027	0.019	0.086	0.046	0.007	1.037	1.518	0.242	0.158	1.474
3/12/13 8:00	3/13/13 8:00	0.043	0.513	0.014	0.013	0.092	0.039	0.007	0.481	0.968	0.085	0.302	1.494
3/13/13 8:00	3/14/13 8:00	0.008	0.140	0.005	0.003	0.035	0.016	0.002	0.080	0.265	0.342	0.199	0.513
3/14/13 8:00	3/15/13 8:00	0.033	1.734	0.035	0.009	0.040	0.036	0.009	2.061	2.669	0.392	0.318	1.104

Start	End												
3/15/13 8:00	3/16/13 8:00	0.090	1.228	0.024	0.023	0.056	0.028	0.006	1.030	2.577	0.106	0.212	1.983
3/16/13 8:00	3/17/13 8:20	0.061	0.889	0.015	0.016	0.043	0.020	0.007	0.975	1.706	0.062	0.206	2.717
3/17/13 8:30	3/18/13 8:00	0.058	0.868	0.029	0.010	0.033	0.056	0.005	0.762	1.605	0.197	0.103	0.813
3/18/13 8:00	3/19/13 8:00	0.055	0.575	0.025	0.011	0.032	0.018	0.007	0.701	1.062	0.057	0.292	2.428
3/19/13 8:00	3/20/13 8:00	0.097	0.554	0.029	0.013	0.063	0.020	0.005	0.563	1.579	0.049	0.217	1.820
3/20/13 8:00	3/21/13 8:00	0.040	0.817	0.020	0.007	0.039	0.028	0.005	0.954	1.233	0.298	0.160	1.860
3/21/13 8:00	3/22/13 8:00	0.039	1.019	0.024	0.008	0.044	0.027	0.004	1.496	1.186	0.522	0.120	1.007
3/22/13 8:00	3/23/13 8:00	0.060	1.306	0.037	0.015	0.069	0.018	0.004	1.977	1.854	0.176	0.274	1.296
3/23/13 8:00	3/24/13 8:00	0.071	0.818	0.048	0.012	0.024	0.023	0.009	1.125	1.471	0.109	0.265	3.706
3/24/13 8:00	3/25/13 8:00	0.068	0.406	0.046	0.010	0.021	0.027	0.008	0.781	0.838	0.090	0.286	1.291
3/25/13 8:00	3/26/13 8:00	0.127	0.519	0.016	0.007	0.024	0.025	0.006	0.394	1.200	0.165	0.236	1.015
3/26/13 8:00	3/27/13 8:00	0.021	0.626	0.012	0.004	0.026	0.020	0.005	0.685	0.939	0.477	0.123	0.529
3/27/13 8:00	3/28/13 8:00	0.095	2.460	0.048	0.023	0.142	0.090	0.010	6.574	1.299	0.656	0.255	0.606
3/28/13 8:00	3/29/13 8:00	0.016	3.811	0.064	0.009	0.063	0.028	0.008	7.845	2.580	1.564	0.428	2.886
3/29/13 8:00	3/30/13 8:00	0.014	2.422	0.041	0.005	0.045	0.029	0.009	5.550	1.509	0.932	0.296	0.753
3/30/13 8:00	3/31/13 8:00	0.029	1.188	0.027	0.010	0.065	0.034	0.006	1.592	1.555	0.472	0.329	2.344
3/31/13 8:00	4/1/13 8:00	0.040	0.530	0.013	0.009	0.053	0.027	0.003	0.363	1.011	0.144	0.157	1.001

		Na⁺	NH₄⁺	K⁺	Mg⁺	Ca⁺	Cl⁻	NO₂⁻	NO₃⁻	SO₄²⁻	NH₃	HNO₃	SO₂	
4/1/13 8:00	4/2/13 8:00	0.036	0.819	0.024	0.012	0.069	0.029	0.006	0.768	1.467	0.294	0.246	1.092	
4/2/13 8:00	4/3/13 8:00	0.026	1.148	0.023	0.011	0.087	0.023	0.006	1.279	1.891	1.105	0.354	1.660	
4/3/13 8:00	4/4/13 8:00	0.021	0.734	0.019	0.011	0.081	0.026	0.004	0.758	1.098	0.938	0.242	0.780	
4/4/13 8:00	4/5/13 8:00	0.027	0.713	0.019	0.010	0.068	0.026	0.006	0.619	1.250	0.809	0.227	1.565	
4/5/13 8:00	4/6/13 8:00	0.017	0.669	0.018	0.010	0.086	0.022	0.004	0.616	0.979	1.899	0.245	0.457	

Fort Union Trading Post (FOUS)

		Na⁺	NH₄⁺	K⁺	Mg⁺	Ca⁺	Cl⁻	NO₂⁻	NO₃⁻	SO₄²⁻	NH₃	HNO₃	SO₂	
2/16/13 8:00	2/17/13 10:39	0.013	0.306	0.015	0.009	0.070	0.060	0.005	0.508	0.289	4.452	0.135	0.572	Short
2/21/13 11:00	2/24/13 10:53	1.128	0.738	0.027	0.022	0.141	0.038	0.007	3.201	0.896	1.497	0.359	1.516	Long
2/25/13 8:00	2/27/13 8:00	0.015	1.141	0.029	0.007	0.040	0.027	0.005	2.143	1.453	4.791	0.245	1.523	
2/27/13 8:00	3/1/13 8:00	0.029	2.173	0.050	0.009	0.049	0.034	0.007	3.128	3.752	0.855	0.313	2.284	
3/1/13 8:00	3/3/13 8:00	0.014	1.686	0.042	0.008	0.045	0.035	0.010	4.252	1.260	1.992	0.320	0.894	
3/4/13 8:00	3/6/13 8:00	0.043	0.908	0.040	0.008	0.034	0.042	0.005	1.265	1.497	0.244	0.229	0.872	
3/6/13 8:00	3/8/13 8:00	0.026	1.421	0.027	0.004	0.020	0.032	0.006	2.232	1.956	1.443	0.219	0.308	
3/8/13 8:00	3/10/13 8:00	0.031	3.325	0.071	0.005	0.030	0.027	0.010	6.305	4.181	0.642	0.720	2.488	
3/11/13 8:00	3/13/13 8:00	0.037	0.716	0.022	0.017	0.054	0.018	0.004	0.923	1.337	0.285	0.206	2.882	
3/13/13 8:00	3/15/13 8:00	0.023	0.947	0.031	0.008	0.039	0.031	0.006	1.382	1.323	2.493	0.287	0.850	

		Na$^+$	NH$_4^+$	K$^+$	Mg$^+$	Ca$^+$	Cl$^-$	NO$_2^-$	NO$_3^-$	SO$_4^{2-}$	NH$_3$	HNO$_3$	SO$_2$	
3/15/13 8:00	3/17/13 8:00	0.061	0.905	0.027	0.016	0.031	0.017	0.004	1.019	1.889	0.470	0.195	1.937	
3/18/13 8:00	3/20/13 8:00	0.061	0.706	0.027	0.014	0.033	0.017	0.005	1.240	1.174	0.353	0.270	2.128	
3/20/13 8:00	3/22/13 8:00	0.035	1.087	0.027	0.011	0.043	0.020	0.006	2.123	1.231	0.453	0.202	1.345	
3/22/13 8:00	3/24/13 8:00	0.061	0.865	0.045	0.011	0.032	0.021	0.005	1.633	1.392	0.182	0.418	1.615	
3/25/13 8:00	3/27/13 8:00	0.036	1.199	0.031	0.010	0.031	0.025	0.017	2.127	1.527	0.316	0.357	1.680	
3/27/13 8:00	3/29/13 8:00	0.018	4.742	0.085	0.012	0.059	0.026	0.009	14.31	2.088	1.249	0.529	0.889	
3/29/13 8:00	3/31/13 8:00	0.015	2.899	0.054	0.006	0.029	0.028	0.009	7.431	1.776	0.862	0.485	1.721	
4/1/13 8:00	4/3/13 8:00	0.037	1.592	0.038	0.011	0.053	0.043	0.005	2.237	2.394	3.983	0.204	0.783	
4/3/13 8:00	4/5/13 8:00	0.014	0.772	0.020	0.006	0.041	0.018	0.006	0.705	1.169	1.826	0.118	0.520	

Medicine Lake (MELA)

		Na$^+$	NH$_4^+$	K$^+$	Mg$^+$	Ca$^+$	Cl$^-$	NO$_2^-$	NO$_3^-$	SO$_4^{2-}$	NH$_3$	HNO$_3$	SO$_2$	
2/16/13 8:00	2/17/13 12:35	0.011	0.389	0.009	0.007	0.050	0.026	0.003	0.418	0.221	0.528	0.184	0.404	Short
2/18/13 8:00	2/20/13 8:00	0.141	1.153	0.149	0.026	0.112	0.339	0.019	0.555	3.404	1.006	0.273	4.032	
2/20/13 8:00	2/22/13 8:00	0.042	1.591	0.024	0.025	0.140	0.032	0.004	4.054	0.906	0.252	0.216	0.795	
2/22/13 8:00	2/24/13 8:00	0.013	0.924	0.015	0.007	0.053	0.021	0.006	2.210	0.616	0.531	0.241	0.595	
2/25/13 8:00	2/27/13 8:00	0.040	1.065	0.035	0.012	0.070	0.041	0.005	1.873	1.357	0.502	0.390	3.574	
2/27/13 8:00	3/1/13 8:00	0.016	1.448	0.038	0.005	0.027	0.025	0.008	1.671	2.953	0.104	0.283	2.317	

Start	End	Na$^+$	NH$_4^+$	K$^+$	Mg$^+$	Ca$^+$	Cl$^-$	NO$_2^-$	NO$_3^-$	SO$_4^{2-}$	NH$_3$	HNO$_3$	SO$_2$	
3/1/13 8:00	3/3/13 8:00	0.013	1.736	0.038	0.005	0.036	0.032	0.007	4.028	1.363	0.674	0.242	1.211	
3/4/13 8:00	3/6/13 8:00	0.069	1.225	0.068	0.010	0.036	0.038	0.012	1.270	2.373	0.163	0.273	2.374	
3/6/13 8:00	3/8/13 8:00	0.030	1.837	0.036	0.006	0.027	0.015	0.006	2.757	2.832	0.260	0.245	2.222	
3/8/13 8:00	3/10/13 8:00	0.035	2.467	0.063	0.008	0.042	0.024	0.015	3.893	3.938	0.086	0.552	2.344	
3/11/13 8:00	3/13/13 8:00	0.055	0.997	0.029	0.021	0.068	0.023	0.019	1.208	1.951	0.238	0.375	5.123	
3/13/13 8:00	3/15/13 8:00	0.055	0.628	0.017	0.012	0.025	0.017	0.005	0.680	1.168	0.561	0.223	0.765	
3/15/13 8:00	3/17/13 8:00	0.027	0.667	0.029	0.006	0.026	0.027	0.005	0.867	1.146	0.103	0.180	2.206	
3/18/13 8:00	3/20/13 8:00	0.151	1.633	0.057	0.026	0.037	0.018	0.018	2.323	3.161	0.134	1.122	9.747	
3/20/13 8:00	3/22/13 8:00	0.077	1.276	0.031	0.015	0.067	0.082	0.006	2.361	1.454	0.277	0.311	4.007	
3/22/13 8:00	3/24/13 8:00	0.075	1.017	0.053	0.012	0.035	0.045	0.008	1.773	1.398	0.091	0.285	2.439	
3/25/13 8:00	3/27/13 8:00	0.069	2.366	0.061	0.013	0.082	0.027	0.012	5.530	3.326	0.152	1.305	2.685	
3/27/13 8:00	3/29/13 8:00	0.057	1.625	0.026	0.001	0.007	0.015	0.009	3.531	1.982	0.044	1.128	2.068	
3/29/13 8:00	3/31/13 8:00	0.015	2.516	0.048	0.006	0.032	0.028	0.010	5.864	1.854	0.432	0.383	2.039	
4/1/13 8:00	4/3/13 8:00	0.028	1.751	0.036	0.010	0.045	0.027	0.008	2.212	2.862	0.753	0.689	3.975	
4/3/13 8:00	4/4/13 10:17	0.010	0.716	0.012	0.004	0.023	0.011	0.005	0.618	1.090	0.782	0.147	0.531	Short

Knife River Indian Villages (KNRI)

		Na$^+$	NH$_4^+$	K$^+$	Mg$^+$	Ca$^+$	Cl$^-$	NO$_2^-$	NO$_3^-$	SO$_4^{2-}$	NH$_3$	HNO$_3$	SO$_2$	

2/15/13 8:00	2/17/13 8:00	0.111	5.141	0.114	0.014	0.145	0.107	0.025	9.522	4.267	2.222	1.524	11.38	
2/17/13 8:00	2/19/13 8:00	0.025	0.444	0.021	0.005	0.019	0.029	0.003	0.496	0.922	0.387	0.105	1.071	
2/20/13 8:00	2/22/13 8:00	0.054	1.610	0.038	0.030	0.216	0.077	0.014	4.004	0.828	0.393	0.256	23.87	
2/22/13 8:00	2/24/13 8:00	0.043	1.928	0.051	0.016	0.109	0.059	0.008	5.206	1.325	0.539	0.338	13.64	
2/24/13 8:00	2/26/13 8:00	0.033	0.756	0.021	0.002	0.015	0.021	0.005	1.779	0.533	0.635	0.128	0.651	
2/27/13 8:00	3/1/13 8:00	0.021	1.322	0.030	0.005	0.028	0.041	0.009	0.880	2.916	0.392	0.133	4.176	
3/1/13 8:00	3/3/13 8:00	0.019	0.456	0.008	0.004	0.016	0.019	0.003	0.333	0.568	0.871	0.257	4.708	
3/3/13 8:00	3/3/13 17:00	0.221	1.547	0.030	0.005	0.056	0.069	0.006	3.315	1.351	2.006	0.102	2.487	Short
3/6/13 8:00	3/8/13 8:00	0.035	2.072	0.044	0.006	0.037	0.039	0.005	3.462	2.489	0.953	0.104	1.890	
3/8/13 8:00	3/10/13 8:00	0.044	3.579	0.084	0.007	0.034	0.029	0.012	4.987	5.603	0.208	0.504	7.317	
3/10/13 8:00	3/12/13 8:00	0.038	1.036	0.040	0.011	0.032	0.028	0.006	1.265	1.729	0.312	0.166	2.941	
3/13/13 8:00	3/15/13 8:00	0.044	0.812	0.019	0.011	0.042	0.024	0.004	1.258	1.081	2.063	0.306	2.355	
3/15/13 8:00	3/17/13 8:00	0.077	0.594	0.027	0.017	0.025	0.023	0.005	0.643	1.226	0.136	0.203	4.865	
3/17/13 8:00	3/19/13 8:00	0.053	0.593	0.025	0.016	0.047	0.025	0.000	0.778	1.223	0.287	0.262	7.443	
3/27/13 8:00	3/29/13 8:00	0.022	2.932	0.043	0.012	0.063	0.057	0.008	6.617	2.127	1.848	0.291	12.36	
3/29/13 8:00	3/31/13 8:00	0.035	3.124	0.054	0.008	0.046	0.052	0.007	7.047	2.473	1.514	0.705	8.818	
3/31/13 8:00	4/2/13 8:00	0.106	0.821	0.021	0.007	0.031	0.017	0.002	1.023	1.363	0.413	0.134	1.284	

Table F.2: Concentrations of inorganic gas and aerosol species (µg m⁻³) collected using the URG sampler at THRO-N, FOUS, and MELA during BAQS II. Replicate samples collected at THRO-N are also listed.

Start	Stop	Aerosol Cations (µg m⁻³)					Aerosol Anions (µg m⁻³)				Gases (µg m⁻³)				Flag

North Unit of Theodore Roosevelt (THRO-N)

Start	Stop	Na^+	NH_4^+	K^+	Mg^+	Ca^+	Cl^-	NO_2^-	NO_3^-	SO_4^{2-}	HNO_2	HNO_3	SO_2	NH_3	
11/22/13 9:08	11/24/13 8:02	0.049	0.938	0.026	0.013	0.046	0.048	0.006	2.187	1.558	0.143	0.332	2.184	0.098	Long
11/24/13 8:06	11/25/13 8:00	0.009	0.177	0.010	0.006	0.037	0.015	0.016	0.157	0.356	0.075	0.285	1.737	0.258	
11/25/13 8:04	11/26/13 8:07	0.027	0.463	0.020	0.020	0.095	0.027	0.004	0.715	0.570	0.066	0.144	1.570	0.246	
11/26/13 8:11	11/27/13 8:00	0.034	0.310	0.014	0.019	0.103	0.038	0.002	0.450	0.485	0.051	0.238	1.034	0.147	
11/27/13 8:03	11/28/13 8:11	0.013	0.911	0.025	0.016	0.084	0.022	0.007	1.322	1.483	0.045	0.205	0.574	0.212	
11/28/13 8:11	11/29/13 8:07	0.010	1.191	0.026	0.013	0.069	0.014	0.002	1.499	1.756	0.036	0.189	0.450	0.107	
11/29/13 8:20	11/30/13 8:03	0.005	0.307	0.007	0.011	0.062	0.019	0.004	0.387	0.513	0.080	0.142	0.535	0.179	
11/30/13 8:09	11/30/13 7:52	0.014	0.837	0.027	0.015	0.070	0.031	0.008	2.158	0.639	0.131	0.124	1.513	0.250	
12/1/13 7:59	12/1/13 8:00	0.010	0.353	0.009	0.011	0.060	0.010	0.008	0.514	0.290	0.060	0.116	1.635	0.225	
12/2/13 8:07	12/3/13 8:15	0.050	1.090	0.039	0.018	0.087	0.085	0.008	1.656	1.355	0.041	0.099	0.138	0.244	
12/3/13 8:18	12/4/13 8:10	0.032	0.296	0.011	0.022	0.065	0.049	0.002	0.381	0.765	0.078	0.124	2.519	0.040	
12/4/13 8:12	12/4/13 8:00	0.054		0.025	0.012	0.021	0.029	0.005	0.495	0.832	0.055	0.215	0.907	0.046	Ext AmB

Start	End															Note
12/5/13 8:20	12/6/13 8:25	0.092	0.362	0.021	0.021	0.036	0.084	0.000	0.713	0.762	0.052	0.142	3.313	0.043	
12/6/13 11:00	12/7/13 8:00														Pump
12/7/13 8:18	12/8/13 15:04														Pump
12/8/13 15:06	12/9/13 8:04	0.069	0.402	0.024	0.013	0.036	0.013	0.000	0.531	0.754	0.111	0.234	2.228	0.017	Short
12/9/13 8:06	12/10/13 8:21	0.035	0.224	0.011	0.009	0.025	0.018	0.001	0.236	0.531	0.056	0.176	1.545	0.029	
12/10/13 8:31	12/11/13 8:10	0.072	0.151	0.009	0.014	0.021	0.040	0.000	0.180	0.402	0.060	0.139	1.295	0.019	
12/11/13 8:10	12/12/13 8:25	0.027	0.174	0.005	0.005	0.018	0.021	0.002	0.091	0.403	0.103	0.130	1.605	0.085	
12/12/13 8:31	12/13/13 7:57	0.046	1.446	0.012	0.008	0.024	0.011	0.006	1.213	1.702	0.181	0.259	3.345	0.075	
12/13/13 7:57	12/14/13 7:52	0.093	1.832	0.029	0.018	0.060	0.016	0.008	1.080	2.880	0.206	0.232	3.330	0.036	
12/14/13 7:57	12/15/13 8:14	0.089	1.534	0.056	0.014	0.082	0.013	0.004	1.487	2.277	0.193	0.473	3.794	0.025	
12/15/13 8:16	12/16/13 8:06	0.032	0.653	0.009	0.007	0.021	0.009	0.004	0.712	1.013	0.114	0.390	2.014	0.122	
12/16/13 8:07	12/17/13 8:13	0.014	0.074	0.008	0.002	0.020	0.006	0.002	0.050	0.166	0.033	0.229	0.794	0.110	
12/17/13 8:14	12/18/13 8:41	0.008	0.090	0.003	0.002	0.013	0.008	0.008	0.032	0.184	0.049	0.199	0.462	0.105	
12/18/13 8:44	12/19/13 8:09	0.059	0.455	0.026	0.014	0.040	0.028	0.008	0.734	0.821	0.098	0.241	1.645	0.087	
12/19/13 8:12	12/20/13 8:26	0.078	0.271	0.021	0.019	0.053	0.027	0.000	0.409	0.709	0.099	0.086	1.716	0.032	
12/20/13 8:28	12/21/13 9:21	0.042	0.370	0.018	0.011	0.034	0.014	0.003	0.813	0.879	0.197	0.219	1.909	0.038	
12/21/13 9:22	12/22/13 8:56	0.064	1.947	0.072	0.012	0.020	0.025	0.015	2.933	2.876	0.247	0.240	5.265	0.073	

12/22/13 8:58	12/23/13 9:30	0.059	0.773	0.032	0.013	0.039	0.020	0.026	2.073	1.194	0.098	0.229	2.076	0.098	Pump
12/23/13 9:30	12/24/13 8:22	0.040	0.867	0.039	0.008	0.043	0.032	0.014	1.547	1.979	0.008	0.681	3.940	0.071	Short
12/24/13 10:20	12/25/13 8:38	0.005	0.229	0.017	0.002	0.009	0.007	0.004	0.473	0.227	0.098	0.301	2.171	0.124	Short
12/25/13 8:45	12/26/13 8:15	0.008	0.132	0.006	0.002	0.009	0.006	0.003	0.102	0.148	0.050	0.391	1.512	0.112	
12/26/13 8:16	12/27/13 8:16	0.011	0.051	0.017	0.002	0.015	0.009	0.003	0.111	0.146	0.053	0.365	0.680	0.247	
12/27/13 8:18	12/28/13 8:00	0.006	0.114	0.007	0.001	0.011	0.009	0.005	0.073	0.141	0.038	0.352	0.552	0.192	
12/28/13 8:03	12/29/13 7:57	0.376	0.345	0.028	0.060	0.030	0.598	0.002	0.212	0.727	0.053	0.269	1.763	0.045	
12/29/13 8:07	12/30/13 8:06	0.042	0.308	0.007	0.007	0.014	0.031	0.000	0.415	0.286	0.180	0.212	1.470	0.056	
12/30/13 8:11	12/31/13 8:12	0.128	0.691	0.023	0.019	0.019	0.029	0.005	1.429	0.691	0.354	0.311	3.985	0.032	
12/31/13 8:20	1/1/14 8:10	0.129	0.708	0.036	0.016	0.018	0.040	0.006	0.796	1.254	0.288	0.268	8.044	0.038	
1/1/14 9:00	1/2/14 8:47	0.107	0.971	0.029	0.014	0.016	0.013	0.005	1.585	1.370	0.231	0.492	4.906	0.029	
1/2/14 8:51	1/3/14 8:20	0.025	0.440	0.010	0.004	0.020	0.017	0.010	0.318	1.152	0.105	0.532	1.921	0.059	
1/3/14 8:22	1/4/14 8:05	0.016	0.304	0.012	0.003	0.007	0.011	0.003	0.167	0.541	0.085	0.280	1.014	0.095	
1/4/14 8:08	1/6/14 13:40	0.029	0.200	0.006	0.004	0.011	0.019	0.000	0.148	0.456	0.069	0.255	1.766	0.022	
1/6/14 13:40	1/7/14 7:58	0.034	0.162	0.005	0.004	0.011	0.024	0.000	0.168	0.301	0.101	0.214	1.716	0.121	
1/7/14 8:00	1/8/14 8:27	0.041	0.284	0.003	0.005	0.009	0.008	0.003	0.643	0.292	0.277	0.700	2.433	0.035	
1/8/14 8:31	1/9/14 8:00	0.019	0.527	0.005	0.003	0.011	0.009	0.005	0.629	0.793	0.173	0.541	2.457	0.045	

Start	End															Label
1/9/14 8:00	1/10/14 8:06	0.005	0.092	0.002	0.001	0.005	0.008	0.000	0.031	0.086	0.096	0.764	0.564	0.093		
1/10/14 8:10	1/11/14 7:55	0.024	0.138	0.004	0.004	0.013	0.020	0.000	0.194	0.055	0.091	0.428	0.832	0.091		
1/11/14 7:55	1/12/14 8:00	0.011	0.097	0.003	0.003	0.013	0.020	0.005		0.094	0.039	0.412	0.731	0.182	Nit
1/12/14 8:00	1/13/14 7:58	0.021	0.257	0.006	0.002	0.010	0.011	0.002	0.248	0.260	0.068	0.329	0.897	0.130	
1/13/14 7:58	1/14/14 8:05	0.007	0.084	0.003	0.003	0.012	0.015	0.006	0.060	0.088	0.053	0.301	1.272	0.178	
1/14/14 8:05	1/15/14 8:01	0.014	0.268	0.004	0.002	0.013	0.009	0.002	0.392	0.145	0.109	0.212	0.999	0.166	
1/15/14 8:02	1/16/14 7:59	0.024	0.083	0.005	0.004	0.022	0.028	0.004	0.042	0.136	0.027	0.219	0.889	0.276	
1/16/14 8:00	1/17/14 8:12	0.038	0.164	0.008	0.008	0.025	0.033	0.003	0.135	0.191	0.164	0.084	0.506	0.142	
1/17/14 8:13	1/18/14 8:05	0.021	0.128	0.007	0.003	0.014	0.018	0.005	0.101	0.115	0.017	0.289	0.783	0.332	
1/18/14 8:05	1/19/14 8:00	0.006	0.139	0.007	0.001	0.015	0.007	0.000	0.046	0.120	0.030	0.115	0.603	0.256	
1/19/14 8:00	1/20/14 8:00	0.021	0.120	0.009	0.003	0.013	0.016	0.001	0.080	0.150	0.017	0.275	0.804	0.363	
1/20/14 8:00															Denuder
1/21/14 8:25	1/22/14 8:05	0.040	0.518	0.013	0.009	0.025	0.022	0.008	0.923	0.578	0.054	0.134	1.290	0.115	
1/22/14 8:00	1/23/14 7:55	0.065	0.088	0.018	0.020	0.084	0.055	0.000	0.297	0.224	0.064	0.125	0.498	0.026	
1/23/14 7:55	1/24/14 8:21	0.041	0.462	0.012	0.004	0.020	0.009	0.000	0.801	0.413	0.053	0.209	1.089	0.158	
1/24/14 8:21	1/25/14 9:30	0.007	0.173	0.009	0.003	0.017	0.020	0.020	0.233	0.171	0.057	0.214	1.204	0.429	
1/25/14 9:30	1/26/14 8:58	0.024		0.051	0.003	0.068	0.010	0.000	0.201	0.127	0.032	0.215	0.826	0.369	

1/26/14 8:20	1/27/14 7:55	0.062	0.107	0.029	0.015	0.076	0.064	0.000	0.141	0.194	0.014	0.047	0.047	0.056	
1/27/14 7:55	1/28/14 8:10	0.077	0.165	0.104	0.013	0.096	0.094	0.007	0.407	0.296	0.060	0.195	0.808	0.037	
1/28/14 8:20	1/29/14 8:00	0.012	0.247	0.013	0.003	0.036	0.008	0.005	0.467	0.190	0.061	0.220	1.094	0.098	
1/29/14 8:00	1/30/14 8:00	0.037	0.622	0.036	0.008	0.048	0.020	0.009	1.453	0.342	0.071	0.259	1.453	0.079	
1/30/14 8:00	1/31/14 8:18	0.033	0.252	0.023	0.009	0.037	0.017	0.000	0.322	0.573	0.013	0.107	0.682	0.039	
1/31/14 8:23	2/1/14 8:10	0.018	0.364	0.029	0.006	0.046	0.009	0.004	0.464	0.565	0.050	0.256	2.376	0.042	
2/1/14 8:12	2/2/14 8:06	0.012	0.237	0.008	0.002	0.013	0.007	0.000	0.135	0.439	0.017	0.151	1.235	0.051	
2/2/14 8:08	2/3/14 8:10	0.027	0.317	0.047	0.005	0.044	0.022	0.004	0.518	0.550	0.054	0.182	1.248	0.091	
2/3/14 8:14	2/4/14 8:00	0.059	0.144	0.020	0.014	0.108	0.020	0.002	0.241	0.144	0.045	0.238	0.446	0.051	
2/4/14 8:01	2/5/14 8:06	0.060	0.184	0.010	0.016	0.058	0.032	0.000	0.504	0.212	0.074	0.271	0.541	0.045	Pump
2/5/14 8:07	2/6/14 7:56	0.071	0.236	0.018	0.014	0.032	0.028	0.002	0.542	0.262	0.047	0.139	1.371	0.042	
2/6/14 7:58	2/7/14 7:58	0.046	0.379	0.026	0.007	0.024	0.014	0.006	0.751	0.485	0.062	0.277	1.607	0.048	
2/7/14 8:00	2/8/14 7:57	0.012	0.246	0.006	0.006	0.045	0.009	0.003	0.299	0.376	0.089	0.205	0.545	0.035	
2/8/14 7:59	2/9/14 7:59	0.055	0.661	0.033	0.023	0.100	0.017	0.006	1.442	0.728	0.103	0.550	3.834	0.052	
2/9/14 8:01	2/10/14 8:23	0.053	0.118	0.036	0.017	0.083	0.021	0.002	0.319	0.529	0.058	0.104	1.587	0.031	
2/10/14 8:23	2/11/14 7:53	0.035	0.739	0.029	0.008	0.062	0.030	0.020	0.931	0.870	0.147	0.448	2.695	0.069	
2/11/14 7:55	2/12/14 7:58	0.045	0.514	0.049	0.013	0.060	0.021	0.007	1.092	0.696	0.071	0.243	0.679	0.083	

2/12/14 8:00	2/13/14 7:54	0.036	0.625	0.023	0.010	0.045	0.017	0.003	0.798	0.818	0.034	0.272	1.220	0.131
2/13/14 7:56	2/14/14 8:03	0.981	1.574	0.039	0.020	0.052	0.026	0.000	2.894	1.955	0.130	0.301	2.630	0.051
2/14/14 8:06	2/15/14 7:54	0.032	0.688	0.021	0.007	0.033	0.016	0.010	1.004	0.747	0.128	0.547	1.339	0.179
2/15/14 7:56	2/16/14 7:58	0.040	1.915	0.019	0.008	0.030	0.018	0.009	1.835	3.887	0.069	0.350	2.982	0.075
2/16/14 8:00	2/17/14 8:16	0.016	0.615	0.006	0.003	0.014	0.022	0.000	0.401	0.852	0.027	0.210	0.505	0.142
2/17/14 8:18	2/18/14 8:04	0.022	0.088	0.005	0.005	0.040	0.020	0.000	0.031	0.125	0.053	0.448	0.321	0.317
2/18/14 8:06	2/19/14 7:58	0.006	0.151	0.002	0.003	0.020	0.011	0.000	0.119	0.139	0.040	0.100	0.554	0.429
2/19/14 8:00	2/20/14 8:05	0.023	0.216	0.008	0.006	0.025	0.025	0.009	0.181	0.340	0.018	0.105	0.384	0.302
2/20/14 8:06	2/21/14 8:02	0.057	0.467	0.015	0.016	0.056	0.037	0.000	0.839	0.653	0.096	0.076	0.386	0.143
2/21/14 8:04	2/22/14 7:50	0.086	0.386	0.022	0.020	0.042	0.030	0.000	0.559	0.505	0.049	0.236	1.488	0.068
2/22/14 7:52	2/23/14 7:55	0.093	0.446	0.024	0.021	0.045	0.038	0.000	0.859	0.669	0.027	0.234	0.678	0.090
2/23/14 7:57	2/24/14 8:07	0.094	0.348	0.014	0.028	0.040	0.023	0.004	0.513	0.700	0.096	0.182	0.480	0.048
2/24/14 8:08	2/25/14 8:09	0.095	0.367	0.016	0.023	0.026	0.020	0.008	0.393	0.868	0.046	0.158	1.294	0.029
2/25/14 8:09	2/26/14 7:53	0.060	0.477	0.013	0.014	0.025	0.013	0.009	0.738	0.785	0.052	0.186	1.111	0.042
2/26/14 7:55	2/27/14 7:55	0.040	0.592	0.021	0.017	0.104	0.017	0.006	1.327	0.534	0.088	0.268	0.939	0.038
2/27/14 7:57	2/28/14 7:53	0.042	0.980	0.028	0.017	0.084	0.033	0.012	1.889	0.846	0.099	0.294	1.441	0.062
2/28/14 7:53	3/1/14 7:59													Denuder

Start	End														Notes
3/1/14 7:59	3/2/14 8:32	0.176	0.254	0.024	0.077	0.089	0.294	0.007	0.196	0.631	0.043	0.074	0.096	0.030	
3/2/14 8:48	3/3/14 8:00	0.104	0.298	0.018	0.035	0.052	0.099	0.000	0.323	0.729	0.043	0.200	1.187	0.031	
3/3/14 8:00	3/4/14 8:00	0.079	0.869	0.017	0.023	0.046	0.044	0.005	1.460	1.019	0.125	0.224	1.498	0.050	
3/4/14 8:00	3/5/14 8:00	0.067	1.331	0.030	0.020	0.048	0.034	0.000	2.293	1.232	0.088	0.187	0.981	0.076	
3/5/14 8:00	3/6/14 8:00	0.016	0.534	0.010	0.004	0.017	0.014	0.005	0.739	0.490	0.208	0.477	0.500	0.321	
3/6/14 8:01	3/7/14 8:00	0.049	1.900	0.065	0.010	0.032	0.029	0.013	2.871	2.455	0.077	0.323	1.036	0.097	
3/7/14 8:00	3/8/14 8:00	0.043	1.635	0.029	0.010	0.030	0.019	0.006	2.248	2.076	0.089	0.205	0.768	0.114	
3/8/14 8:00	3/9/14 8:00	0.011	0.355	0.010	0.003	0.013	0.006	0.005	0.188	0.554	0.033	0.363	0.375	0.387	Daylight
3/9/14 8:00	3/10/14 8:00	0.027	0.062	0.002	0.002	0.014	0.035	0.000	0.022	0.052	0.072	0.131	0.265	0.807	
3/10/14 8:00	3/11/14 8:08	0.008	0.398	0.014	0.003	0.015	0.017	0.008	0.618	0.180	0.153	0.242	0.468	0.626	
3/11/14 8:08	3/12/14 8:00	0.014	0.283	0.017	0.002	0.033	0.006	0.000	0.541	0.232	0.085	0.181	0.520	0.441	
3/12/14 8:00	3/13/14 7:59	0.008	0.145	0.012	0.002	0.030	0.006	0.004	0.071	0.204	0.030	0.152	0.200	0.720	
3/13/14 7:59	3/14/14 7:55	0.009	0.206	0.004	0.004	0.026	0.011	0.003	0.181	0.246	0.060	0.172	0.570	0.627	
3/14/14 7:55	3/15/14 7:57	0.019	0.761	0.008	0.006	0.031	0.015	0.000	0.647	0.967	0.048	0.103	0.802	0.500	
3/15/14 7:57	3/16/14 7:58	0.036	0.865	0.007	0.007	0.016	0.034	0.000	0.776	1.138	0.036	0.098	0.403	0.427	
3/16/14 7:58	3/17/14 7:59	0.023	0.189	0.005	0.006	0.025	0.010	0.000	0.136	0.278	0.134	0.112	0.202	0.612	
3/17/14 8:00	3/18/14 8:08	0.012	0.797	0.013	0.006	0.025	0.018	0.009	1.590	0.424	0.119	0.268	1.393	0.582	

Start	End														
3/18/14 8:08	3/19/14 8:00	0.009	0.316	0.003	0.004	0.022	0.008	0.005	0.341	0.356	0.035	0.099	0.095	0.350	
3/19/14 8:00	3/20/14 8:00	0.009	0.506	0.004	0.003	0.019	0.008	0.003	0.471	0.657	0.062	0.204	0.396	0.399	
3/20/14 8:00	3/21/14 7:59	0.150	0.443	0.005	0.003	0.012	0.011	0.001	0.260	0.680	0.018	0.199	0.173	0.434	
3/21/14 7:59	3/22/14 8:00	0.052	0.553	0.020	0.016	0.050	0.069	0.020	0.405	0.999	0.038	0.075	0.088	0.116	
3/22/14 8:00	3/23/14 7:58	0.025	0.663	0.013	0.012	0.054	0.031	0.002	0.542	1.108	0.030	0.041	0.206	0.090	
3/23/14 7:58	3/24/14 7:59	0.062	0.865	0.010	0.018	0.071	0.021	0.004	1.243	1.044	0.091	0.166	0.352	0.178	
3/24/14 7:59	3/25/14 8:00	0.085	0.589	0.008	0.007	0.028	0.019	0.004	0.626	0.903	0.033	0.173	0.259	0.097	
3/25/14 8:00	3/26/14 8:04	0.023	0.499	0.009	0.006	0.036	0.018	0.000	0.504	0.632	0.033	0.095	0.254	0.293	
3/26/14 8:13	3/27/14 7:00	0.040	1.015	0.017	0.025	0.117	0.017	0.004	2.204	0.767	0.097	0.164	0.517	0.770	
Replicate Samples															
12/10/13 8:31	12/11/13 8:10	0.079	0.152	0.010	0.018	0.027	0.051	0.019	0.194	0.425	0.057	0.129	1.325	0.048	
12/12/13 8:31	12/13/13 7:57	0.040	1.246	0.009	0.009	0.045	0.010	0.004	1.301	1.849	0.182	0.253	3.640	0.068	
2/10/14 8:14	2/11/14 7:55	0.028	0.722	0.025	0.006	0.037	0.011	0.003	0.909	0.726	0.063	0.331	2.196	0.091	
2/18/14 8:07	2/19/14 8:00	0.007	0.123	0.001	0.002	0.014	0.011	0.001	0.100	0.113	0.022	0.145	0.383	0.338	
2/25/14 8:09	2/26/14 7:55	0.059	0.469	0.013	0.014	0.023	0.015	0.007	0.722	0.779	0.050	0.164	1.116	0.029	
3/26/14 8:15	3/27/14 7:00	0.061	0.926	0.020	0.051	0.264	0.043	0.014	1.930	0.854	0.119	0.218	0.613	0.771	

Fort Union Trading Post (FOUS)

		Na$^+$	NH$_4^+$	K$^+$	Mg$^+$	Ca$^+$	Cl$^-$	NO$_2^-$	NO$_3^-$	SO$_4^{2-}$	HNO$_2$	HNO$_3$	SO$_2$	NH$_3$	
11/23/13 12:45	11/24/13 11:00	0.056	1.458	0.063	0.018	0.085	0.094	0.018	2.903	1.503	0.376	0.240	1.848	0.647	
11/24/13 11:00	11/25/13 11:00	0.010	0.175	0.007	0.004	0.024	0.020	0.024	0.265	0.282	0.136	0.292	1.325	1.045	
11/25/13 11:07	11/26/13 11:00	0.019	0.468	0.014	0.006	0.031	0.039	0.035	0.763	0.653	0.089	0.115	1.488	0.343	
11/26/13 11:00	11/27/13 11:00	0.034	0.510	0.014	0.021	0.099	0.035	0.012	0.801	0.691	0.157	0.308	1.027	0.735	
11/27/13 11:12	11/28/13 11:00	0.008	0.760	0.020	0.010	0.054	0.015	0.009	0.940	1.417	0.033	0.176	0.241	0.135	
11/28/13 11:00	11/29/13 11:00	0.016	1.073	0.018	0.012	0.068	0.028	0.008	1.662	1.457	0.141	0.133	0.348	0.348	
11/29/13 11:04	11/30/13 11:00	0.017	0.683	0.037	0.019	0.109	0.036	0.010	1.358	0.680	0.686	0.086	0.586	1.519	
11/30/13 11:06	12/1/13 11:00	0.050	1.850	0.047	0.027	0.114	0.036	0.017	4.724	1.067	0.379	0.159	2.832	2.347	
12/1/13 11:00	12/3/13 11:00	0.017	0.792	0.021	0.011	0.043	0.040	0.016	1.381	0.914	0.057	0.169	0.619	0.971	
12/3/13 11:24	12/4/13 11:00	0.034	0.319	0.029	0.015	0.057	0.037	0.005	0.288	0.705	0.041	0.055	1.277	0.167	
12/4/13 11:00	12/5/13 11:00	0.065	0.414	0.030	0.014	0.026	0.034	0.008	0.624	0.859	0.093	0.185	1.830	0.064	
12/5/13 11:00	12/6/13 11:00	0.226	0.419	0.038	0.046	0.076	0.114	0.020	0.926	1.078	0.086	0.213	3.350	0.038	
12/6/13 11:00	12/7/13 11:00	0.387	0.866	0.039	0.069	0.051	0.104	0.019	2.110	1.350	0.190	0.426	2.441	0.019	
12/7/13 11:00	12/8/13 11:00	0.304	0.911	0.047	0.054	0.052	0.079	0.013	2.187	1.927	0.218	0.226	2.533	0.024	
12/8/13 11:00	12/8/13 11:00	0.079		0.024	0.015	0.044	0.029	0.007	0.949	1.187	0.163	0.253	2.137	0.023	Ext AmB

Start	End														
12/9/13 11:00	12/10/13 11:00	0.054	0.304	0.024	0.014	0.040	0.050	0.014	0.413	0.678	0.119	0.213	2.352	0.032
12/10/13 11:00	12/11/13 11:00	0.083	0.272	0.016	0.019	0.036	0.054	0.004	0.324	0.740	0.133	0.113	1.237	0.020
12/11/13 11:00	12/12/13 11:07	0.048	0.783	0.018	0.010	0.031	0.029	0.015	1.552	0.695	0.325	0.308	1.037	0.138
12/12/13 11:00	12/13/13 11:00	0.051	1.120	0.022	0.012	0.031	0.027	0.005	2.035	1.497	0.188	0.211	2.141	0.280
12/13/13 11:09	12/14/13 11:00	0.076	1.148	0.025	0.018	0.056	0.015	0.014	1.256	2.583	0.244	0.338	1.990	0.044
12/14/13 11:00	12/15/13 11:00	0.148	1.270	0.123	0.018	0.182	0.062	0.004	2.359	2.259	0.332	0.387	3.826	0.079
12/15/13 11:00	12/16/13 11:02	0.054	0.743	0.018	0.009	0.037	0.046	0.031	1.218	0.983	0.133	0.408	1.720	0.275
12/16/13 11:04	12/17/13 11:00	0.041	0.104	0.017	0.003	0.026	0.013	0.000	0.099	0.202	0.092	0.186	0.489	0.250
12/17/13 11:00	12/18/13 11:12	0.028	0.402	0.023	0.007	0.039	0.024	0.012	0.758	0.384	0.185	0.371	1.143	0.603
12/18/13 11:19	12/26/13 11:24	0.039	0.761	0.028	0.010	0.023	0.016	0.010	1.603	0.909	0.037	0.404	2.796	0.209
12/26/13 11:25	1/2/14 11:30	0.119	0.509	0.039	0.020	0.028	0.155	0.005	0.940	0.850	0.001	0.259	0.703	0.160
1/2/14 11:30	1/9/14 10:25	0.034	0.420	0.029	0.009	0.024	0.019	0.006	0.644	0.757	0.071	0.530	2.769	0.071
1/9/14 10:30	1/16/14 10:45	0.018	0.213	0.011	0.007	0.022	0.020	0.003	0.390	0.196	0.043	0.309	1.608	0.498
1/16/14 10:45	1/23/14 10:50	0.041	0.206	0.021	0.013	0.042	0.066	0.002	0.363	0.281	0.028	0.311	0.927	0.581
1/23/14 10:50	1/31/14 10:58	0.023	0.310	0.026	0.010	0.039	0.030	0.007	0.549	0.369	0.033	0.228	0.926	0.457
1/31/14 11:04	2/1/14 11:00	0.020	0.477	0.049	0.014	0.079	0.000	0.003	0.517	0.633	0.087	0.228	3.926	0.110
2/1/14 11:00	2/2/14 11:00	0.034	0.339	0.038	0.008	0.078	0.059	0.003	0.431	0.427	0.066	0.135	0.829	0.147

2/2/14 11:00	2/3/14 11:00	0.043	0.401	0.040	0.024	0.157	0.048	0.004	0.553	0.540	0.067	0.254	1.482	0.100
2/3/14 11:05	2/4/14 11:00	0.026	0.115	0.017	0.022	0.135	0.053	0.008	0.251	0.084	0.062	0.218	0.212	0.161
2/4/14 11:00	2/5/14 11:00	0.061	0.174	0.015	0.016	0.054	0.038	0.002	0.376	0.183	0.061	0.137	0.703	0.061
2/5/14 11:00	2/6/14 11:00	0.056	0.299	0.016	0.019	0.083	0.028	0.002	0.465	0.388	0.106	0.321	9.155	0.058
2/6/14 11:00	2/7/14 11:00	0.046	0.364	0.032	0.011	0.072	0.027	0.005	0.692	0.444	0.100	0.226	0.953	0.042
2/7/14 11:08	2/7/14 11:00	0.045	0.649	0.035	0.036	0.209	0.059	0.019	1.407	0.622	0.230	0.333	1.928	0.158
2/8/14 11:00	2/9/14 11:00	0.043	0.509	0.046	0.015	0.080	0.020	0.005	0.846	0.729	0.057	0.291	2.129	0.050
2/9/14 11:00	2/10/14 10:53	0.090	0.332	0.027	0.034	0.136	0.114	0.008	0.596	0.486	0.205	0.341	0.652	0.085
2/10/14 10:59	2/11/14 11:00	0.041	0.848	0.048	0.017	0.084	0.024	0.004	1.488	0.935	0.161	0.304	1.267	0.330
2/11/14 11:00	2/12/14 11:00	0.061	0.756	0.070	0.016	0.067	0.033	0.004	1.340	1.002	0.098	0.216	0.751	0.109
2/12/14 11:00	2/13/14 11:00	0.039	0.492	0.036	0.015	0.054	0.018	0.004	0.684	0.842	0.101	0.268	1.526	0.393
2/13/14 11:00	2/14/14 11:00	0.095	1.188	0.058	0.026	0.093	0.036	0.005	2.275	1.615	0.328	0.294	2.162	0.133
2/14/14 11:00	2/15/14 11:00	0.035	1.039	0.055	0.010	0.044	0.032	0.013	1.864	0.973	0.374	0.434	2.932	0.649
2/15/14 11:00	2/16/14 11:00	0.058	1.405	0.079	0.012	0.048	0.030	0.019	1.226	3.807	0.157	0.414	4.503	0.125
2/16/14 11:00	2/17/14 11:16	0.024	0.464	0.018	0.004	0.035	0.029	0.002	0.283	0.639	0.074	0.271	0.359	0.494
2/17/14 11:18	2/18/14 11:00	0.048	0.140	0.053	0.005	0.040	0.050	0.080	0.123	0.131	0.117	0.197	0.344	1.121
2/18/14 11:00	2/19/14 11:00	0.009	0.150	0.006	0.004	0.028	0.021	0.017	0.147	0.094	0.161	0.213	0.669	1.210

2/19/14 11:00	2/20/14 11:00	0.038	0.259	0.025	0.009	0.032	0.061	0.000	0.208	0.455	0.039	0.121	0.418	0.524
2/20/14 11:00	2/21/14 11:00	0.061	0.540	0.040	0.021	0.081	0.053	0.015	0.893	0.613	0.240	0.302	3.621	0.528
2/21/14 11:00	2/22/14 11:00	0.046	0.362	0.026	0.013	0.049	0.040	0.003	0.356	0.583	0.048	0.162	1.374	0.129
2/22/14 11:00	2/23/14 11:00	0.075	0.364	0.032	0.021	0.061	0.059	0.007	0.364	0.671	0.082	0.140	0.390	0.162
2/23/14 11:00	2/24/14 11:00	0.092	0.317	0.025	0.027	0.049	0.037	0.003	0.488	0.741	0.090	0.221	0.650	0.071
2/24/14 11:04	2/25/14 11:00	0.086	0.444	0.026	0.025	0.051	0.036	0.017	0.625	0.917	0.134	0.198	1.481	0.059
2/25/14 11:00	2/26/14 11:00	0.054	0.458	0.020	0.018	0.064	0.027	0.004	0.718	0.731	0.095	0.260	1.732	0.121
2/26/14 11:00	2/27/14 11:00	0.056	0.588	0.029	0.017	0.068	0.026	0.037	1.282	0.602	0.133	0.453	1.225	0.094
2/27/14 11:00	2/28/14 11:00	0.047	0.706	0.032	0.022	0.089	0.061	0.020	1.405	0.768	0.130	0.240	1.036	0.182
2/28/14 11:00	3/1/14 11:00	0.137	0.196	0.023	0.040	0.039	0.291	0.000	0.132	0.652	0.031	0.062	0.135	0.061
3/1/14 11:00	3/2/14 11:00	0.135	0.190	0.020	0.053	0.088	0.295	0.000	0.159	0.667	0.059	0.073	0.872	0.037
3/2/14 11:00	3/3/14 11:00	0.086	0.418	0.017	0.031	0.081	0.099	0.000	0.533	0.953	0.107	0.273	1.443	0.068
3/3/14 11:00	3/4/14 11:00	0.074	0.990	0.026	0.024	0.056	0.062	0.007	1.651	1.429	0.154	0.323	1.437	0.084
3/4/14 11:00	3/5/14 11:00	0.070	1.063	0.033	0.018	0.055	0.056	0.008	1.900	1.431	0.100	0.273	1.221	0.193
3/5/14 11:00	3/6/14 11:00	0.061	1.781	0.058	0.014	0.069	0.068	0.027	3.832	1.729	0.392	0.398	0.870	0.581
3/6/14 11:00	3/7/14 11:00	0.066	1.223	0.101	0.011	0.054	0.040	0.016	1.591	2.311	0.072	0.195	0.844	0.252
3/7/14 11:00	3/8/14 11:00	0.047	0.883	0.026	0.018	0.069	0.042	0.010	1.251	1.272	0.197	0.497	0.733	0.308

Start	End														
3/8/14 11:00	3/9/14 11:00	0.012	0.292	0.008	0.004	0.026	0.026	0.004	0.209	0.381	0.145	0.203	0.387	1.887	
3/9/14 11:00	3/10/14 11:00	0.005	0.098	0.004	0.004	0.029	0.013	0.000	0.069	0.037	0.196	0.294	0.146	1.817	
3/10/14 11:00	3/11/14 11:00	0.010	0.434	0.023	0.004	0.023	0.023	0.008	0.844	0.209	0.116	0.191	0.914	1.202	
3/11/14 11:00	3/12/14 11:00	0.143	0.237	0.016	0.006	0.046	0.021	0.013	0.274	0.221	0.094	0.362	0.508	1.771	
3/12/14 11:00	3/13/14 11:00	0.009	0.156	0.010	0.007	0.043	0.016	0.002	0.087	0.238	0.119	0.276	0.156		Ext
3/13/14 11:00	3/14/14 11:00	0.012	0.222	0.009	0.009	0.059	0.019	0.000	0.284	0.232	0.145	0.206	0.830	1.170	
3/14/14 11:00	3/15/14 11:00	0.064	0.857	0.018	0.013	0.060	0.037	0.008	0.942	1.330	0.135	0.232	0.896	1.133	
3/15/14 11:00	3/16/14 11:00	0.029	0.748	0.010	0.007	0.020	0.044	0.000	0.758	1.028	0.088	0.105	0.243	1.020	
3/16/14 11:00	3/17/14 11:00	0.022	0.328	0.011	0.009	0.045	0.026	0.003	0.502	0.251	0.280	0.346	0.451	2.498	
3/17/14 11:00	3/18/14 11:00	0.023	0.618	0.015	0.008	0.041	0.024	0.002	1.164	0.375	0.199	0.220	2.021	1.430	
3/18/14 11:00	3/19/14 11:00	0.008	0.332	0.005	0.008	0.045	0.021	0.002	0.254	0.342	0.129	0.294	0.109	2.335	
3/19/14 11:00	3/20/14 11:00	0.020	0.449	0.009	0.010	0.059	0.030	0.002	0.438	0.538	0.299	0.418	0.267	1.703	
3/20/14 11:00	3/21/14 11:00	0.020	0.447	0.008	0.005	0.028	0.021	0.006	0.254	0.724	0.017	0.154	0.198	0.607	
3/21/14 11:00	3/22/14 11:00	0.049	0.440	0.022	0.013	0.030	0.079	0.001	0.277	0.895	0.034	0.100	0.068	0.230	
3/22/14 11:00	3/23/14 11:00	0.034	0.802	0.022	0.016	0.071	0.037	0.012	0.692	1.284	0.132	0.138	0.728	0.447	
3/23/14 11:00	3/24/14 11:00	0.042	0.957	0.020	0.015	0.064	0.045	0.017	1.134	1.281	0.081	0.181	0.412	0.539	
3/24/14 11:00	3/25/14 11:00	0.044	0.541	0.011	0.013	0.067	0.031	0.005	0.451	0.800	0.104	0.136	0.209	0.247	

| 3/25/14 11:00 | 3/26/14 9:03 | 0.165 | 0.482 | 0.010 | 0.016 | 0.088 | 0.030 | 0.013 | 0.526 | 0.719 | 0.153 | 0.306 | 0.250 | 0.521 | |

Medicine Lake (MELA)

		Na^+	NH_4^+	K^+	Mg^+	Ca^+	Cl^-	NO_2^-	NO_3^-	SO_4^{2-}	HNO_2	HNO_3	SO_2	NH_3	
11/23/13 16:04	12/5/13 13:20														Tubing
12/5/13 13:24	12/11/13 13:04	0.169	0.481	0.022	0.031	0.025	0.071	0.005	1.091	1.073	0.026	0.235	3.507	0.031	
12/11/13 13:05	12/18/13 13:48	0.039	0.811	0.024	0.009	0.019	0.011	0.006	1.307	1.569	0.028	0.401	1.835	2.089	
12/18/13 13:50	12/26/13 14:44	0.036	0.791	0.026	0.010	0.020	0.015	0.003	1.303	0.713	0.018	0.193	1.963	0.871	
12/26/13 14:44	1/2/14 13:53	0.117	0.775	0.017	0.018	0.016	0.108	0.003	1.486	0.592	0.096	0.235	3.720	0.585	
1/2/14 13:54	1/9/14 12:55	0.029	0.507	0.012	0.007	0.018	0.013	0.004	0.788	0.469	0.041	0.286	3.816	0.647	
1/9/14 13:00	1/16/14 13:39	0.014	0.232	0.007	0.003	0.009	0.013	0.003	0.479	0.115	0.006	0.286	1.696	1.793	
1/16/14 13:13	1/23/14 13:13	0.049	0.247	0.016	0.014	0.037	0.052	0.001	0.449	0.191	0.017	0.212	1.624	3.952	
1/23/14 13:13	1/31/14 13:04	0.023	0.379	0.012	0.008	0.021	0.020	0.003	0.706	0.243	0.009	0.214	1.457	1.707	
1/31/14 13:08	2/7/14 13:03	0.028	0.304	0.011	0.008	0.021	0.011	0.002	0.527	0.273	0.018	0.193	1.301	0.195	
2/7/14 13:03	2/14/14 12:40	0.069	0.845	0.033	0.022	0.062	0.046	0.005	1.753	0.616	0.047	0.260	1.189	0.347	
2/14/14 12:43	2/21/14 12:33	0.029	0.707	0.011	0.007	0.022	0.016	0.002	0.978	0.710	0.014	0.374	1.006	0.976	
2/21/14 12:39	2/28/14 13:05	0.075	0.596	0.019	0.020	0.038	0.023	0.003	1.138	0.549	0.026	0.206	0.856	0.314	
2/28/14 13:05	3/7/14 13:31	0.084	1.290	0.026	0.028	0.042	0.091	0.004	2.020	1.177	0.032	0.297	1.188	0.241	

3/7/14 13:31	3/14/14 12:49	0.021	0.311	0.006	0.004	0.019	0.006	0.003	0.524	0.239	0.021	0.363	0.704	2.703
3/14/14 12:50	3/21/14 13:00	0.023	0.605	0.008	0.007	0.026	0.014	0.003	0.805	0.522	0.008	0.321	0.294	3.462
3/21/14 13:00	3/26/14 12:32	0.034	0.745	0.011	0.014	0.049	0.026	0.002	0.867	0.726	0.032	0.165	0.238	0.945

F.2 IMPROVE OC/EC Data from BAQS II

The average IMPROVE Module C measured organic carbon (OC, µg m^{-3}) and elemental carbon

(EC, µg m^{-3}) and uncertainty (Unc) values are presented in the table below. Each filter was

sampled for 24 hours at THRO-N, starting and ending at 8:00 am Mountain Standard Time.

Table F.3: The concentrations and uncertainties (µg m-3) for organic carbon (OC) and
elemental carbon (EC) collected at THRO-N during BAQS II.

Start Time	OC	OC Unc.	EC	EC Unc.
		(µg m^{-3})		
11/22/13 8:00	0.22	0.04	0.00	0.01
11/23/13 8:00	0.19	0.04	0.00	0.01
11/24/13 8:00	0.75	0.05	0.18	0.03
11/25/13 8:00	0.67	0.05	0.22	0.03
11/26/13 8:00	0.49	0.04	0.13	0.02
11/27/13 8:00	0.86	0.06	0.23	0.03
11/28/13 8:00	0.64	0.05	0.16	0.02
11/29/13 8:00	0.80	0.06	0.20	0.03
11/30/13 8:00	1.01	0.07	0.47	0.07
12/1/13 8:00	0.83	0.06	0.27	0.04
12/2/13 8:00	0.86	0.06	0.20	0.03
12/3/13 8:00	0.58	0.05	0.30	0.04
12/4/13 8:00	0.68	0.05	0.23	0.03
12/5/13 8:00	0.67	0.05	0.24	0.03
12/6/13 8:00	0.96	0.06	0.20	0.03
12/7/13 8:00	0.69	0.05	0.12	0.02
12/8/13 8:00	1.13	0.07	0.19	0.03
12/9/13 8:00	0.73	0.05	0.09	0.01
12/10/13 8:00	0.51	0.04	0.09	0.01
12/11/13 8:00	0.57	0.05	0.11	0.02
12/12/13 8:00	0.57	0.05	0.24	0.04
12/13/13 8:00	0.62	0.05	0.24	0.03
12/14/13 8:00	0.73	0.05	0.38	0.05
12/15/13 8:00	0.65	0.05	0.22	0.03
12/16/13 8:00	0.18	0.03	0.03	0.01
12/17/13 8:00	0.44	0.04	0.05	0.01
12/18/13 8:00	0.72	0.05	0.26	0.04
12/19/13 8:00	0.47	0.04	0.29	0.04
12/20/13 8:00	0.72	0.05	0.35	0.05
12/21/13 8:00	1.07	0.07	0.44	0.06

12/22/13 8:00	1.10	0.07	0.54	0.08
12/23/13 8:00	1.02	0.07	0.24	0.03
12/24/13 8:00	0.61	0.05	0.16	0.02
12/29/13 8:00	0.43	0.04	0.26	0.04
12/30/13 8:00	0.53	0.04	0.37	0.05
12/31/13 8:00	0.54	0.04	0.16	0.02
1/1/14 8:00	0.73	0.05	0.42	0.06
1/2/14 8:00	0.59	0.05	0.20	0.03
1/3/14 8:00	0.64	0.05	0.13	0.02
1/4/14 8:00	0.39	0.04	0.11	0.02
1/6/14 8:00	0.42	0.05	0.09	0.02
1/7/14 8:00	0.47	0.04	0.57	0.08
1/8/14 8:00	0.53	0.05	0.14	0.02
1/9/14 8:00	0.52	0.04	0.08	0.01
1/10/14 8:00	0.36	0.04	0.12	0.02
1/11/14 8:00	0.46	0.04	0.04	0.01
1/12/14 8:00	0.67	0.05	0.13	0.02
1/13/14 8:00	0.40	0.04	0.05	0.01
1/14/14 8:00	0.48	0.05	0.16	0.02
1/15/14 8:00	0.44	0.04	0.14	0.02
1/16/14 8:00	0.57	0.05	0.08	0.01
1/17/14 8:00	0.66	0.05	0.10	0.02
1/18/14 8:00	0.60	0.05	0.06	0.01
1/19/14 8:00	0.66	0.05	0.10	0.02
1/20/14 8:00	0.38	0.04	0.07	0.01
1/21/14 8:00	0.66	0.05	0.16	0.02
1/22/14 8:00	0.38	0.04	0.25	0.04
1/23/14 8:00	0.74	0.05	0.13	0.02
1/24/14 8:00	0.86	0.06	0.25	0.04
1/25/14 8:00	0.61	0.05	0.07	0.01
1/26/14 8:00	0.48	0.05	0.06	0.01
1/27/14 8:00	0.49	0.04	0.21	0.03
1/28/14 8:00	0.55	0.05	0.06	0.01
1/29/14 8:00	1.19	0.08	0.30	0.04
1/30/14 8:00	0.66	0.05	0.08	0.01
1/31/14 8:00	1.10	0.07	0.13	0.02
2/1/14 8:00	0.60	0.05	0.05	0.01
2/5/14 8:00	0.49	0.05	0.06	0.01
2/6/14 8:00	0.75	0.06	0.08	0.01
2/7/14 8:00	0.80	0.06	0.18	0.03
2/8/14 8:00	1.11	0.07	0.52	0.07
2/9/14 8:00	0.68	0.05	0.21	0.03
2/10/14 8:00	1.10	0.07	0.20	0.03
2/11/14 8:00	1.12	0.07	0.24	0.03
2/12/14 8:00	0.82	0.06	0.16	0.02

2/13/14 8:00	0.93	0.06	0.40	0.06
2/14/14 8:00	0.65	0.05	0.19	0.03
2/15/14 8:00	0.97	0.07	0.48	0.07
2/16/14 8:00	0.60	0.05	0.12	0.02
2/17/14 8:00	0.52	0.05	0.10	0.02
2/18/14 8:00	0.37	0.04	0.05	0.01
2/19/14 8:00	0.43	0.04	0.04	0.01
2/20/14 8:00	0.53	0.05	0.29	0.04
2/21/14 8:00	0.51	0.05	0.37	0.05
2/22/14 8:00	0.60	0.05	0.17	0.03
2/23/14 8:00	0.62	0.05	0.18	0.03
2/24/14 8:00	0.69	0.05	0.14	0.02
2/25/14 8:00	0.67	0.05	0.11	0.02
2/26/14 8:00	0.70	0.05	0.26	0.04
2/27/14 8:00	0.85	0.06	0.14	0.02
2/28/14 8:00	0.65	0.05	0.15	0.02
3/1/14 8:00	0.57	0.05	0.22	0.03
3/2/14 8:00	0.50	0.05	0.12	0.02
3/3/14 8:00	0.71	0.05	0.21	0.03
3/4/14 8:00	0.71	0.05	0.15	0.02
3/5/14 8:00	0.99	0.07	0.27	0.04
3/6/14 8:00	1.30	0.08	0.50	0.07
3/7/14 8:00	0.69	0.05	0.27	0.04
3/8/14 8:00	0.78	0.05	0.12	0.02
3/9/14 8:00	0.44	0.04	0.04	0.01
3/10/14 8:00	0.59	0.04	0.32	0.05
3/11/14 8:00	0.37	0.04	0.07	0.01
3/12/14 8:00	0.45	0.04	0.04	0.01
3/13/14 8:00	0.39	0.04	0.06	0.01
3/14/14 8:00	0.73	0.05	0.14	0.02
3/15/14 8:00	0.52	0.04	0.09	0.01
3/16/14 8:00	0.59	0.05	0.16	0.02
3/17/14 8:00	0.64	0.05	0.46	0.07
3/18/14 8:00	0.46	0.04	0.07	0.01
3/19/14 8:00	0.45	0.04	0.12	0.02
3/20/14 8:00	0.40	0.04	0.10	0.02
3/21/14 8:00	0.45	0.04	0.20	0.03
3/22/14 8:00	0.49	0.04	0.20	0.03
3/23/14 8:00	0.49	0.04	0.27	0.04
3/24/14 8:00	0.39	0.04	0.27	0.04
3/25/14 8:00	0.40	0.04	0.10	0.02

F.3 Precipitation Data from BAQS I and BAQS II

Presented here are triplicate pH measurements and ionic composition (µN) of precipitation samples collected during BAQS I and BAQS II. Blanks were obtained weekly which are listed previously in Tables 2.5 and 2.6. The volume of precipitation sample is also listed, which is converted from measured sample mass assuming a density of 1 g mL^{-1}. Small sample volumes prevented the measurement of pH, represented by the blank cells in the tables below.

Table F.4: Analysis of Precipitation Samples Collected During BAQS I at THRO-N, FOUS, MELA, and KNRI including ionic composition (µN), pH and precipitation volume (mL).

Start	Stop	Cations (µN)					Anions (µN)				pH				Vol. (mL)

Theodore Roosevelt North Unit (THRO-N)

Start	Stop	Na^+	NH_4^+	K^+	Mg^+	Ca^+	Cl^-	NO_2^-	NO_3^-	SO_4^{2-}	1	2	3	Avg	Vol (mL)
2/13/13 8:00	2/14/13 8:00	3.40	36.40	1.58	11.27	34.26	2.52	0.13	33.13	23.41	5.62	5.36	5.29	5.42	67.5
2/14/13 8:00	2/15/13 8:00	1.83	36.56	0.75	10.28	28.64	1.48	0.36	23.52	25.81	6.57	6.11	6.09	6.26	29.4
2/15/13 8:00	2/16/13 8:00	8.11	60.85	1.09	7.20	38.22	6.31	0.55	43.83	24.68					8.7
2/16/13 8:00	2/18/13 9:40	0.89	9.25	0.39	2.15	7.80	0.45	0.04	8.28	5.81	5.79	5.19	5.16	5.38	116.1
2/19/13 10:13	2/22/13 8:30	30.72	59.42	4.42	24.54	162.4	11.53	0.32	67.49	51.84					16.1
2/24/13 8:20	2/28/13 9:00	0.94	11.30	0.20	6.07	19.97	2.00	0.00	50.31	17.09	4.7	4.45	4.43	4.53	164.4
2/28/13 9:00	3/4/13 9:00	0.21	12.11	0.17	0.69	2.48	0.68	0.00	8.84	4.81	5.4	5.29	5.21	5.30	544
3/4/13 14:50	3/6/13 9:00	7.76	15.83	4.89	17.96	60.73	2.56	0.00	26.22	12.47					16.2
3/6/13 9:00	3/9/13 8:50	24.65	80.52	2.66	14.48	105.3	12.84	0.76	84.38	57.13					26
3/9/13 8:50	3/13/13 8:30	17.87	22.05	3.54	30.32	91.60	3.80	0.32	33.94	57.05					15.1
3/13/13 8:30	3/18/13 9:00	27.59	71.97	1.74	19.89	65.02	3.03	0.22	35.95	51.54	5.46	5.74	5.94	5.71	88.5
3/18/13 9:50	3/22/13 15:21	0.86	23.33	0.32	4.44	24.52	0.81	0.00	11.62	8.37					388

		Na$^+$	NH$_4^+$	K$^+$	Mg$^+$	Ca$^+$	Cl$^-$	NO$_2^-$	NO$_3^-$	SO$_4^{2-}$	1	2	3	Avg	Vol (mL)
3/22/13 15:21	3/25/13 16:30	0.86	11.91	0.30	4.22	11.64	1.99	0.00	32.65	8.94	4.7	4.69	4.73	4.71	143
3/25/13 16:30	3/30/13 8:40	1.20	69.86	0.58	4.62	20.28	2.14	0.20	26.84	18.59	5.89	5.86	5.86	5.87	45
3/30/13 8:40	3/31/13 20:00	1.04	19.95	0.20	4.62	17.27	1.96	0.00	17.82	8.46	5.71	5.53	5.43	5.56	76.2
4/5/13 8:00	4/6/13 7:50	6.84	121.6	3.51	19.12	100.5	6.37	0.67	40.30	32.37	6.55	6.49	6.57	6.54	12.7

Fort Union (FOUS)

		Na$^+$	NH$_4^+$	K$^+$	Mg$^+$	Ca$^+$	Cl$^-$	NO$_2^-$	NO$_3^-$	SO$_4^{2-}$	1	2	3	Avg	Vol (mL)
2/17/13 10:00	2/24/13 10:20	4.58	34.30	0.71	10.06	38.73	4.34	0.78	18.66	23.78					20.8
2/24/13 10:20	3/3/13 11:15	5.66	62.24	1.57	27.42	82.91	7.08	0.23	117.6	57.02					26.3
3/3/13 11:15	3/10/13 10:35	1.37	38.83	0.36	2.86	11.47	1.99	0.00	25.49	16.44	5.45	5.38	5.36	5.40	491.3
3/10/13 10:35	3/17/13 11:30	5.88	43.62	1.20	22.47	70.32	6.42	0.40	36.78	30.29					15.6
3/17/13 11:30	3/24/13 12:00	1.74	36.44	0.58	7.94	30.25	1.70	0.22	17.64	17.91	5.75	5.9	5.94	5.86	240.2
3/24/13 12:00	3/31/13 11:45	1.15	34.22	0.26	4.58	17.93	2.05	0.27	18.59	12.74	5.61	5.63	5.64	5.63	113.2

Medicine Lake (MELA)

		Na$^+$	NH$_4^+$	K$^+$	Mg$^+$	Ca$^+$	Cl$^-$	NO$_2^-$	NO$_3^-$	SO$_4^{2-}$	1	2	3	Avg	Vol (mL)
2/15/13 14:00	2/24/13 13:30	3.07	14.96	0.95	8.86	51.76	3.23	0.87	19.23	14.63					8.8
2/24/13 13:30	3/3/13 14:05	8.05	50.53	3.48	30.04	77.12	10.33	0.83	115.7	45.11					742.5
3/3/13 14:05	3/10/13 13:25	3.99	34.46	0.51	8.32	31.17	2.60	0.20	30.75	18.99	6.21	5.83	5.73	5.92	97.3

Start	Stop	Na⁺	NH₄⁺	K⁺	Mg⁺	Ca⁺	Cl⁻	NO₂⁻	NO₃⁻	SO₄²⁻	1	2	3	Avg	Vol (mL)
3/10/13 13:25	3/17/13 14:00	0.53	22.30	0.18	2.47	8.06	0.60	0.00	6.73	9.30	6.21	6.13	6.23	6.19	330.6
3/17/13 14:00	3/24/13 15:20	1.34	26.21	0.47	4.79	19.39	1.66	0.07	17.50	15.56	5.42	5.48	5.49	5.46	218.3

Knife River Indian Villages National Historic Site (KNRI)

		Na⁺	NH₄⁺	K⁺	Mg⁺	Ca⁺	Cl⁻	NO₂⁻	NO₃⁻	SO₄²⁻	1	2	3	Avg	Vol (mL)
3/31/13 11:45	2/14/13 12:00	1.15	26.27	0.38	4.19	17.25	1.83	0.11	30.18	14.23	5.35	5.03	5.01	5.13	82.6
2/14/13 12:00	2/19/13 13:27	3.04	44.60	0.68	10.53	42.43	2.35	0.31	28.61	35.54	6.5	6.16	6.15	6.27	137.3
2/26/13 14:15	3/5/13 15:00	2.50	86.52	0.63	4.59	18.54	3.91	0.21	40.38	41.16	5.63	5.58	5.62	5.61	367.6
3/12/13 15:00	3/19/13 15:00	9.87	73.93	1.85	27.83	82.43	6.17	0.24	56.75	66.08	6.17	6.24	6.25	6.22	111.2

Table F.5: Analysis of Precipitation Samples Collected During BAQS II at THRO-N including ionic composition (µN), pH and precipitation volume (mL).

Start	Stop	Cations (µN)					Anions (µN)				pH				Vol. (mL)

North Unit of Theodore Roosevelt National Park

		Na⁺	NH₄⁺	K⁺	Mg⁺	Ca⁺	Cl⁻	NO₂⁻	NO₃⁻	SO₄²⁻	1	2	3	Avg	
11/22/13 8:41	11/23/13 8:00	3.7	209.1	1.0	12.6	35.0	10.3	0.7	84.2	16.9					2.1
11/23/13 8:00	12/1/13 10:15	1.5	51.6	0.5	3.5	23.2	2.5	0.3	28.1	14.7					2.9

Start	End	C1	C2	C3	C4	C5	C6	C7	C8	C9	C10	C11	C12	C13	C14
12/1/13 10:15	12/2/13 8:13	0.8	6.3	1.2	1.5	3.7	0.8		6.4	4.5	5.44	5.64	5.61	5.56	396.3
12/2/13 8:13	12/3/13 15:58	2.4	41.7	1.0	7.0	16.2	2.9	0.1	21.4	20.5	7.65	7.53	6.81	7.33	65.5
12/3/13 15:58	12/4/13 8:40	0.8	5.4	0.2	4.3	9.7	1.3	0.0	18.4	2.8	5.56	5.08	5.12	5.25	133.4
12/4/13 8:40	12/5/13 8:31	3.4	17.1	1.0	6.2	21.4	1.7	0.3	10.6	4.1					6.7
12/9/13 8:15	12/10/13 8:39	2.4	4.0	1.3	10.9	29.3	1.9	0.0	22.9	7.2	5.82	5.28	5.11	5.40	65.9
12/10/13 8:39	12/11/13 8:18	4.3	16.3	1.0	6.2	18.3	2.7	0.1	24.6	5.9					6.6
12/13/13 7:53	12/14/13 7:54	4.4	18.1	0.6	6.2	22.8	5.2	0.0	56.1	12.9	4.82	4.59	4.56	4.66	23.4
12/17/13 8:24	12/20/13 8:30	0.5	2.5	0.1	3.2	7.9	0.8	0.1	7.1	1.1	5.62	5.38	5.38	5.46	168.7
12/20/13 8:31	12/22/13 16:30	1.0	18.4	0.2	1.5	6.4	1.8	0.0	16.1	2.6	5.63	5.55	5.53	5.57	149.8
12/22/13 16:30	12/25/13 8:50	2.3	24.1	0.2	3.6	12.5	2.7	0.3	41.4	7.2	4.73	4.66	4.65	4.68	62.8
12/25/13 8:50	12/27/13 16:50	2.9	8.5	0.2	2.5	9.8	2.2	0.0	10.2		5.65	5.68	5.61	5.65	29.2
12/29/13 8:00	12/30/13 17:00	1.8	6.5	0.1	3.9	12.0	1.2	0.0	20.5	3.0					111.2
12/30/13 17:00	12/31/13 17:00	0.8	2.5	0.0	0.8	3.9	0.6	0.0	10.3	2.5	5.53	5.43	5.34	5.43	262.9
1/1/14 17:00	1/3/14 16:30	0.9	8.6	0.3	2.6	7.9	1.0	0.1	22.1	4.1	4.25	4.71	4.10	4.35	99.7
1/6/14 8:00	1/7/14 17:00	1.2	4.2	0.1	5.5	15.5	1.5	0.1	17.4	4.5	5.08	5.04	4.98	5.03	69.2
1/25/14 8:00	1/26/14 16:00	5.6	44.1	1.7	10.7	42.7	2.4	0.3	17.6	25.2					12.6
1/26/14 16:00	1/30/14 8:05	5.3	13.6	0.6	16.7	66.3	5.7	0.3	39.5	5.6	5.29	5.71	5.81	5.60	9.6

Start	End														
2/3/14 17:00	2/4/14 15:00	1.5	11.5	0.2	7.7	29.8	1.9	0.0	40.3	2.1	5.05	5.14	5.06	5.08	20.1
2/6/14 15:15	2/9/14 15:45	0.9	4.4	0.1	6.3	22.9	0.2	0.0	2.1	0.0					2.3
2/9/14 15:45	2/13/14 7:52	7.9	22.5	0.8	9.2	40.7	2.9	0.1	24.6	11.8	6.23	6.05	5.99	6.09	22.3
2/13/14 7:52	2/14/14 8:20	2.3	14.6	0.2	4.0	22.2	1.7	0.0	15.4	5.0	6.01	5.93	5.88	5.94	99.2
2/14/14 8:20	2/15/14 8:00	8.3	38.5	0.9	5.3	20.8	5.0	0.0	25.1	11.5	5.52	5.63	5.55	5.57	11.6
2/15/14 8:00	2/16/14 8:00	65.4	84.3	4.0	16.5	64.5	52.0	0.0	119.3	37.1					1.5
2/16/14 8:00	2/17/14 8:12	6.3	16.7	19.1	21.2	33.4	5.3	0.0	43.5	15.3	5.76	5.59	5.55	5.63	221.7
2/18/14 8:00	2/20/14 15:30	5.2	44.6	1.5	13.8	46.6	2.0	0.2	31.9	23.3	6.39	5.80	5.79	5.99	10.7
2/23/14 8:20	2/25/14 10:10	0.7	3.5	0.1	4.6	15.3	0.8	0.0	18.4	1.8	4.97	5.02	4.98	4.99	75.2
2/25/14 10:10	3/3/14 8:10	4.4	8.1	0.5	8.2	42.7	2.7	0.2	22.3	6.5	5.40	5.71	5.69	5.60	57.0
3/3/14 8:10	3/4/14 4:00	1.8	17.2	0.2	3.2	13.6	1.7	0.0	15.8	5.6	5.33	5.37	5.36	5.35	91.3
3/14/14 4:00	3/15/14 16:00	3.9	44.0	0.4	8.5	32.3	3.3	0.0	23.9	13.3	5.94	6.00	6.02	5.99	73.0
3/17/14 8:00	3/18/14 8:16	9.3	106.0	1.5	14.8	48.9	6.1	0.0	51.9	52.5					42.3
3/18/14 8:16	3/19/14 8:40	1.0	41.1	0.1	5.0	14.8	1.2	0.2	24.5	9.7					29.8
3/19/14 8:40	3/21/14 16:30	8.0	73.7	3.8	15.8	54.7	3.5	0.3	31.9	32.2					16.2
3/21/14 16:30	3/24/14 16:41	3.0	49.7	0.6	12.4	42.2	2.9	0.3	41.0	8.6	6.68	6.19	6.60	6.49	12.6

F.4 Passive Sampler Data from BAQS I

Three different passive samplers were deployed to collect ammonia (NH_3), ozone (O_3), and nitrogen dioxide (NO_2) and sulfur dioxide (SO_2). Passive samplers were collected at Theodore Roosevelt National Park, North Unit (THRO-N) and South Unit (THRO-S), Fort Union Trading Post National Historic Site (FOUS), Medicine Lake National Wildlife Refuge (MELA), and Knife River Indian Villages National Historic Site (KNRI) during BAQS I. Unreliable data, marked with an asterisk, are flagged using the key below.

*Flags
- Ship: Passive sampler broke or was otherwise compromised during shipping
- Prep: Something during sample preparation affected the analysis (e.g. some of the O_3 granular absorbant was spilled, extraction water was spilled, etc.)

Table F.6: Ammonia passives samples, blank values and replicate samples (Day et al., 2012). Aqueous concentrations are not blank corrected and ambient concentrations are blank corrected.

Sample Type	Start	Stop	Aqueous Conc (μN)	Ambient Conc. (ppb)	Sample Rate (mL min^{-1})	Temp (K)	Pressure (atm)	Flags
Blank	2/13/13		1.66					
Blank	2/18/13		1.37					
Blank	3/4/13		2.25					
Blank	3/11/13		3.45					
Blank	3/11/13		0.45					
Blank	3/25/13		0.86					
Blank	4/1/13		2.81					
Blank	4/1/13		2.41					
Blank	4/1/13		2.96					

THRO-N

Sample	2/13/13 11:00	2/18/13 10:20	4.27	0.44	177.7	271	0.933
Replicate	2/13/13 11:00	2/18/13 10:20	4.01	0.40	177.7	271	0.933
Sample	2/18/13 10:25	2/25/13 14:10	5.88	0.55	172.1	266	0.933
Replicate	2/18/13 10:25	2/25/13 14:10	6.82	0.67	172.1	266	0.933
Sample	2/25/13 14:15	3/5/13 9:00	6.66	0.54	177.9	271	0.933
Replicate	2/25/13 14:15	3/5/13 9:00	6.51	0.52	177.9	271	0.933
Sample	3/5/13 9:08	3/11/13 9:35	5.34	0.44	174.4	268	0.933
Replicate	3/5/13 9:08	3/11/13 9:35	5.07	0.40	174.4	268	0.933
Sample	3/11/13 9:40	3/18/13 10:22	5.07	0.38	175.3	269	0.933
Replicate	3/11/13 9:40	3/18/13 10:22	4.69	0.33	175.3	269	0.933
Sample	3/18/13 10:28	3/25/13 9:00	6.36	0.51	170.2	265	0.933
Replicate	3/18/13 10:28	3/25/13 9:00	5.18	0.36	170.2	265	0.933
Sample	3/25/13 9:00	4/1/13 9:00	4.73	0.29	179.8	273	0.933
Replicate	3/25/13 9:00	4/1/13 9:00	10.05	0.96	179.8	273	0.933
Sample	4/1/13 9:45	4/6/13 8:45	9.08	1.17	184.4	277	0.933
Replicate	4/1/13 9:45	4/6/13 8:45	9.19	1.19	184.4	277	0.933

FOUS

Sample	2/15/13 13:39	2/24/13 10:35	28.99	2.83	174.0	268	0.930
Sample	2/24/13 10:40	3/3/13 11:30	28.96	3.38	179.8	273	0.930
Sample	3/3/13 11:30	3/10/13 11:32	12.55	1.30	173.3	267	0.930
Sample	3/10/13 11:35	3/17/13 11:16	17.56	1.97	176.2	269	0.930
Sample	3/17/13 11:23	3/24/13 12:05	6.07	0.47	167.5	262	0.930
Sample	3/24/13 12:05	3/31/13 12:00	9.83	0.94	175.6	269	0.930
Sample	3/31/13 12:05	4/4/13 15:23	12.32	2.10	181.4	274	0.930

MELA

Sample	2/17/13 13:30	2/24/13 13:40	9.01	0.97	169.2	264	0.931
Sample	2/24/13 13:45	3/3/13 14:10	7.97	0.76	177.7	271	0.931
Sample	3/3/13 14:15	3/10/13 14:05	4.98	0.33	170.0	264	0.931
Sample	3/10/13 14:10	3/17/13 14:47	6.75	0.60	173.4	267	0.931
Sample	3/17/13 14:47	3/24/13 15:35	3.15	0.10	167.7	262	0.931
Sample	3/24/13 15:35	3/31/13 15:30	6.23	0.49	170.6	265	0.931

Sample Type	Start	Stop						
Sample	3/31/13 15:35	4/4/13 10:44	5.24	0.66	177.7	271	0.931	

<div align="center">

KNRI

</div>

Sample Type	Start	Stop						
Sample	2/14/13 17:20	2/19/13 13:30	5.41	0.67	170.9	266	0.940	
Sample	2/19/13 13:40	2/26/13 14:25	10.93	1.20	171.1	267	0.940	
Sample	2/26/13 14:30	3/5/13 16:40	12.14	1.27	175.5	270	0.940	
Sample	3/5/13 16:46	3/12/13 13:48	7.58	0.67	171.4	267	0.940	
Sample	3/12/13 13:53	3/19/13 14:40	7.97	0.75	169.9	266	0.940	
Sample	3/19/13 14:45	3/26/13 14:20	6.04	0.47	169.7	265	0.940	
Sample	3/26/13 14:20	4/2/13 12:27	9.74	0.94	176.0	271	0.940	

<div align="center">

THRO-S

</div>

Sample Type	Start	Stop						
Sample	2/12/13 10:26	2/18/13 14:30	5.73	0.57	183.9	272	0.905	
Sample	2/18/13 14:30	2/26/13 10:55	8.92	0.85	178.8	268	0.905	
Sample	2/26/13 11:00	3/5/13 12:17	6.86	0.62	184.3	272	0.905	
Sample	3/5/13 12:22	3/12/13 10:20	6.01	0.47	179.8	268	0.905	
Sample	3/12/13 10:20	3/19/13 10:52	7.79	0.72	181.2	270	0.905	
Sample	3/19/13 10:53	3/26/13 9:50	5.35	0.38	176.0	265	0.905	
Sample	3/26/13 9:50	4/2/13 17:51	14.36	1.42	188.0	275	0.905	

Table F.6: O_3 passives samples, blank values and replicate samples. Aqueous concentrations are not blank corrected and ambient concentrations are blank corrected.

Sample Type	Start	Stop	Total Mass (µg O_3)	Ambient Conc. (ppb)	Sample Rate (mL min^{-1})	Temp (K)	Pressure (atm)	Flags
Blank	2/13/13		0.35					
Blank	2/18/13		0.37					
Blank	3/5/13		0.39					
Blank	3/25/13		0.35					

<div align="center">

THRO-N

</div>

Sample Type	Start	Stop	Total Mass (µg O_3)	Ambient Conc. (ppb)	Sample Rate (mL min^{-1})	Temp (K)	Pressure (atm)	Flags
Sample	2/13/13 11:00	2/18/13 10:20	11.75	38.86	21.35	271	0.933	

Replicate	2/13/13 11:00	2/18/13 10:20	12.34	40.87	21.35	271	0.933	
Sample	2/18/13 10:25	2/25/13 14:10	13.23	29.90	20.79	266	0.933	
Replicate	2/18/13 10:25	2/25/13 14:10	13.77	31.13	20.79	266	0.933	
Sample	2/25/13 14:15	3/5/13 9:00	16.14	32.69	21.38	271	0.933	
Replicate	2/25/13 14:15	3/5/13 9:00	16.12	32.65	21.38	271	0.933	
Sample	3/5/13 9:08	3/11/13 9:35	17.72	45.39	21.03	268	0.933	
Replicate	3/5/13 9:08	3/11/13 9:35	18.28	46.80	21.03	268	0.933	
Sample	3/11/13 9:40	3/18/13 10:22	*0.15			269	0.933	Ship
Replicate	3/11/13 9:40	3/18/13 10:22	20.62	44.83	20.90	269	0.933	
Sample	3/18/13 10:28	3/25/13 9:00	20.52	45.58	20.37	265	0.933	
Replicate	3/18/13 10:28	3/25/13 9:00	17.01	37.79	20.37	265	0.933	
Sample	3/25/13 9:00	4/1/13 9:00	16.62	36.31	21.37	273	0.933	
Replicate	3/25/13 9:00	4/1/13 9:00	16.43	35.89	21.37	273	0.933	
Sample	4/1/13 9:45	4/6/13 8:45	13.35	40.88	21.85	277	0.933	
Replicate	4/1/13 9:45	4/6/13 8:45	13.06	40.01	21.85	277	0.933	

FOUS

Sample	2/15/13 13:39	2/24/13 10:35	18.82	34.46	20.87	268	0.930
Sample	2/24/13 10:40	3/3/13 11:30	13.58	30.01	21.51	273	0.930
Sample	3/3/13 11:30	3/10/13 11:32	19.92	44.05	20.86	267	0.930
Sample	3/10/13 11:35	3/17/13 11:16	21.85	48.13	21.15	269	0.930
Sample	3/17/13 11:23	3/24/13 12:05	20.96	46.33	20.48	262	0.930
Sample	3/24/13 12:05	3/31/13 12:00	18.73	41.61	21.09	269	0.930
Sample	3/31/13 12:05	4/4/13 15:23	11.26	42.59	21.67	274	0.930

MELA

Sample	2/17/13 13:30	2/24/13 13:40	16.74	39.02	20.46	264	0.931	
Sample	2/24/13 13:45	3/3/13 14:10	*14.70	*33.07	21.31	271	0.931	Prep
Sample	3/3/13 14:15	3/10/13 14:05	20.95	46.55	20.54	264	0.931	
Sample	3/10/13 14:10	3/17/13 14:47	22.74	49.99	20.88	267	0.931	
Sample	3/17/13 14:47	3/24/13 15:35	20.73	45.91	20.31	262	0.931	
Sample	3/24/13 15:35	3/31/13 15:30	24.59	54.75	20.60	265	0.931	
Sample	3/31/13 15:35	4/4/13 10:44	12.57	51.87	21.31	271	0.931	

KNRI

Sample	2/14/13 17:20	2/19/13 13:30	12.48	42.50	20.80	266	0.940
Sample	2/19/13 13:40	2/26/13 14:25	14.81	33.85	20.82	267	0.940
Sample	2/26/13 14:30	3/5/13 16:40	17.18	37.99	21.26	270	0.940
Sample	3/5/13 16:46	3/12/13 13:48	23.18	51.56	20.85	267	0.940
Sample	3/12/13 13:53	3/19/13 14:40	19.46	42.48	20.70	266	0.940
Sample	3/19/13 14:45	3/26/13 14:20	21.99	48.21	20.69	265	0.940
Sample	3/26/13 14:20	4/2/13 12:27	17.63	39.10	21.32	271	0.940

THRO-S

Sample	2/12/13 10:26	2/18/13 14:30	15.22	41.38	21.23	272	0.905
Sample	2/18/13 14:30	2/26/13 10:55	15.97	33.55	20.72	268	0.905
Sample	2/26/13 11:00	3/5/13 12:17	18.78	42.94	21.27	272	0.905
Sample	3/5/13 12:22	3/12/13 10:20	21.00	47.93	20.82	268	0.905
Sample	3/12/13 10:20	3/19/13 10:52	18.05	40.40	20.96	270	0.905
Sample	3/19/13 10:53	3/26/13 9:50	21.06	48.03	20.43	265	0.905
Sample	3/26/13 9:50	4/2/13 17:51	19.04	40.64	21.66	275	0.905

Table F.7: NO_2 / SO_2 passives samples, blank values and replicate samples. Aqueous concentrations are not blank corrected and ambient concentrations are blank corrected. Each THRO-N passive sample and replicate sample and select samples from FOUS, KNRI, and THRO-S were analyzed twice by IC ("IC Rep") for NO_2 only.

Sample Type	Start	Stop	NO₂ Aqueous Conc (ng)	NO₂ Ambient Conc. (ppb)	SO₂ Aqueous Conc (ng)	SO₂ Ambient Conc. (ppb)	Sample Rate (mL min⁻¹)	Temp (K)	Pressure (atm)	Flags
Blank	2/13/13		0		932					
Blank	2/13/13		379		917					
Blank	2/18/13		0		0					
Blank	2/18/13		368		870					
Blank	3/5/13		626		1964					

Blank	3/5/13		807		1303				
Blank	3/11/13		888		1540				
Blank	3/11/13		913		883				
Blank	3/25/13		395		882				
Blank	3/25/13		316		883				
Blank	3/25/13		353		821				
Blank	3/25/13		318		876				
Blank	3/25/13		364		1022				
Blank	3/25/13		0		927				
Blank	4/1/13		384		818				
Blank	4/1/13		0		905				

THRO-N

Sample	2/13/13 11:00	2/18/13 10:20	1284	1.73	2328	0.39	0.07	271	0.93
Replicate	2/13/13 11:00	2/18/13 10:20	915	1.02	2629	0.48	0.07	271	0.93
IC Rep	2/13/13 11:00	2/18/13 10:20	909	1.01			0.07	271	0.93
Sample	2/18/13 10:25	2/25/13 14:10	1182	1.21	3768	0.57	0.06	266	0.93
Replicate	2/18/13 10:25	2/25/13 14:10	1218	1.26	2302	0.26	0.06	266	0.93
IC Rep	2/18/13 10:25	2/25/13 14:10	1210	1.25			0.06	266	0.93
Sample	2/25/13 14:15	3/5/13 9:00	1154	0.94	4225	0.61	0.07	271	0.93
IC Rep	2/25/13 14:15	3/5/13 9:00	1147	0.93			0.07	271	0.93
Replicate	2/25/13 14:15	3/5/13 9:00	1217	1.02	3612	0.49	0.07	271	0.93
IC Rep	2/25/13 14:15	3/5/13 9:00	1209	1.01			0.07	271	0.93
Sample	3/5/13 9:08	3/11/13 9:35	890	0.86	4710	0.91	0.07	268	0.93
IC Rep	3/5/13 9:08	3/11/13 9:35	885	0.86			0.07	268	0.93
Replicate	3/5/13 9:08	3/11/13 9:35	1082	1.19	3242	0.55	0.07	268	0.93
IC Rep	3/5/13 9:08	3/11/13 9:35	1167	1.34			0.07	268	0.93
IC Rep	3/5/13 9:08	3/11/13 9:35	1075	1.18			0.07	268	0.93
IC Rep	3/5/13 9:08	3/11/13 9:35	1159	1.32			0.07	268	0.93
Sample	3/11/13 9:40	3/18/13 10:22	1340	1.37	3898	0.61	0.07	269	0.93
IC Rep	3/11/13 9:40	3/18/13 10:22	1331	1.36			0.07	269	0.93
Replicate	3/11/13 9:40	3/18/13 10:22	1128	1.07	3276	0.47	0.07	269	0.93
IC Rep	3/11/13 9:40	3/18/13 10:22	1120	1.06			0.07	269	0.93
Sample	3/18/13 10:28	3/25/13 9:00	1192	1.31	4462	0.74	0.06	265	0.93

IC Rep	3/18/13 10:28	3/25/13 9:00	1184	1.30			0.06	265	0.93
Replicate	3/18/13 10:28	3/25/13 9:00	551	0.27	1273	0.05	0.06	265	0.93
IC Rep	3/18/13 10:28	3/25/13 9:00	548	0.27			0.06	265	0.93
Sample	3/25/13 9:00	4/1/13 9:00	1784	1.83	2866	0.39	0.08	273	0.93
IC Rep	3/25/13 9:00	4/1/13 9:00	1772	1.81			0.08	273	0.93
Replicate	3/25/13 9:00	4/1/13 9:00	1424	1.36	2746	0.36	0.08	273	0.93
IC Rep	3/25/13 9:00	4/1/13 9:00	1415	1.35			0.08	273	0.93
Sample	4/1/13 9:45	4/6/13 8:45	965	0.97	1876	0.25	0.08	277	0.93
IC Rep	4/1/13 9:45	4/6/13 8:45	959	0.96			0.08	277	0.93
Replicate	4/1/13 9:45	4/6/13 8:45	951	0.95	1885	0.26	0.08	277	0.93
IC Rep	4/1/13 9:45	4/6/13 8:45	945	0.94			0.08	277	0.93

FOUS

Sample	2/15/13 13:39	2/24/13 10:35	3591	3.79	3555	0.00	0.07	268	0.93
Replicate	2/15/13 13:39	2/24/13 10:35	2868	2.58	3713	0.45	0.08	273	0.93
Sample	2/24/13 10:40	3/3/13 11:30	2075	2.22	3853	0.60	0.08	273	0.93
Replicate	2/24/13 10:40	3/3/13 11:30	2328	2.55	4478	0.73	0.08	273	0.93
Sample	3/3/13 11:30	3/10/13 11:32	2264	2.86	2369	0.28	0.07	267	0.93
Replicate	3/3/13 11:30	3/10/13 11:32	2444	3.13	2325	0.27	0.07	267	0.93
Sample	3/10/13 11:35	3/17/13 11:16	1958	2.25	3885	0.61	0.07	269	0.93
Replicate	3/10/13 11:35	3/17/13 11:16	2627	3.20	7975	1.48	0.07	269	0.93
Sample	3/17/13 11:23	3/24/13 12:05	1854	2.54	5010	0.84	0.06	262	0.93
Replicate	3/17/13 11:23	3/24/13 12:05	2076	2.92	6322	1.12	0.06	262	0.93
Sample	3/24/13 12:05	3/31/13 12:00	4897	6.52	2959	0.41	0.07	269	0.93
Replicate	3/24/13 12:05	3/31/13 12:00	4998	6.67	2691	0.35	0.07	269	0.93
Sample	3/31/13 12:05	4/4/13 15:23	1280	1.93	1180	0.05	0.08	274	0.93
Replicate	3/31/13 12:05	4/4/13 15:23	1246	1.86	1292	0.09	0.08	274	0.93
IC Rep	3/31/13 12:05	4/4/13 15:23	1276	1.92	0	0.00	0.08	274	0.93

MELA

Sample	2/17/13 13:30	2/24/13 13:40	1641	2.09	2588	0.33	0.06	264	0.93
Replicate	2/17/13 13:30	2/24/13 13:40	843	0.77	3746	0.58	0.06	264	0.93
Sample	2/24/13 13:45	3/3/13 14:10	1440	1.45	5096	0.86	0.07	271	0.93
Replicate	2/24/13 13:45	3/3/13 14:10	841	0.63	4281	0.69	0.07	271	0.93

Sample	3/3/13 14:15	3/10/13 14:05	1001	1.01	3758	0.58	0.06	264	0.93	
Replicate	3/3/13 14:15	3/10/13 14:05	1074	1.13	3888	0.61	0.06	264	0.93	
Sample	3/10/13 14:10	3/17/13 14:47	1006	0.94	4695	0.78	0.07	267	0.93	
Replicate	3/10/13 14:10	3/17/13 14:47	*905	*0.79	*7114	*1.29	0.07	267	0.93	Prep
Sample	3/17/13 14:47	3/24/13 15:35	1268	1.52	7404	1.35	0.06	262	0.93	
Replicate	3/17/13 14:47	3/24/13 15:35	962	0.99	6098	1.07	0.06	262	0.93	
Sample	3/24/13 15:35	3/31/13 15:30	1241	1.38	3571	0.54	0.06	265	0.93	
Replicate	3/24/13 15:35	3/31/13 15:30	1110	1.17	4215	0.68	0.06	265	0.93	
Sample	3/31/13 15:35	4/4/13 10:44	754	0.94	2472	0.56	0.07	271	0.93	
Replicate	3/31/13 15:35	4/4/13 10:44	754	0.94	2343	0.51	0.07	271	0.93	

KNRI

Sample	2/14/13 17:20	2/19/13 13:30	656	0.61	3588	0.79	0.06	266	0.94	
Replicate	2/14/13 17:20	2/19/13 13:30	822	0.98	3316	0.70	0.06	266	0.94	
Sample	2/19/13 13:40	2/26/13 14:25	1498	1.70	13810	2.71	0.06	267	0.94	
Replicate	2/19/13 13:40	2/26/13 14:25	1636	1.91	14555	2.87	0.06	267	0.94	
Sample	2/26/13 14:30	3/5/13 16:40	1033	0.89	5280	0.89	0.07	270	0.94	
Replicate	2/26/13 14:30	3/5/13 16:40	829	0.61	4487	0.73	0.07	270	0.94	
IC Rep	2/26/13 14:30	3/5/13 16:40	824	0.61			0.07	270	0.94	
Sample	3/5/13 16:46	3/12/13 13:48	1082	1.08	12753	2.54	0.07	267	0.94	
Replicate	3/5/13 16:46	3/12/13 13:48	892	0.79	7491	1.40	0.07	267	0.94	
Sample	3/12/13 13:53	3/19/13 14:40	1265	1.38	15461	3.06	0.06	266	0.94	
Replicate	3/12/13 13:53	3/19/13 14:40	1044	1.04	12200	2.37	0.06	266	0.94	
Sample	3/19/13 14:45	3/26/13 14:20	891	0.81	6971	1.27	0.06	265	0.94	
Replicate	3/19/13 14:45	3/26/13 14:20	1201	1.30	6094	1.08	0.06	265	0.94	
Sample	3/26/13 14:20	4/2/13 12:27	1544	1.61	9753	1.88	0.07	271	0.94	
Replicate	3/26/13 14:20	4/2/13 12:27	1508	1.56	8782	1.67	0.07	271	0.94	

THRO-S

Sample	2/12/13 10:26	2/18/13 14:30	847	0.71	1940	0.22	0.07	272	0.91	
Replicate	2/12/13 10:26	2/18/13 14:30	1027	0.98	1943	0.22	0.07	272	0.91	
IC Rep	2/12/13 10:26	2/18/13 14:30	1021	0.97			0.07	272	0.91	
Sample	2/18/13 14:30	2/26/13 10:55	1625	1.65	1738	0.13	0.07	268	0.91	
IC Rep	2/18/13 14:30	2/26/13 10:55	860	0.64	0	0.00	0.07			

Replicate	2/18/13 14:30	2/26/13 10:55	1120	0.98	2300	0.24	0.07	268	0.91
Sample	2/26/13 11:00	3/5/13 12:17	967	0.77	2259	0.26	0.07	272	0.91
Replicate	2/26/13 11:00	3/5/13 12:17	1066	0.90	2264	0.26	0.07	272	0.91
Sample	3/5/13 12:22	3/12/13 10:20	1085	1.04	2890	0.40	0.07	268	0.91
Replicate	3/5/13 12:22	3/12/13 10:20	914	0.79	2544	0.32	0.07	268	0.91
Sample	3/12/13 10:20	3/19/13 10:52	1165	1.11	3038	0.42	0.07	270	0.91
Replicate	3/12/13 10:20	3/19/13 10:52	1639	1.78	4069	0.64	0.07	270	0.91
Sample	3/19/13 10:53	3/26/13 9:50	1359	1.56	1853	0.18	0.06	265	0.91
Replicate	3/19/13 10:53	3/26/13 9:50	1054	1.07	2247	0.26	0.06	265	0.91
IC Rep	3/19/13 10:53	3/26/13 9:50	1024	1.03			0.06	265	0.91
Sample	3/26/13 9:50	4/2/13 17:51	2179	2.11	2007	0.20	0.08	275	0.91
IC Rep	3/26/13 9:50	4/2/13 17:51	2165	2.09			0.08	275	0.91
Replicate	3/26/13 9:50	4/2/13 17:51	2293	2.24	1849	0.17	0.08	275	0.91
IC Rep	3/26/13 9:50	4/2/13 17:51	2278	2.22			0.08	275	0.91